

Novel rhenium(I) tricarbonyl complexes towards catalytic, photophysical and biological applications

Menglan He

▶ **To cite this version:**

Menglan He. Novel rhenium(I) tricarbonyl complexes towards catalytic, photophysical and biological applications. Other. Université Paris sciences et lettres; East China normal university (Shanghai), 2019. English. ⟨NNT : 2019PSLEE005⟩. ⟨tel-02426024⟩

HAL Id: tel-02426024

https://theses.hal.science/tel-02426024v1

Submitted on 1 Jan 2020

HAL is a multi-disciplinary open access archive for the deposit and dissemination of scientific research documents, whether they are published or not. The documents may come from teaching and research institutions in France or abroad, or from public or private research centers.

L'archive ouverte pluridisciplinaire **HAL**, est destinée au dépôt et à la diffusion de documents scientifiques de niveau recherche, publiés ou non, émanant des établissements d'enseignement et de recherche français ou étrangers, des laboratoires publics ou privés.



HAL Authorization

PSL UNIVERSITÉ PARIS

THÈSE DE DOCTORAT
DE L'UNIVERSITÉ PSL

Préparée à [Ecole Normale Supérieure]
Dans le cadre d'une cotutelle avec [East China Normal University]

Nouveaux Complexes Rhénium(I) Tricarbonyles vers des Applications en Catalyse, Photophysique et Biologie

Novel Rhenium(I) Tricarbonyl Complexes Towards Catalytic, Photophysical and Biological Applications

Soutenue par
Menglan HE
Le 06 mai 2019

Ecole doctorale n° 406
Chimie moléculaire de Paris Centre

Spécialité
Chimie bio inorganique

Composition du jury :

Gilles, GASSER Professeur, Chimie ParisTech	*Président*
Shaodong, ZHANG Professeur, Shanghai Jiaotong University	*Rapporteur*
Gilles, LEMERIER Professeur, Universite Reims Champagne-Ardenne	*Rapporteur*
Jian, ZHOU Professeur, East China Normal University	*Examinateur*
Clotilde, POLICAR Professeur, Ecole Normale Supérieure	*Directeur de thèse*
Haibo, YANG Professeur, East China Normal University	*Codirecteur de thèse*
Hélène, BERTRAND Maître de conférence, Sorbonne Université	*Co-encadrant*

ENS | PSL

Acknowledgements

First and most important, I would like to thank the programme of Sino-French education for research (PROSFER) between East China Normal University (ECNU) and Ecole Normale Supérieure (ENS) to offer this great opportunity to spend my PhD study in Paris. Also, I would like to thank China Scholar Council for the financial support. I really appreciate the chance to spend almost four years at ENS in Paris for my PhD study, during which I really enjoyed the sophisticated and elegant life in this splendid city. I would like to give my sincerely gratitude to all those who helped and supported me during this period.

I would like to express my great gratitude to my supervisor professor Clotilde Policar of the department of chemistry at ENS, who kindly accepted me as one of the members in her group. She is intelligent and her continuous spirit of exploration always surprised me. Her supervision will have an influence throughout my life. Meanwhile, I am immensely grateful to Doctor Hélène Bertrand of the department of chemistry at Sorbonne Université. I am always impressed by her rigorous attitude towards science, excellent problem-solving abilities and high efficiency. I really appreciate her patient instruction and kind assistance during my PhD study. Both of them made great efforts on correcting my PhD manuscript.

I would also like to thank my co-supervisor professor Haibo Yang of key laboratory of green chemistry and chemical process at East China Normal University, who supported me to join the PROSFER program and with whom I spent three-year master study. He is always available when I have problems with administration paper. I really appreciate that he will come to Paris for my PhD defence. I am so excited to see him again.

I acknowledge all the members in my defence committee: professor Gilles Lemercier of unviversité de Reims Champagne-Ardenne, professor Shaodong Zhang of Shanghai Jiaotong university for the precious evaluation of this work; professor Gilles Gasser of PSL université and professor Jian Zhou of ECNU for assessing the examination of this thesis. I also ackowledge all the reporters for evaluating my manuscript: professor Laurence Grimaud of Ecole Normale Supérieure, professor Fethi Bedioui of Chimie ParisTech and professor Rodrigue Lescouezec of Sorbonne Université.

Special thanks to everyone who helped and contributed in the development of my projects. I am grateful to Doctor Sophie Griveau of Chimie Paris Tech for her kindly help for the electrochemistry part. I am so glad that we have collaboration with her. She is busy with teaching but she is always ready to help me at any time. I learnt a lot of electrochemistry in three months working with her. I also thank Marc Fentacave's group for their collaboration. Many thanks to Professor Laurence Grimaud and professor Jean-Maurice Mallet of ENS for their valuable advises for the organic synthesis. I would thank Nicoas Delsuc of CNRS for his kindly help for peptide synthesis. He is very experienced.

I extend my thanks to all my colleagues in the groups I worked: Sarah Hostach, Paul Demay-Dourhard, Emillie Mathieu, Vincent Ching, Anne-Sophie Bernard, Lucas Henry, Amandine Vincent, Koudedja Coulibaly, Martha Zoumpoulaki. They offered friendly working environment, which is also important for me. I would thank the internship students: Noemi Perujo, Jennifer Rodon, Scott Hobbs and Azalea Micottis. We spent pleasant time together doing synthesis in the laboratory. Best wishes them for their bright future.

Special thanks to all my friends who keeps me accompany when I am depressed. They accept all my deficiency and always try to cheer me up. We walked through mountains and water, discussed philosophy and literature and agued with each other. These years will be one of the most important periods in my life.

Last but not the least, I would thank my parents for their financial and spiritual support during the PhD study. They are very open-minded though sometimes they don’t understand me very well. I really appreciate their selfless love. I wish them a very happy life.

Table of contents

Abbreviation list **4**

Compound list **5**

General introduction **21**

1. Photophysical study of Re(I) tricarbonyl complexes: structural variations **24**

1.1 Introduction **24**

1.1.1 Photophysical properties of rhenium(I) tricarbonyl complexes 25

1.1.2 "Click-to-chelate" tridentate ligands 26

1.1.3 Pyta based Re(I) complexes - structural and application study 28

1.1.4 Tapy based Re(I) complexes 31

1.1.5 Other bidentate ligands 32

1.1.6 Proposal of the project 33

1.2 Rhenium complexes with modified Pyta ligands **35**

1.2.1 Synthesis and characterisations 36

1.2.2 Photophysical investigation 41

1.2.3 Computational investigation 43

1.2.4 Summary 47

1.3 Rhenium complexes bearing acetylide ligands **48**

1.3.1 Synthesis and stability 48

1.3.2 Photophysical investigation 50

1.3.3 Electrochemical investigation 52

1.3.4 Computational investigation 52

1.3.5 Summary 56

1.4 Rhenium complexes with arenethiolate ligands **57**

1.4.1 Synthesis and stability 57

1.4.2 Photophysical investigation 59

1.4.3 Electrochemical investigation 62

1.4.4 Computational investigation 63

1.4.5 Summary 68

1.5 General conclusions and perspectives **70**

1.6 Conclusion générale et perspectives **71**

2. Rhenium(I) complexes as catalysts for CO_2 electroreduction **72**

2.1 Introduction **72**

2.1.1 Useful notations 74

2.1.2 Mechanistic investigation 74

2.1.3 Rhenium(I) tricarbonyl complexes as homogeneous catalysts 77

2.1.4 Rhenium(I) tricarbonyl complexes as heterogeneous catalysts 81

2.1.5 Proposal of the project 88
2.2 Rhenium complexes as homogeneous catalysts for CO_2 electroreduction 90
2.2.1 Structure-activity study 90
2.2.2 Catalytic activity of complex 16 91
2.3 Rhenium complexes towards electrochemical immobilisation on electrode 98
2.3.1 Synthesis of the complexes 98
2.3.2 Electrochemical characterisation 100
2.3.3 Electrochemical immobilisation on the electrode 101
2.3.4 Summary 108
2.4 Rhenium complexes towards non-covalent immobilisation on electrode 109
2.4.1 Synthesis of the complexes 109
2.4.2 Electrochemical characterisation in the absence/presence of CO_2 110
2.4.3 Non-covalent immobilisation on the electrode and catalytic abilities 111
2.4.4 Summary 114
2.5 General conclusions and perspectives 115
2.6 Conclusion générale et perspectives 116

3. Rhenium(I) complexes as macrocyclic linkers in Keap1-Nrf2 peptidomimetics inhibitors 117
3.1 Introduction 117
3.1.1 Regulation of Keap1-Nrf2 pathway 117
3.1.2 Peptide inhibitors of the Keap1-Nrf2 interaction 121
3.1.3 Proposal of the project 126
3.2 Synthesis of modified amino acids 127
3.2.1 Synthesis of azido-modified amino acid 127
3.2.2 Synthesis of 2-ethynylpyridyl-modified amino acid 128
3.3 Peptide mimics synthesis 135
3.3.1 Synthesis of linear peptides 135
3.3.2 Synthesis of the cyclic peptide 138
3.4 Summary 143
3.5 Résumé 144

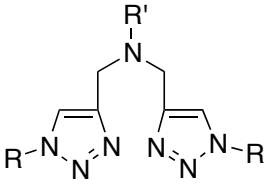
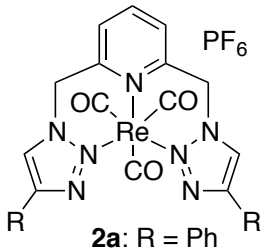
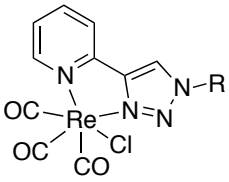
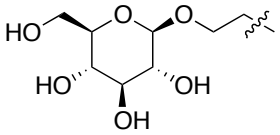
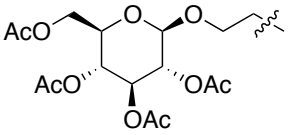
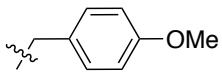
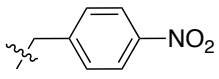
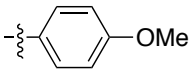
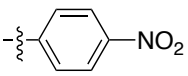
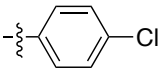
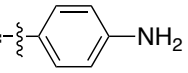
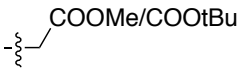
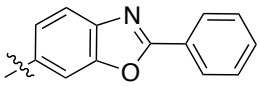
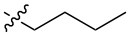
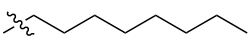
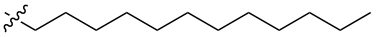
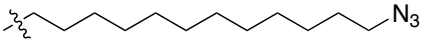
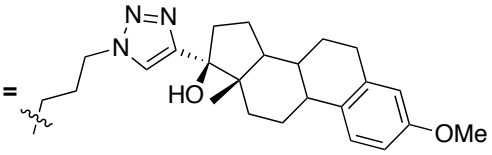
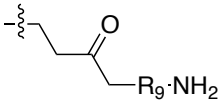
4. Experimental part 145
4.1 General information 145
4.2 Synthesis for photophysical study 147
4.2.1 Synthesis of Rhenium complexes with modified Pyta ligands 147
4.2.2 Synthesis of Rhenium complexes bearing acetylide ligands 156
4.2.3 Synthesis of Rhenium complexes with arenethiolate ligands 161
4.2.4 Luminescence quantum yield determination 164
4.2.5 DFT calculations 165
4.2.6 Electrochemistry 165
4.3 Synthesis for catalysts for CO_2 electroreduction 166

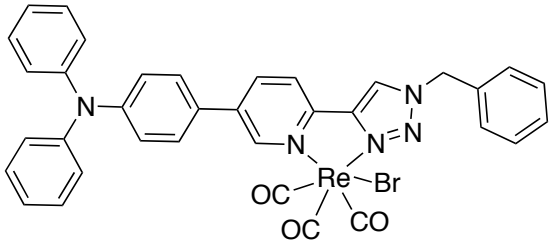
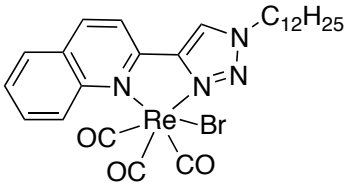
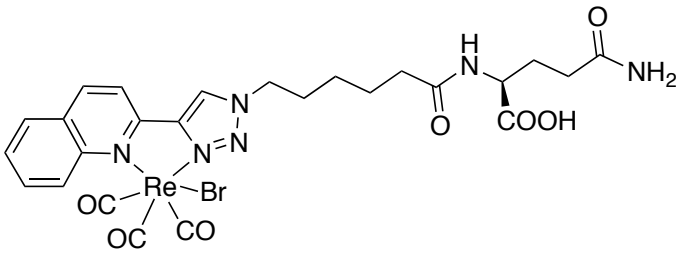
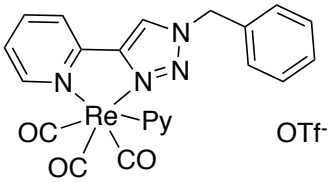
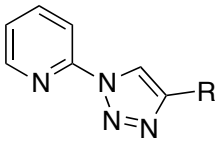
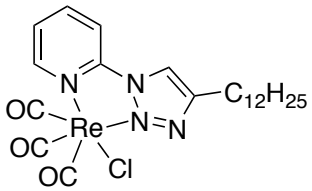
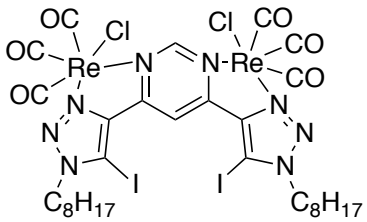
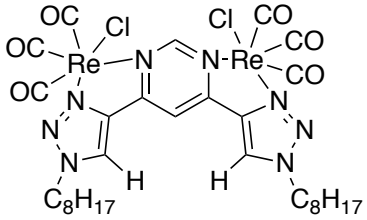
4.3.1 Synthesis of catalysts for covalent immobilisation method 166
4.3.2 Synthesis of catalysts for non-covalent immobilisation method 174
4.3.3 Electrochemistry 175
4.3.4 Chemical Analysis 176
4.4 Synthesis for Keap1-Nrf2 peptidomimetics inhibitors 177
4.4.1 Synthesis of azido-modified amino acid 177
4.4.2 Synthesis of 2-ethynylpyridyl-modified amino acid using amidation 178
4.4.3 Synthesis of 2-ethynylpyridyl-modified amino acid using other strategy 183
4.4.4 Peptide synthesis 185
4.4.5 Quantification of Fmoc loading 187
References 188
Appendix 201

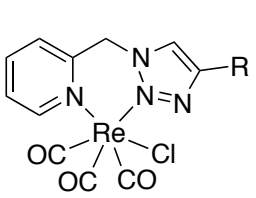
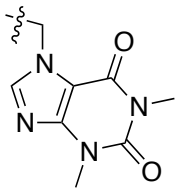
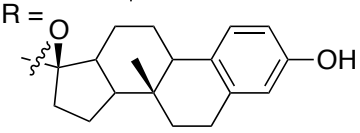
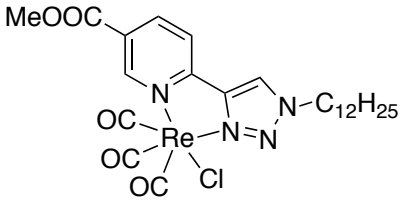
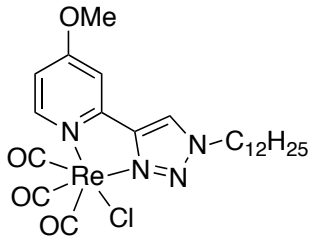
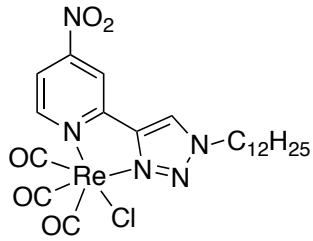
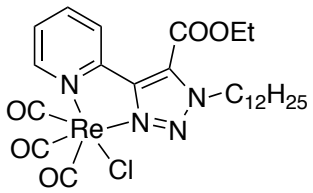
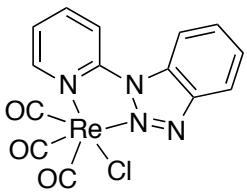
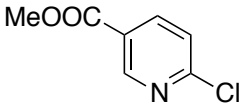
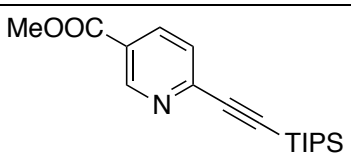
Abbreviation list

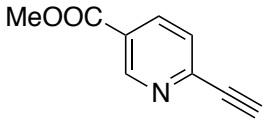
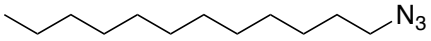
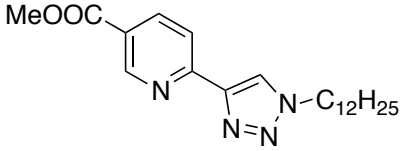
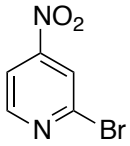
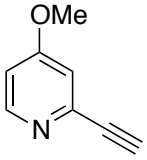
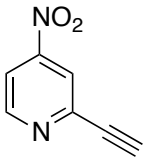
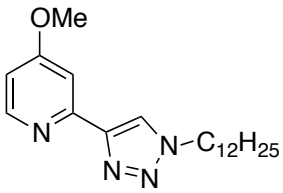
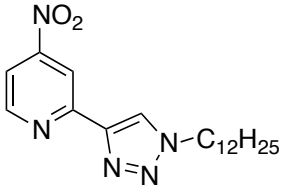
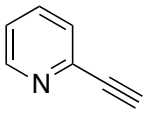
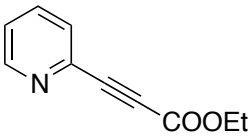
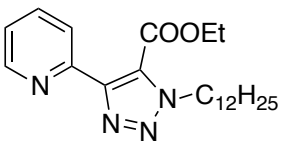
BOC	Tert-Butyloxycarbonyl
CuAAC	Copper(I)-catalyzed alkyne-azide cycloaddition
DBU	1,8-diazabicyclo(5.4.0)undec-7-ene
DFT	Density functional theory
DIEA	N,N-Diisopropylethylamine
EDG	Electron-donating group
ESI	Electrospray ionisation
EWG	Electron-withdrawing group
Fmoc	fluorenylmethyloxycarbonyl
HATU	1-[Bis(dimethylamino)methylene]-1H-1,2,3-triazolo[4,5-b]pyridinium 3-oxide hexafluorophosphate
HBTU	3-[Bis(dimethylamino)methyliumyl]-3*H*-benzotriazol-1-oxide hexafluorophosphate
HPLC	High performance liquid chromatography
HRMS	High resolution mass spectrometry
ICT	Intraligand charge transfer
ISC	Intersystem crossing
LLCT	Ligand-to-ligand charge transfer
MALDI	Matrix-assisted laser desorption/ionisation
MLCT	Metal-to-ligand charge transfer
MS	Mass spectrometry
NMP	*N*-methyl-2-pyrrolidone
NMR	Nuclear magnetic resonance
OCP	Open circuit potential
PPI	Protein-protein interaction
SCE	Saturated calomel electrode
SHE	Stardard hydrogen electrode
TIPS	Triisopropylsilyl
TMS	Trimethylsilyl
ToF	Time-of-flight

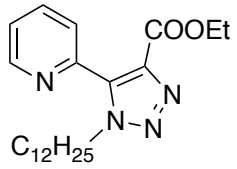
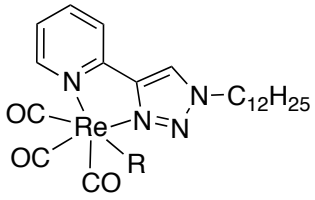
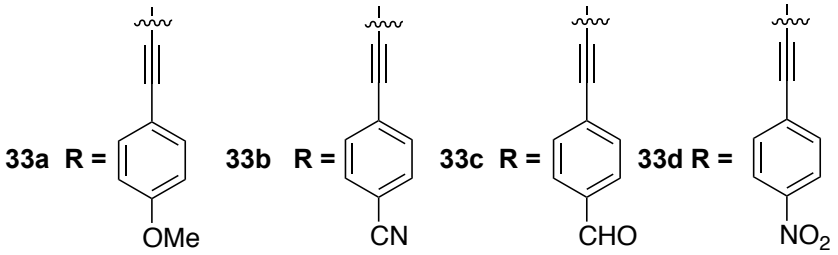
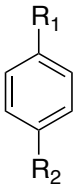
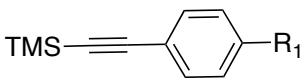
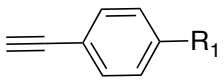
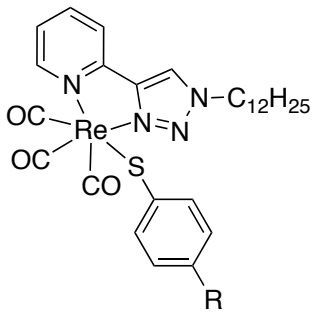
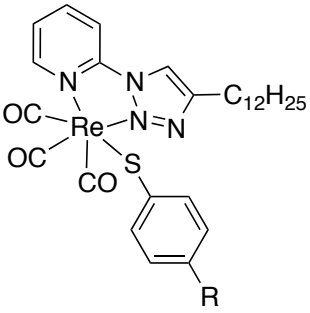
Compound list

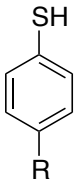
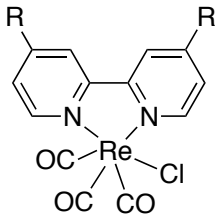
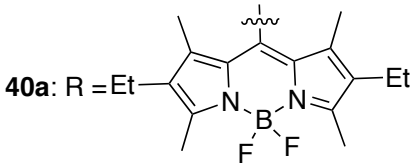
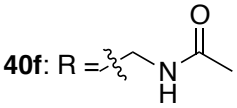
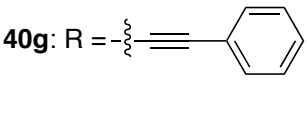
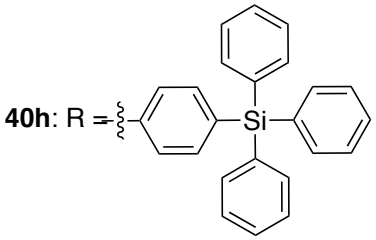
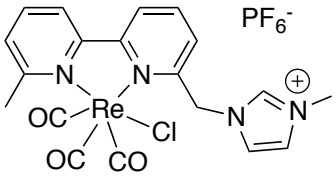
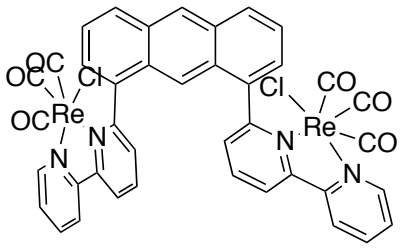
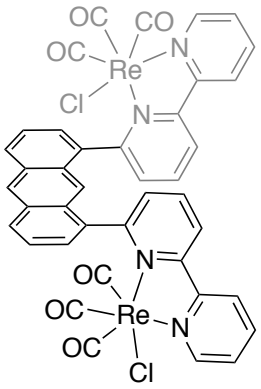
Number	structure
1	
2	 **2a**: R = Ph **2b**: R = C_3H_7
3	 **3** **3a: R = Bn** **3b: R =**  **3c: R =**  **3d: R =** C_8H_{17} **3e: R = CH_2Ph** **3f: R =**  **3g: R =**  **3h: R = Ph** **3i: R = Fc** **3j: R =**  **3k: R =**  **3l: R =**  **3m: R =**  **3n: R =**  **3o: R =**  **3p: R =**  **3q: R =**  **3r: R =**  **3s: R =**  **3t: R =**  **3u: R =** 

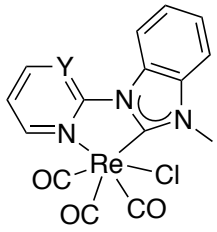
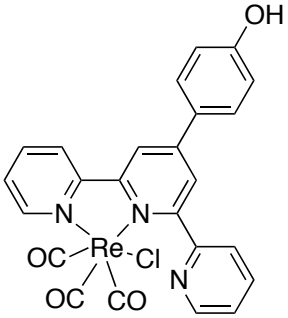
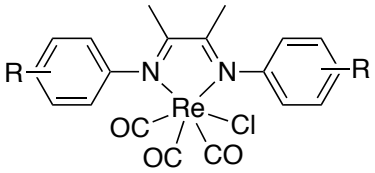
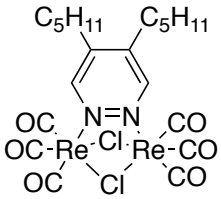
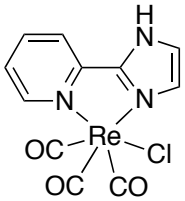
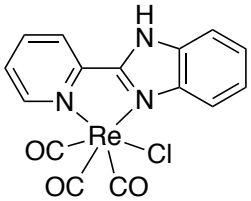
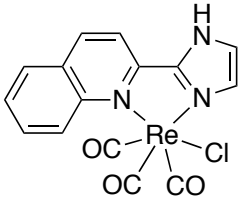
4	
5	
6	
7	
8	
9	
10	
11	

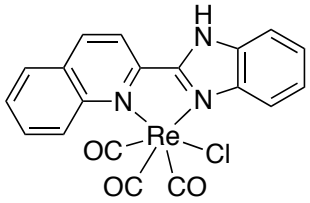
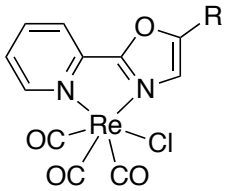
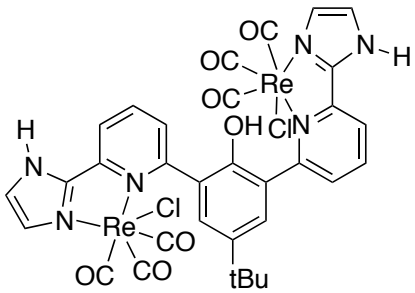
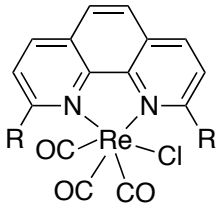
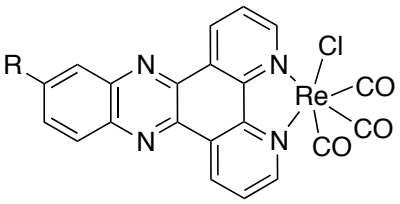
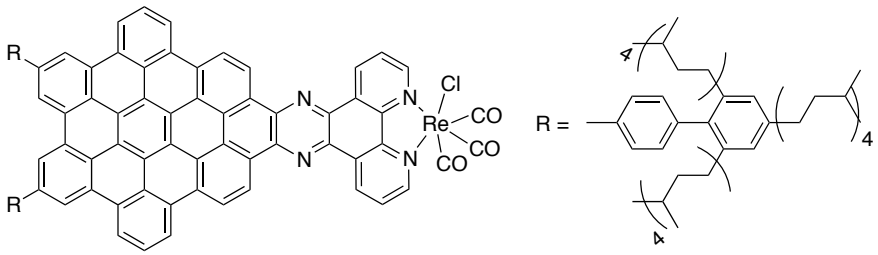
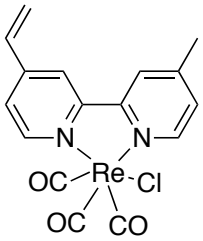
12	 **12a**: R = Ph **12b**: R = 4-NO_2Ph **12c**: R = 4-MePh **12d**: R = Bn **12e**: R =  **12f**: R =  **12g**: R = graphene
13	
14	
15	
16	
17	
18	
19	

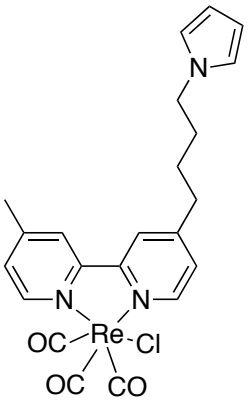
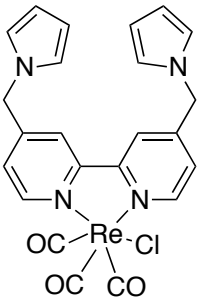
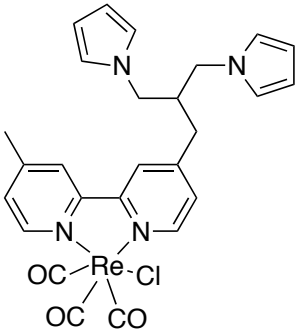
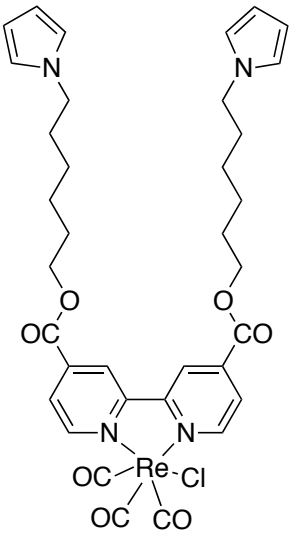
20	
21	
22	
23	**Re(CO)5Cl**
24	
25	
26	
27	
28	
29	
30	
31	

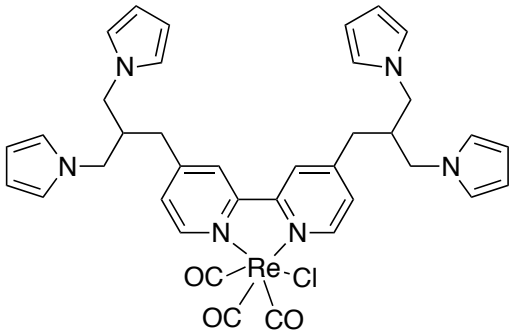
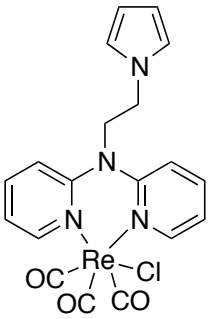
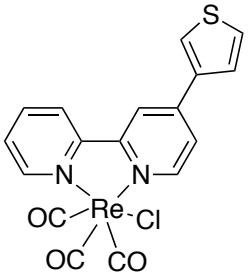
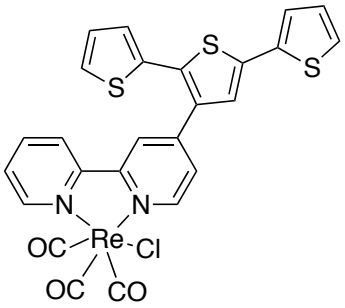
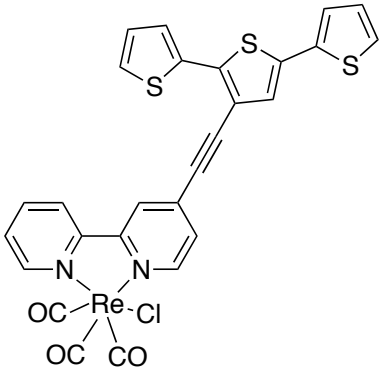
32	
33	 **33**  **33a R =** **33b R =** **33c R =** **33d R =**
34	 **34a:** R_1 = OMe, R_2 = I **34b**: R_1 = CN, R_2 = Br **34c**: R_1 = CHO, R_2 = Br **34d**: R_1 = NO_2, R_2 = Br
35	 **35a**: R_1 = OMe, 93% **35b**: R_1 = CN, 42% **35c**: R_1= CHO, 83% **35d**: R_1 = NO_2, 18%
36	 **36a**: R_1 = OMe, 55**%** **36b**: R_1 = CN, 72% **36c**: R_1 = CHO, 23% **36d**: R_1 = NO_2, 95%
37	 **37a**: R = H, 45% **37b**: R = OMe, 20% **37c**: R = CO_2Me, 48% **37d**: R = NO_2, 54%
38	 **38a**: R = H, 37% **38b**: R = OMe, 35% **38c**: R = CO_2Me, 56% **38d**: R = NO_2, 37%

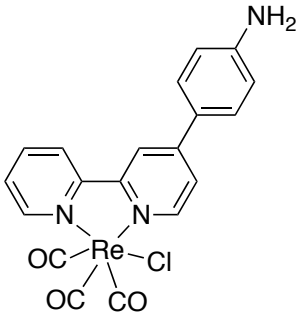
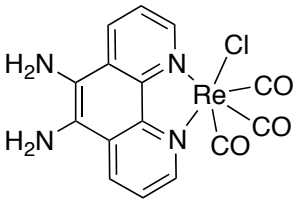
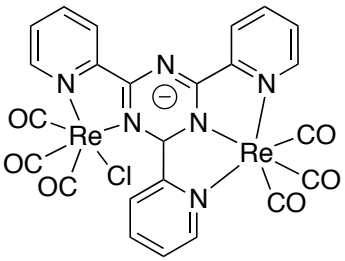
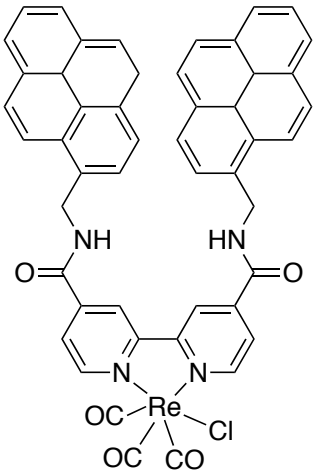
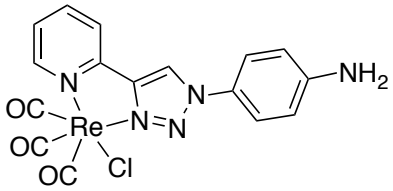
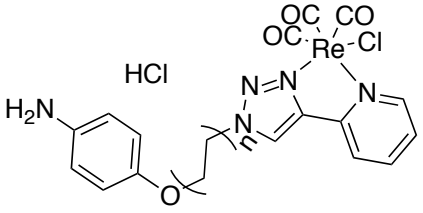
39	 **39a**: R = H **39b**: R = OMe **39c**: R = CO_2Me **39d**: R = NO_2
40	 **40**  **40a**: R = Et **40b**: R = tBu 40c: R = carboxy **40d**: R = methyl **40e**: R = methoxy  **40f**: R =  **40g**: R =  **40h**: R =
41	
42	 ***cis*-42**  ***trans*-42**

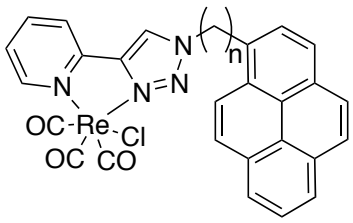
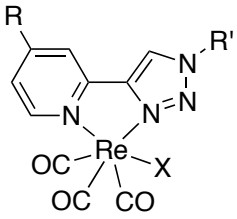
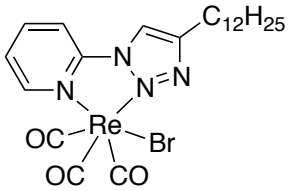
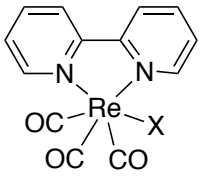
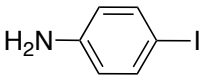
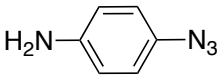
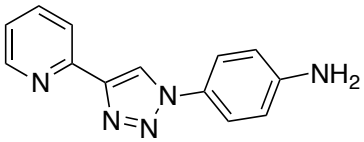
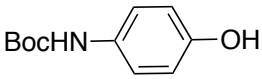
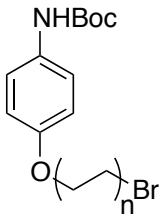
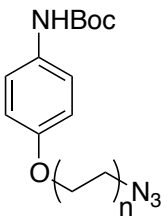
43	 **43a** R = C-H **43b** R = N
44	
45	 **45a** R = 2,4,6-Me_3 **45b** R = 2,6-$^{i}Pr_2$ **45c** R = 4-Br **45d** R = 2-CF_3
46	
47	
48	
49	

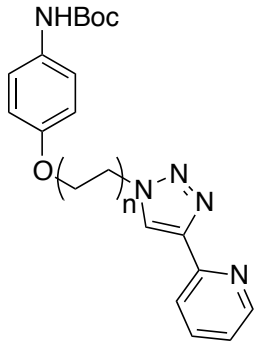
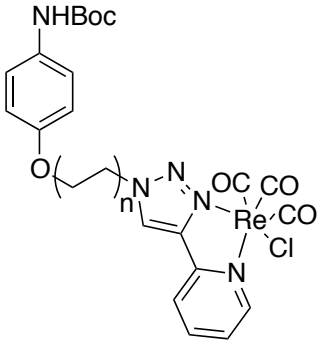
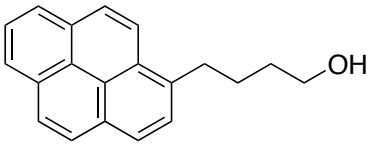
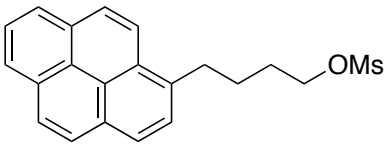
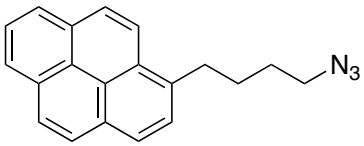
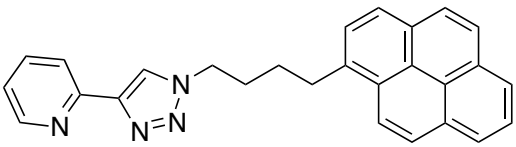
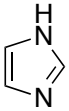
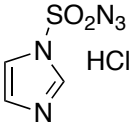
50	
51	 **51a** R = H **51b** R = CH_3 **51c** R = Ph
52	
53	 **53a**: R = Methyl **53b**: R = 2,4,6-trimethylphenyl **53c**: R = 2,4,6-trimethoxyphenyl **53d**: R = 3,4,5-trimethoxylphenyl
54	 **54a**: R = CF_3 **54b**: R = NO_2 **54c**: R = H **54d**: R = tBu
55	
56	

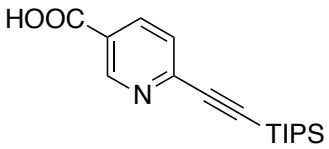
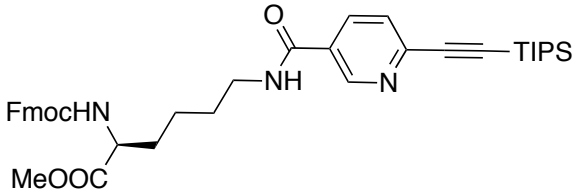
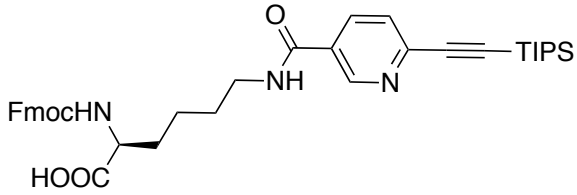
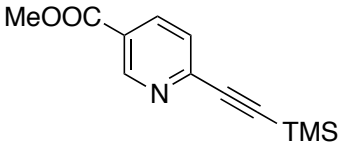
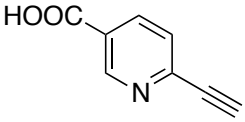
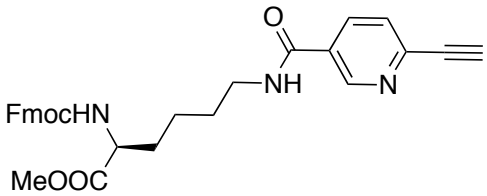
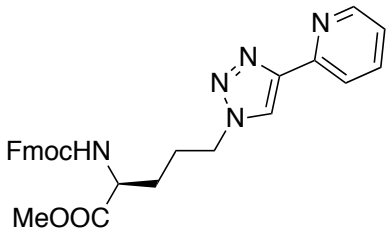
57	
58	
59	
60	

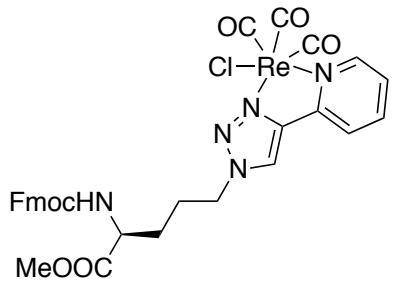
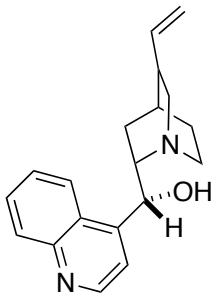
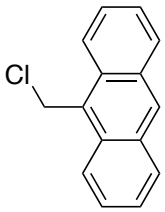
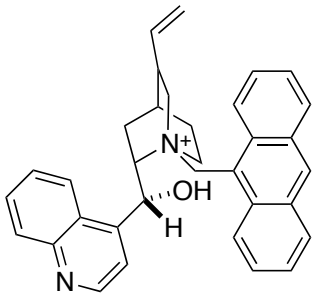
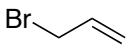
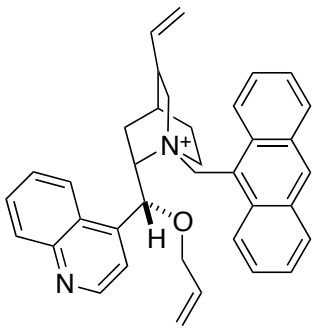
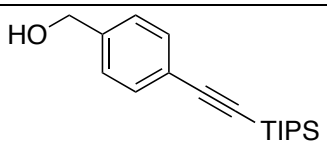
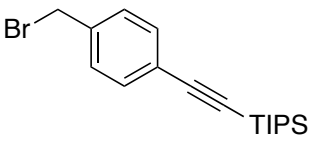
61	
62	
63	
64	
65	

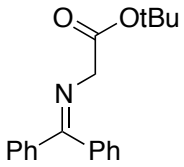
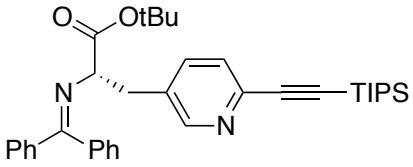
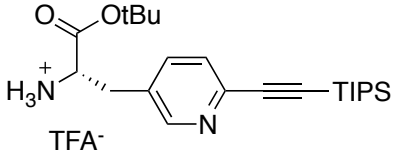
66	
67	
68	
69	
70	
71	 **71a**: n = 2 **71b**: n = 3 **71c**: n = 4

72	 **72a:** n = 0 **72b:** n = 1 **72c:** n = 4
73	 **73a**: X = Cl, R = H, R' = tolyl **73b**: X = Cl, R = H, R' = tri(tert-butyl)phenyl **73c**: X = Cl, R = H, R' = C_3H_6OH **73d**: X = Br, R = H, R' = $C_{12}H_{25}$
74	
75	 **75a**: X = Cl **75b**: X = Br
76	
77	
78	
79	
80	 **80a**: n = 2 **80b**: n = 3 **80c**: n = 4
81	 **81a**: n = 2 **81b**: n = 3 **81c**: n = 4

82	 **82a**: n = 2 **82b**: n = 3 **82c**: n = 4
83	 **83a**: n = 2 **83b**: n = 3 **83c**: n = 4
84	
85	
86	
87	
88	
89	
90	Fmoc-Lys-OH
91	Fmoc-Lys(N_3)-OH · HCl

92	
93	Fmoc-Lys-OH
94	Fmoc-Lys-OMe · HCl
95	
96	
97	
98	
99	
100	Fmoc-Orn(tBu)-OH
101	Fmoc-Orn-OH · TFA
102	Fmoc-Orn-OMe · HCl
103	Fmoc-Orn(N3)-OMe · HCl
104	

105	
106	
107	
108	
109	
110	
111	
112	

113	
114	
115	

General introduction

The past few decades have witnessed a rapid growth in the development of rhenium *fac*-tricarbonyl complexes of general formula $[Re(N^N)(CO)_3X]^{n+}$ in the field of CO_2 reduction,[1–4] materials,[5,6] sensors[7–11] and bio-imaging[8,12–15] owing to their unique photophysical and electronic properties.

$[Re(N^N)(CO)_3X]^{n+}$ complexes have relatively high photostability and long-lived phosphorescence that allow time-resolved detection, as well as large Stokes shifts that can minimize the possible self-quenching effect. Therefore, various sensors for chemical substance and probes based on luminescent Re(I) tricarbonyl complexes (protons,[16,17] ions,[10,18–20] oxygen,[21–29] etc.) were developed. Meanwhile, generally displaying good cellular uptake properties, biological stability and low toxicity, luminescent Re(I) tricarbonyl complexes attracted considerable interest as cellular imaging reagents in recent years.[12,13,30,31]

The photophysical behaviour of $[Re(N^N)(CO)_3X]^{n+}$ has been well investigated due to their dynamic and tuneable excited state properties.[31,32] For most of these complexes with N^N ligands showing low lying π^* orbitals, the lowest energy electronic absorption and emitting state is assigned to a $d\pi(Re)\rightarrow\pi^*(N^N)$ metal-to-ligand charge transfer state (MLCT), which was first reported by M. Wrighton *et al.* in year 1974.[33] There are also several examples in which the lowest emissive excited state was characterized as a mixture of ^{3}MLCT and a triplet intraligand (^{3}IL) state.[34–38] It is possible to tune the MLCT energy[39] by the modulation of either the N^N ligand or the axial ligand X which will mainly have an influence on the energies of the $\pi^*(N^N)$ and high lying filled orbitals, respectively. Thus, varieties of ligands, especially polypyridyl ligands[40–42] were developed to tune the MLCT energy and modify the photophysical properties of the corresponding complexes. Inspired from 4, 4'-bipyridine,[43] the 4-(2'-pyridyl)-1,2,3-triazole (Pyta) ligand was first reported by M. Obata, S. Yano et al. in a $Re(Pyta)CO_3Cl$ complex in 2008.[44] Since then, different modifications of the side chains of this ligand have been developed because of its simple and efficient synthetic access through copper-catalysed azide-alkyne cycloaddition reaction (CuAAC).[44–47] Meanwhile, our group found that the inversion of the bridge between the triazole ring and the pyridine in the ligand (generating the 1-(2'-pyridyl)-1,2,3-triazole called Tapy) leads to a red shift of the absorption and emission bands and an increase of quantum yield in aqueous solution.[48]

Re tricarbonyl complexes are also interesting vibrational probes as they show intense absorption bands in the 1800 – 2200 cm^{-1} range, where the biological samples do not absorb (IR transparency window). This property offers an additional possibility for rhenium tricarbonyl complexes to be mapped in IR imaging.[13,49,50] Recently, we have also shown that they can be imaged with a third modality, X-fluorescence using the Re-atom.[51]

Based on these advantages, our group has developed series of Pyta-based rhenium tricarbonyl complexes with applications in multimodal (luminescent and IR) imaging in cells and coined the term single-core multimodal probe for imaging (SCoMPI)[49,52–56] for these complexes.

We have a continuing interest in investigating the impact of structural modifications on the photophysical properties of rhenium tricarbonyl complexes. Typical excitation wavelength of $Re(Pyta)(CO)_3X$ complexes is around 330 nm, while typical excitation wavelength of $Re(Tapy)(CO)_3X$ complexes is around 350 nm, which are not ideal for bioimaging. Complexes that could be excited with visible light while keeping a reasonable quantum yield would be highly desirable. Thus, in this work, we explored diverse modifications on either the diimine ligand or the X axial ligand towards this goal. We synthesized several series of new complexes, characterized their electrochemical and photophysical properties and performed DFT calculations to rationalize our observations. These studies will constitute the first chapter of this manuscript.

As mentioned above, rhenium tricarbonyl complexes are also used as catalysts for CO_2 electro-reduction. The development of human society has been accelerated with the use of coal, petroleum oil, natural gas and fossil fuels, accompanied with large amount of CO_2 emissions, which disturbs the natural carbon cycle and causes global environmental warming. Meanwhile, these energy sources are limited and non-renewable, meaning that they will be depleted someday. Thus, the recycling and conversion of CO_2 to renewable chemicals and fuels is a valuable alternative to deal with this issue. However, due to its chemical stability, CO_2 requires activation for its conversion. The standard potential of the $CO_2/CO_2^{\cdot-}$ couple is -1.97 V versus SHE in DMF[57] and -1.90 V versus SHE in water,[58] which means it is quite difficult to reduce. Thus, catalysts have been developed for this purpose.[59] First reported as Ni and Co macrocyclic complexes in 1980 by B. J. Fisher and R. Elsenberg,[60] metal complexes with Fe, Re, Ru, Ir, Rh, Mn, and others[19,61] have attracted considerable interest. Metal complexes are able to store multiple electrons not only at the metal centre but also in the ligand π system, which may facilitate the reduction of CO_2. Among all of them, [2,2′-bipyridine]-chlorotricarbonylrhenium(I) ($[Re(bpy)(Cl)(CO)_3]$) is known to have a high Faradaic efficiency for the generation of CO in the presence of Brønsted acids.[62]

In collaboration with F. Bedioui and M. Fontecave's groups, we have explored the structure-activity relationship of a series of Re diimine complexes as catalysts for CO_2 electroreduction.[63] Although some of the complexes showed good catalytic ability in solution, the non-recyclable character and high cost are limitations and implementation in devices are needed for industrial utilisation. We thus turned our attention to heterogeneous systems through the functionalisation or modification of the electrode with catalytically effective complexes.[64] Two approaches were explored: electrochemical immobilisation by electrochemical oxidation of aniline or electrochemical reduction of aryl diazonium salts on the glassy carbon electrode surface and non-covalent immobilisation *via* π-π interactions on carbon nanotubes. New series of Pyta rhenium(I) complexes bearing aniline groups or a pyrene unit were designed and synthesized. Modified electrodes were prepared and their catalytic ability towards CO_2 electroreduction and selectivity were evaluated. This work will be described in the second chapter of this manuscript.

Finally, we started to explore the use of rhenium tricarbonyl complexes in the design of secondary structure mimics for the modulation of protein-protein interactions (PPIs). The metal

carbonyl core plays a dual role of structural constraint – taking advantage of its chemical stability and octahedral geometry – and imaging moiety for applications in cells. Protein-protein interactions (PPIs) are involved in most cellular processes and biological functions such as enzymatic activity, subcellular localisation and binding properties. The modulation of PPIs is one of the most important strategies towards next-generation therapeutics[65] and modulators of PPIs are promising candidates in drug development.[65–67] Among all of the PPIs that have been investigated, Keap1/Nrf2 has attracted attention due to its relevance in inflammatory diseases and neurodegenerative disorders (Alzheimer's disease, Parkinson's disease, Huntington's disease, ischaemia and stroke) and its implication in important defence mechanisms against oxidative stresses.[68] The Keap1/Nrf2 protein-protein interaction has been well investigated and involves a high affinity binding site in Nrf2 - ^{77}ETGE^{82}, which is folded into a β-turn upon interaction with Keap1.[69] Several peptide mimics have been developed as Keap1/Nrf2 inhibitors though few of them showed cellular activity[70–74] due to their limited cell penetration. In addition, peptides tend to lose their secondary structure in solution and exist in an ensemble of conformational states, which may result in relatively low target affinity upon binding.[75] Thermodynamically, a reaction leading to more disorder is entropically favoured. Starting from a system with a wide conformational space and organizing it, as it is the case with disordered peptides that bind to a target, is thus entropically disfavoured. A way to enhance the association constant is to reduce the starting conformational space, by pre-organizing the peptides appropriately for binding. Therefore, the pre-organisation can be seen as a way to pay the entropic penalty for the binding reaction. A classical strategy to pre-organise the secondary structures of the peptide is the introduction of a staple in helical peptides or macrocyclisation of the structure.[76] Here we explored the synthesis of macrocyclic Nrf2 peptidomimetics using a rhenium Pyta tricarbonyl complex as the macrocyclic linker and as core for luminescent and IR imaging. The generation of the Pyta ligand through a CuAAC reaction will close the macrocycle as well as offering a reaction site for rhenium complexation. The synthesis of modified amino acids, preparation of linear peptide sequence and first evaluations of cyclisation conditions will be presented in the last chapter of this thesis.

1. Photophysical study of Re(I) tricarbonyl complexes: structural variations

1.1 Introduction

As one of the kinetically inert d^6 transition metal centre, rhenium(I) complexes have been attracting a lot of interest in different fields such as CO_2 (photo)electroreduction,[63,77,78] organic light emitting diodes (OLED),[79,80] materials,[81] sensors,[82] bio-imaging[31,83] and anti-cancer reagents[84,85] over the past few decades due to their unique photophysics and photochemistry. Specifically, rhenium tricarbonyl complexes are examples of metal carbonyls, which are emissive in aerated fluid solution. Much efforts have been made to develop new diimine-containing complexes of the type *fac*-$[Re(N\hat{}N)(CO)_3X]^{0/+}$, in which the diimine ligand N^N is usually 2,2'bipyridine (bpy), 1,10-phenanthroline or their derivatives and X could be a halide or neutral-donor ligand like pyridine and 4-dimethylaminopyridine.

One of the keys to successfully modulate the photophysical properties of the rhenium(I) complexes is efficient ligand design and synthesis. Metal complexes with ligands based on 1,4-disubstituted-1,2,3-triazoles have been explored[86–89] due to their efficient synthesis based on copper(I)-catalysed alkyne-azide cycloaddition (CuAAC)[90] under mild conditions and with wide substrate scope.

The CuAAC process has emerged as the premier example of click chemistry, as coined in 2001 by K. B. Sharpless to describe a series of bond-forming processes that meet a set of stringent criteria: the reaction is modular, wide in scope, high-yielded, stereospecific, utilises readily available starting materials and reagents with simple reaction conditions and generates only inoffensive by-products and stereospecific product which are easy to isolate.[91] On one hand, alkynes are available from commercial suppliers or from reliable and robust Sonogashira cross coupling reactions. Alternatively, a synthetic route has been also developed from aldehyde precursors using Bestmann-Ohira reagent.[92] On the other hand, azides are easily accessible from amine precursors *via* diazonium salts using suitable diazo transfer reagents[93] or from halide precursors *via* nucleophilic substitution using sodium azide.

There are several commonly used ligands in rhenium(I) tricarbonyl complexes containing a 1,2,3-triazole motif, which is synthesized using CuAAC reactions (Figure 1.1). 1,4-Disubstitued-1,2,3-triazoles possess two positions available for coordination to a metal, N(2) and N(3) of which N(3) is more basic. Due to the high functional group tolerance of CuAAC reactions, it is easy to introduce other donor moieties to be incorporated in either/both of the substituents at the 1- and 4- positions thus enabling access to a wide range of chelating ligands.[86] CuAAC has been employed as a useful method to construct functional metal complexes[89] since the reaction shows a high functional group tolerance. Regioselective generation of 1,4-disubstituted-1,2,3-triazole by CuAAC reactions between azide and alkynes can easily afford bidentate ligand. Based on this reaction, several "click" ligands were developed (Figure 1.1).

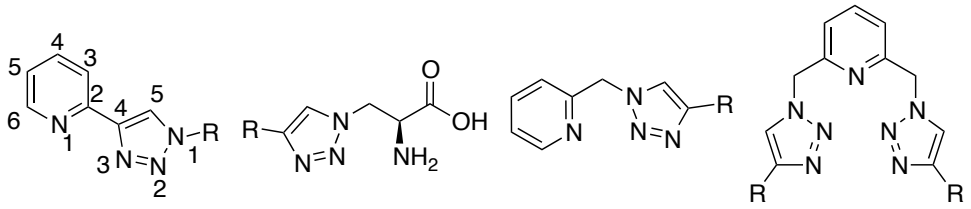


Figure 1.1 Selected "click" ligands for complexation of the *fac*-$[M(CO)_3]^+$ motif.[86]

Here, the photophysical properties of *fac*-$[Re(N^N)(CO)_3X]^{0/+}$ are shortly summarized.[94] The photophysical properties and the related applications of the rhenium(I) complexes in which the N^N ligand contains a 1,2,3-triazole and a pyridyl rings and is synthesized from CuAAC reactions, especially Pyta ligand and its derivatives, are reviewed.

1.1.1 Photophysical properties of rhenium(I) tricarbonyl complexes

fac-$[Re(bpy)(CO)_3Cl]$ is taken as an example to explain the general molecular orbital distribution.[95,96] Typically, *fac*-$[Re(bpy)(CO)_3Cl]$ exhibits a HOMO dominated by Re 5d-orbital (with carbonyl π^* contribution and p contribution when X is a halide) and a LUMO on diimine π^* orbital. Therefore, the lowest energy electronic absorbing state is assigned to a $d\pi(Re) \rightarrow \pi^*(N^N)$ metal-to-ligand charge transfer state (^{1}MLCT) which was first reported by M. Wrighton and co-workers in year 1974.[33] Then inter-system crossing (ISC) leads to the emissive ^{3}MLCT excited state (Figure 1.2). The photophysical behaviour of $[Re(N^N)(CO)_3X]^{n+}$ has been well investigated due to their dynamic and tuneable excited state properties by the modification of the diimine ligand thereby modulating the energy of the LUMO.[32,94,97]

There are several examples in which the lowest excited state was characterized as a mixture of ^{3}MLCT and a triplet intraligand (^{3}ICT) [34–38].

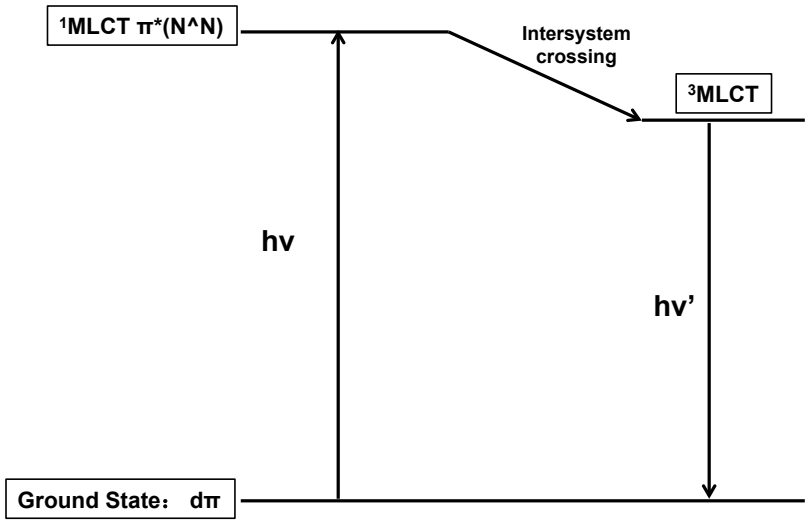
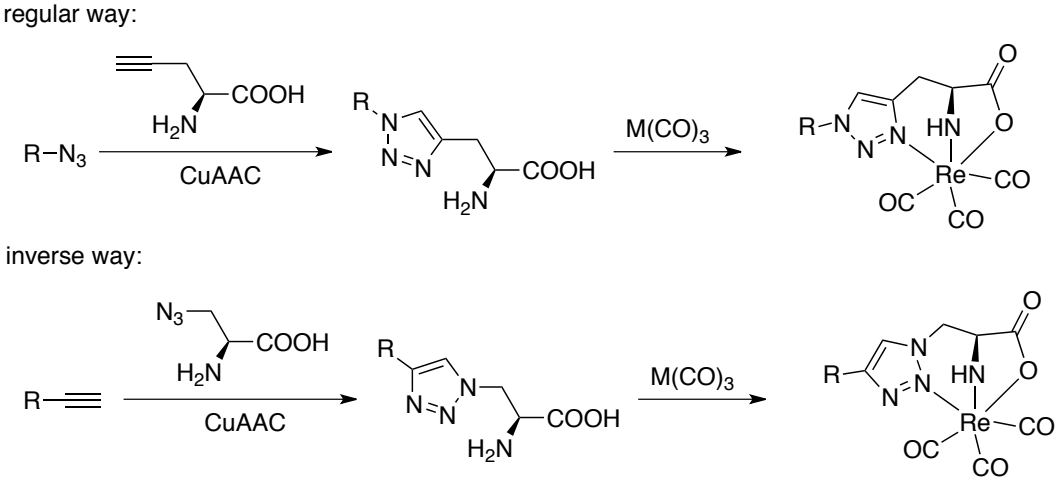


Figure 1.2 Simplified Jablonski diagram for $[Re(N^N)(CO)_3Cl]$ complexes (MLCT model).

Different kinds of ligands, especially polypyridyl ligands[40–42] were developed in order to modulate the photophysical properties of these complexes. On the other hand, it is also possible to modulate the photophysical properties by modifying the ligand X which will mainly influence the high lying occupied orbitals.

1.1.2 "Click-to-chelate" tridentate ligands

The advantages of CuAAC reactions, for example efficiency and selectivity under mild reaction conditions, have been exploited in the development of radiotracers.[98] Technetium-99m ($T_{1/2}$ = 6h) complexes have been developed for the radiolabelling of biomolecules.[99] Rhenium is a non-radioactive alternative to technetium for radiochemical study due to the fact that Re(I) is an excellent mimic of the group 7 congener ^{99m}Tc.[100] The preparation of the ligands classically requires multiple steps of synthesis, and their labelling reaction with biomolecules is often not efficient enough.



Scheme 1.1 "Click-to-chelate" approach: regular and inverse ways.[101]

T. L. Mindt and R. Schibli first reported the use of a CuAAC reaction to synthesize and install metal chelates into biomolecules in a single step, coining the term "click-to-chelate" to this approach.[101] The formation of 1,2,3-triazole not only builds a connection to the radiometal chelate, but also generate a part of the ligand system forming coordination bonds with rhenium(I) or ^{99}Technetium(I) (Scheme 1.1). In this work, different azido-functionalized biomolecules (tumour-affine peptide bombesin, thymidine, carbohydrate and phospholipid) were used to demonstrate the versatility of the approach. The CuAAC procedures avoid the use of protecting groups and allow the synthesis of optically pure ligands in one single step with quantitative yield. Using this strategy, it is possible to conjugate different functional groups such as aliphatic and aromatic backbones[102] or histidine folate derivatives.[103] D. W. Kim developed tridentate ligands using the same strategy and the resulting rhenium(I) and technetium(I) complexes were studied as potential c-met receptors kinase-positive tumour imaging agents.[104] Later, T. L. Mindt and R. Schibli developed a tridentate ligand **1** (Figure 1.3) symmetrically containing two

1,2,3-triazole motifs as complementary to the "click-to-chelate" approach where R and R' groups are easily functionalized.[105]

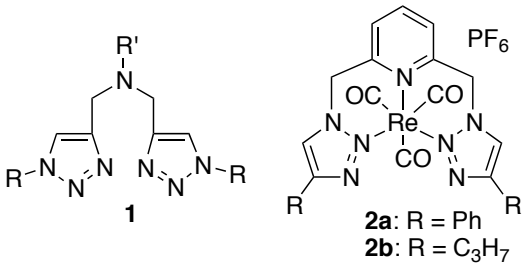


Figure 1.3 Molecular structures of compounds **1** – **2**.

Until now, the pyridyl moiety still remains one of the most common donor motifs incorporated into chelate ligands. Based on ligand **1**, D. Crowley *et al.* synthesized a "click" ligand to form the complexes **2** (Figure 1.3).[106] The lowest energy absorption bands were cantered at ca. 290 nm and were assigned to MLCT character. The modification of the side chain does not affect the electronic properties of the complexes, implying that the metal centre was insulated by the heterocycles from the electronic properties of the ligand's side chain.

1.1.3 Pyta based Re(I) complexes - structural and application study

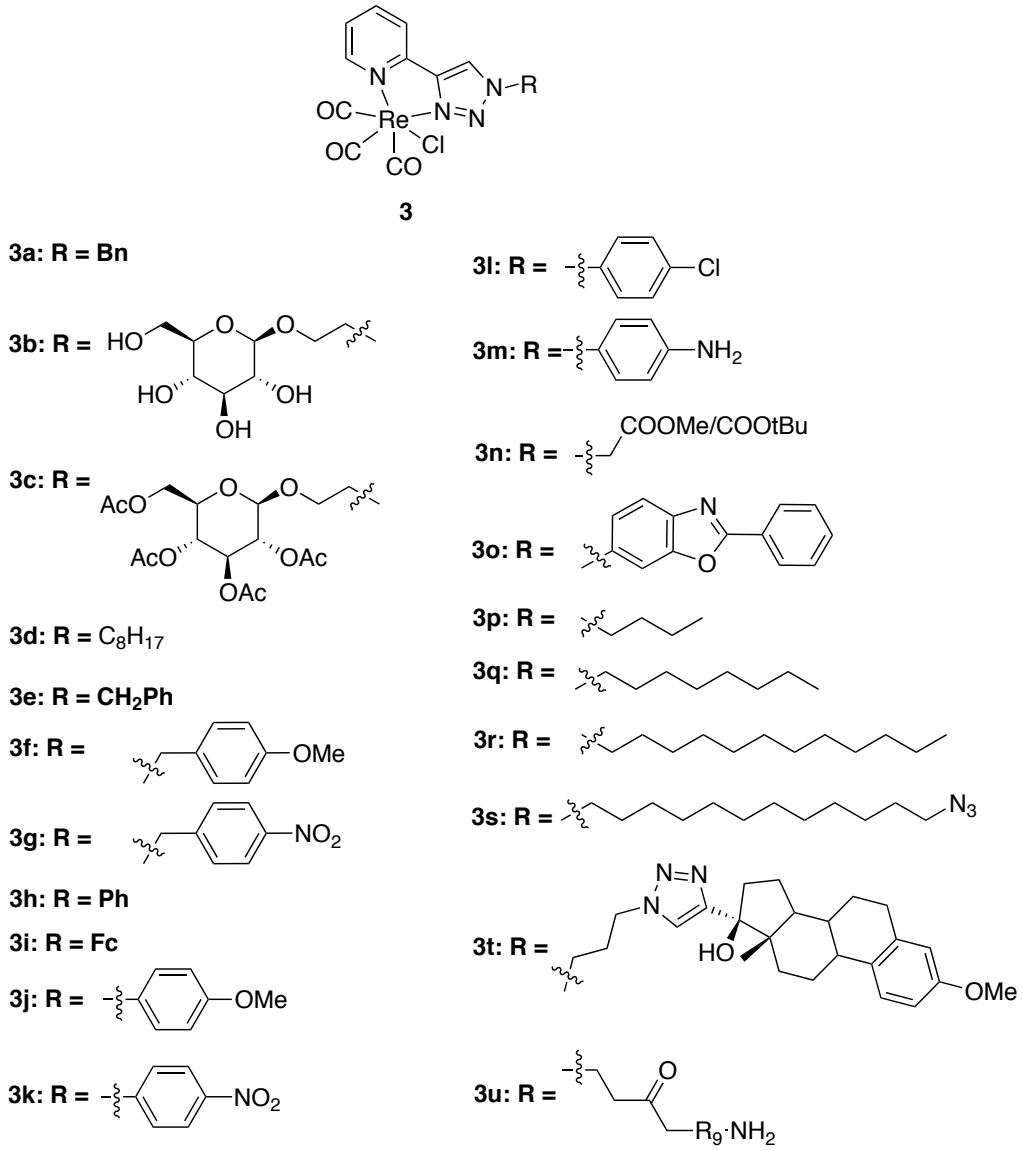


Figure 1.4 Molecular structure of complexes **3a – u**.[44,46,52,53,55,56,107–110]

One of the most widely investigated bidentate ligand based on CuAAC reaction is based on the 2-(1*H*-1,2,3-triazol-4-yl)pyridine motif (Pyta). Originated from 2,2'-bipyridine,[43] the 4-(2'-pyridyl)-1,2,3-triazole (Pyta) ligand was first reported by M. Obata, S. Yano *et al.* as the *fac*-[Re(Pyta-Bn)(CO)$_3$Cl] complex in 2008.[44] The X-ray structure of complex **3a** indicated that the Pyta-Bn ligand coordinated *via* the nitrogen atoms of the 2-pyridyl group and the N(3) of the 1,2,3-triazole ring, in a similar coordinating fashion to that of the 2,2'-bipyridine derivative.
Many modifications on the 1-position of the triazole on the Pyta framework were described. Complex **3a** displayed an electronic absorption band centred at 333 nm in acetonitrile, assigned to a MLCT character, and blue-shifted compared to that of *fac*-[Re(bpy)(CO)$_3$Cl].[44] The emission wavelength was 538 nm in acetonitrile. The LUMO was essentially the π* orbital of Pyta ligand and the HOMO-1 was predominantly localized at the Re(I) and Cl atoms, which formed a π-antibonding orbital. Its luminescence lifetime of 8.90 μs in 2-methyltetrahydrofuran

at 77 K was longer than that of *fac*-[Re(bpy)$(CO)_3$Cl] (3.17 μs). Additionally, the extended X-ray absorption fine structure (EXAFS) analyses of *fac*-[Re(Pyta-Glc)$(CO)_3$Cl] **3b** and *fac*-[Re(Pyta-AcGcl)$(CO)_3$Cl] **3c** suggested that the glycol conjugation at the 1-position of the 1,2,3-triazole hardly had any influence on the coordinating fashion of Pyta ligand. This was further confirmed by K. C. Gordon, J. D. Crowley *et al.*[111] The introduction of either unconjugated (complex **3d – g**) or conjugated (complex **3h – k**) substituent showed absorption bands in the resulting complexes centred around 330 nm, which were assigned to a metal-to-ligand charge transfer. The HOMOs of the complexes **3d – k** were Re dπ in nature and the LUMOs of the complexes **3d – g** were localised on the triazole unit while for conjugated complexes **3h – k** the LUMOs were spread over the substituent. The emission spectroscopy also showed similar results, with an emission band centred at 532 nm for complexes **3d – h** and **3j – k**. However, the lifetime of the complexes was altered by these substituents. The lifetimes of those with conjugated substituents were longer than that of complexes with unconjugated functionalisation, possibly arising from the "free-rotor" effect, which allowed molecules to relax through non-radiative pathways.

The introduction of phenyl-based groups (4-nitro-phenyl, 4-chloro-phenyl) on the 1-position of the 1,2,3-triazole motif resulted in complexes **3k – l** respectively, displaying similar HOMO, HOMO-1 and HOMO-2 energy levels with significant metallic character.[46,107] However, the introduction of a phenyl-based group with electron-donating character (4-amino-phenyl complex **3m**) raised the energy of the HOMO compared to that of complexes **3k – l**, as a result of increasing the π orbital energy levels of the chelate ligand. The HOMO of complex **3m** was localized on the 4-amino-phenyl part rather than the metal centre. A significant metallic character is observed in HOMO-1, HOMO-2 and HOMO-3. On the other hand, the LUMO of complex **3k** is localized on the $PhNO_2$ part whereas the LUMOs of complexes **3l** and **3m** are localized on Pyta π* orbitals. Similarly, the introduction of an ester on this position (complex **3n**) and even dimeric complexes, formed from the complex **3n** under treatment with potassium carbonate, where the chlorine atom of the labile Re-Cl bond of one monomer is substituted by the oxygen of the carboxylate arm of the second one, did not shift the excitation (333 nm for complex **3n**, 326 nm for the dimers) or emission maximum (526 nm for complex **3n** and dimers).[108]

It is notable that the introduction of 2-phenylbenzoxazole (PBO) moiety at the 1-position of 1,2,3-triazole motif still keeps the whole ligand in a planar fashion allowing for electron delocalisation on the whole ligand and the corresponding complex **3o** showed phosphorescence both in organic solvents and in the solid state.[109]

As shown in these examples above, the photophysical properties of such complexes is not strongly affected by modification on the 1-position of the triazole motif; it is thus easy to introduce functional groups at this position while keeping the desired photophysical properties. D. Crowley, K. C. Gordon et al. developed luminescent $[Pd_2L_4]^{4+}$ cages with exo-functionalized emissive Pyta-Re(I) complexes using pre-modification[112] and post-modification[113] strategies. Exo-functionalisation refers to one of the methods to incorporate functionalities into

supramolecular metal-organic assemblies: covalent attachment of functional moiety on the periphery of coordination driven self-assembled metallacages or metallacycles.[114] In this functional method, the functional groups are well separated and normally have no communication with each other. The formation of the cages did not affect the absorption and excitation properties of the modified Pyta-Re(I) motif due to the essentially discrete of the metal centre in the exo-functionalisation approach.

The influence of the length of an alkyl side-chain (C_4, C_8 and C_{12}) on the 1-position of the 1,2,3-triazole ring in Pyta complexes **3p – r** on lipophilicity, cell penetration and cytotoxicity was investigated using IR and luminescent spectroscopies.[55] Complex **3r** showed a higher cellular penetration due to its higher lipophilicity, causing higher cytotoxicity among complexes **3p – r**. Meanwhile, the solvents also showed influence on the emission properties. Complexes **3p – r** showed the same photophysical behaviour in acetonitrile (with 0.2% DMSO). However, in Dulbecco's phosphate-buffered saline (DPBS) buffer (with 0.2% of DMSO), complex **3p** was not emissive while complexes **3q – r** displayed an emission slightly blue shifted and enhanced compared to that in acetonitrile and similar to *fac*-[Re(bpy)$(CO)_3$py]$^+$ complexes.[110] Complex **3r** showed a stronger enhancement of the emission than that of complex **3q**. In aqueous solution, the metal core of complex **3p** with a short side chain is indeed accessible to water and the emission is quenched due to dipolar coupling favouring the non-radiative decay of the excited state, while for complexes **3q** and **3r**, the metal core is shielded by the folding of the long alkyl chain. The blue shift in the emission of complexes **3q** and **3r** also pointed at the effect of a hydrophobic environment onto the photophysical properties. As previously suggested, the alkyl chain most probably folds around the Re core, shielding it from water desexcitation.[49] C. Policar *et al.* have developed a series of *fac*-[Re(Pyta)$(CO)_3$Cl] complexes diversely functionalized at the 1-position of the 1,2,3-triazole ring as Single Core Multimodal Probes for Imaging (SCoMPI) combining luminescence,[52,53,56] as well as infrared and recently X-ray fluorescence[51] properties. For example, complex **3s** with an azidoalkyl side chain was found to unambiguously localize at the Golgi apparatus in MDA-MB-231 breast cancer cells using both infrared and luminescent spectroscopies.[52] Complex **3t** with a mestranol at the end of the side chain showed a Golgi apparatus distribution by infrared and luminescent spectroscopies.[53] Complex **3u** conjugated with the nona-arginine peptide SR_9 was shown to target epidermis in skin biopsies which was confirmed by IR and luminescence microscopies.[56]

Modification on the pyridyl ring was relatively less investigated (Figure 1.5). The introduction of a triphenylamine (TPA) moiety on the 5-position of the pyridyl ring in complex **4**, led to a red shift in both the absorption (*ca.* 50 nm) and emission (*ca.* 20 nm) maxima compared to complex **3a**.[47] The lowest excited state of this complex displayed an ICT character involving electron transfer from the TPA motif to Pyta π* orbitals rather than the typically observed MLCT character.

It is also possible to extend the π-system of the pyridyl motif. Replacing the pyridine ring in the Pyta ligand by a quinoline resulted in a new ligand, noted Quinta.[48] Complex *fac*-[Re(Quinta)$(CO)_3$Cl] **5** showed a red-shift in the emission maximum arising from a stabilisation

of the ligand-centred LUMO, as expected with the increase in conjugation (accompanied by a decrease in quantum yield). The complex **6** with a glutamine-targeting agent was shown to display significant concentration-dependent uptake using fluorescence microscopy.[45]

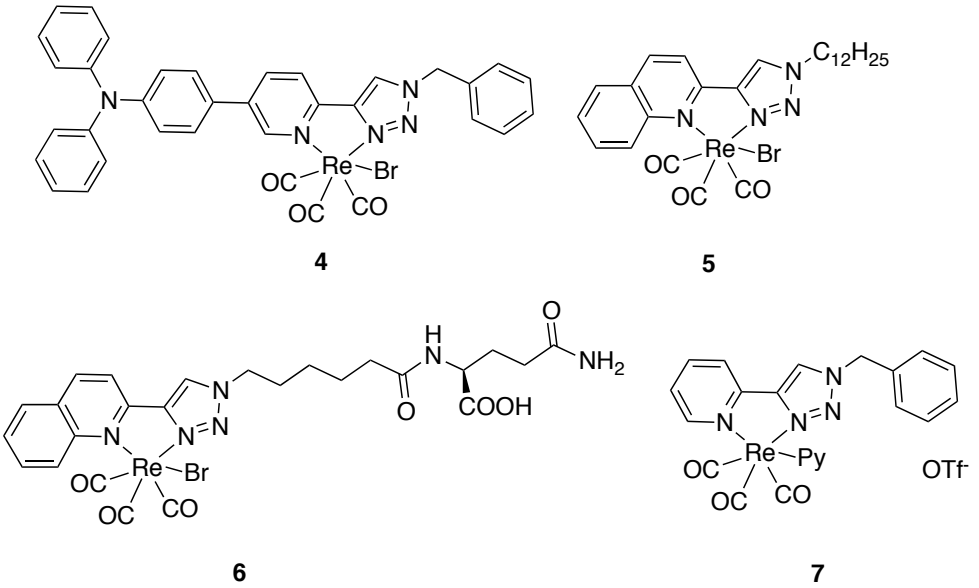


Figure 1.5 Molecular structure of complexes **4** – **7**.

The replacement of the halide ligand by a neutral pyridine donor in complex **7** showed a blue-shift in emission compared to that of complex **3a** with a 10-fold increase in quantum yield in acetonitrile which is similar to the behaviour of parent bipyridine complexes.[115] This is due to the stabilisation of dπ(Re) HOMO orbital by the pyridiyl motif. Functionalized pyridyl motif is able to tune the photophysical properties of the resulting Re(I) complexes[116] and endued the resulting complexes fluorescent imaging ability.[117]

1.1.4 Tapy based Re(I) complexes

The inverse isomers of Pyta, the 2-(1*H*-1,2,3-triazol-1-yl)pyridine (Tapy, **8**) ligands are less common. The starting material 2-azidopyridine is in a tautomeric equilibrium with the corresponding thermodynamically favoured ring-closed tetrazole and for this reason the standard click conditions are usually not applicable in this case (Figure 1.6). The conditions to form open chain species from the ring-closed form of electron-poor pyridotetrazole are harsh.[118] Thanks to recent progress, this transformation can be reliably accomplished under relatively mild conditions with copper(I) based catalysis.[119,120] Our group first found that inversion of the bridge between the triazole ring and pyridine in the Tapy ligand (complex **9** in Figure 1.6) (inverse coordination vs normal coordination with Pyta ligands) led to a red shift of the absorption and emission bands and an increase of quantum yield in aqueous solution for the corresponding Re(I) complexes.[48] Meanwhile, the reduced stability observed for the Tapy-Re(I) complexes is in agreement with a lower electron density on the N(2) of the triazole in

comparison with the coordinating N(3)[121] in the Pyta ligand. J. D. Crowley et al. showed that *fac*-[Re(Tapy)(CO)$_3$Cl] complexes had slower non-radiative decay.[107]

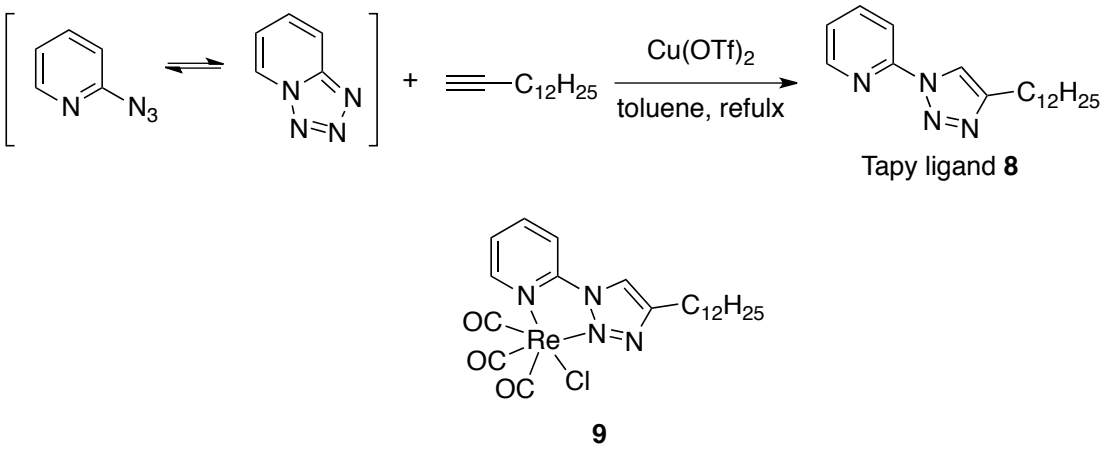


Figure 1.6 Synthesis of Tapy ligand **8** and structure of *fac*-[Re(Tapy)(CO)$_3$Cl] complex **9**.

1.1.5 Other bidentate ligands

There are other bidentate ligands synthesized using CuAAC reactions. P. D. Beer *et al.* developed neutral bimetallic rhenium(I) complexes **9** as halogen bonding (XB, complex **10**) or hydrogen bonding (HB, complex **11**) acyclic anion receptors (Figure 1.7).[122] The addition of the corresponding anions increased the intensity of the ^{3}MLCT emission as a consequence of anion binding by the complexes causing an increased rigidness of the system and disfavouring non-radiative decay pathways. It is notable that complex **10** was a significantly superior anion recognition host showing good selectivity for halides, especially for iodide, over a variety of mono charged oxanions.

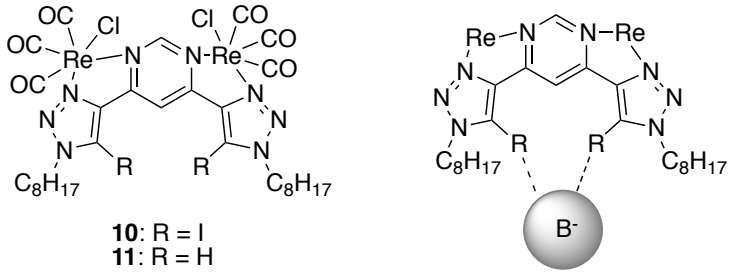


Figure 1.7 Molecular structure of complexes **10** – **11** and schematic diagram of HB/XB receptor.

J. D. Crowley *et al.* synthesized inverse "click" ligands and formed complexes **12**.[123] All of the complexes displayed lowest energy absorption bands centred at ca. 290 nm which were assigned to MLCT transitions except for complex **12b**, having its absorption centred at 301 nm, which involved a donor molecular orbital (MO) spread over the metal centre and an acceptor MO based on the 4-nitrophenyl. Thus, the effect of changing the side chain was minimal on the absorption except for the complex with nitrophenyl group. This indicated that the 1,2,3-triazole motif acted as an insulating unit in this type of ligand. The short emission lifetimes and the low

quantum yield of the complexes compared to *fac*-[Re(Pyta)(CO)$_3$Cl] were explained by the flexibility of the ligand that facilitates non-radiative decay.

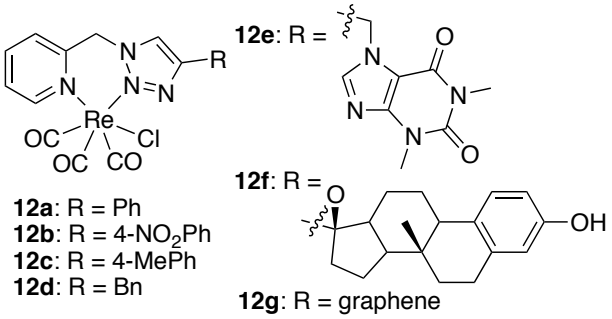


Figure 1.8 Molecular structure of complexes **12**.

1.1.6 Proposal of the project

The impact of N^N ligand modifications in bpy and phen Re(I) complexes has been deeply investigated. According to the study towards bpy Re(I) complexes, the introduction of electron donating groups on the N^N ligand such as *tert*-butyl groups on the 4,4'- position of bpy ligand blue shifted the lowest absorption band which is consistent with the higher π* orbital energies of *t*Bu$_2$bpy as a result of its poorer π-accepting abilities due to the presence of the more electron-rich *tert*-butyl motif on the bpy ligand.[124]

As shown above, in complexes bearing a Pyta ligand, modifications on the 1-position of the triazole is synthetically easy and do not affect much the photophysical properties of the resulting complexes. It is a promising position to introduce interesting functional groups to endow the whole molecules with additional applications. Modifications of the pyridyl motif on the Pyta ligand or at the 5-position of the triazole ring were less investigated. In this chapter, we are considering tuning the electronic properties of the complexes through the modification of the pyridine motif of the Pyta ligand. 4- or 5- Position was chosen due to the relatively easy access of the starting materials. Moreover, we explored for the first-time modifications on the 5-position of the 1,2,3-triazole ring on the Pyta framework.

The extension of the π-system of pyridine ring in Tapy ligands has been explored by replacing the pyridine ring by a quinoline and the resulting Taquin rhenium(I) complexes showed an absorption centred at 380 nm which is 20 nm red shifted compared to the Tapy rhenium(I) complex **9** and an emission centred at 617 nm which is 67 nm red shifted compared to the Tapy rhenium(I) complex **9**. This red shift in both the excitation and the emission wavelength is accompanied by a decrease of quantum yield to 0.006 as classically observed in these cases.[48] The balance between these two is subtle. Previous results showed that the 1,2,3-triazole ring might be a good isolation for electron communication so that the resulting rhenium(I) complexes may keep an acceptable quantum yield. Meanwhile, extending the π-system on the 1,2,3-triazole ring of such ligand systems has not been explored. We therefore prepared and investigated the rhenium(I) complex in which the 1,2,3-triazole ring was replaced by a benzotriazole.

The modifications of axial ligands have been well studied because the nature of the axial ligands will affect the origin of the low energy excited states. Metal complexes with axial ligands which are good σ-donors will cause a red shift in the low energy absorption.[124–126] V. W.-W. Yam *et al.* have made great efforts for the development of acetylide axial ligands for *fac*-[Re(N^N)$(CO)_3$X] system.[124,126–132] However, the related study based on Pyta Re(I) complexes has not been performed yet. Thus, we designed complexes with different functional groups at 4-position of the phenylacetylene ligand. Electron withdrawing groups (EWG) (-CN, CHO, -NO_2) or electron donating group (EDG) (-OMe) were chosen to investigate the influence on the photophysical properties as well as the molecular orbital distribution.

The introduction of the sulphur based functional groups on the N^N ligands endowed the corresponding Re(I) complexes with mixed MLCT/ICT excited states.[133,134] However, thiolates have been rarely used for the synthesis of Re(I) complexes as axial ligands. Only a few examples were reported on the use of thiolate ligands,[135,136] in which some are used as bridging ligand.[137,138] J. A. G. Williams *et al.* introduced thiolate ligands into platinum(II) complexes and the resulting complexes displayed strong red shift in both excitation and emission wavelengths compared to their parent chloride platinum(II) complex.[139] The introduction of methyl-4-mercaptobenzoate ligand into *fac*-[Pt$(Me)_3$(bpy)X] complexes caused low energy absorptions due to the mixed metal and inter ligand charge transfer transition and resulted in complexes displaying near-infrared emission.[140] Inspired by these results, we designed rhenium(I) complexes with Pyta or Tapy ligand bearing diverse arenethiolate axial ligands to investigate the influence of the thiolate ligand and the different electronic properties on photophysical properties.

1.2 Rhenium complexes with modified Pyta ligands

The modification of the bpy ligand to tune the photophysical properties of the resulting Re(I) complexes is already well investigated.

We first evaluated the influence on the photophysical properties of the introduction of different functional groups on the pyridyl-1,2,3-triazole based ligand.

On one hand, we modified the pyridine ring of the Pyta ligand with –COOMe at 5-position (Figure 1.9, complex **13**) or –OMe/–NO_2 at 4-position (Figure 1.9, complex **14** and **15**) due to the relatively easy access of the starting materials and less steric hindrance. Complexes **14** and **15** were originally designed for carbon dioxide electroreduction purpose. Meanwhile, we investigated for the first time the modification of the 5-position of the triazole ring of the Pyta framework (Figure 1.9, complex **16**). On the other hand, we extended the π-conjugation system of the 1,2,3-triazole of the Tapy framework to study the photophysical properties of the resulting new complex (complex **17** versus **9**). The ligand used for complex **17** has been used for the generation of stable Au(III) complexes as efficient catalysts for the synthesis of allenes[141] and E-α-haloenones[142]. Other metal complexes such as Co(II),[143] Ru(II),[144] Cu(II)[143] were reported in structural studies. However, there is still no photophycial investigation for Re-complexes based on this ligand.

The stability of some the synthesized complexes was studied by time dependent ^{1}H NMR experiments. The photophysical properties were investigated in acetonitrile and DFT and TD-DFT calculations were performed for selected complexes.

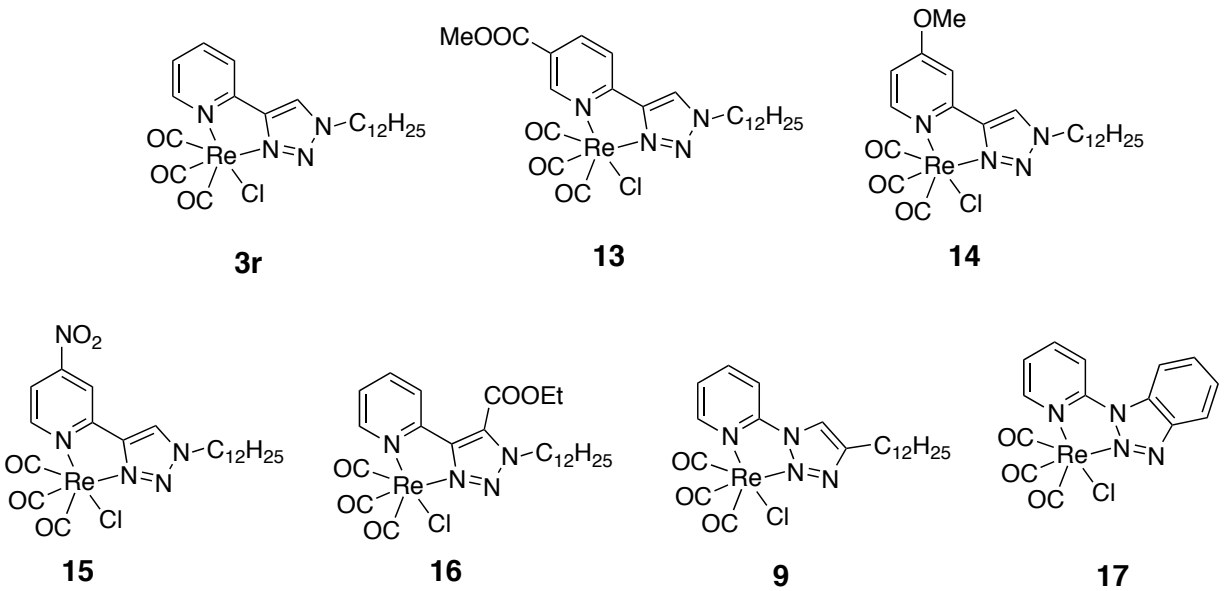


Figure 1.9 Molecular structure for complexes **3r**, **9** and **13** – **17**.

1.2.1 Synthesis and characterisations

In most cases, the modified Pyta ligands were synthesized using a copper(I) catalysed azide alkyne cycloaddition CuAAC reaction. Complexes **3r** and **9** were synthesized according to previous literature.[48]

We obtained crystals of Tapy rhenium(I) complex **9** suitable for X-ray crystallography by slow evaporation of a *d*-chloroform solution. The X-ray diffraction data were collected and resolved by Regis Guillot of Institut de Chimie Moléculaire et des Matériaux d'Orsay, Université Paris-Sud. The perspective drawing of complex **9** is depicted in Figure 1.10. The crystallographic data is given in Table appendix-1. The coordination geometry of complex **9** is distorted octahedral with one carbonyl ligand and chloride ligand in an axial fashion. The N-Re-N bond angle was 74.02° which is much smaller than 90°, in agreement with previous literature for Tapy rhenium(I) complexes,[107] due to the bite distance exerted by steric demand of the chelating Tapy ligand. This angle is also similar to that of Pyta rhenium(I) complexes.[44] The Re-Cl bond length is 2.476 Å.

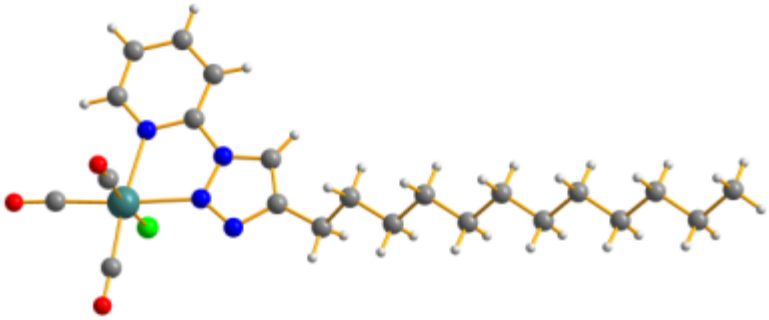
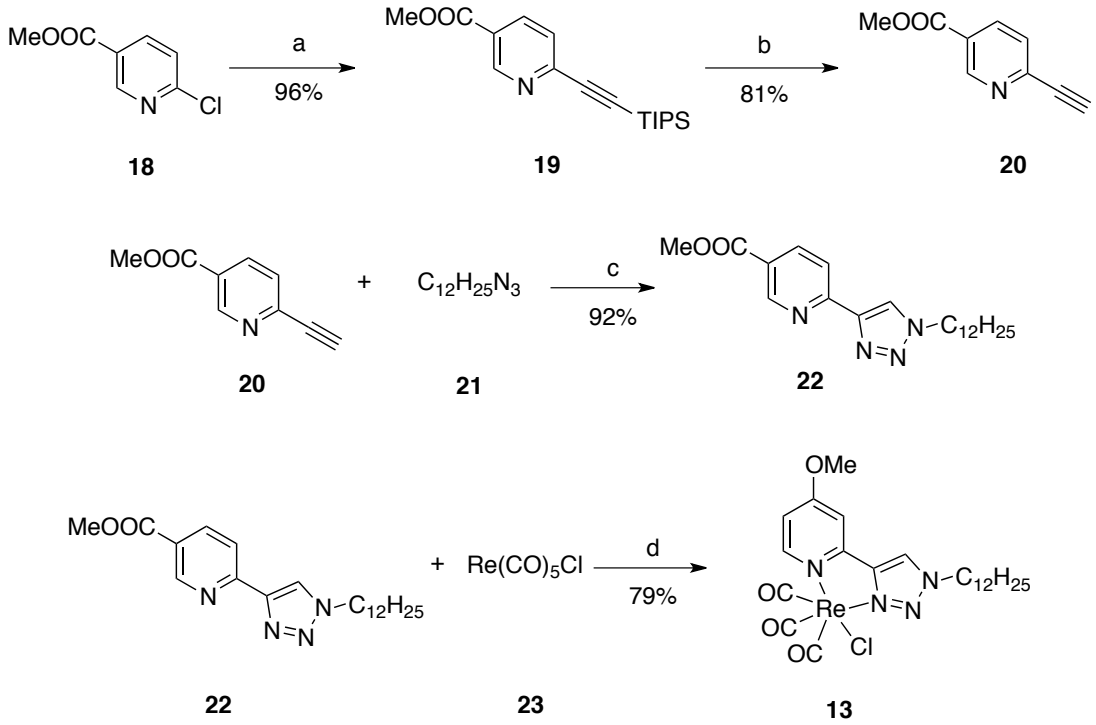


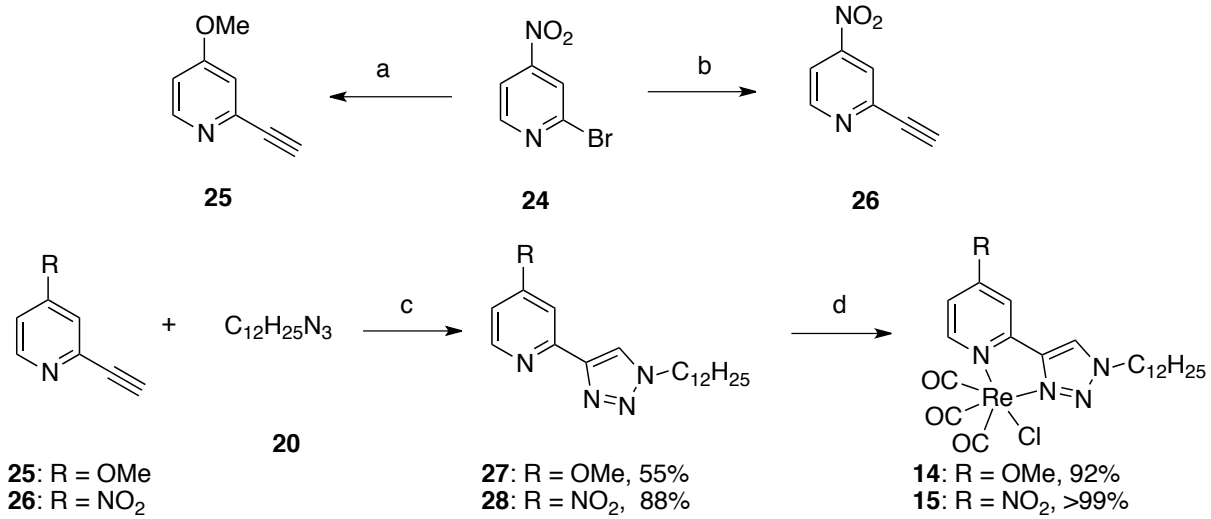
Figure 1.10 Crystal structure. The perspective drawing of **9**. White: hydrogen atom; gray: carbon atom; red: oxygen atom; blue: nitrogen atom; bright green: chloride atom; deep green: rhenium atom.

The synthesis of complex **13** (Scheme 1.2) started from the commercially available compound methyl-6-chloronicotinate **18**. A first step of high yield (96%) Sonogashira cross coupling reaction using $Pd(PPh_3)_2Cl_2$ and CuI as catalysts followed by the deprotection of the triisopropylsilyl (TIPS) protecting group using tetrabutylammonium fluoride (1.6 M in tetrahydrofuran) (Yield: 81%) afforded the alkynyl precursor **20** efficiently. A classical CuAAC reaction using copper sulfate pentahydrate (10 mol%) and sodium ascorbate (30 mol%) in a mixture of dichloromethane and water was conducted with 1-azidododecane at room temperature to generate the ester modified Pyta ligand **22** in high yield (92%). The complexation of the ligand **22** with $Re(CO)_5Cl$ in refluxing toluene (referred thereafter as classical conditions) gave the desired complex **13** in moderate yield (79%).



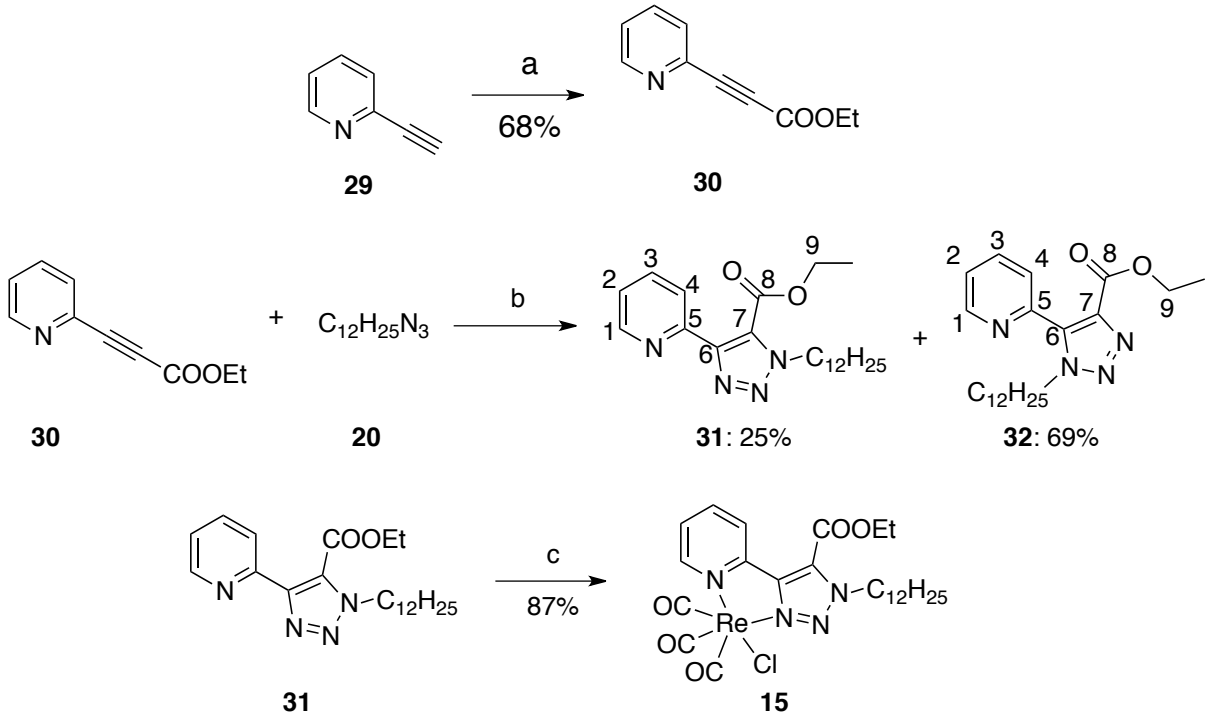
Scheme 1.2 Synthetic route for complex **13**. Condition a: TIPSA (1.2 equiv.), $Pd(PPh_3)_2Cl_2$ (2 mol%), CuI (1 mol%), THF, Et_3N, room temperature, overnight; b: TBAF (1.0 M in THF, 0.95 equiv.), THF, 0 °C, 10 minutes; c: Na ascorbate (30 mol%), $CuSO_4$ $5H_2O$ (10 mol%.), DCM, H_2O, room temperature, overnight; d: $Re(CO)_5Cl$ (1.0 equiv.), toluene, 120 °C, 2 hours.

For complexes **14** and **15** (Scheme 1.3), the synthesis used the same commercially available starting material 2-bromo-4-nitropyridine. A first Sonogashira reaction was conducted using different silylacetylenes followed by deprotection of the silyl protecting group: coupling with TIPSA and deprotection with TBAF afforded 2-ethynyl-4-nitropyridine **25** in 33% overall yield while coupling with ethynyltrimethylsilane (TMSA) and deprotection with potassium carbonate in methanol gave 2-ethynyl-4-methoxypyridine **26** in 33% overall yield. Then the alkynyl precursor **25** or **26** was reacted with 1-azidododecane under classical CuAAC reaction to afford the ligands **27** and **28** in moderate to good yield. Finally, the complexation between the ligand and $Re(CO)_5Cl$ in classical conditions afforded the target complexes **14** and **15** in high yield.



Scheme 1.3 Synthetic route of complexes **14** and **15**. Condition a: 1) TMSA (1.2 equiv.), $Pd(PPh_3)_2Cl_2$ (2 mol%), CuI (1 mol%), THF, Et_3N (2.0 equiv.), 60 °C, overnight, 41%, 2) K_2CO_3 (5.0 equiv.), MeOH, room temperature, 4 hours, 81%; b: 1) TIPSA (1.2 equiv.), $Pd(PPh_3)_2Cl_2$ (2 mol%), CuI (1 mol%), THF, Et_3N (2 equiv.), 60 °C, overnight, 44%, 2) TBAF (1.0 M in THF, 0.95 equiv.), THF, 0 °C, 30 minutes, 76%; c: Na ascorbate (30 mol%), $CuSO_4$ $5H_2O$ (10 mol%.), DCM, H_2O, room temperature, overnight; d: $Re(CO)_5Cl$ (1.0 equiv.), toluene, 120 °C, 2 hours.

Complex **16** was synthesized (Scheme 1.4) from the commercially available 2-ethynylpyridine **29**. The metalation reaction of compound **29** with n-butyllithium at -78 °C, followed by the addition on ethyl chloroformate gave the acetylene precursor **30** in moderate yield (68%). Then a Huisgen type 1,3-dipolar cycloaddition between precursor **30** and 1-azidododecane was performed under heating. The two regioisomers **31** and **32** were formed, the 1,5-isomer being isolated as the major product. This is a type II 1,3-dipole cycloaddition where both HOMO-LUMO separations of the azide and alkyne are similar and, mainly due to the reduced steric hindrance, structure **32** is preferred in this reaction. The two isomers were separated by silica gel column chromatography; ligand **31** was isolated with 25% yield while the isomer **32** was isolated with 69% yield. The identification of compounds **31** and **32** is discussed in detail below. Finally, the complexation of compound **31** with rhenium(I) pentacarbonyl chloride in refluxing toluene gave the desired complex **16** with 87% yield.



Scheme 1.4 Synthetic route for complex **16**. Condition a: ethyl chloroformate (5.5 equiv.), n-butyllithium (1.0 M in hexane, 3.4 equiv.), THF, -75 °C ~ room temperature, 2 days; b: toluene, 120 °C, 12 hours; c: $Re(CO)_5Cl$ (1.0 equiv.), toluene, 120 °C, 1 hour.

To identify the two isomers **31** and **32**, heteronuclear multiple bond correlation (HMBC) experiments were conducted (Figure 1.11). The HMBC experiment gives correlations between carbon and protons that are separated by two, three and, sometimes, in conjugated systems, four bonds. Direct one-bond correlations are suppressed. For compound **31**, the C_{10}-*H* which are the protons on the first carbon of the C12 chain showed a correlation signal with the carbon signal of C_7 indicating a direct proximity of this carbon with the C12 chain. For compound **32**, the C_{10}-*H* showed a correlation signal with the carbon signal of C_6 and no correlation with carbon C_7. These experiments allowed us to identify **31** as the 1,4-isomer and **32** as the 1,5-isomer.
Though we were not able to get crystals of compound **31** suitable for X-ray crystallography, we obtained the single crystal structure of compound **32** under slow evaporation in *d*-chloroform (Figure 1.12 and Table appendix-1), which is a direct proof for the structure of the isomers. In compound **32**, the torsion angle between the pyridine and the triazole rings is 94.60°, while the Pyta ligand structure shows a slightly distorted plane.
Complex **17** was synthesised by N. P. Holland (Erasmus Imperial College 2016). All the rhenium(I) complexes were characterized by ^{1}H, ^{13}C NMR, IR and high-resolution mass spectroscopy. The IR spectra of all the complexes show the two intense bands around 2020 and 1900 cm^{-1} for the A1 symmetric and E antisymmetric vibrations respectively characteristic for *fac*-rhenium tricarbonyl complexes, the vibration frequencies being very close for all the complexes.

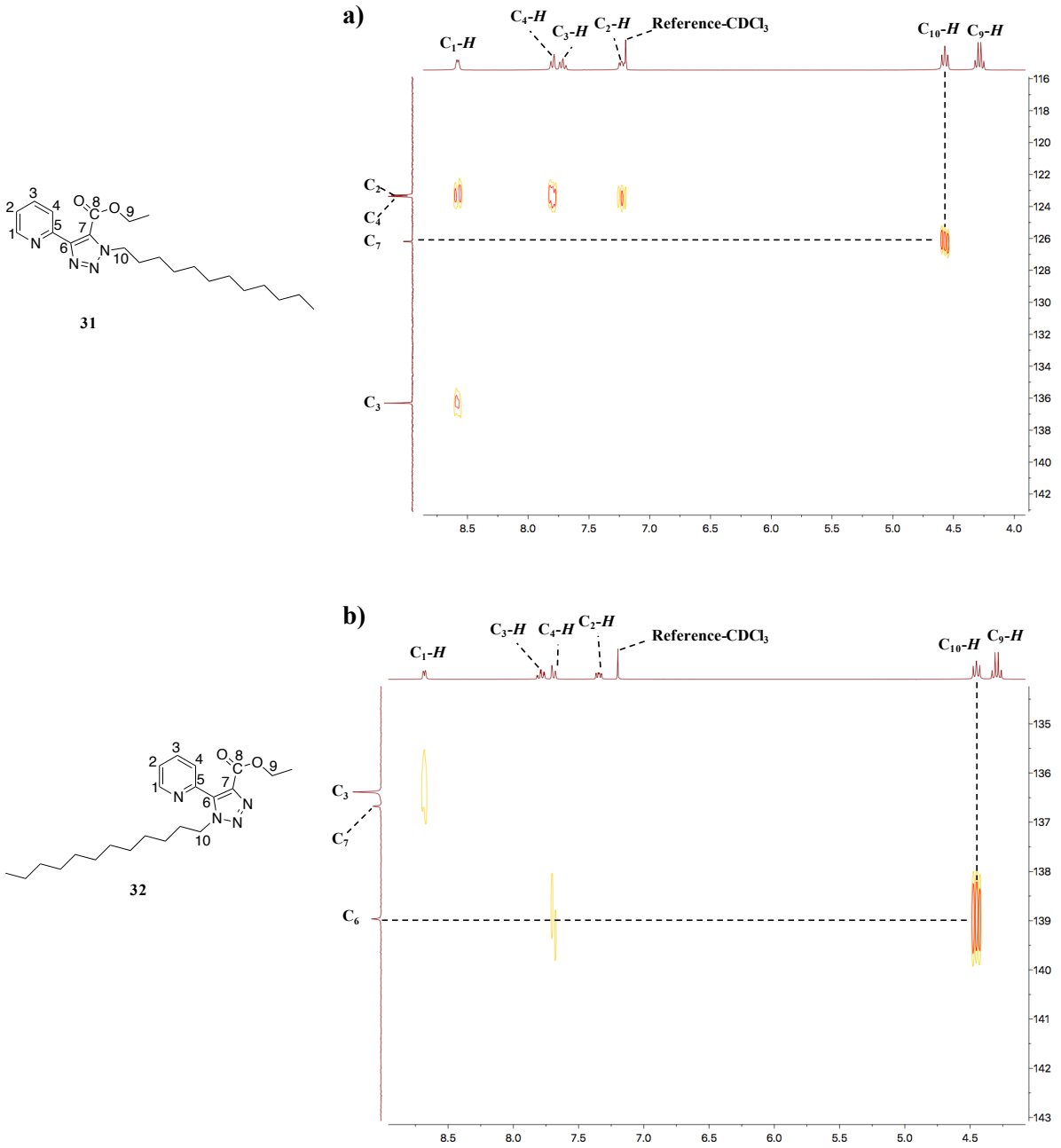


Figure 1.11 Partial 2D HMBC spectra for ligands **31** (a) and **32** (b).

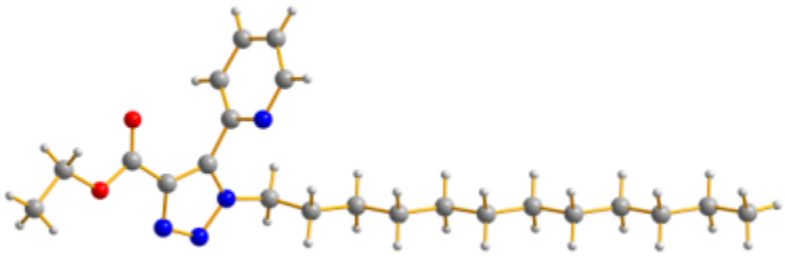


Figure 1.12 The perspective drawing of **32**. White: hydrogen atom; gray: carbon atom; red: oxygen atom; blue: nitrogen atom.

1.2.2 Photophysical investigation

Photophysical properties of all the complexes were investigated in acetonitrile at a concentration of 20 μM at 298 K. The absorption data are summarised Figure 1.13 and Table 1.1. Complex **3r** showed a high-energy absorption at ca. 280 nm which is assigned to $\pi \rightarrow \pi^*$ intraligand transition (^{1}IL) and a lower-energy band of metal-to-ligand charge transfer (MLCT) character at 332 nm as previously described.[48] Complexes **13** showed a high-energy absorption centred at around 290 nm, assigned to intraligand charge transfer. Complex **13** functionalized with an ester group on the 5-position of the pyridine ring of the Pyta ligand exhibited a 20 nm red-shifted lowest absorption wavelength compared to that of complex **3r**. The behaviour of complex **13** originates from the electron withdrawing effect of carbonyl groups, which decreases the energy of the π* acceptor orbitals while it only has a moderate effect on the electron density for the rhenium centre.[145] Such effect was expected from an electron withdrawing group in the *meta*- position of the pyridine where its effect should be maximized. Complex **14** modified with a methoxy group on the 4-position of the pyridine of the Pyta ligand showed an absorption centred at 321 nm, which is slightly blue-shifted compared with the bare complex **3r** while complex **15** modified with a nitro group at the same position showed no obvious shift for this absorption band. Electron donating groups were expected to have a stronger influence on the photophysical properties when introduced in the *para*- position of the pyridine. The blue shift of the absorption for complex **14** is due to the electron-rich property of methoxy, which makes the ligand poorer π-acceptor and thus increases the π* orbital energy.
Complex **16** functionalized with an ester group at the 5-position of the triazole ring of Pyta ligand showed a 10 nm red shift of the MLCT absorption band compared to the parent complex **3r.** This is due to the electron withdrawing property of the ester group that makes the ligand a better π-acceptor and thus decreases the π* orbital energy. However, the effect is less pronounced than in complex **13**, which will be investigated by DFT calculations.
Complex **9** showed a low-energy absorption centred at 355 nm, which is assigned to a MLCT character, and a higher-energy absorption centred at 280 nm, which is assigned to the LLCT character, in agreement with what has been reported.[48] Complex **17** showed a low-energy absorption band centred at 372 nm, which may be assigned to the MLCT character and unstructured absorption bands around 320 nm and 280 nm (Figure 1.14-a). The nature of these bands will be discussed below in the calculation part.
The emission spectra showed interesting results. The origin of the emission is ascribed to a ^{3}MLCT dπ(Re)→ π*(N^N) excited state, similar to that of complex **3r**. With the introduction of an ester on 5-position of the pyridine ring, complex **13** exhibited an emission wave centred at 600 nm, having a 70 nm red shift compared with that of complex **3r**. However, emission intensity is weakened. This is expected since usually in the Re complexes the non-radiative rate constant increases and the quantum yield decreases when the energy of the MLCT state decreases, in line with the energy gap law.[145]

The introduction of a methoxy group on the 4-position of the pyridine ring (complex **14**) caused a 30 nm blue shift of the emission band compared to that of complex **3r**, consistent with the presence of an electron-donating group on the diimine ligand, which renders the π* orbital energy of the modified Pyta ligand higher-lying than the parent Pyta ligand. With the introduction of electron-deficient nitro group on the 4-position of pyridine, complex **15** exhibited slightly red-shifted emission wave (538 nm) compared to that of complex **3r**, which is due to the decrease the π* orbital energy of the modified Pyta ligand. But this red shift is very subtle at the 4-position of pyridine ring.

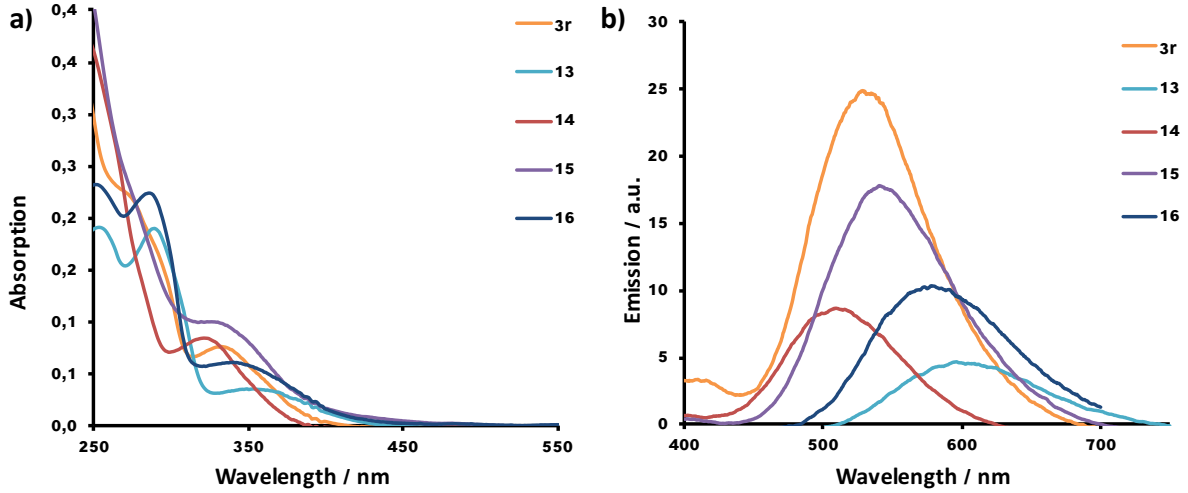


Figure 1.13 a) Absorption spectra of complexes **3r** and **13 – 16** in acetonitrile (20 μM); b) emission spectra of complexes **3r** and **11 – 15** in acetonitrile (20 μM). Complex **3r** is $Re(Pyta)(CO)_3Cl$, complex **13** is $Re[(5\text{-}COOMe)Pyta](CO)_3Cl$, complex **14** is $Re[(4\text{-}OMe)Pyta](CO)_3Cl$, complex **15** is $Re[(4\text{-}NO_2)Pyta](CO)_3Cl$, complex **16** is $Re[Pyta(5\text{-}COOEt)](CO)_3Cl$.

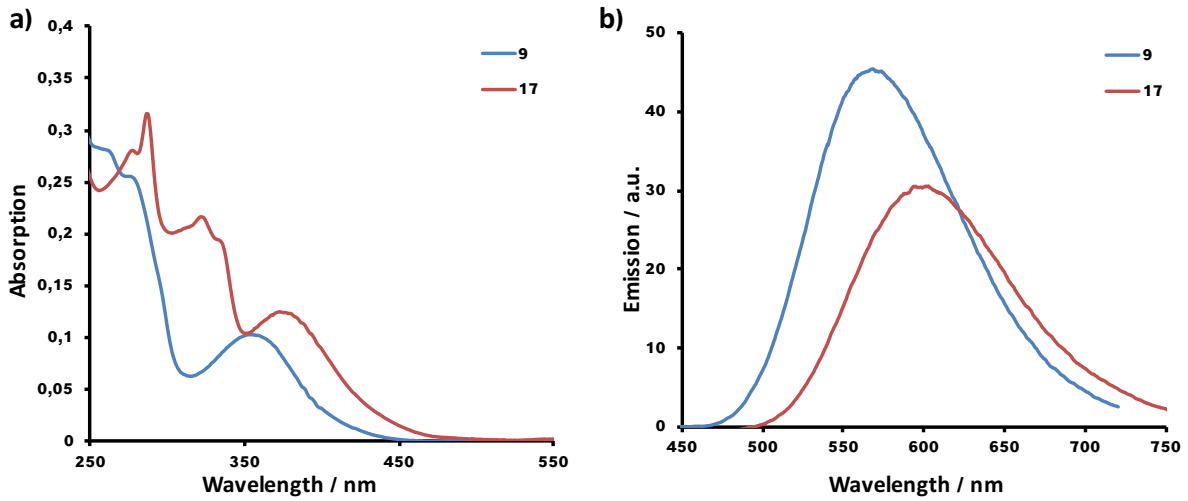


Figure 1.14 a) Absorption spectra of complexes **9** and **17** in acetonitrile (20 μM); b) emission spectra of complexes **9** and **17** in acetonitrile (20 μM).

Complex **16** also showed a red-shifted emission band (570 nm) compared with that of complex **3r** due to the electron-deficient ester group. The effect is weaker on both the absorption and the emission for complex **16** compared to complex **13**. It may be explained by an electronic communication less efficient through the triazole ring compared to the pyridine on the overall delocalisation. Nevertheless, modification of the 5- position of the triazole in Pyta ligand seems to show stronger impact than at the 1- position. This position might be an interesting alternative for further investigation.
Complex **9** showed an emission centred at 567 nm, which originated from ^{3}MLCT transition. Complex **17** showed an emission band centred at 600 nm (Figure 1.14-b), which is red shifted compared that of complex **9**.

Table 1.1 Photophysical data for complexes **3r**, **9** and **13 – 17** at room temperature in acetonitrile (20 μM).

Complex	Abs (nm)	Excitation (nm)	Emission (nm)	Range (nm)	Stokes shift (nm)	φ (%)
3r	280, 330	330	530	450 – 660	200	0.09
13	291, 350	350	600	500 – 600	250	0.01
14	299, 321	321	500	450 – 600	179	0.03
15	245, 330	330	538	450 – 700	208	0.05
16	290, 340	340	570	500 – 700	230	0.06
9	355	355	567	480 – 700	212	0.24
17	372	372	600	500 – 760	228	0.07

1.2.3 Computational investigation

DFT calculations were performed using Gaussian 09 software package[146] (B3LYP functional, PCM model for acetonitrile, LANL2DZ basis set for rhenium and 6-311G** basis set for the other atoms) for complex **3r**, **9**, **13**, **16**, **17** to better analyse the absorption and emission data. The alkyl chain length was reduced into an ethyl group in order to save calculation time since the length does not affect the photophysical properties much in organic solvent.[55] The corresponding structures are named **3r'**, **9'**, **13'**, **16'** and **17'** (Figure 1.15). The Cartesian coordinates of all the complexes were listed in Table appendix 2 – 6.

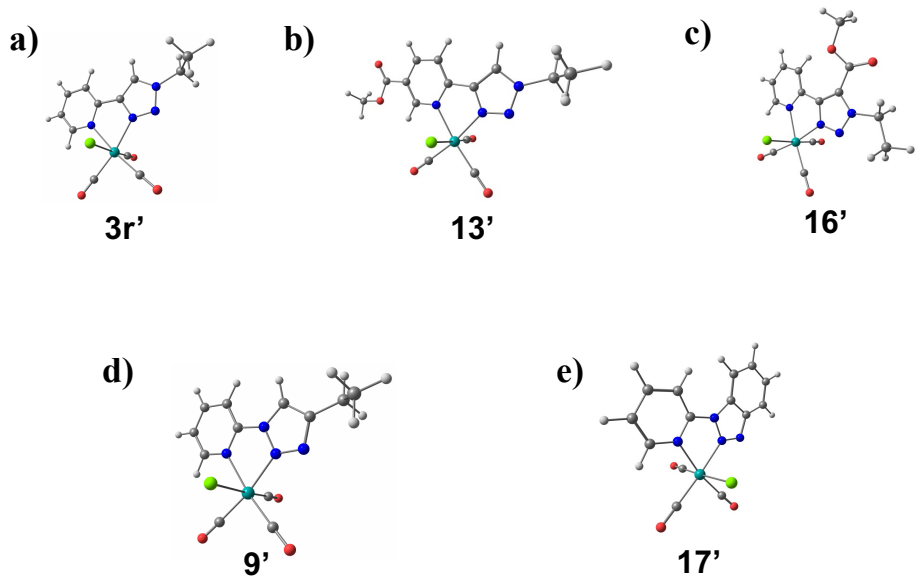


Figure 1.15 Optimized geometries of complex **3r'** (a), **13'** (b), **16'** (c), **9'** (d), **17'** (e). H atoms are in light grey, C atoms in grey, O atoms in red, N atoms in blue, Cl atoms in bright green, Re atoms in green. Complex **3r'** is Re(Pyta)$(CO)_3$Cl, complex **13'** is Re[(5-COOMe)Pyta]$(CO)_3$Cl, complex **16'** is Re[Pyta(5-COOEt)]$(CO)_3$Cl, complex **9'** is Re(Tapy)$(CO)_3$Cl, complex **17'** is Re(Benzotriazole-Py)$(CO)_3$Cl.

Table 1.2 Selected predicted bond lengths (unit: Å).

	C(1)≡O(1)	C(2)≡O(2)	C(3)≡O(3)	Re−C(1)	Re−C(2)	Re−C(3)	Re–N(1)	Re–(N2)
3r'	1.153	1.153	1.157	1.925	1.929	1.909	2.243	2.176
13'	1.153	1.153	1.157	1.925	1.929	1.910	2.245	2.176
16'	1.153	1.153	1.157	1.927	1.930	1.910	2.230	2.166
9'	1.151	1.152	1.156	1.927	1.930	1.912	2.231	2.169
17'	1.151	1.151	1.155	1.929	1.933	1.914	2.220	2.158

(1) refers to the CO trans to pyridine, (2) to the CO trans to triazole and (3) to the CO trans to axial ligand, N(1) refers to pyridine and N(2) to triazole ring.

The predicted coordination geometries of the complexes are distorted octahedral with tricarbonyl moiety in a *facial* fashion and chlorine atom at the axial position. The N^N moiety keeps planar as in complex **3r** and **9**. Generally, the modifications on the pyridine ring (complex **13'**) had no influence on the Re-C, Re-N and C≡O bonds compared to complex **3r'**, which is in agreement with the IR data. Complex **16'** showed both shorter Re-N(pyridine) and Re-N(triazole) bonds than that of complex **3r'**. Complex **17'** also displayed shorter Re-N(pyridine) and Re-N(benzotriazole) bonds than that of complex **9'**.

Frontier orbital diagrams for these complexes are shown in the Figure 1.16 – 1.17 and Figure appendix 1-5. The HOMO of all complexes localized mainly on dπ(Re) and chlorine. However, for complex **3r'**, **13'**, **16', 9'** and **17'**, the HOMO showed also small contributions on carbonyl

ligands. Meanwhile, the introduction of electron-deficient groups on Pyta ligand hardly affected the HOMO compared with that of complex **3r'**, the HOMO energy of complexes **13'**, and **16'** being very close to each other. The HOMO energy of **9'** and **17'** are closed to each other, indicating the less effect of the modification of the N^N ligand on the electron density of the metal centre.

The LUMO of all the complexes were localized on the N^N ligand. However, with different functional groups at different positions, the LUMO distribution on the Pyta ligand was slightly different. For complex **13'**, the LUMO was not only localized on the Pyta but also on the ester group with main contributions on the pyridine ring. For complex **16'**, the LUMO was mainly localized on the triazole ring rather than on the pyridine. The energy gap of complex **13'** is 3.67 eV, which is smaller than that of complex **16'** (3.75 V). This is in line with the fact that the lowest energy absorption of complex **13** (350 nm) has longer wavelength than that of complex **16** (340 nm). Both the modification on pyridine and triazole modify the distribution of LUMO. However, the impact on the stabilisation of LUMO level is different. Complex **16'** showed less strong effect on the stabilisation of LUMO level. The extension of π-system of triazole (complex **17'**) stabilize the LUMO level compared that of complex **9'** and thus lead to a lower energy gap (3.65 eV for complex **17'** and 3.82 eV for complex **9'**), which is in agreement with the fact that complex **17** (372 nm) showed longer wavelength of lowest energy wave than that of complex **9** (355 nm).

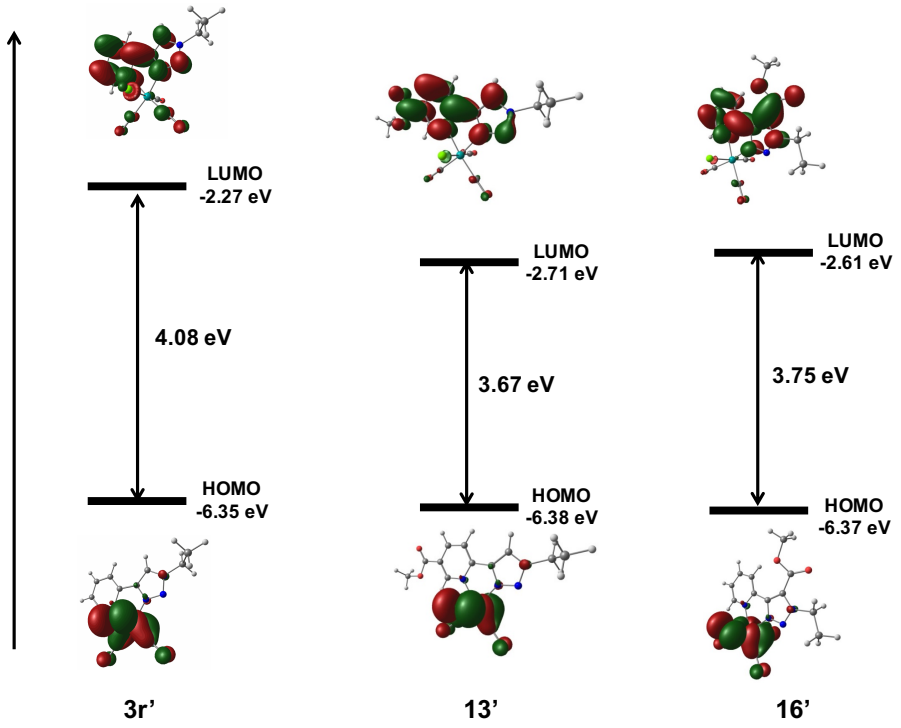


Figure 1.16 Frontier molecular orbitals for complexes **3r'**, **13'** and **16'**.

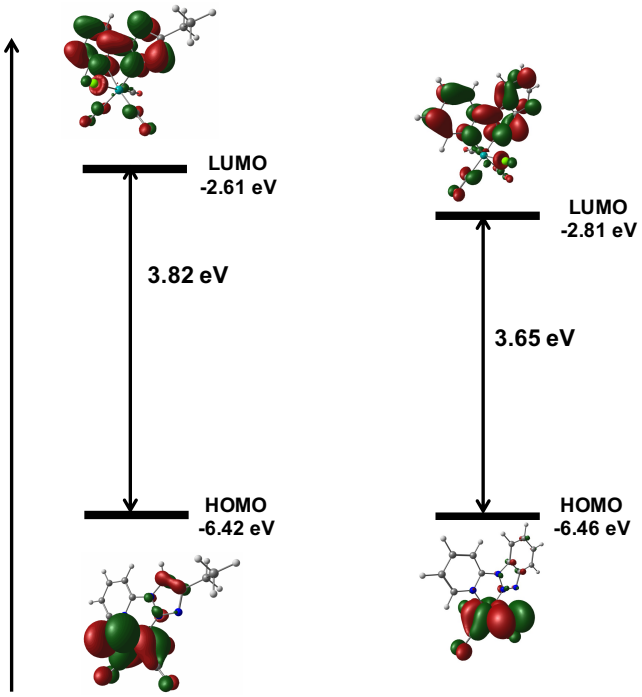


Figure 1.17 Frontier molecular orbitals for complexes **9'** and **17'**.

The ten first singlet excited states of complexes **13'**, **16'** and **17'** were evaluated with TD-DFT using Gaussian 09 with the same parameters (Table 1.3 and Table appendix 19 – 21). For complex **13'**, according to the predicted transitions with significant oscillator strength, the lowest energy absorption band predicted at 402 nm is assigned to dπ(Re)→ π*(Pyta) metal-to-ligand charge transfer and the absorption band predicted at 298 nm is assigned to mainly π(Pyta)→ π*(Pyta) intraligand charge transfer. Complex **16'** was predicted to have a low-energy absorption band at 393 nm, assigned to dπ(Re)→ π*(Pyta) metal-to-ligand charge transfer, and a higher-energy absorption band at 289 nm which is assigned to a mixed π(Pyta)→ π*(Pyta) intraligand charge transfer and dπ(Re)→ dπ*(Re) metal-centered transition. The predicted lowest-energy absorption wavelength of complex **16'** is shorter than that of complex **13'**, which satisfactorily reproduced the experimental results. Complex **17'** was predicted to have several absorption band assigned to dπ(Re)→ π*(Tapy) metal-to-ligand charge transfer, which explain the unstructured absorption band obtained from UV-Vis spectrometry and a higher-energy absorption band assigned to π(Pyta) → π*(Tapy) intraligand charge transfer.

Table 1.3 Selected singlet excited states for complexes **13'**, **16'** and **17'** in acetonitrile.

	Trans.	**Orbital excitations (Contributions)**	**Character**	**Calcd/nm (*f*)**
13'	2	HOMO-1→LUMO, 99%	dπ(Re)→ π*(Pyta), MLCT	402 (0.0856)

	6	HOMO – 3→LUMO, 81%	π(Pyta)→ π*(Pyta), ICT	298 (0.4824)
16'	2	HOMO-1→LUMO, 98%	dπ(Re)→ π*(Pyta), MLCT	393 (0.1044)
	9	HOMO-3→LUMO, 24% HOMO-1→LUMO+3, 57%	π(Pyta)→π*(Pyta), ICT dπ(Re)→ dπ*(Re), metal-centred transition	289 (0.1402)
17'	2	HOMO-1→LUMO, 98%	dπ(Re)→ π*(Pyta), MLCT	479 (0.2551)
	4	HOMO-3→LUMO, 27% HOMO-1→LUMO+1, 70%	dπ(Re)→π*(Pyta), MLCT dπ(Re)→π*(Pyta), MLCT	355 (0.1693)
	5	HOMO-3→LUMO, 63% HOMO-1→LUMO+1, 9% HUMO→LUMO+1, 27%	dπ(Re)→ π*(Pyta), MLCT dπ(Re)→π*(Pyta), MLCT dπ(Re)→π*(Pyta), MLCT	352 (0.2278)
	6	HOMO-3→LUMO, 8% HOMO-1→LUMO+1, 89%	dπ(Re)→π*(Pyta), MLCT dπ(Re)→π*(Pyta), MLCT	336 (0.2102)
	7	HOMO-7→LUMO, 3% HOMO-4→LUMO, 94%	dπ(Re)→π*(Pyta), MLCT π(Pyta)→π*(Pyta), ICT	311 (0.2195)

1.2.4 Summary

Here, we have designed and synthesised Pyta-based Re(I) tricarbonyl complexes with electron-donating group (methoxy group) or electron-withdrawing groups (ester or nitro group) to investigate their impact on the photophysical properties in rhenium Pyta complexes. DFT calculations were performed to have a better understanding of the photophysical behaviours.
The introduction of nitro group on the 4- position (*para*-) of pyridine ring had less impact on the photophysical properties than that of the methoxy group. The introduction of methoxy group on this position led to a destabilisation of the LUMO, which led to a blue shift of the absorption and emission waves, as observed in complexes with the classical bpy ligands.[124]
We modified the 5-position of the triazole on the Pyta framework for the first time. This position seems partially isolated from the whole ligand, meaning the electron communication through this position is moderate.
This may be a potential position to perform further investigations since it showed good balance between red-shifting the excitation wavelength and keeping a reasonable quantum yield. Other functional groups with moderate electron withdrawing effect such as –CHO and –COR will be

considered for this position. It also advantageously offers an additional position for further functionalisation with objects of interest along with position 1.
In this first series, complexes **16** and **17** showed fairly interesting properties in acetonitrile. These complexes will be further characterized in aqueous medium before exploring their potential as probes in bioimaging studies.
Furthermore, complexes **14**, **15** and **17** showed interesting behaviours for catalysing carbon dioxide electroreduction, which will be discussed in the next chapter.

1.3 Rhenium complexes bearing acetylide ligands

As σ-donating ligand, acetylide ligand has been introduced in different metal complexes (Pt,[147–151] Au,[148,151,152] Hg,[151] Cu,[153] *etc.*) for applications mainly based on their luminescent properties. In 1994, Che *et al.* reported the brightly emissive Pt(phen)(C≡CC_6H_5)$_2$ complex and proposed a ^{3}MLCT emissive state.[154] Yam *et al.* have also developed platinum-acetylide complexes[155] and rhenium-acetylide complexes.[124,126–132] Generally, the introduction of acetylide ligand causes red shift of the low energy absorption because the dπ(Re) orbital in the alkynyl complex is higher-lying in energy as a result of the stronger σ-donating ability of the alkynyl ligand than the chloro counterpart.[124] However, the related study based on Pyta Re(I) complexes had not been performed yet.
In this part, we designed a series of rhenium complexes bearing acetylide ligands to tune their photophyscial properties. *para*-Substituted ethynylbenzene were introduced to investigate the influence of electron withdrawing groups (–CN, –CHO, –NO_2) or electron donating group (–OMe) on the photophysical properties (Figure 1.18). The stability of all the complexes was confirmed by time-dependent ^{1}H NMR experiments. Then the photophysical properties and electrochemistry behaviour were investigated in acetonitrile. DFT and TD-DFT calculations were performed to have a better understanding of the experimental observations.

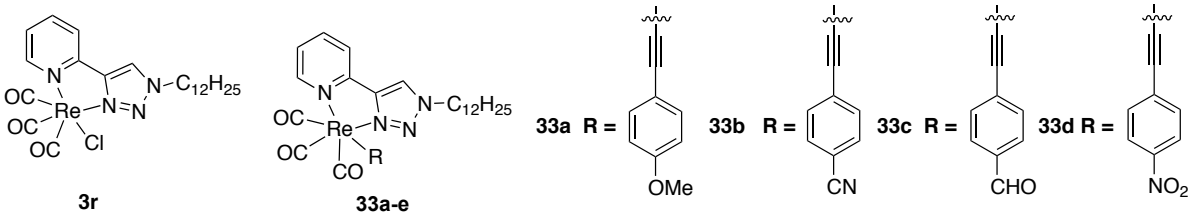
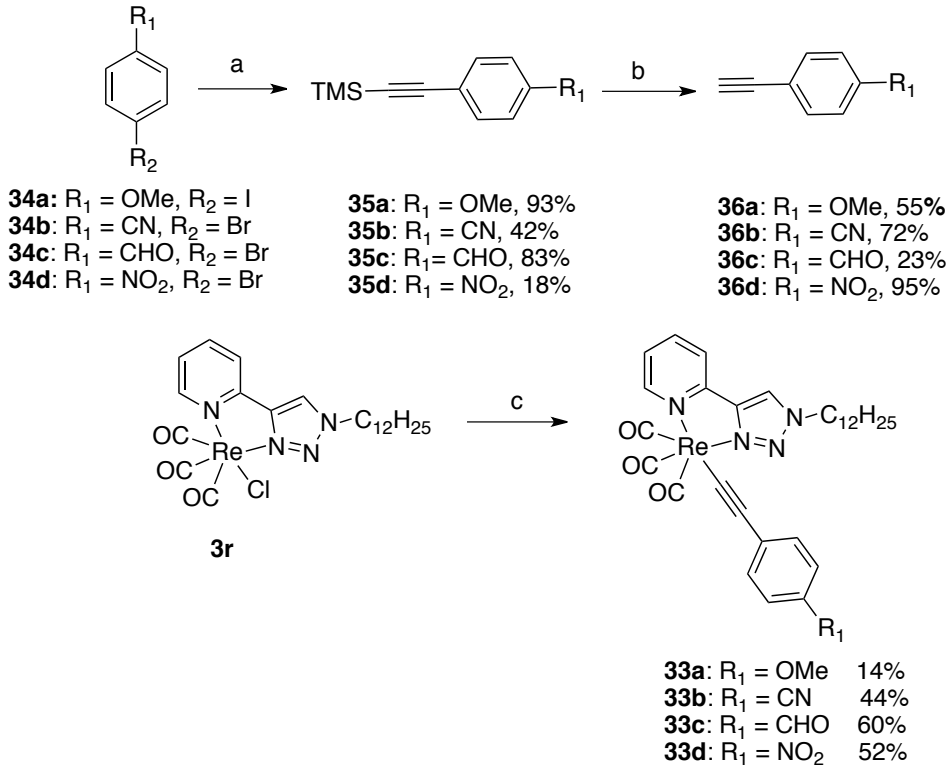


Figure 1.18 Molecular structure of complexes **3r** and **33a** – **d**.

1.3.1 Synthesis and stability

The corresponding acetylene ligands were synthesised from commercially available compounds **34a – d**. The Sonogashira cross coupling reactions with TMSA and the following deprotection reaction using potassium carbonate afforded the desired acetylene compounds in diverse yields, as shown in scheme 1.5.



Scheme 1.5 Synthetic route for complexes **33a – d**. Condition a: TMSA (1.2 equiv.), $Pd(PPh_3)_2Cl_2$ (5 mol%), CuI (5 mol%), Et_3N, THF, room temperature, overnight; b: K_2CO_3 (3.0 equiv.), THF, MeOH, room temperature, 30 minutes; c: AgOTf (1.1 equiv.), corresponding compound **36a – d** (1.1 equiv.) Et_3N (4.0 equiv.), THF, reflux in dark for 24 hours.

Complexes **33a – d** were synthesised by refluxing compound **3r** and the corresponding acetylene with silver trifluoromethanesulfonate and triethylamine in anhydrous tetrahydrofuran. The yields were moderate for complexes **33b – d**, which is close to reported yield using similar protocole,[156,157] while that for complex **33a** was low. It may due to the reduced reactivity of the corresponding acetylene compound due to the EDG –OMe. All the complexes were characterized by ^{1}H NMR, ^{13}C NMR and IR spectrometry. The IR spectra of all the complexes show two intense bands around 2006 and 1881 cm^{-1} for the A1 symmetric and E antisymmetric vibrations respectively characteristic for *fac*-rhenium tricarbonyl complexes. The IR spectra also showed the C≡C stretching vibration signal at *ca.* 2088 cm^{-1} for complexes **33a – d**.
The stability of all the complexes was investigated by time-dependent ^{1}H NMR experiments at a concentration of 4 mM. The results obtained for complex **33a** are shown in Figure 1.19 as an example and the others are in Figure appendix 20 – 22. All of the complexes were stable for more than 72 hours.

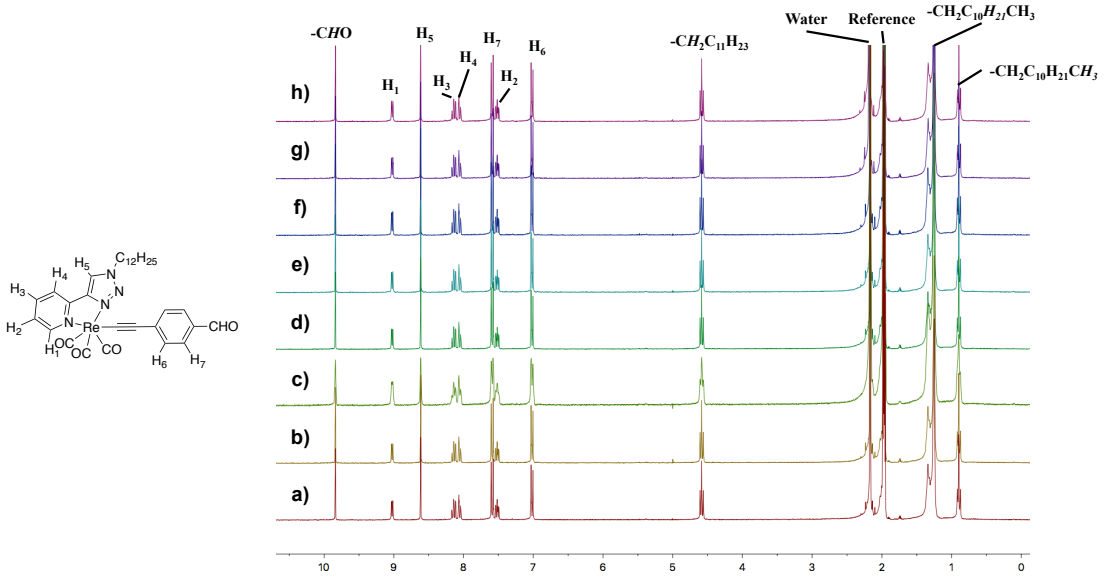


Figure 1.19 Partial ^{1}H NMR spectrum of complex **33c** in acetonitrile-d_3 at a concentration of 4 mM after 0 hour a), 1 hour b), 4 hours c), 8 hours d), 12 hours e), 24 hours f), 48 hours g), 72 hours h).

1.3.2 Photophysical investigation

The photophysical properties of the complexes were investigated in acetonitrile at a concentration of 20 µM at 298 K. The absorption data are summarized in Table 1.4, and the absorption spectra are shown in Figure 1.20 – a. Complexes **33a – d** also showed intense high-energy absorptions at around 280 nm which were assigned to $\pi \rightarrow \pi^*$ intraligand transition of the Pyta ligand and the acetylide ligand as well as absorption bands in the range of 330–380 nm assigned to partial ^{1}MLCT character. The absorption in the range of 330–380 nm also accounted for the observed yellow colour of complexes **33a – d**, which was similar to the yellow parent chloride complexes **3r**. Complexes **33a** exhibited similar absorption intensity as that of complex **3r** at 330 nm. However, for complexes **33b – d**, this band was much more intense**,** which suggests a contribution of a transition involving the acetylide ligand, probably of π(acetylide)→π*(Pyta ligand) ligand-to-ligand charge transfer character (LLCT). The introduction of an acetylide ligand with a nitro group led to a 20 nm red-shift of this band compared to the precursor complex **3r** (Re-Pyta-Cl). The trend of the low-energy absorption wavelength, ie. $\lambda_{max\ Abs}$: **33d**>**33c**>**33b,** followed the same trend as that of electron-withdrawing inductive effect (–NO_2>–CHO>–CN).

In line with the trend in MLCT absorption energies, the lower absorption energy for complexes **33a** – **b** compared with their chloride analogue is assigned to the better σ-donor ability of the acetylide moiety which would render the rhenium centre more electron rich and hence lower the MLCT emission energy.

Table 1.4 Photophysical data for complexes **3r** and **33a–d** at room temperature in acetonitrile (20 μM).

Complex	Abs (nm)	Excitation (nm)	Emission (nm)	Range (nm)	Stokes shift (nm)	Φ(%)
3r	280, 330	330	530	450-600	200	0.09
33a	275, 330	330	560	-	230	-
33b	255, 332	332	553	460-680	221	0.014
33c	270, 350	350	518	-	168	-
33d	275, 380	380	-	-	-	

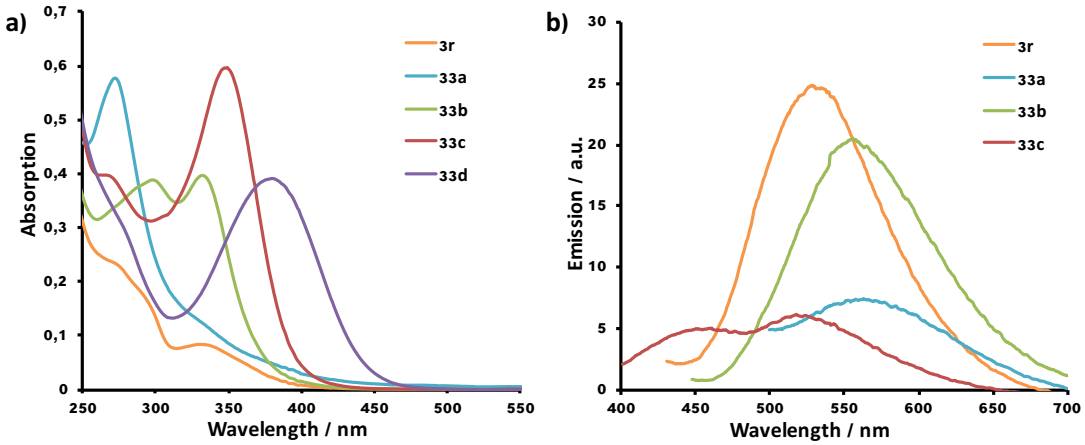


Figure 1.20 a) Absorption spectra of complexes **3r** and **33a – d** in acetonitrile (20 μM); b) emission spectra of complexes **3r** and **33a – d** in acetonitrile (20 μM).

The emission spectra of all the rhenium complexes were recorded in acetonitrile at 20 μM (Table 1.4 and Figure 1.20–b). Complex **3r** exhibited a broad emission band centred at 530 nm. Generally, the introduction of the alkynyl ligands decreased the quantum yield and the nitro group on the acetylide ligand (**33d**) totally quenched the emission. Complex **33a** with methoxy group exhibited an emission band 30 nm red-shifted compared with that of the complex **3r** while complex **33c** with aldehyde group showed an unstructured emission band 12 nm blue-shifted compared with that of the complex **3r**. The unstructured emission band of complex **33c** showed roughly two overlapping bands, which may be due to two emissive excited states of mixed characters. Complex **33b** displayed an emission band centred at 553 nm while keeping a reasonable emission intensity. The emission wavelength followed the trend of **33a**>**33b**>**33c**, which is in agreement of the electron donating abilities of the functional groups –OMe>-CN>-CHO, which is consistent with the observations by R. Eisenberg,[158] V. W. W. Yam,[159] and others[160] on the aromatic diimine, terpyridyl, and cyclometalated platinum(II) acetylide complexes.

1.3.3 Electrochemical investigation

The cyclic voltammograms (CV) of all the complexes were performed in acetonitrile at a concentration of 2 mM (Table 1.5). At a scan rate of 500 mV/s, irreversible oxidation waves were observed at *ca*. 1.2 to 1.5 V versus SCE for all of the complexes, and were assigned to Re(I)/Re(II) oxidation. The observation that the complexes bearing acetylide ligands showed a less positive potential for the first oxidation wave than their chloride counterpart **3r** is due to the better σ-donating ability of the acetylide ligand than the chloride atom which makes the metal centre more electron rich and destabilizes the HOMO thus facilitates the oxidation of rhenium(I). The first oxidation potentials of the complexes **33b** – **d** were in the order **33d**>**33c**>**33b**, which is in agreement with the electron withdrawing ability (–NO_2>–CHO>–CN). With electron withdrawing groups on the *para*-position of the acetylide ligands, the electron density on the metal centre is weaker than that with electron donating groups, which makes the oxidation more difficult and lead to a more positive oxidation potential.
All of the compounds showed irreversible (compound **3r**, **33a** and **33c, 33d**) or quasi-reversible (compound **33b**) reduction wave at ca. -1.7 to -2.0 V versus SCE, which is assigned as Pyta-ligand-centred reduction. The quasi-reversibility and reversibility for complexes **33b** and **33d** suggest that they remained intact on the experimental scan timescale. The reduction potential for compounds **33a** – **d** was at ca. -1.78 to -1.93 V versus SCE which is more negative than that of their chloride counterpart **3r**, which is also due to the good σ-donating properties of acetylide ligands that further influence the electron density on Pyta ligand. Complex **33d** showed an additional reversible wave at -1.06 V versus SCE, which is assigned to the reduction of –NO_2 group, as well investigated.[161]

Table 1.5 Electrochemical data of complexes **3r** and **33a** – **d**.

Compound	Letter	Oxidation (E_p vs SCE[a])	Reduction (E_p or $E_{1/2}$ vs SCE[a])
Re-Pyta-Cl	**3r**	1.46[d]; 1.88[d]	-1.70[d]
Re-Pyta-C≡C-PhOMe	**33a**	1.02[d]; 1.43[d]	-1.84[d]
Re-Pyta-C≡C-PhCN	**33b**	1.23[d]; 1.53[d]	-1.78[c]
Re-Pyta-C≡C-PhCHO	**33c**	1.28[d]	-1.93[d]
Re-Pyta-C≡C-PhNO_2	**33d**	1.30[d]	-1.06[b]; -1.88[d]

[a] In acetonitrile solution with 0.2 M nBu$_4$NPF$_6$ as supporting electrolyte at room temperature under argon; $E_{1/2} = (E_{pa} + E_{pc})/2$; E_{pa} and E_{pc} are anodic peak and cathodic peak potentials. [b] Reversible waves. [c] Quasi-reversible waves. [d] Irreversible waves.

1.3.4 Computational investigation

The corresponding structures are named **33a'** − **d'**. The optimised structures are shown in figure 1.21 and the Cartesian coordinates of all the complexes were listed in Table appendix 7 – 10.

The rhenium(I) complexes **33a' – d'** adopt a distorted octahedral geometry, in which the three carbonyl groups are in a *facial* fashion. As shown in Table 1.6, the introduction of the acetylide ligands increased the distance of the Re−N (N atoms on N^N ligand) bond by ca. 0.02 Å. The Re-C≡C unit showed a linear arrangement (**33a'**: 178.9°; **33b'**: 178.9°; **33c'**: 179.2°; **33d'**: 178.8°) as expected for the sp hybridisation of C≡C bond in the acetylide moiety. The C≡C bond lengths (**33a'**: 1.225 Å; **33b'**: 1.226 Å; **33c'**: 1.227 Å; **33d'**: 1.227 Å) are typical of terminal σ-bonded metal-acetylide bonds.[156,157,162,163] The introduction of the acetylide ligands mainly affected the bond length of Re-C which is trans to acetylide ligand [marked Re-C(3)]. Compared to that of **3r'** which is 1.909 Å, the Re-C(3) length for complexes **33' – d'** is ~1.97 Å, which is due to tetragonal elongation. The C≡O bond distances are little impacted, which is consistent with the experimental IR vibration frequencies.

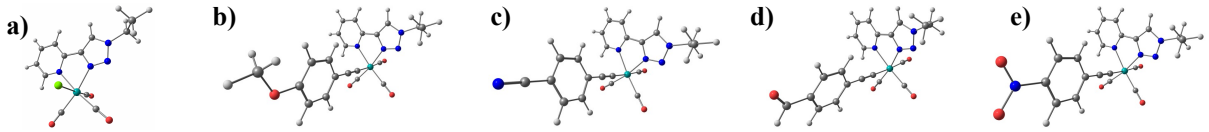


Figure 1.21 Optimized geometries of complexes **3r'** (a, Pyta-Re-Cl), **33a'** (b, Pyta-Re-C≡C-PhOMe), **33b'** (c, Pyta-Re-C≡C-PhCN), **33c'** (d, Pyta-Re-C≡C-PhCHO), **33d'** (e, Pyta-Re-C≡C-PhNO$_2$). H atoms are in light gray, C atoms in gray, O atoms in red, N atoms in blue, Re atoms in green.

Table 1.6 Selected predicted bond lengths in complexes **3r'** and **33a' – d'** (unit: Å).

	3r'	**33a'**	**33b'**	**33c'**	**33d'**
Re–N(1)	2.243	2.262	2.259	2.260	2.259
Re–N(2)	2.176	2.196	2.194	2.193	2.193
Re-C(1)	1.925	1.918	1.920	1.921	1.921
Re-C(2)	1.929	1.921	1.923	1.923	1.924
Re-C(3)	1.909	1.971	1.973	1.973	1.975
C(1)≡O(1)	1.153	1.156	1.156	1.155	1.155
C(2)≡O(2)	1.153	1.157	1.156	1.156	1.156
C(3)≡O(3)	1.157	1.155	1.153	1.153	1.153

(1) refers to the CO trans to pyridine, (2) to the CO trans to triazole and (3) to the CO trans to axial ligand, N(1) refers to pyridine and N(2) to triazole ring.

Frontier orbital diagrams for all complexes are shown in Figure 1.22 and Figure appendix 6 – 9. The LUMO orbital localized on the N^N ligand for complexes **3r'**, **33a' – c'** while it localized mainly on the nitro group for complex **33d'**. In the CV for complex **33d** we assigned the first reduction wave to the reduction of the nitro group and in UV-Vis spectra for **33d** the strong absorption band at ca. 400 nm was assigned to a strong intraligand charge transfer (ICT) transition π(acetylide) → π*(NO$_2$). The introduction of the acetylide ligands increased the LUMO energy for complexes **33a' – c'** as well as the LUMO+1 energy for complex **33d'** due to the better *σ*-donating ability of the acetylide ligand than that of the chloride counterpart in

agreement with the electrochemical data. The LUMO energy of complexes **33a' – c'** and the LUMO+1 energy of complex **33d'** are quite similar which is expected because the LUMOs are mainly localized on the Pyta ligand.

The HOMO of the complexes **33a' – d'** showed significant contribution from the π orbital of the acetylide ligands, along with some on the rhenium(I) centre. The introduction of the acetylide ligands raised the HOMO energy of the complexes **33a' – d'** compared with that of **3r'** to a level in agreement with the electron donating character of the substituent in *para* position: complex **33a'** functionalized with the electro-donating group –OMe showed the more destabilized HOMO (-5.33 eV). The HOMO energy of complexes **33b'** and **33c'** were similar (-5.78 eV and -5.75 eV respectively) while that of complex **33d'** is lower (-5.84 eV).

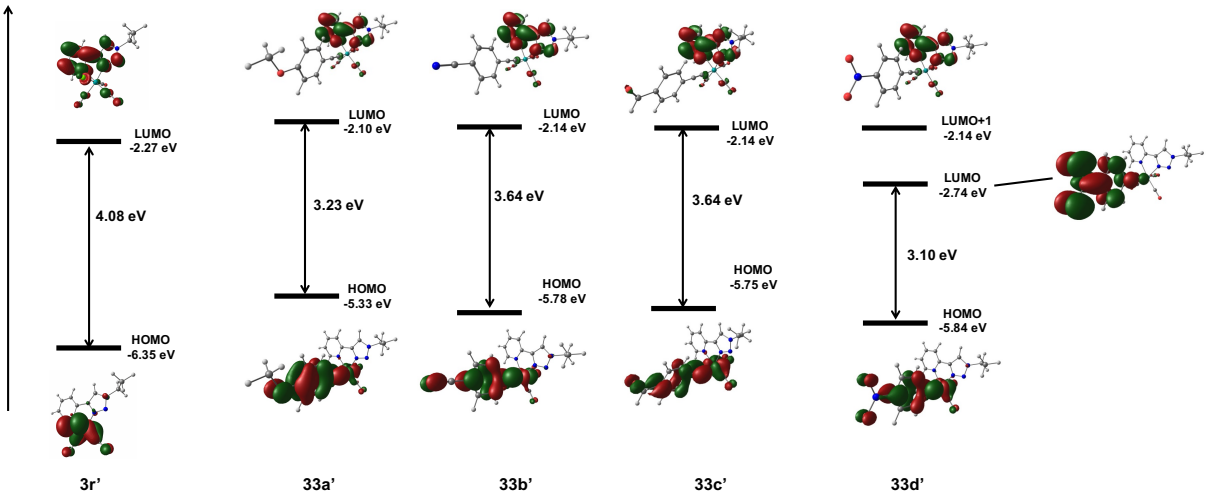


Figure 1.22 Frontier molecular orbitals for complexes **3r'** and **33a' – d'**.

The ten first singlet excited states of complexes **33a' – d'** were evaluated with TD-DFT using Gaussian 09 with the same parameters (Table 1.7 and Table appendix 22 – 25).

For complex **33a'**, according to the predicted transitions with significant oscillator strength, the lowest energy absorption band predicted at 479 nm is assigned to dπ(Re)→ π*(Pyta) metal-to-ligand charge transfer and the absorption band predicted at 373 nm is assigned to mainly π(acetylide)→ π*(acetylide) intraligand charge transfer. For complex **33b'**, the lowest energy absorption band predicted at 465 nm is assigned to a pure dπ(Re)→ π*(Pyta) MLCT and a higher energy absorption predicted at 398 nm is assigned to a pure π(acetylide)→ π*(–CN) intraligand charge transfer. Complex **33c'** showed a low energy absorption band predicted at 468 nm with mainly dπ(Re)→ π*(Pyta) MLCT as well as a high-energy absorption (423 nm) with stronger oscillator strength which is assigned to mainly π(acetylide)→ π*(acetylide) intraligand charge transfer. Complex **33d'** had a lower energy absorption band (526 nm) which is assigned to mainly dπ(Re)→ π*(–NO_2) transition and a higher energy absorption band (340 nm) which is assigned to mainly π(acetylide)→ π*(–NO_2) ICT mixed with small part of dπ(Re)→ π*(pyridine) MLCT.

Table 1.7 Selected singlet excited states for complexes **33a'** – **d'** in acetonitrile.

	Trans.	Orbital excitations (contributions)	Character	Calcd/nm (*f*)
33a'	2	HOMO -1 → LUMO (99%)	dπ(Re)→ π*(Pyta), MLCT	479 (0.0846)
	7	HOMO→LUMO+3 (91%)	π(acetylide)→π*(acetylide), ICT	373 (0.5399)
33b'	2	HOMO -1 → LUMO (99%)	dπ(Re)→ π*(Pyta), MLCT	465 (0.1050)
	3	HOMO → LUMO + 1 (95%)	π(acetylide)→ π*(–CN), ICT	398 (1.0171)
33c'	2	HOMO-1 → LUMO (97%)	dπ(Re)→ π*(Pyta), MLCT	468 (0.1136)
	3	HOMO → LUMO+1 (95%)	π(acetylide)→ π*(acetylide), ICT	423 (1.0140)
33d'	2	HOMO-1→LUMO (97%)	dπ(Re)→ π*(–NO_2), MLCT	526 (0.8793)
	9	HOMO-3→LUMO (73%); HOMO-1→LUMO+2 (14%)	π(acetylide)→ π*(–NO_2), ICT; dπ(Re)→ π*(pyridine), MLCT	340 (0.2386)

Calcd: calculated absorption wavelength; *f*: Oscillator strength.

The predicted oscillator strengths fit the experimental data well. The band predicted around 470 nm for complexes **33a' – c'** corresponds to the observed band around 330 nm which confirms the MLCT character of this band. The higher energy absorption band for complexes **33a' – c'** showed the trend of the red shifting which is in agreement with the electron properties of the functional groups on the acetylide ligand. The higher energy predicted band for complexes **33a' – b'** (373 nm and 398 nm, respectively) has ~100 nm difference from the predicted MLCT bands, which means that on UV spectra, these two bands are probably also separated. This higher energy band corresponds to the more intense band at shorter wavelength in the UV spectra (275 nm for complex **33a** and 255 nm for complex **33b**), which is confirmed as intraligand charge transfer character. Thus, for complex **33a** and **33b**, the excitation at the lowest energy absorption band is mainly MLCT transition. For complex **33c'**, the predicted higher energy absorption (423 nm) displays a strong red shift compared to complexes **33a'** and **33b'** and is close to the predicted MLCT band (468 nm), which may lead to the experimental observation of a single broad intense band. The intense absorption at ~330 nm in UV spectrum of complex **33c** may be due to a mixture of transitions of MLCT and ICT character. Excitation at this wavelength may lead to mixed ^{3}MLCT and ^{3}ICT transitions. This would explain the unstructured and much weaker emission wave of complex **33c**. For complex **33d'**, the band

predicted at 526 nm corresponds to the observed band around 380 nm, which is in agreement with the significant red shift of the lowest energy absorption band when compared with that of complexes **33a – c**. Also, the band at 526 nm showed different MLCT character [π(Re)→ π*(-NO_2)] from the other **33a' – c'** complexes [π(Re)→ π*(Pyta)]. This π(Re)→ π*(-NO_2) MLCT is not emissive, which explains the total quench of the emission. However, the π(acetylide) → π*(N^N) LLCT transition is not predicted for all the complexes **33a – d**, which will sometimes appear for acetylide complexes.[164]

1.3.5 Summary

Here, we designed and synthesised a series of Pyta-based Re(I) tricarbonyl complexes with a *para*-substituted phenylacetylide as axial ligand, which showed diverse emission properties. All the complexes were characterized using ^{1}H, ^{13}C NMR, IR and high-resolution mass spectroscopy. The complexes were stable in acetonitrile for at least 3 days. The electrochemical behaviour of the complexes was investigated, and DFT/TD-DFT calculations were performed. The replacement of the chloride by an acetylide ligand caused intraligand charge transfer to arise in these complexes. The component of π(alkynyl)→ π*(functional group) intraligand charge transfer increased when the acetylides bear electron withdrawing groups (–CN, –CHO) compared with electron donating group (–OMe).

As a stronger σ-donating ligand, acetylide ligands may be interesting in $[Re(N^N)(CO)_3X]^{n+}$ systems as the resulting compounds are stable enough to perform further study. Complex **33b** with –CN showed overall interesting emission properties at the same concentration though the absorption is also more intense. It might be interesting to introduce other electron donating groups on the acetylide ligand, such as amino group which could produce complexes with photophysical properties sensitive to pH, valuable tools since the pH in cells could reflect a disease state. Thus, the careful introduction of alkynyl ligands could also offer inspiration for the design of novel $[Re(N^N)(CO)_3X]^{n+}$ complexes.

1.4 Rhenium complexes with arenethiolate ligands

In this part, we designed two series of rhenium complexes, *fac*-[Re(Pyta)(CO)$_3$X] and *fac*-[Re(Tapy)(CO)$_3$X], bearing arenethiolate ligands to study their impact on photophysical properties. The introduction of EWG/EDG will modulate the ligand donor strength of the arenethiolate (Figure 1.23). The stability of all the complexes was studied by time dependent ^{1}H NMR experiments. Then the photophysical properties and electrochemistry behaviour were investigated in acetonitrile. DFT and TD-DFT calculations were performed to have a better understanding of the experimental observations. This work has been published.[165]

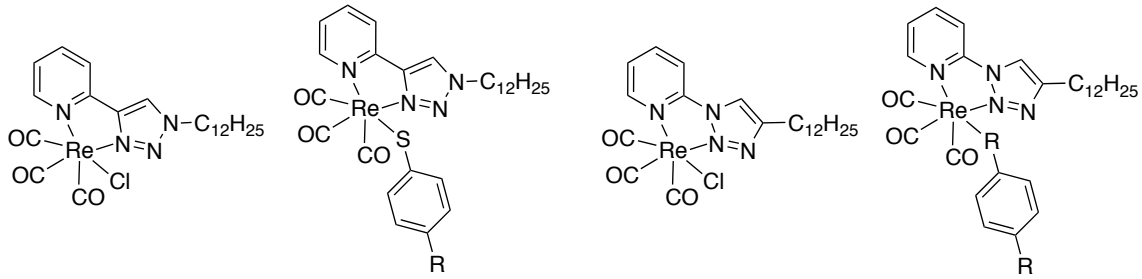
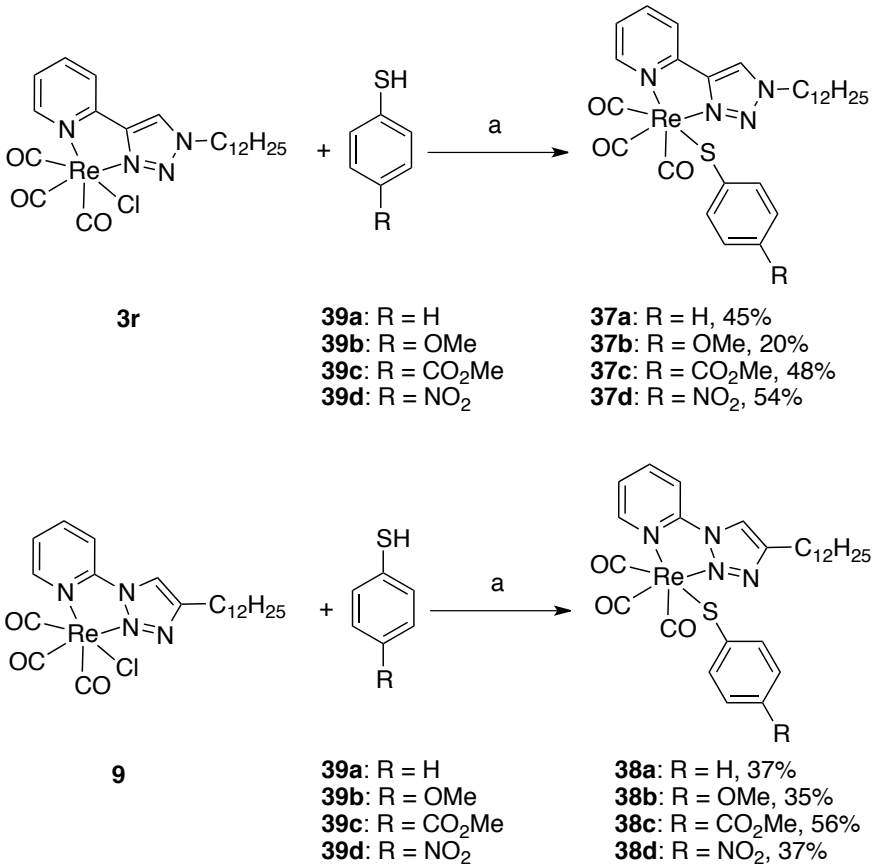


Figure 1.23 Molecular structures of the complexes.

1.4.1 Synthesis and stability

Complexes **37a – d** and **38a – d** were synthesized in moderate yields by ligand exchange using silver triflate in anhydrous THF followed by the addition of the corresponding benzenethiol in the presence of triethylamine.[138] The moderate yields may be due to the potential formation of dinuclear rhenium(I) complexes bridged by sulphur atoms or in some cases to the incomplete reaction of the second-step ligand exchange.

All the complexes were characterized by ^{1}H NMR, ^{13}C NMR, IR and high-resolution mass spectroscopy. The IR spectra of all the complexes showed two intense bands around 2020 and 1900 cm^{-1} for the A1 symmetric and E antisymmetric vibrations respectively characteristic for *fac*-rhenium tricarbonyl complexes.[166,167] These vibrations frequencies are higher than that for acetylide Re(I) complexes **33a – d**, indicating stronger C≡O bonds in thiolate Re(I) complexes. This is due because the stronger σ-donor character of acetylide ligand strengthens the π-backbonding from Re(I) to CO thus weaken the C≡O bond. The vibration frequencies did not shift a lot for all the complexes whether the axial ligand is a chloride or an arenethiolate, which means that the introduction of the arenethiolate ligand does not perturb the strength of the C≡O bonds.



Scheme 1.6 Synthetic route of complexes **37a – d** and **38a – d**. Condition a: 1) AgOTf (1.1 equiv.), THF, room temperature in dark for 2 hours; 2) corresponding compound **39** (1.0 equiv.), Et_3N (4.0 equiv.), THF, room temperature in the dark for 24 hours.

Parent Pyta and Tapy-based Re tricarbonyl complexes may undergo halogen ligand exchange in coordinating solvents or degradation in solution by decoordination of the diimine ligand. Thus, the stability of all the newly prepared arenethiolate complexes was investigated by time-dependent ^{1}H NMR experiments in acetonitrile-d_3 at a concentration of 4 mM at room temperature (For the time-dependent ^{1}H NMR of all the complexes, see figures in Figure appendix 23 – 30, Figure 1.24 shows partial ^{1}H NMR spectrum of complex **38a**). The solutions were exposed to air and the NMR tubes were kept in the dark.

Here partial (10 – 5 ppm) ^{1}H NMR of complex **38a** was chosen as an example (Figure 1.24). ^{1}H NMR of complex **38a** showed the slow appearance of new sets of peaks after 8 hours, among which ^{1}H signals corresponding to that of the free Tapy ligand (Figure 1.24-j) indicating a decoordination of the Tapy ligand.

According to the time-dependent ^{1}H NMR experiments, all the complexes were stable for more than eight hours in acetonitrile. A slow and partial degradation occurred over 72 hours for some of them (benzenethiolate complexes **37a** and **38a** as well as *p*-methoxy benzenethiolate complexes **37b** and **38b**) and the Tapy complexes **38a** and **38b** were less stable than complexes **37a** and **37b**. The photophysical studies were therefore performed using freshly prepared solutions in acetonitrile.

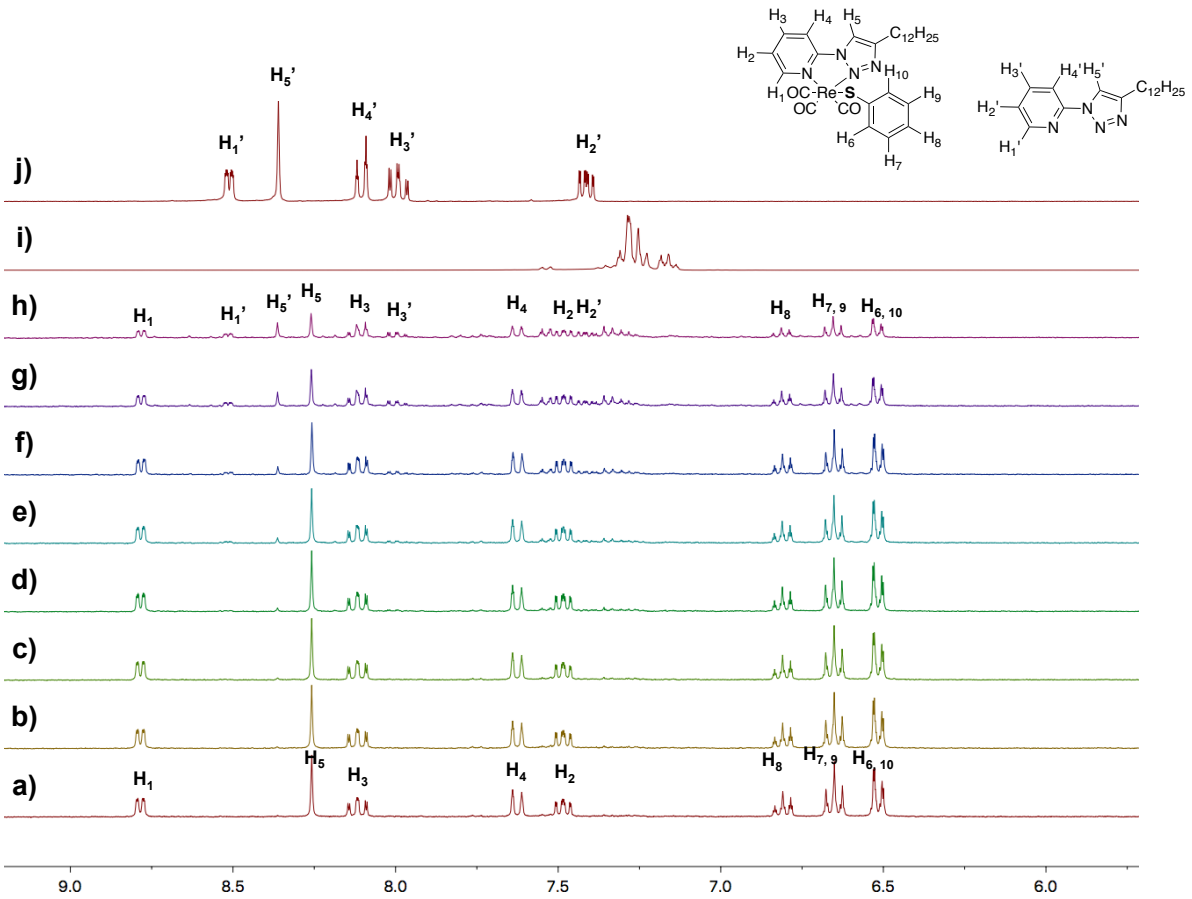


Figure 1.24 Partial ^{1}H NMR spectrum of complex **38a** in acetonitrile-d_3 at a concentration of 4 mM after 0 hour a), 1 hour b), 2 hours c), 8 hours d), 16 hours e), 24 hours f), 48 hours g), 72 hours h), thiophenol i) and Tapy ligand j) in acetonitrile-d_3.

1.4.2 Photophysical investigation

The photophysical properties of all the complexes were investigated in acetonitrile at a concentration of 20 µM at 298 K. The absorption data are summarized in Table 1.8, and the absorption spectra are shown in Figure 1.25. All the complexes bearing arenethiolate ligands showed absorption bands between 430~450 nm which explain the observed orange-red colour of these complexes compared to their yellow parent chloride complexes **3r** and **9**. Complexes **37a – d** and **38a – d** displayed absorption in the range of 330-345 nm assigned to partial ^{1}MLCT character. In the Pyta series (complexes **3r** and **37a – d**), this band was slightly blue-shifted for complexes **37a**, **37b** and **37d** compared to the chloride parent complex **3r** and it was 15 nm red-shifted for complex **37c**. In the Tapy series (complexes **9** and **38a – d**), this band is blue shifted for all the arenethiolate complexes compared to the chloride complex **9**. This phenomenon suggests a contribution of a transition involving the arenethiolate ligand, hypothesized that this absorption band may be controlled by the arenethiolate ligand.

Nitro functionalized complexes **37d** and **38d** showed an intense absorption band at 430 and 420 nm, respectively. This band is assigned to a strong intraligand charge transfer (ICT) transition

π(benzenethiolate) → π*(NO_2) which has been observed previously with acetylide Re(I) complexes as well as in platinum(I) complexes.[139]

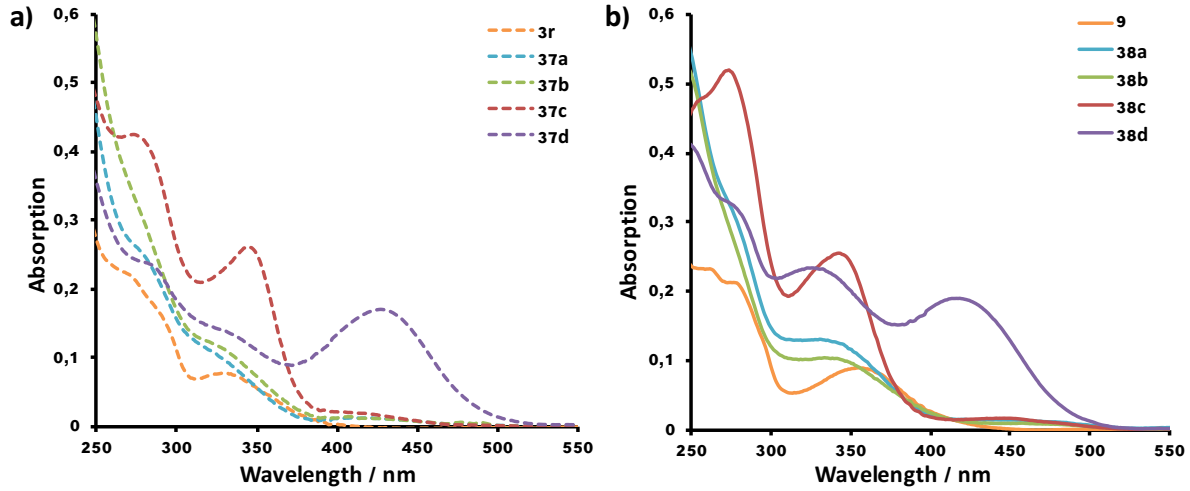


Figure 1.25 a) UV-Vis absorption spectra of complexes **3r** and **37a – d** in acetonitrile (20 μM); b) UV-Vis absorption spectra of complexes **9** and **38a – d** in acetonitrile (20 μM).

The emission spectra of all the rhenium complexes were recorded in acetonitrile at 20 μM (Table 1.8 and Figure 1.26). The introduction of a nitro group at the *para*- position of the arenethiolate ligand (**37d** and **38d**) quenched the emission of the complexes. The Tapy complex **38b** with methoxy group at the *para* position of the arenethiolate ligand was also non-emissive while the Pyta complex **37b** was weakly emissive with an emission band centred at 450 nm. Complexes **37c** and **38c** exhibited a very broad emission band of low intensity centred at 608 and 650 nm, respectively, characterized by a larger Stokes shift (258 nm for complex **37c** and 300 nm for complex **38c**) compared with that of their parent chloride complexes. Complex **37a** displayed a very weak emission band at 633 nm red-shifted compared to **3r**, while the complex **38a** showed a weak emission at 526 nm blue-shifted compared to **9**. This phenomenon has been observed for *fac*-[$Pt(Me)_3(bpy)SR$] complexes.[140] It indicated that the simple assumptions of the substituent effects sometimes can be misleading and its significance cannot be estimated simply from electron-donating/withdrawing arguments.

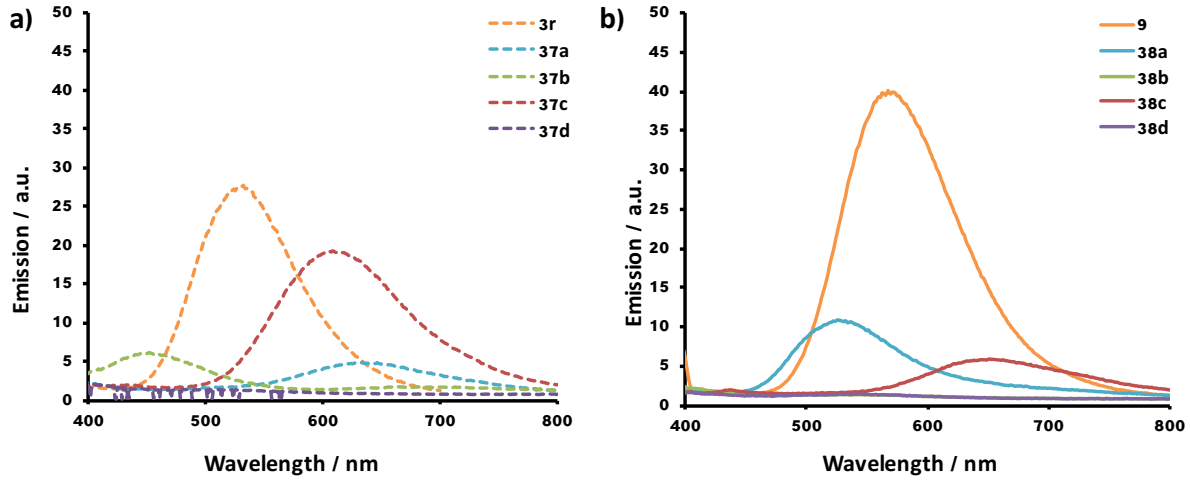


Figure 1.26 a) Emission spectra of complexes **3r** and **37a – d** in acetonitrile (20 μM); b) emission spectra of complexes **9** and **38a – d** in acetonitrile (20 μM).

The introduction of the arenethiolate ligands decreased the quantum yields compared to the corresponding chloride complexes. The emission wavelengths depend on both the nature of the N^N ligand and the arenethiolate ligand, by contrast with the dinuclear rhenium complexes with bridging thiolate ligands which emissive excited state is mainly of ^{3}MLCT character.[138] This may suggest an emission of mixed ^{3}MLCT/^{3}LLCT character originating from a Re(d)/π(benzenethiolate) → π* (N^N) transition. To have a better understanding of the photophysical observations, DFT and TD-DFT calculations were performed.

Table 1.8 Photophysical data for complexes at room temperature in acetonitrile (20 μM).

Complex	Absorption (nm)	Excitation (nm)	Emission (nm)	Range (nm)	Stokes shift (nm)	Φ(%)
3r	332	330	532	450 – 640	202	0.15
37a	330/421	330	633	550 – 750	303	0.03
37b	330/421	330	450	-	110	-
37c	347/415	350	608	500 – 800	258	0.06
37d	330/430	330/430	-	-	-	-
9	355	355	567	480 – 700	212	0.24
38a	330/457	330	526	450 – 650	196	0.04
38b	334/460	330	-	-	-	-
38c	344/450	350	650	570 – 800	300	0.02
38d	327/420	330/420	-	-	-	-

1.4.3 Electrochemical investigation

The cyclic voltammograms (CV) of all the complexes were performed in acetonitrile at a concentration of 1 mM and the data were summarised in Table 1.9. The electrochemical data for the chloride complexes **3r** and **9** agreed with the photophysical properties and previous observations.[63] At a scan rate of 100 mV/s, complexes **3r** and **9** showed irreversible oxidation waves with potentials (E_p) of 1.46 and 1.51 V versus SCE, respectively, which were assigned to the oxidation of Re(I)→Re(II). The similar potential of the oxidation indicated the closeness of the HOMO energy levels of the two complexes. Complexes **3r** and **9** also showed irreversible reduction waves with E_p of -1.70 and -1.43 V versus SCE, respectively which were assigned to the reduction of the N^N ligand. The more positive reduction potential for Tapy rhenium(I) complex indicated that it is easier to reduce Tapy ligand than Pyta ligand, which means that the Tapy ligand is a better electron acceptor than the Pyta ligand.

When bearing thiolate ligands, the oxidation waves of Pyta complexes **37a – d** were irreversible with much less positive potentials E_p of 0.77, 0.73, 0.88 and 0.97 V versus SCE respectively, compared to complex **3r** (1.46 V versus SCE). The oxidation potential follows the order **37b** < **37a** < **37c** < **37d**, reflecting the electron donating character of the substituents on the thiolate ligands (–OMe > –H > –COOMe > $–NO_2$). Electron donating groups (with a mesmeric effect) in *para*- position of the benzenethiolate increased the electron density and made the ligand a better π-donor, thus destabilized the HOMO (centred on Re) energy, leading the resulting complex easier to oxidize. A similar trend was observed for complexes **38a – d** except for the inversion of the complexes **38c** and **38d**, which showed close oxidation potential values (Table 1.9). Both the metal centre and the arenethiolate ligand were probably involved during the oxidation process.

Complexes **37a – c** showed quasi-reversible reduction waves with $E_{1/2}$ values that were in the same region as the E_p for complex **3r** (-1.76, -1.67 and -1.67 V versus SCE for **37a**, **37b** and **37c**, respectively). The quasi-reversibility of the reduction waves of complexes **37a – c** suggests that unlike complex **3r** where the chloride ligand decoordinates upon reduction, these complexes remained to some extent intact during the CV timescale. Complex **37d** showed a reversible reduction wave at $E_{1/2}$ of -1.17 V versus SCE, which is assigned to the reduction of the nitro group, and an irreversible reduction wave at -1.69 V versus SCE. Complexes **38a – c** showed irreversible reduction waves with E_p values slightly more negative than that of **8** (-1.52, -1.48, and -1.44 V vs SCE for **38a, 38b** and **38c**, respectively). Similar with complex **37d**, complex **38d** also displayed a first reversible reduction wave at -1.16 V versus SCE which is assigned to the reduction of the nitro group and a second quasi-reversible wave at -1.46 V verse SCE. The introduction of the arenethiolate ligands did not affect much the first reduction potential of complexes **37a – c** and **9**, **38a – c**, which is centred on the N^N ligands. The second reduction in **37d** and **38d** also fits this trend.

Table 1.9 Electrochemical data of complexes.

Complex	Oxidation (E_p vs SCE[a])	Reduction (E_p or $E_{1/2}$ vs SCE[a])
3r	+1.46	-1.70[d]
37a	+0.77	-1.76[c]
37b	+0.73	-1.67[c]
37c	+0.88	-1.67[c]
37d	+0.97	-1.17[b], -1.69[d]
9	+1.51	-1.43[d]
38a	+0.83	-1.52[d]
38b	+0.73	-1.48[d]
38c	+0.88	-1.44[d]
38d	+0.90	-1.16[b], -1.46[c]

[a] In acetonitrile solution with 0.1 M nBu$_4$NPF$_6$ as supporting electrolyte at room temperature under argon; $E_{1/2} = (E_{pa} + E_{pc})/2$; E_{pa} and E_{pc} are anodic peak and cathodic peak potentials. [b] Reversible waves. [c] Quasi-reversible waves. [d] Irreversible waves.

1.4.4 Computational investigation

DFT calculations were performed as indicated before. The corresponding structures are named **37a'** − **d'** and **38a'** − **d'** (Figure 1.27). The Cartesian coordinates of all the complexes were listed in Table appendix 11 – 18.

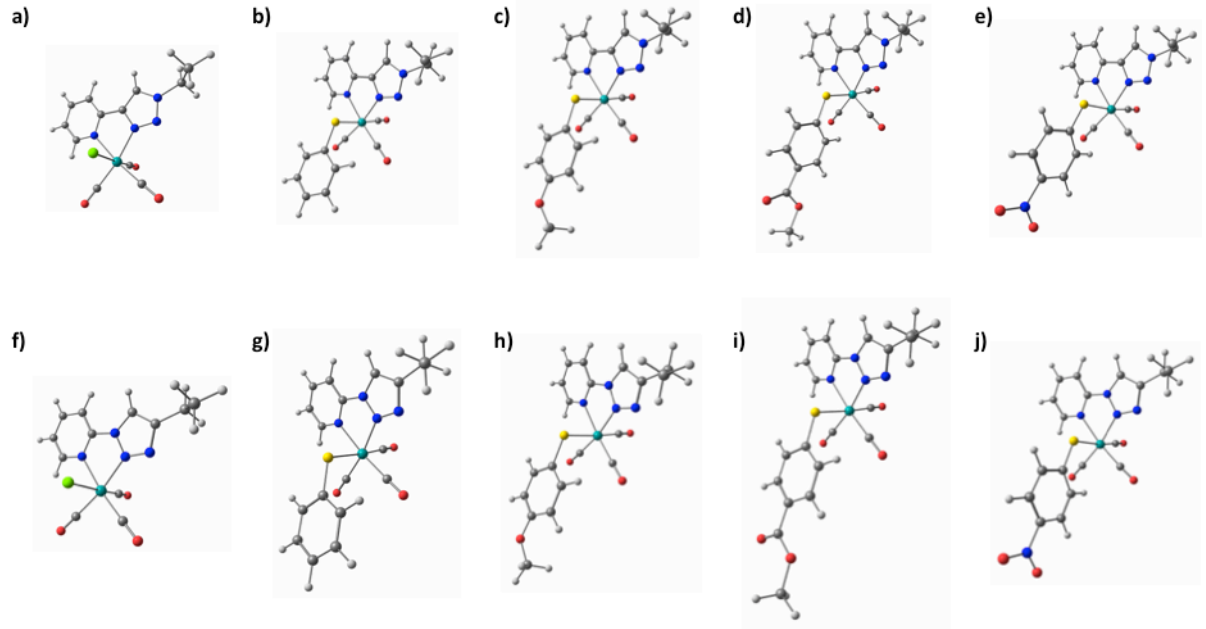


Figure 1.27 Optimized geometries of complex **3r'** (a), **37a'** (b), **37b'** (c), **37c'** (d), **37d'** (e), **9'** (f), **38a'** (g), **38b'** (h), **38c'** (i), **38d'** (j). H atoms are in light grey, C atoms in grey, O atoms in red, N atoms in blue, S atoms in yellow, Cl atoms in light green, re atoms in green.

In the optimized geometries of the complexes, the Pyta and Tapy ligands were planar as previously reported.[48] The introduction of the arenethiolate ligands increased the distance of the Re−N (N atoms in N^N ligand) bond in all complexes by ca. 0.01 Å, explaining their reduced stability compared with the chloride complexes. The replacement of chloride into benzenethiolate ligand leads to an increase of the length of the Re-C bond which is trans to the arenethiolate ligand (1.909 Å to 1.924-1.927 Å and 1.912 Å to 1.927-1.930 Å in the Pyta and Tapy series, respectively) and the effect is stronger for thiolates substituted with electron withdrawing groups (ester and nitro) as in complexes **37c**, **37d** and **37c**, **37d** (Table 1.10). The Re−N bond distances are longer in the Pyta series than in the Tapy series as reported before for bromide complexes.[48] On the contrary, the lengths of the C≡O bonds are little impacted, which is consistent with the experimental IR data. The Re−S bond lengths are similar to Re-Cl bond (2.57−2.58 Å).

Table 1.10 Selected predicted bond lengths in complexes (unit: Å)

	3r'	**37a'**	**37b'**	**37c'**	**37d'**	**9'**	**38a'**	**38b'**	**38c'**	**38d'**
Re–N(1)	2.243	2.254	2.253	2.253	2.252	2.231	2.240	2.240	2.240	2.240
Re–(N2)	2.176	2.185	2.186	2.184	2.183	2.169	2.169	2.179	2.178	2.177
C(1)≡O(1)	1.153	1.155	1.155	1.154	1.154	1.151	1.153	1.154	1.153	1.153
C(2)≡O(2)	1.153	1.155	1.155	1.155	1.155	1.152	1.154	1.154	1.154	1.153
C(3)≡O(3)	1.157	1.157	1.157	1.155	1.155	1.156	1.156	1.156	1.156	1.154
Re-C(1)	1.925	1.921	1.921	1.923	1.924	1.927	1.922	1.922	1.923	1.925
Re-C(2)	1.929	1.925	1.924	1.926	1.927	1.930	1.925	1.925	1.926	1.928
Re-C(3)	1.909	1.924	1.909	1,927	1.927	1.912	1.927	1.928	1.926	1.930

C(1)≡O(1) refers to the CO trans to pyridine, C(2)≡O(2) to the CO trans to triazole, C(3)≡O(3) to the CO trans to axial ligand, N(1) to pyridine and N(2) to triazole ring.

Frontier orbital diagrams for all complexes is shown in the Figure 1.28 (for Pyta rhenium(I) complexes), Figure 1.29 (for Tapy rhenium(I) complexes) and Figure appendix (10 – 17). The HOMO energy of complexes **37a' – d'** with arenethiolate ligands was higher than that of **3r'**, which was due to the better π-donating ability of the arenethiolate ligand than chloride atom. For complexes **37a' – c'**, all the HOMOs showed a mixture of the dπ(Re) and π(S) character. The introduction of arenethiolate ligands led to arenethiolate contributions to the HOMO energy levels. With stronger electron withdrawing groups on arenethiolate ligands, the HOMO was less centred on the metal centre. Thus, the HOMO of complex **37d'** was mainly π(S) character. The HOMO energy of complexes **37a' – b'** and **37d'** followed the trend of **37b'**>**37a'**>**37d'**, which was in agreement with the electron donating abilities –OMe > –H > –NO_2 although the predicted HOMO energy of complex **37c'** did not fit this trend. The HOMO of complexes **38a' – d'** followed the same pattern: their energy followed the trend **38b'**>**38a'**>**38c'**=**38d'**, which was in agreement with the electron donating abilities –OMe > –H > –COOMe ≈ –NO_2. The HOMO-1 of complexes **37a' – b'** and **38a' – c'** were mainly

localized on benzenethiolate (SPh) and the energy gap between the HOMO and the HOMO-1 of these complexes increases as the electron donating ability of the thiolate ligand decreases (–OMe > –H > –CO_2Me) because the filled orbital centred on the benzenethiolate was stabilized by electron withdrawing groups. The HOMO-1 of complexes **37c' – d'** and **37d'** were significantly lower in energy and were of mixed dπ(Re) and π(S) character.

The LUMO of complexes **3r** and **37a' – c'** were localized on the Pyta ligand while that of complex **37d'** was mainly localized on –NO_2 moiety. The LUMO energy of complexes **37a' – c'** was close to that of complex **3r'** as centred on the diimine ligand but slightly higher than complex **3r'** due to the π -donating ability of the arenethiolate ligand. The LUMO energy of Pyta rhenium(I) complexes follows the trend **3r'** < **37d'** < **37c'** < **37a'** < **37b'**, indicating an increasing destabilisation with the electron donating ability of the axial ligand. In agreement with the electrochemical observations, the LUMO of **37d'** is predicted to be localized on the thiolate ligand with major contributions from the nitro group. This agreement was not observed for **37e**, where DFT calculations predicted the nitro-centred vacant orbital to be at the LUMO+1 level. However, the energy of this level (-2.54 eV) was relatively closed to the LUMO (-2.60 eV).

Since the Tapy ligand has better electron acceptor ability than Pyta ligand, the predicted energies of the LUMO for Tapy rhenium(I) complexes are lower than those of Pyta rhenium(I) complexes, in agreement with the electrochemical observations in reduction potential. The LUMO of the Tapy rhenium(I) complexes **9'** and **38a' – c'** showed the same pattern as that for Pyta rhenium(I) complexes. However, the LUMO of complex **38d'** is predicted to be on Tapy ligand while the LUMO+1 is predicted to be mainly on the nitro group. Nevertheless, the energies of LUMO (2.60 eV) and LUMO+1 (-2.54 eV) are close enough to be considered as an acceptable error.

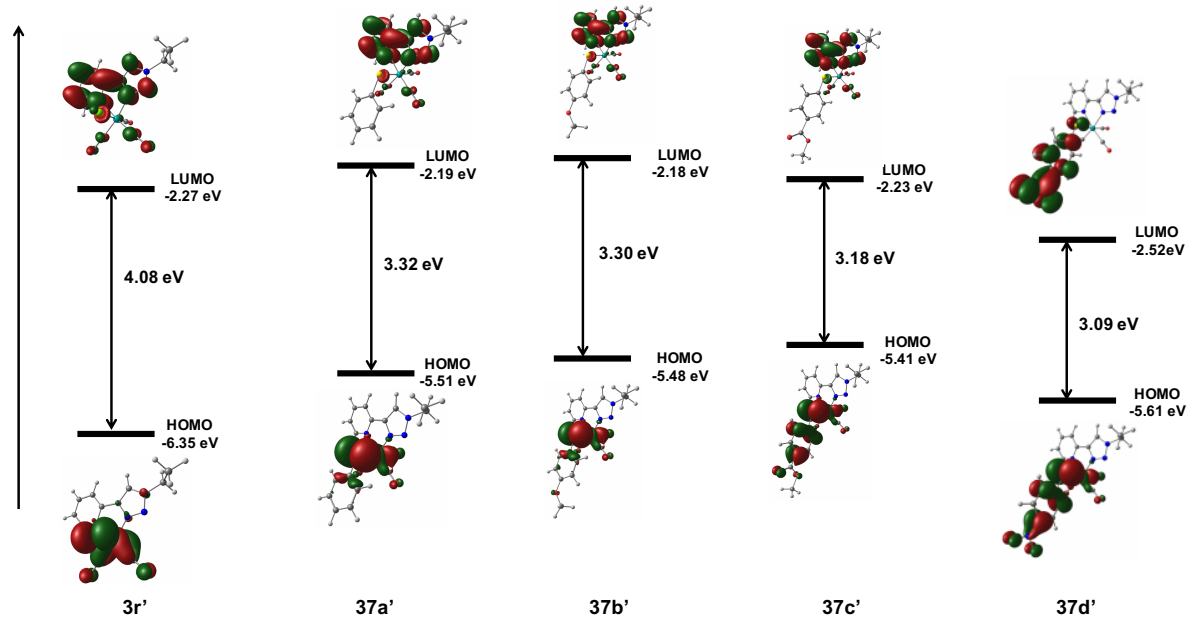


Figure 1.28 Frontier molecular orbitals for Pyta rhenium(I) complexes.

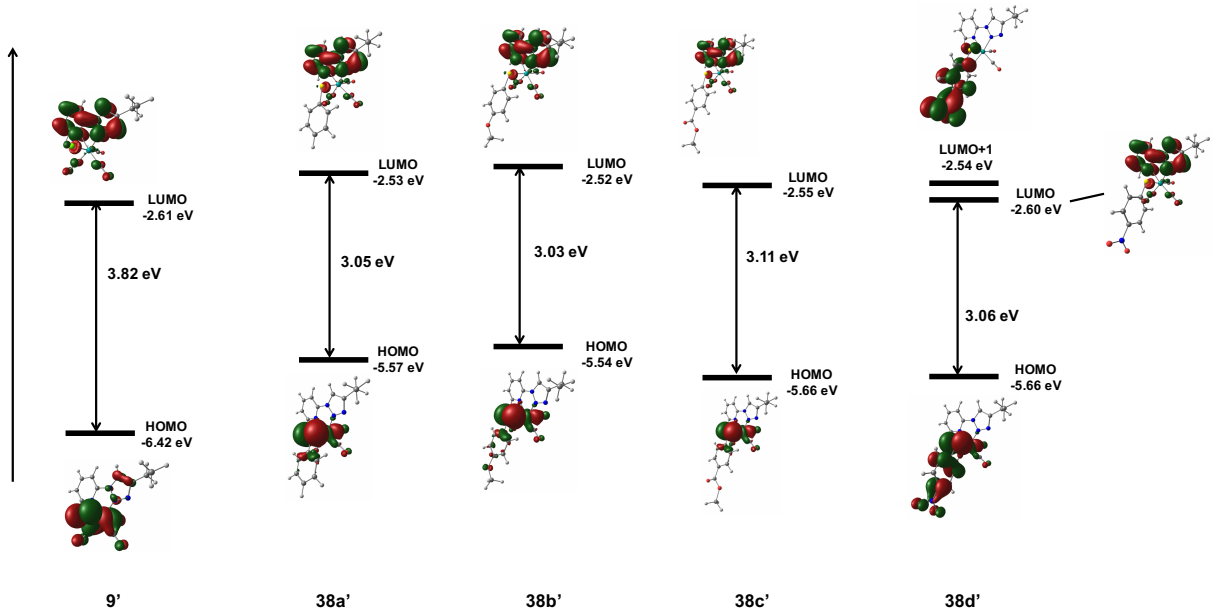


Figure 1.29 Frontier molecular orbitals for Tapy rhenium(I) complexes.

The ten first singlet excited states of complexes **37a' – d'** and **38a' – d'** were evaluated with TD-DFT using Gaussian 09 (Table 1.11 and Table appendix 26 – 33).

For Pyta rhenium(I) complexes, a transition of significant oscillator strength is calculated around 390 nm for complexes **37a' – c'** showing a mixture of dπ(Re)→ π*(Pyta) MLCT and other transitions. For complex **37a'**, the lowest energy absorption band predicted at 395 nm and 391 nm is assigned to a mixture of π(arenethiolate)→ π*(Pyta) ligand-to-ligand charge transfer and dπ(Re)→ π*(Pyta) MLCT. For complex **37b'**, the absorption band predicted at 389 and 387 nm is assigned to mainly dπ(Re) → π*(Pyta) MLCT transition and dπ(Re)→ dπ*(Re) transition, respectively. For complex **37c'**, the absorption band predicted at 390 nm is assigned to a mixture of π(arenethiolate) → π*(Pyta) ligand-to-ligand charge transfer and dπ(Re) → π(Pyta) MLCT. For complex **37d'**, the absorption band predicted at 478 nm is assigned to π(arenethiolate) → π*(Pyta) LLCT and there is a higher energy absorption band predicted at 386 nm assigned to dπ(Re) → π*(-NO_2) charge transfer. To conclude, for Pyta rhenium(I) complexes, the introduction of arenethiolate ligands may cause ligand-to-ligand charge transfer which is offering other pathways for non-radiative emission and causing the decrease of the emission intensity. This hypothesis is reasonable as complexes with stronger donating amido and phosphido ligands have been described to have a lowest excited state of pure LLCT character.[168]

For Tapy rhenium(I) complexes, a transition of significant oscillator strength was calculated around 420 nm for complexes **38a' – c'**, showing diverse transition characters. Complex **38a'** showed a lower energy absorption band at 424 nm which is assigned to π(arenethiolate) → π*(Tapy) ligand-to-ligand charge transfer and a higher energy absorption band at 366 nm which is assigned to dπ(Re) → dπ*(Re) transition. Complex **38b'** gave a predicted absorption band at 422 nm which is assigned to a mixture of dπ(Re) → π*(Tapy) MLCT and π(arenethiolate) → π*(Tapy) LLCT. Complex **38c'** had an energy absorption band at 419 nm which is assigned to

mainly π(arenethiolate) → π*(Tapy) LLCT and small part of dπ(Re) → π*(pyridine) charge transfer. Complex **38d'** showed an absorption band predicted at 469 nm which is assigned to dπ(Re) → π(arenethiolate) MLCT which is different from the dπ(Re) → π(Tapy) MLCT for complex **9'**, similar with that for complex **33d** discussed before. This indicated that the electron withdrawing ability of nitro group is probably too strong to keep the emissive MLCT transition when it is on the N^N ligand. To conclude, for Tapy rhenium(I) complexes, the introduction of arenethiolate ligands generates alternative transitions for the lowest absorption bands, π(arenethiolate) → π*(Tapy) ligand-to-ligand charge transfer, which impact both the emission wavelength and intensity and explain the decrease of the emission intensity compared to the parent complex **9**.

For both complexes **37** and **38**, an increasing LLCT character of the excited state to the detriment of MLCT is expected in complexes fitting the general order **c** < **a** < **b**, as supported by experimental observations; the nature of the excited state being finely tuned by the diimine ligand.

Table 1.11 Selected singlet excited states for complexes.

	Trans.	**Orbital excitations (Contributions)**	**Character**	**Calcd/nm (*f*)**
37a'	3	HOMO-1→LUMO (47%); HOMO→LUMO+2 (52%)	π(arenethiolate)→ π*(Pyta), LLCT; dπ(Re)→ π*(triazole), MLCT	395 (0.0698)
	4	HOMO→LUMO (50%); HOMO→LUMO+2 (47%)	dπ(Re)→ π*(Pyta), MLCT; dπ(Re)→ π*(triazole), MLCT	391 (0.0967)
	7	HOMO→LUMO+3 (95%)	dπ(Re)→ dπ*(Re), CT	361 (0.1588)
37b'	5	HOMO-2→LUMO (90%)	dπ(Re)→ π*(Pyta), MLCT;	389 (0.1318)
	6	HOMO→LUMO+3 (96%)	dπ(Re)→ dπ*(Re), metal-centered transition	387 (0.1417)
37c'	2	HOMO-1→LUMO (72%); HOMO→LUMO+1 (21%);	dπ(Re)→ π*(Pyta), MLCT; π(arenethiolate) → π*(pyridine), CT;	391 (0.1667)
	3	HOMO-1→LUMO (19%); HOMO→LUMO+1 (78%)	dπ(Re) → π*(Pyta), MLCT; π(arenethiolate) →π*(pyridine), CT	390 (0.0994)
37d'	2	HOMO→LUMO+1(99%)	π(arenethiolate) → π*(Pyta), LLCT	478 (0.5946)
	3	HOMO-1→LUMO (93%)	dπ(Re) → π*(NO_2), CT	386 (0.1156)

38a'	3	HOMO-1→LUMO (98%)	π(arenethiolate) →π*(Tapy), LLCT	424 (0.2004)
	6	HOMO→LUMO+2 (96%)	dπ(Re) → dπ*(Re), metal-centered trnsition	366 (0.1582)
38b'	4	HOMO-2→LUMO (90%);	dπ(Re) →π*(Tapy), MLCT;	422 (0.1502)
	5	HOMO→LUMO+2 (93%)	dπ(Re) → dπ*(Re), metal-centered trnsition	396 (0.1158)
38c'	3	HOMO-1→LUMO(79%); HOMO→LUMO+1(19%)	π(arenethiolate) →π*(Tapy), LLCT; dπ(Re) →π*(pyridine), CT	419 (0.2228)
	6	HOMO→LUMO+2 (86%); HOMO→LUMO+3 (11%)	dπ(Re) →π*(arenethiolate), MLCT dπ(Re) → dπ*(Re), metal-centered trnsition	369 (0.5854)
38d'	2	HOMO→LUMO+1 (97%)	dπ(Re)→ π(arenethiolate), MLCT	469 (0.6489)
	3	HOMO-1→LUMO (86%); HOMO→LUMO+2 (10%)	dπ(Re) →π*(Tapy), MLCT; dπ(Re) →π*(pyridine), CT	417 (0.0965)

1.4.5 Summary

Here, we have designed and synthesised a series of Pyta and Tapy-based Re(I) tricarbonyl complexes with a *para*-substituted benzenethiolate as axial ligand, which showed diverse emission properties. A slow decoordination for some complexes mainly with a benzenethiolate substituted by a donor group was observed after 8 hours in acetonitrile. Otherwise all the complexes were stable in acetonitrile for at least 3 days. The electrochemical and photophysical behaviours of the complexes were investigated, DFT and TD-DFT calculations were performed. The rhenium(I) complexes bearing arenethiolate ligands showed more intense absorption band around 330 nm, assigned to a mixture of MLCT and π(arenethiolate) → π*(N^N) LLCT character. In nitro functionalized complexes, a strong intraligand charge transfer (ICT) transition π(arenethiolate) → π*(NO_2) was observed which corresponds to the broader and intense absorption band at around 430 nm. All the complexes bearing thiolate ligands showed decreased emission intensities compared to their chloride complexes, some being totally quenched (complexes **38b**, **37d** and **38d**) which is mainly due to the tuning of the emitting excited state from ^{3}MLCT to a mixed ^{3}MLCT/^{3}LLCT character. There is no general trend for the emission maxima or the intensity simply depending on the arenethiolate ligands.
For complexes **37c**, **38c** and **37a**, the emission is mainly ^{3}MLCT originated while for complex **38a**, it is proposed as a ^{3}LLCT origin. The emission of complexes **37b** and **38b** is essentially

quenched. The HOMO destabilisation of **3r** to **37a** and **37c** results in a decrease in MLCT energy *i.e.* in a red shift in the emission wavelength.

Depending on its electronic properties, the introduction of an arenethiolate ligand may change the nature of the lowest energy excited state, thus risking of losing the emission. However, as mentioned before, it is not easy to anticipate. The resulting photophysical properties depend both on the N^N ligand and the axial ligand.

Furthermore, complex **37c** with –COOMe at the *para* position of the arenethiolate ligand displayed near infrared emission with a tail of excitation in the visible range with large Stokes shift, which might be interesting for cell imaging. Since there are also sulphur-based compounds in cells such as glutathione and cysteine, the competition experiments towards these compounds need to be performed before going further towards cell imaging studies.

Compared with the acetylide ligands, the introduction of the arenethiolate ligands may decrease the stability of the resulting complexes because of the weakening of the coordination bond due to the electron donating properties of the arenethiolate ligand. Furthermore, the introduction of acetylide ligands in $[Re(N^N)(CO)_3X]^{n+}$ systems is predicted to generate π(acetylide) → π*(acetylide) intraligand charge transfer mixed with MLCT transition while the introduction of arenethiolate ligands is predicted to lead to a π(arenethiolate) → π*(Pyta) ligand-to-ligand charge transfer mixed with MLCT transition.

1.5 General conclusions and perspectives

In the chapter, we investigated the possibility to tune the photophysical properties of *fac*-[Re(N^N)$(CO)_3$X] complexes by the modification of N^N (Pyta or Tapy) ligand, the introduction of σ-donating acetylide axial ligands or π-donating arenethiolate axial ligands. All the complexes were well-characterized and the photophysical properties were investigated using UV-Vis and emission spectroscopy in acetonitrile. DFT and TD-DFT calculations were performed for selected compounds.

For the modification of N^N ligand, we have designed and synthesised both Pyta-based Re(I) tricarbonyl complexes with electron-donating group (methoxy group) or electron-withdrawing groups (ester or nitro group) and π-extended Tapy-based Re(I) tricarbonyl complex. Generally speaking, the introduction of electron withdrawing groups on either pyridine or triazole may lead to red shift of excitation and emission wave. The introduction of electron withdrawing groups on the 5- position of the pyridine ring showed more influence on the distribution of LUMO of the resulting Re(I) complexes than that on the 5-triazole. 5-Position of triazole may be a potential position since it showed good balance between red-shifting the excitation wavelength and keeping the reasonable quantum yield. Other functional groups with moderate electron withdrawing effect such as –CHO and –COR would be suitable for further investigation. Furthermore, complexes **14**, **15** and **16** showed interesting behaviours for catalysing carbon dioxide electroreduction, which will be discussed in the next chapter.

The introduction of acetylide ligands caused intraligand charge transfer. The resulting compounds are stable. Complex **33b** with –CN showed overall interesting emission intensity though the absorption is also more intense. It might be interesting to introduce other electron donating groups on the acetylide ligand, such as amino groups which could endow the resulting complexes with pH sensitive photophysical properties.

The series of Pyta and Tapy-based Re(I) tricarbonyl complexes with a *para*-substituted benzenethiolate as axial ligand showed more intense absorption band assigned to a mixture of MLCT and π(arenethiolate) → π*(N^N) LLCT character. In nitro functionalized complexes, a strong intraligand charge transfer (ICT) transition π(arenethiolate) → π*(NO_2) arises, which is non emissive. All of the complexes bearing thiolate ligands showed decreased emission intensities mainly due to a mixed ^{3}MLCT/^{3}LLCT transition. There is no general trend of the emission maxima or the intensity depending only on the arenethiolate ligands, which has already been reported for platinum complexes.[139] Complex **37c** with –COOMe at the *para* position of the arenethiolate ligand displayed near infrared emission with large Stokes shift, which is promising for cell imaging. Similar complexes have been used for subcellular imaging.

1.6 Conclusion générale et perspectives

Dans ce chapitre, nous avons étudié la possibilité de moduler les propriétés photophysiques des complexes *fac*-[Re(N^N)$(CO)_3$X] en modifiant le ligand N^N (Pyta ou Tapy), par l'introduction de ligands axiaux σ donneurs (acétylure) ou des ligands axiaux arénéthiolés π donneurs . Tous les complexes ont été intégralement caractérisés et les propriétés photophysiques ont été étudiées par UV-Vis et spectroscopie d'émission dans l'acétonitrile. Des calculs DFT et TD-DFT ont également été effectués pour des composés sélectionnés.

Pour la modification du ligand N^N, nous avons conçu et synthétisé à la fois des complexes Re(I) tricarbonyle à base de Pyta avec un groupe donneur d'électrons (groupe méthoxy) ou des groupes attracteurs d'électrons (groupe ester ou nitro) et des Re (I) tricarbonyle avec des ligands Tapy π - étendus. De manière générale, l'introduction de groupes électro-attracteurs sur la pyridine ou le triazole à entraîner un décalage vers le rouge de la longueur d'onded'excitation et d'émission. L'introduction de groupes électro-attracteurs en position 5 du noyau pyridine a eu davantage d'influence sur la distribution de LUMO des complexes Re (I) résultants que celle du en position 5 du triazoletriazole. La position 5 du triazole peut être une position intéressante puisqu'elle a montré un bon équilibre entre le décalage du rouge de la longueur d'onde d'excitation et le maintien du rendement quantique raisonnable. D'autres groupes fonctionnels à effet électro-attracteurs modérés, tels que –CHO et –COR, pourraient faire l'objet d'une étude plus approfondie. En outre, les complexes **14**, **15** et **16** ont montré des comportements intéressants pour la catalyse de l'électroréduction au dioxyde de carbone, qui seront abordés dans le chapitre suivant.

L'introduction de ligands acétylure a induit un transfert de charge intraligand. Les composés résultants sont stables. Le complexe **33b** avec –CN a montré une intensité d'émission globale intéressante, bien que l'absorption soit également plus intense. Il pourrait être intéressant d'introduire d'autres groupes donneurs d'électrons sur le ligand acétylure, tels que des groupes amino qui pourraient conférer aux complexes résultants des propriétés photophysiques sensibles au pH.

La série de complexes de Re (I) tricarbonyle à base de Pyta et de Tapy avec un benzènethiolate substitué en para comme ligand axial a montré une bande d'absorption plus intense du fait d'un mélange de MLCT et de caractère LLCT de π(arénéthiolate) → π*(N^N). Pour les complexes fonctionnalisés par un groupement nitro, une forte transition π (arénéthiolate) → π * ($–NO_2$) se produit, celle-ci s'avérant être non émissive. Tous les complexes portant des ligands thiolates présentaient des intensités d'émission réduites principalement en raison d'une transition mixte ^{3}MLCT / ^{3}LLCT. Il n'y a pas de tendance générale pour les maxima d'émission ou l'intensité. Le complexe **37c** avec –COOMe en position para du ligand arénéthiolate présente une émission dans le proche infrarouge avec un déplacement de Stokes important, ce qui est prometteur pour l'imagerie cellulaire.

2. Rhenium(I) complexes as catalysts for CO_2 electroreduction

2.1 Introduction

The use of coal, petroleum oil, natural gas and fossil fuels allows for rapid development of human society but large amount of anthropogenic carbon dioxide emissions at the same time, which disturbs the natural carbon cycle and causes global environmental changes. Meanwhile, these energy sources are limited and non-renewable, meaning that it will be depleted in the future. Thus, recycling and conversion of carbon dioxide into renewable chemicals and fuels is an alternative to deal with this issue.

However, carbon dioxide is chemically inert with a low affinity towards electron, as well as a large energy gap (13.7 eV) between the LUMO and the HOMO.[13,48,53,55] Meanwhile, the standard potential of the $CO_2/CO_2^{\cdot -}$ couple is -1.97 V versus standard hydrogen electrode (SHE) in DMF[169] and -1.90 V versus SHE in water,[57] which means it is quite difficult to reduce carbon dioxide. Carbon dioxide can be reduced into diverse stable products though multi-electron (two-, four-, six-, and eight-electron) reduction pathways in gaseous, aqueous, and non-aqueous phases at both low and high temperatures.[58] The thermodynamic electrochemical half-reactions of carbon dioxide reduction and their associated standard electrode potentials in aqueous solutions are listed in Table 2.1.[170] Due to the chemical stability of carbon dioxide, catalysts are required to enable carbon dioxide reduction by lowering the reaction activation energy.

Table 2.1 Selected standard potentials of CO_2 reductions in aqueous solutions (V vs. SHE) at 1.0 atm and 25 ^oC, calculated according to the standard Gibbs energies of the reactants in reactions.[171]

Half-electrochemical thermodynamic reactions	Electrode potentials (V vs. SHE)
$CO_2(g) + 4H^+ + 4e^- = C(s) + 2H_2O(l)$	0.210
$CO_2(g) + 2H_2O(l) + 4e^- = C(s) + 4OH^-$	-0.627
$CO_2(g) + 2H^+ + 2e^- = HCOOH(l)$	-0.250
$CO_2(g) + 2H_2O + 2e^- = HCOO^-(aq) + OH^-$	-1.078
$CO_2(g) + 2H^+ + 2e^- = CO(g) + H_2O(l)$	-0.106
$CO_2(g) + 2H_2O(l) + 2e^- = CO(g) + 2OH^-$	-0.934
$CO_2(g) + 4H^+ + 4e^- = CH_2O(l) + H_2O(l)$	-0.070
$CO_2(g) + 3H_2O(l) + 4e^- = CH_2O(l) + 4OH^-$	-0.898
$CO_2(g) + 6H^+ + 6e^- = CH_3OH(l) + H_2O(l)$	0.016
$CO_2(g) + 5H_2O(l) + 6e^- = CH_3OH(l) + 6OH^-$	-0.812
$CO_2(g) + 8H^+ + 8e^- = CH_3OH(l) + H_2O(l)$	0.169
$CO_2(g) + 6H_2O(l) + 8e^- = CH_4(g) + 8OH^-$	-0.659
$2CO_2(g) + 2H^+ + 2e^- = H_2C_2O_4(aq)$	-0.500
$2CO_2(g) + 2e^- = C_2O_4^{2-}(aq)$	-0.590

$2CO_2(g) + 12H^+ + 12e^- = CH_2CH_2(g) + 4H_2O(l)$	0.064
$2CO_2(g) + 8H_2O(l) + 12e^- = CH_2CH_2(g) + 12OH^-$	-0.764
$2CO_2(g) + 12H^+ + 12e^- = CH_3CH_2OH(l) + 3H_2O(l)$	0.084
$2CO_2(g) + 9H_2O(l) + 12e^- = CH_3CH_2OH(l) + 12OH^-$	-0.744

Generally, two procedures can be used for carbon dioxide reduction: a photoelectrochemical and an electrochemical procedure. In the photoelectrochemical approach, the photocatalysts transfer electrons to carbon dioxide and at the same time, sacrificial reagents will consume the photogenerated holes in the photocatalyst's valence band.[171] Chemists have developed nanosheets[172] and metal complexes[173,174] as photocatalysts for carbon dioxide reduction. O. Ishitani[78] and E. Fujita[4,175–179] have developed a wealth of rhenium(I) tricarbonyl complexes as photocatalysts for carbon dioxide reduction. Another approach is the electrochemical reduction of carbon dioxide. In this procedure, the catalyst is first reduced by the electrons from the electrode (figure 2.1) while in the photochemical procedure, the catalyst is first reduced by the photosensitizer. Electroreduction has some advantages compared with photocatalytic carbon dioxide reduction: 1) the procedure can be controlled by the potentials and reaction temperature used; 2) because the electrolytes can be recycled, chemical consumption can be minimized into water; 3) the setup is easy to scale up.[180–182] However, the electroreduction of carbon dioxide is often competed with electrocatalytic dehydrogenation because normally the electroreduction of carbon dioxide process needs proton source. In aqueous solution at 25 °C, the standard electrode potential is 0.0 V for proton, which is much easier to reduce than carbon dioxide. Thus, a catalyst is important to orient the selectivity of the reaction.

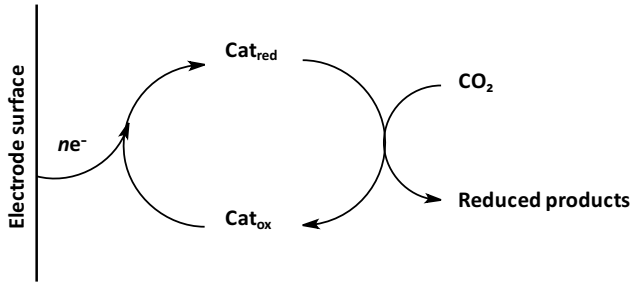


Figure 2.1 Electrochemical process with catalyst.

First reported as Ni and Co macrocyclic complexes in 1980 by B. J. Fisher and R. Elsenberg,[183] metal complexes have attracted interests including Fe, Re, Ru, Ir, Rh, Mn, and others[60] because metal complexes are able to store multiple electrons not only at the metal centre but also in the ligand π system, which is facilitating the reduction of CO_2. Here the progress of rhenium(I) tricarbonyl complexes as catalysts for carbon dioxide reduction is reviewed. The detailed parameters of the complexes were summarised at the end in Table 2.2.

2.1.1 Useful notations

Overpotential

In electrochemistry, the overpotential is the potential difference (voltage) between a half-reaction's thermodynamically determined reduction potential and the potential at which the redox event is experimentally observed. In an electrolytic cell the existence of overpotential implies the cell requires more energy than thermodynamically expected to drive a reaction. The overpotential can be investigated using cyclic voltammetry.

Turnover number (TON)

The turnover number (TON) is defined as the number of moles of substrate transformed by 1 mol of both forms of the catalyst present on the surface.[19,59,61,77,184–187] In homogeneous phase with stable catalyst, it can be calculated using equation 2.1 where mol P is the amount of the product and mol Cat is the amount of the catalyst.

$TON = \frac{mol\ P}{mol\ Cat}$ in $mol_{product}$ /$mol_{catalyst}$ Equation 2.1

Turnover frequency (TOF)

Turnover frequency is used to refer to the turnover per unit time and is calculated using equation 2.2.

$TOF = \frac{TON}{Time}$ in $mol_{product}$ $(mol_{catalyst})^{-1}$ / time $^{-1}$ Equation 2.2

Faradaic efficiency (FE)

The Faradaic efficiency is the percentage of electrons employed to generate a desired product. It indicates the selectivity of the products during the reduction process. It can be calculated by equation 2.3.

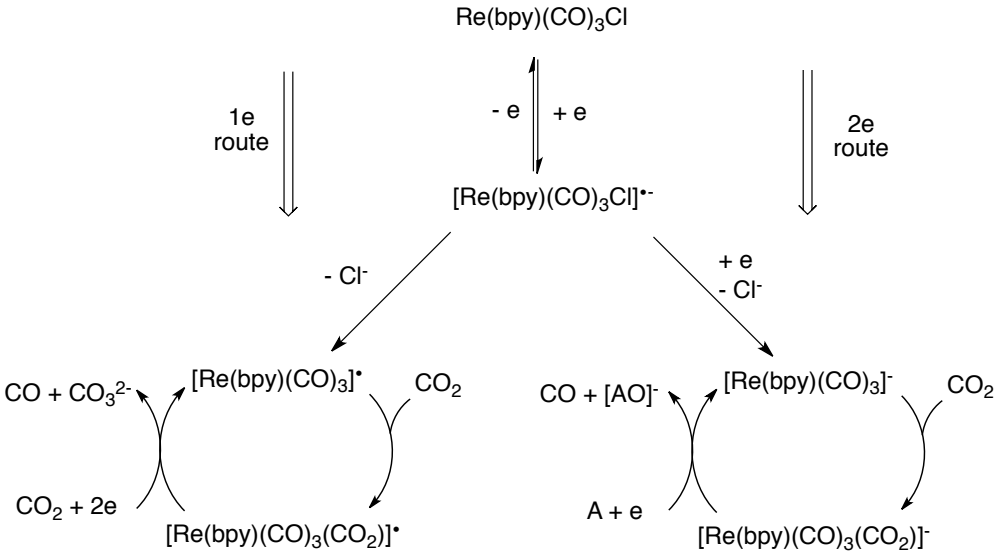
$FE = \frac{\alpha \times n \times F}{Q}$ Equation 2.3

whereas α is the number of electron transferred, n is the number of mole of a desired product, F is Faraday's constant (96485 C·mol^{-1}), and Q is the total charge passed. The number of mole of each product could be obtained from analytical techniques such as gas chromatograph, liquid chromatograph or mass spectrometry, and the total charge passed is determined by the electrochemical data.

2.1.2 Mechanistic investigation

First reported by J.-M. Lehn in 1984,[188] the *fac*-Re(bpy-R)$(CO)_3$X (bpy = 2,2'-bipyridine with R as a functional group on the bpy system, X = Cl, Br, OTf...) system is very efficient for carbon dioxide reduction to carbon monoxide in acetonitrile with an average current efficiency higher than 90% in the presence of proton sources.[189] The mechanism was investigated by cyclic voltammetry and UV-Vis spectrophotometry using bulk electrolysis. During the reduction

process of *fac*-Re(bpy-R)$(CO)_3Cl$ without carbon dioxide, the reduced species $[Re(bpy)(CO)_3]^-$ is coupled to formation of the dimer $[Re(bpy)(CO)_3]_2$.[3] Two different mechanisms for the electrocatalytic reduction of carbon dioxide by *fac*-Re(bpy)$(CO)_3Cl$ in acetonitrile were first proposed by T. J. Meyer (Scheme 2.1) in which the dimerisation is suppressed: a one-electron pathway, which is involving $[Re(bpy)(CO)_3Cl]^-$, and a two-electron pathway, involving $[Re(bpy)(CO)_3Cl]^-$.[190] In both pathways, the first step is the reduction of bpy ligand involving a one-electron procedure, forming the intermediate $[Re(bpy)(CO)_3Cl]^{\bullet-}$. In the two-electron pathway, the intermediate $[Re(bpy)(CO)_3Cl]^{\bullet-}$ was reduced by one electron to form $[Re(bpy)(CO)_3]^-$, followed by the entrance of carbon dioxide in the reduction cycle to form $[Re(bpy)(CO)_3(CO_2)]^-$. The resulting $[Re(bpy)(CO)_3(CO_2)]^-$ was then reduced using an oxide ion accepter and another electron to finish the reduction cycle and produce carbon monoxide at the same time. The one-electron pathway involves the radical $[Re(bpy)(CO)_3]^{\bullet}$ and results in producing both carbon monoxide and carbonate. A next publication showed that in the two-electron pathway, the intermediate $[Re(bpy)(CO)_3Cl]^{\bullet-}$ is able to form $[Re(bpy)(CO)_3]^-$ through the cleavage of Cl and incorporation of a molecule of acetonitrile to form $[Re(bpy)(CO)_3(CH_3CN)]^{\bullet}$, followed by the one-electron reduction to get $[Re(bpy)(CO)_3]^-$.[190] Thus, $[Re(bpy)(CO)_3]^{\bullet}$ and $[Re(bpy)(CO)_3]^-$ are produced simultaneously in acetonitrile and can catalyze the reduction of carbon dioxide to both carbon monoxide and carbonate through a one-electron or two-electron pathway, respectively.



Scheme 2.1 Mechanism proposed by T. J. Meyer (A refers to an oxide ion acceptor).[191]

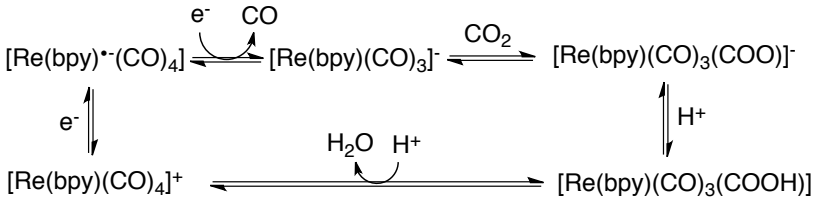
Meanwhile, infrared spectroelectrochemical (IR-SEC) technique was also employed to explore the mechanisms in acetonitrile in the presence or absence of water using the [Re(dmdpy)$(CO)_3Cl$] (dmbpy = 4,4'-dimethyl-2,2'-bipyrdyl) complex.[190] In the pathway without appreciable concentrations of water, the intermediate $[Re(dmbpy^{\bullet-})(CO)_3Cl]$ was directly attacked by carbon dioxide to form $[Re(dmbpy)(CO)_3(CO_2)]$, which upon reaction with water with one electron forms [Re(dmbpy)$(CO)_3$(COOH)]. The species [Re(dmbpy)$(CO)_3$(COOH)] is further reduced to yield $[Re(dmbpy)(CO)_3(COOH)]^-$. In the

presence of water, the species [Re(dmbpy)$(CO)_3$(COOH)] is protonated and COOH is easily replaced by acetonitrile to form [Re(dmbpy)$(CO)_3$(MeCN)]$^+$ as well as CO and water, which explains the formation of the water from carbon dioxide reduction. IR-SEC also provided the evidence the introduction of suitable Lewis bases like phosphine or CH_3CN will prevent rapid dimerisation and meanwhile the rhenium centre is still able to coordinate and reduce carbon dioxide through one-electron pathway.[192]

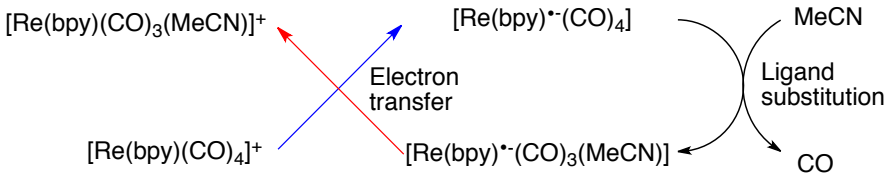
Since the mechanism involves radicals, it can be studied by electron paramagnetic resonance (EPR) spectroscopy. *In situ* reduction of [Re(bpy)$(CO)_3$Cl] under carbon dioxide atmosphere in acetonitrile showed a series of EPR spectra, attributed to ($bpy^{\cdot-}$) containing species and revealed the interaction of the unpaired electron with the metal nuclei.[193]

Moreover, the addition of weak Brønsted acids was shown to enhance the rate of the catalytic process as well as to improve the lifetime of the rhenium catalyst in acetonitrile probably by stabilizing the rhenium-carbon dioxide intermediate through protonation and facilitating the cleavage of the C-O bond to yield carbon monoxide.[194] The efficiency of the acid to improve the catalytic process increases with the acidity. Thus, trifluoroethanol (TFE) and phenol are more effective than methanol and water. Water is less effective than methanol because water will compete with carbon dioxide for binding to rhenium, which is a very important step for carbon dioxide reduction.

C. P. Kubiak *et al.* have performed structural studies of [Re(bpy)$(CO)_3$Cl] species as CO_2 reduction catalysts focusing on modifications on either the 4,4' positions of bipyridine or of the axial ligand. They investigated a series of bpy derivatives with diverse degrees of electron withdrawing/donating substituents (carboxyl, methyl, tert-butyl, methoxy groups) in the 4,4' position of the bipyridine to investigate the two-electron pathway mechanism which involves a carboxylate species [Re(bpy)$(CO)_3$(COO)]$^-$ formed upon reaction of carbon dioxide with [Re(bpy)$(CO)_3$]$^-$ (Scheme 2.2).[195] Complex [Re(4,4'-*t*Bu-bpy)$(CO)_3$Cl] showed a significantly improved catalytic activity which may be due to the formation of Re(0) radical rather than dimers during the catalytic cycle. They also crystallized some [Re(bpy-R)$(CO)_3$]$^-$ (R = OMe, Me) anions which are the active species that bind carbon dioxide.[196] By replacing Cl by OTf (triflate), they performed a detailed study and proposed an electron-transfer-catalyzed ligand substitution reaction to explain the product-releasing step in carbon dioxide reduction (Scheme 2.3).[197] The [Re(bpy)$^{\cdot-}$$(CO)_4$] complex is a transient intermediate in this reaction. Ligand exchange with the solvent occurs if the [Re(bpy)$^{\cdot-}$$(CO)_4$] is formed, and therefore forms [Re(bpy)$^{\cdot-}$$(CO)_3$(MeCN)]. The species [Re(bpy)$^{\cdot-}$$(CO)_3$(MeCN)] undergoes additional electron transfer (Scheme 2.3) with the starting material [Re(bpy)$(CO)_4$] to finish the catalytic cycle. The existence of the [Re(bpy)$(CO)_3$(COOH)] intermediate was also confirmed using Raman spectrometry.[193] The addition of the proton source changed the mechanism from a one-electron pathway to a two-electron pathway and increased the activity at the same time.[198] The decreasing of aromaticity to pyridine monoimine ligand led to the catalysis of two equivalents of carbon dioxide to carbon monoxide and carbonate at a single Re site and the formed carbonate was observed to decrease the catalytic ability.[199]



Scheme 2.2 Mechanism proposed by C. P. Kubiak.[200]



Scheme 2.3 Electron-transfer-catalyzed ligand substitution proposed by C. P. Kubiak.[196]

2.1.3 Rhenium(I) tricarbonyl complexes as homogeneous catalysts

2.1.3.1 Lehn-type catalysts

Based on these mechanisms, the recent decade has witnessed a booming development of catalysts for carbon dioxide electroreduction based on $[Re(bpy)(CO)_3Cl]$ systems (Lehn-type catalyst). The most popular positions to modify the bipyridine ligand are in 4,4' positions due to the well-developed synthetic methodologies[193]. The introduction of ancillary BODIPY moieties (compound **40a**) resulted in a 3400 $M^{-1}s^{-1}$ second order rate constant for the reduction of carbon dioxide at -2.0 V versus SCE, which is approximately three times greater than for $[Re(bpy)(CO)_3Cl]$ though the complex is reduced at potentials that are more positive than $[Re(bpy)(CO)_3Cl]$.[201]

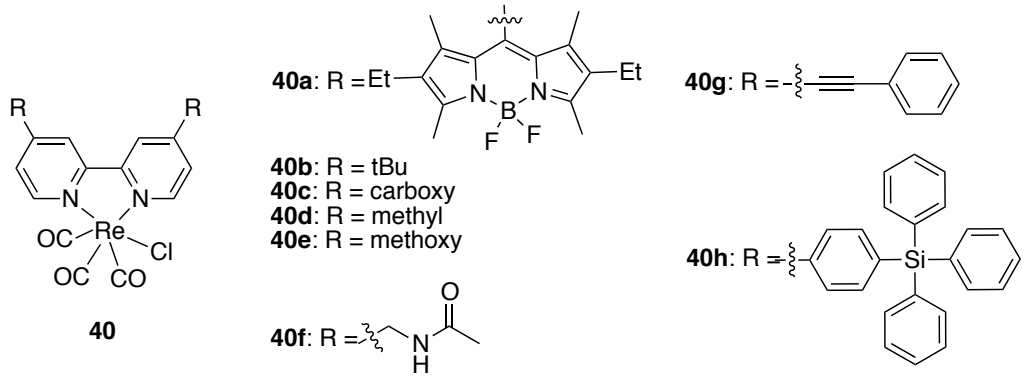


Figure 2.2 Molecular structure of complexes **40a** – **h**.

A series of bipyridine derivatives with diverse degrees of electron donating/withdrawing substituents in the 4,4' position of the bipyridine was also investigated by C. P. Kubiak et al.[202] As mentioned above they found that $[Re(bpy\text{-}tBu)(CO)_3Cl]$ complex (compound **40b**) showed enhanced catalytic activity with a Faradaic efficiency of 99±2% in acetonitrile at -1.85 V versus SCE compared to the others (compound **40c – e**) due to the formation of a stable Re(0) radical

and decreased of the formation of the $[Re(bpy)(CO)_3]_2$ dimer. M. K. Gilson and C. P. Kubiak found that introducing moderate electron-donating groups (*t*Bu and CH_3) at the 4,4' position of bipyridine increased the activity while the introduction of too much electron density ($–OCH_3$, –CN, $–CF_3$) destabilized the catalyst.[196]

J. Pérez *et al.* introduced methyl acetamidomethyl groups and the resulting complex **40f** showed enhanced rate of a bimolecular reduction at a low overpotential (*ca.* 0.25 V) by a hydrogen-bonded dimer promoted by the methyl acetamidomethyl groups.[199]

The introduction of phenylethynyl motif (complex **40g**) showed an eleven-fold increase in the current density due to the larger delocalisation of π-electron density[203] while the same functional groups at the 5,5' positions of bipyridine only caused a 6.5-fold increase in the current density.[204] The introduction of (4-(triphenylsilyl)phenyl functional group in the 4,4' position of bipyridine (compound **40h**) also showed a Faradaic efficiency of 76%.[205]

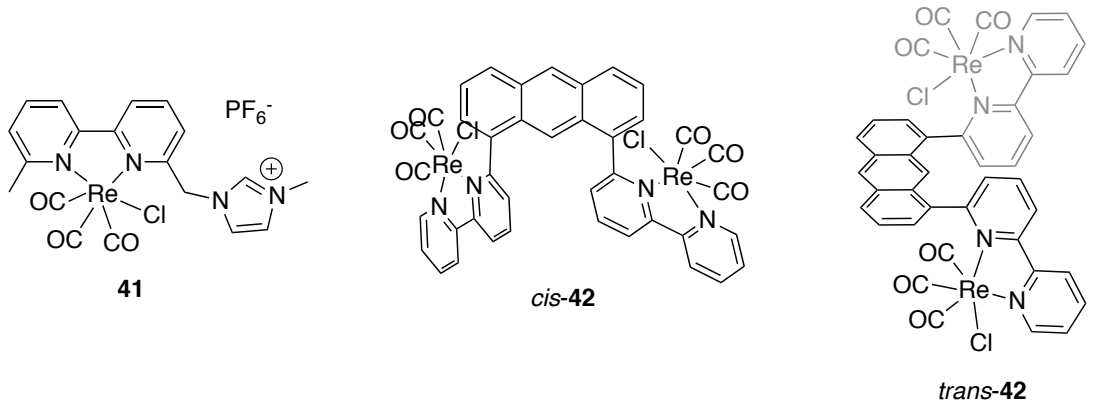


Figure 2.3 Molecular structure of complexes **41** and **42**.

There are few examples for asymmetrically modified bipyridine ligands for Lehn-type catalysts. M. Nippe *et al.* reported complex **41** with ethyl-methyl imidazolium on the 2-position resulting in better catalytic activity and the C(2)-H···Cl interaction of the imidazolium moiety with the chloride on the rhenium center played a crucial role.[206] J. W. Jurss *et al.* found that the electrocatalytic carbon dioxide reduction with *cis* and *trans* conformers of a rigid dinuclear rhenium complex underwent different pathways.[207] Both *cis* and *trans* complexes **42** are active for electrochemical reduction of carbon dioxide. For *cis*-**42**, a pathway involving a bimetallic carbon dioxide activation and conversion was proposed while for *trans*-**42**, a similar pathway to Lehn-type catalyst is observed. Due to the decrease of the formation of a deactivated Re-Re bonded species, *cis*-**42** was found to be more active (TOF of 35 s^{-1}) than *trans*-**42** (TOF is 23 s^{-1}).

2.1.3.2 Rhenium(I) tricarbonyl complexes bearing other diimine ligands

Apart from modified bipyridine, other diimine ligands have been evaluated for the CO_2 reduction ability of their corresponding rhenium tricarbonyl complexes. Complexes **43a** and **43b** showed ability to mediate the two-electron reduction of carbon dioxide with a Faradaic efficiency >60% for the formation of carbon monoxide.[208] Complex **44** with a terpyridine

ligand,[209] and complexes **45a – d** with substituted 1,4-diazabutadiene (DAB) ligand[210] showed some catalytic activity. Di-rhenium(I) complex **46** with a diazine bridge[211] showed a high efficiency (TOF = 25 h^{-1} at E = 0 V) which is two times higher than the very efficient [Re(bpy)$(CO)_3$(Cl)] complex (TOF = 11 h^{-1} under the same conditions). It might be related to the antibonding character of the HOMO orbitals on the Re–Cl moiety[212], making somewhat labile the Re(η-Cl)Re interaction then affording catalytic sites available to the coordination and subsequent reduction of CO_2.

The investigation of the catalytic ability of complexes **47 – 50** with modified pyridylimidazole ligands showed that complexes **47** and **48** with a pyridyl motif had no catalytic activity while complexes **49** and **50** with a quinolyl motif instead of pyridyl had increased current in CO_2-saturated acetonitrile.[213] Complexes **51a – c** with modified pyridyloxazoline ligands[214] showed activity towards the electroreduction of carbon dioxide but no catalytic enhancement compared to *fac*-[Re$(CO)_3$(bpy)Cl] complex. The faster reaction rates of complexes **51a** and **51b** $((i_{cat}/i_p)^2$ of 66 for complex **51a** and 85 for complex **51b**) were due to the presence of the oxazoline ligand, which is a better σ donor than pyridine. For complex **52** with a dirhenium(I) metal centre, the phenol group in the ligand may act as a proton relay during catalysis because it is in close proximity to the active centre and thus it showed slightly higher activities than [Re(bpy)$(CO)_3$Cl] in acetonitrile/water mixture. This shows the potential importance and benefit of introducing second coordination sphere interactions on the catalytic efficiency.

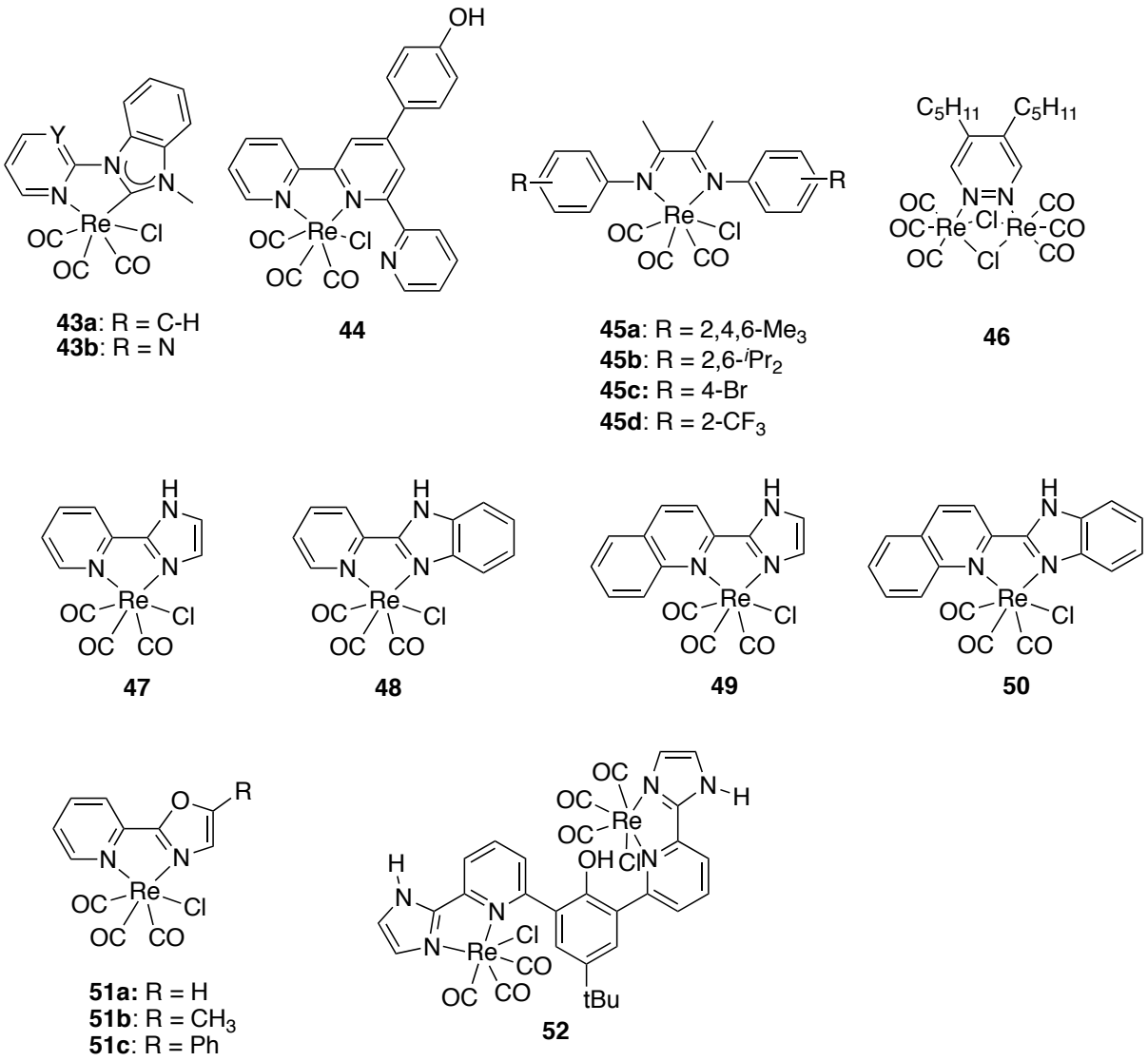
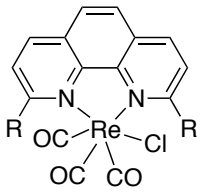


Figure 2.4 Molecular structure of complexes **43** – **52**.

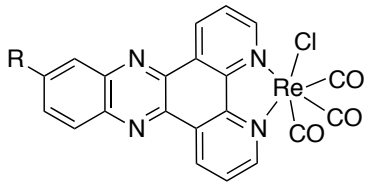
2.1.3.3 Ligands with large conjugation systems

Meanwhile, there are also rhenium(I) tricarbonyl complexes with other ligands with larger conjugation systems reported as catalysts for the electroreduction of carbon dioxide. Recently, a series of *fac*-[Re(phen–R)(CO)$_3$Cl] complexes **53** (phen–R = 2,9-disubstituted-1,10-phenanthroline) bearing steric and electronic motifs like methyl (complex **53a**), 2,4,6-trimethylphenyl (complex **53b**), 2,4,6-methoxyphenyl (complex **53c**) or 3,4,5-methoxyphenyl (complex **53d**) were reported to have catalytic effect and the catalytic efficiency was affected by electronic factors.[215] The reduction followed a two-electron pathway and the introduction of electron-donating aryl-substituted functional groups enhanced the catalytic activity. The substituted dipyrido[3,2-a:2',3'-c]phenazine (dppz) ligands functionalized with electron donating or electron withdrawing groups were also used as ligands for rhenium(I) complexes for this purpose.[216] The study of catalytic activity of complexes **54a – d** indicated that the large conjugation of the dppz ligand helps to store multiple electrons and lower the energy barrier for carbon dioxide reduction. A ligand with a larger conjugation was synthesized by the

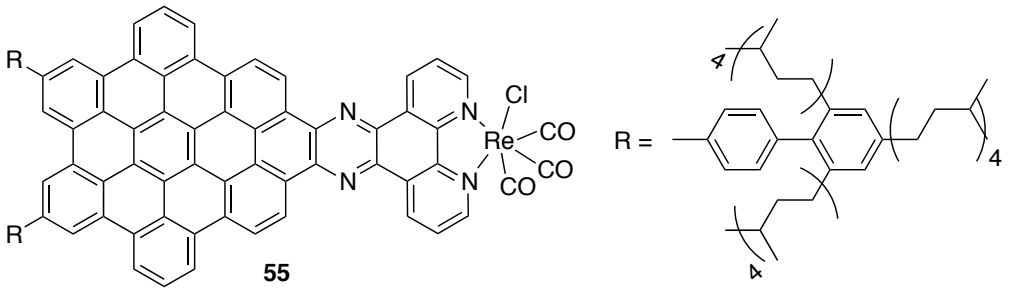
introduction of nanographene.[217] Complex **55** showed electron delocalisation over the nanographene and the reduction of carbon dioxide in tetrahydrofuran was at -0.48 V versus SHE, which means it significantly decreased the reduction energy towards carbon dioxide.[218,219] Theoretical computations indicated that the redox states of the metal centre are not involved in the carbon dioxide reduction procedure and the metal only provides a binding site for carbon dioxide and a conduit for electron transfer.[218]



53a: R = Methyl
53b: R = 2,4,6-trimethylphenyl
53c: R = 2,4,6-trimethoxyphenyl
53d: R = 3,4,5-trimethoxylphenyl



54a: R = CF_3
54b: R = NO_2
54c: R = H
54d: R = tBu



55

Figure 2.5 Molecular structure of complexes **53** – **55**.

2.1.4 Rhenium(I) tricarbonyl complexes as heterogeneous catalysts

Since the molecular catalysts in homogeneous phase show high activity, their immobilisation on the electrodes for the generation of active heterogeneous catalysts was also investigated. Their integration onto electrodes can sometimes give an enhancement of the catalytic activity.[219] Immobilisation also enables insoluble catalysts to operate in water and overcomes limitations from diffusion-controlled electrocatalysis with catalysts in the bulk solution.[220–222] Meanwhile, it is more economic since it is possible to reuse the modified electrode and to reduce the amount of solvents used. Therefore, the immobilisation of the rhenium(I) tricarbonyl complexes on the electrode surface to catalyse carbon dioxide reduction is a promising strategy.

2.1.4.1 Electro-polymerisation

Electrode surfaces can be modified with rhenium(I) complexes by electropolymerisation. Complex **56** was firstly used to investigate this approach.[223–227] By introducing a vinyl motif on the bipyridine ligand, complex **56** underwent electro-reductively-initiated polymerisation to form stable polymer films on Pt and glassy carbon or semiconductor electrodes (p-Si and polycrystalline thin films of p-WSe_2). The modified electrode was active towards the catalytic reduction of carbon dioxide with a quantitative yield of carbon monoxide formation with a

current efficiency of over 95%, which showed the potential of this approach. The rate determining step of the reduction of carbon dioxide in the films is the electron transport to the catalytic sites as the film thickness increased rather than the chemical reaction between the reduced rhenium and carbon dioxide.[228] However this film was less active than the corresponding homogeneous catalyst probably due to the formation of the hydrogencarbonato complex [Re(bpy)$(CO)_3(HCO_3)$], which is kept in solution as cation-bonded ion pairs.[229] This species will be slowly formed and the charge compensation by hydrogencarbonate ions will increase. To increase the catalytic yield, F. Cechet *et al.* reported on the electrodeposition of compound **58** bearing a pyrrole group on a nanocrystalline TiO_2, followed by the deposition of the electroactive **56**-polymer on the electrode surface.[229] The modified nanoporous TiO_2 structures enhanced the rate of the charge transfer reactions.[230]

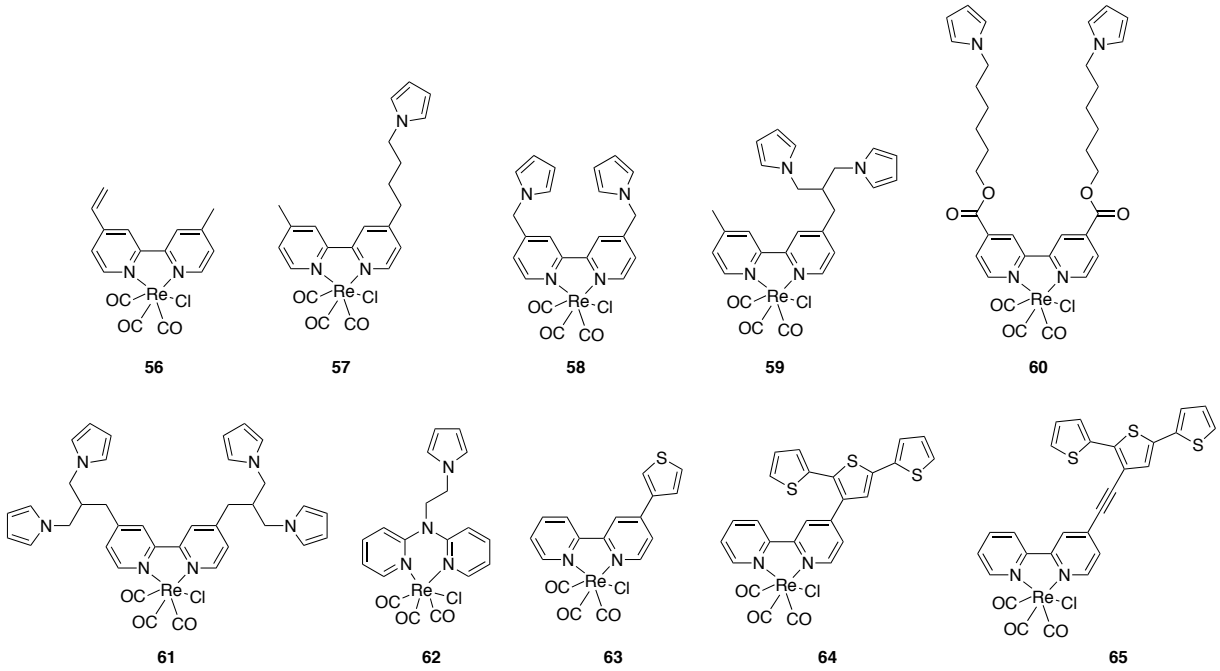


Figure 2.6 Molecular structure of complexes **56** – **65**.

Since the first report of electropolymerisation of ethyne by the electropolymerisation,[231] the introduction of an ethynyl motif on Lehn-type Re(I) complex enabled to perform electropolymerisation on the electrode to form a polymer film in a noncovalent fashion.[232] The use of 5-ethynyl-2,2'-bipyridine (ethynyl–bpy) ligand endowed the resulting Re(I) complex with ability to reduce carbon dioxide to carbon monoxide with lower overpotential (0.525 V) and higher selectivity (FE 96%). Also, the resulting Re(I) complex showed ability to electropolymerize on the glassy carbon electrode surface and the modified electrode showed high selectivity towards CO with 97% FE in the presence of 2,2,2-trifluoroethanol.

Pyrrole is another monomer for electropolymerisation. Complexes **57 – 61** having pyrrole on the bipyridine ligand were able to undergo oxidative electropolymerisation and form films with different thickness on platinum and carbon felt electrodes.[233] Rhenium(I) tricarbonyl complex **62** with a dipyridylamine ligand with a pendant pyrrole also showed the ability to

electrochemically polymerize on glassy carbon electrode, rendering the electrode active for carbon dioxide reduction.[234] The rhenium(I) complex with phenylethynyl group at 5,5' position of the bipyridine also showed electropolymerisation on a Pt electrode, which is highly selective for carbon dioxide reduction to carbon monoxide at relatively low reduction potentials and high current densities.[235] Thiophene complexes **63 – 65** were also deposited on glassy carbon electrodes to form stable electron conducting films.[235] The electro-polymerized compounds showed higher stability than the complexes in homogeneous solution, indicating that the film may protect the active form from decomposition.

Another way of electropolymerisation is the electrochemical reduction of an aniline terminal group on the electrode surface.[236] In the presence of 2,4,6-collidine, complex **66** formed polymers at the glassy carbon electrode surface at ca. 0.72 V and the resulting modified electrode was stable for one week exposed to air.[237] The modified electrode showed an increased current by 86-fold in the first cycle compared to the argon saturated solution but after 10 CV cycles the surface completely lost the catalytic activity.

2.1.4.2 Electrochemical redox grafting

Complex **66** (Figure 2.7) was also immobilized on the electrode surface by forming strong C-C bonds using electroreduction of *in situ* generated diazonium salts. This method provided the possibility to form multilayers by increasing the cycle number and the surface was more stable than the C-N bond approach. The modified electrode using both grafting methods (electropolymerisation and electrografting) was much more efficient than the corresponding homogenous catalyst solutions.

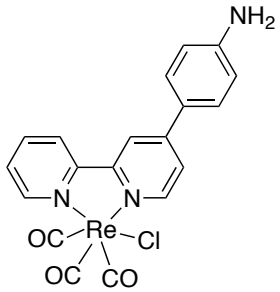


Figure 2.7 Molecular structure of complex **66**.

2.1.4.3 Physical adsorption

Complex **67** (Figure 2.8) was described to undergo condensation to *o*-quinone edge defects on graphitic carbon surface, forming graphite-conjugated rhenium catalyst on the electrode surface.[238] The modified electrode showed high activity for carbon dioxide reduction with 96 ± 3% Faradaic efficiency for the formation of carbon monoxide, in which a one-electron transfer was involved. Complex **68** (Figure 2.8) with dinuclear rhenium(I) was physically adsorbed on a carboxylated multiwall carbon nanotubes (CMWCNTs) modified pencil graphite electrode (PGE) and the resulting electrode showed higher cathodic current and a lower overpotential compared with its homogeneous catalyst.[239]

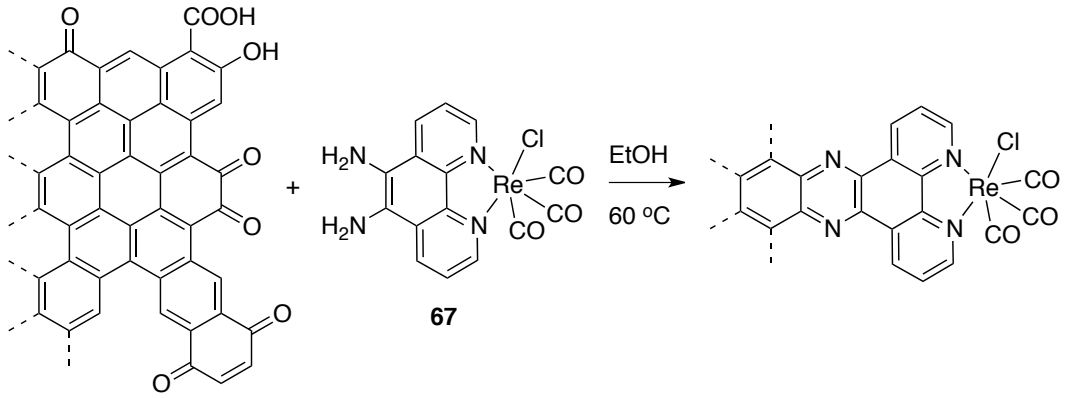
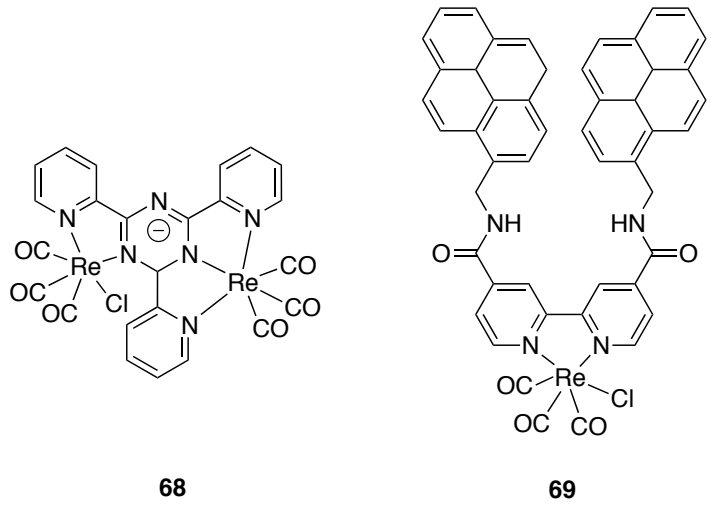


Figure 2.8 molecular structure of complex **67** and the reaction with *o*-quinone edge defects of graphitic carbon surfaces.



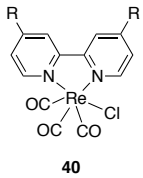
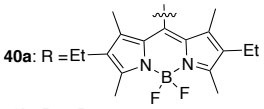
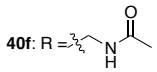
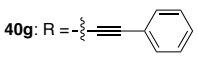
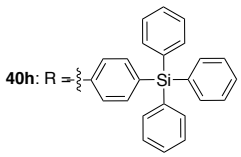
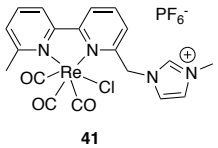
68 **69**

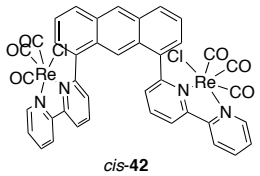
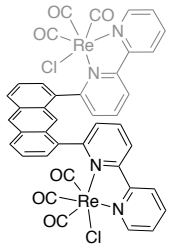
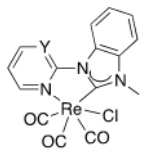
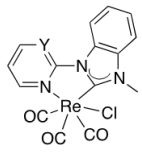
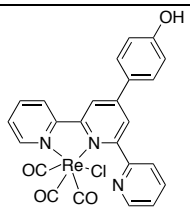
Figure 2.9 Molecular structure of complex **68** and **69**.

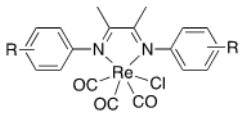
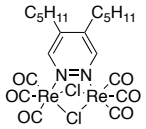
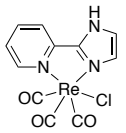
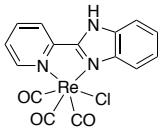
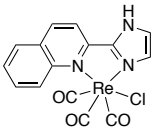
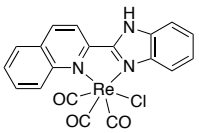
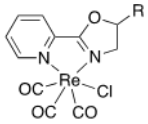
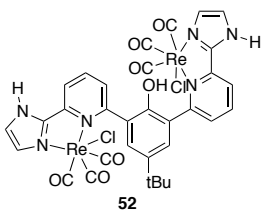
Recently, a new immobilisation approach involving non-covalent interactions using carbon nanotubes was developed[240] which was first reported in 2013.[241–245] Anchored by a pyrene unit on the carbon nanotubes with the help of π-π interactions, the metal complexes transformed to a quasi-heterogeneous system.[244] For rhenium(I) complexes, H. B. Gray has developed Lehn type rhenium(I) complex **69** (Figure 2.9) bearing pyrene at the 4,4' position of bipyridine using this strategy and the resulting electrode was found to be selective, stable, and a fast catalyst for CO_2- to-CO conversion at low overpotential (0.48 V) in neutral pH unbuffered water.[241,243,244,246] The use of carbon nanotubes gave a more stable electrode[244] and water as working solvent created a particular environment at the catalytic site facilitating the adsorption and further reaction of carbon dioxide.[244] The loading of the catalyst on the carbon nanotubes is another parameter for the product selectivity.[245]

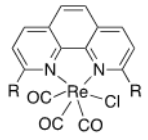
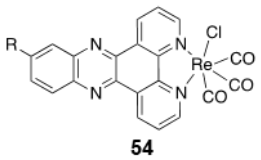
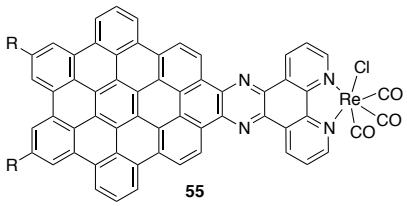
The complexes mentioned here are summarized in Table 2.2 below along with available catalysis data.

Table 2.2 Rhenium(I) tricarbonyl complexes as homogeneous catalysts for carbon dioxide electroreduction.

Molecule		Applied potential (V)	solvent	Proton source	Time (h)	Products (Faradaic yields, %)	ref
 40	 **40a**: R = Et	-2.0 VS SCE	MeCN	-	-	-	241
	40b: R = *t*Bu	-1.85 V vs SCE	MeCN	-	2	CO (99)	202
	40c: R = carboxy	-	-	-	-	-	
	40d: R = methyl	-	-	-	-	-	
	40e: R = methoxy	-	-	-	-	-	
	 **40f**: R =	-1.60 vs Ag/AgCl	MeCN	0.5 M TEE	-	CO (56, 73)	196
		-2.0 vs Ag/AgCl	DMF	10% H_2O	-	CO (95)	
		-2.20 vs Ag/AgCl	MeCN	-	-	CO (54)	
	 **40g**: R =	−1.9 V vs. Ag/AgCl	DMF	-	5	CO (12)	203
	 **40h**: R =	-2.36 V vs Fc/Fc^+	DMF	-	-	CO (58)	204
		-2.1109 V vs. Fc/Fc^+		-	-	CO (76)	
		-1.66 V vs. Fc/Fc^+		-	-	n.d.	
 41		-1.77 V vs. Fc/Fc^+	MeCN	2.8 M H_2O	-	CO (60)	206
		-1.74 V vs. Fc/Fc^+	MeCN	9.4 M H_2O	-	CO (73)	
		-2.5 V vs. Fc/Fc^+	DMF	-	1	CO (81)	207

 *cis*-**42**	-2.4 V vs. Fc/Fc^+		3 M H_2O	1	CO (59)	
	-2.0 V vs. Fc/Fc^+		-	3	CO (52)	
	-2.0 V vs. Fc/Fc^+		3 M H_2O	10	CO (47)	
 *trans*-**42**	-2.5 V vs. Fc/Fc^+	DMF	-	1	CO (81)	
	-2.4 V vs. Fc/Fc^+		3 M H_2O	1	CO (59)	
	-2.0 V vs. Fc/Fc^+		-	3	CO (52)	
	-2.0 V vs. Fc/Fc^+		-	10	CO (52)	
	-2.0 V vs. Fc/Fc^+		3 M H_2O	10	CO (47)	
 **43a**: Y = C-H	−2.2 V vs Fc/Fc^+	MeCN	0.5 M phenol	-	H_2 (26), CO (60), HCO_2H (2)	208
 **43b**: Y = N				-	H_2 (17), CO (62), HCO_2H (4)	
 **44**	-	MeCN	-	-	-	209

 45	**45a**: R = 2,4, 6-Me_3	-	MeCN	TFE	-	-	210
	45b: R = 2,6-*i*Pr_2				-	CO (<10%)	
	45c: R = 4-Br				-	-	
	45d: R = 2-CF_3				-	-	
 46		0, 0.5, -1, -1.5, -1.7 V versus SCE	MeCN	-	-	-	211
 47		-	MeCN	1 M MeOH	-	-	212
 48							
 49							
 50							
 51	**51a**: R = H	−2.8 V vs Fc/Fc^+	MeCN	-	0.5	CO (55), H_2 (<3)	214
	51b: R = CH_3					CO (55), H_2 (<3)	
	51c: R = Ph					CO (30), H_2 (<3)	
 52		−2.6 V vs Fc/Fc^+	DMF	10% H_2O	1	CO (61)	215
					2	CO (60)	
					5	CO (65)	
	53a: R = methyl	-	MeCN	-	-	-	215
	53b: R = 2,4,6-trimethoxyphenyl						

 53	**53c**: R = 3,4,5-trimethyoxylphenyl						
 54	**54a**: R = CF_3	−1.9 V vs Fc/Fc^+	MeCN	0.45 M PhOH	-	CO (19)	216
	54b: R = NO_2	−2.1 V vs Fc/Fc^+				CO (53)	
	54c: R = H	−2.0 V vs Fc/Fc^+				CO (48)	
	54d: R = *t*Bu	−2.0 V vs Fc/Fc^+				CO (27)	
 55		-0.86 V Vs NHE	THF	5% methanol	2	CO (96)	217

2.1.5 Proposal of the project

As described above, most of the rhenium(I) complexes studied for catalysing carbon dioxide electroreduction are based on bipyridine ligand with few examples using other diimine ligands. Since the construction of the Pyta ligand using copper(I)-catalysed azide-alkyne cycloaddition proceeds efficiently in mild conditions, this ligand allows a systematic structure-activity relationship study. Here, we were interested in evaluating the rhenium(I) tricarbonyl complexes based on Pyta/Tapy ligand for their activity towards CO_2 electroreduction in both homogenous and heterogeneous phases. Pyta complexes initially designed for photophysics (complexes **14** and **15**) and some specifically designed complexes were first evaluated as catalysts in homogenous phase (Figure 2.10). The synthetic work and electrochemical studies were performed by V. H. Ching, post-doctoral researcher supported by a PSL-funded project involving Collège de France (M. Fontecave and M. Gomez-Mingot), ENSCP (F. Bedioui, S. Griveau and C. Slim), ENS (C. Policar and H. Bertrand). The results will be presented briefly.[218] Meanwhile, complex **16** with an ester group on the 5- position of the triazole ring was also investigated for its activity towards carbon dioxide electroreduction.

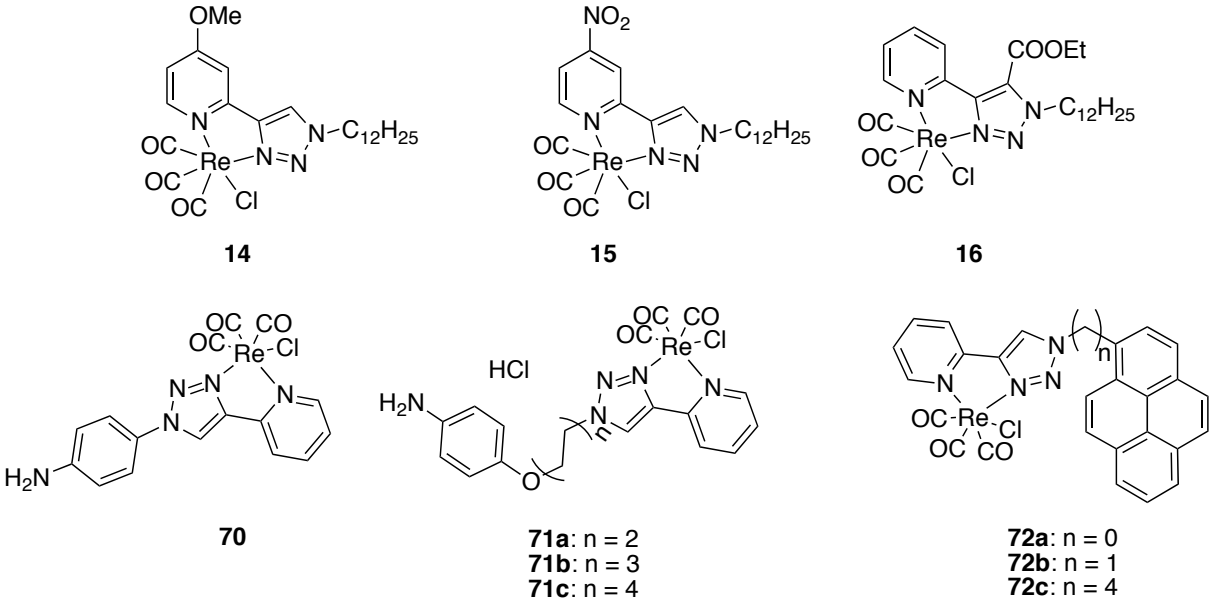


Figure 2.10 Molecular structure of complexes **14** – **16** and **70** – **72**.

Based on these results in homogeneous phase, we turned to immobilisation strategies on electrodes using either electrochemical or non-covalent method.

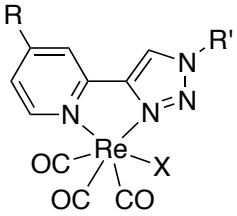
For the electrochemical strategy, we designed and synthesized a series of Pyta rhenium(I) complexes **71a – c** bearing aniline to anchor on the glassy carbon electrode surface as well as complex **70** as reference. The design and synthesis of the complexes and the preliminary results for electrochemical immobilisation on the electrodes of complex **70** will be presented.

Meanwhile, inspired by the recent literature using π-π interactions between carbon nanotubes and pyrene,[240 – 245] we applied this approach to our Re Pyta complexes. For this purpose, we also designed and synthesized a series of Pyta rhenium(I) complexes **72a – c** with a pyrene as anchor. The design and synthesis of the complexes and the preliminary results for non-covalent immobilisation on the electrodes as well as their activity towards carbon dioxide reduction will also be presented.

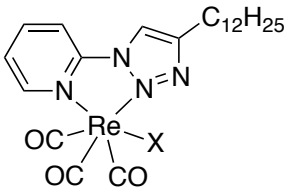
2.2 Rhenium complexes as homogeneous catalysts for CO_2 electroreduction

2.2.1 Structure-activity study

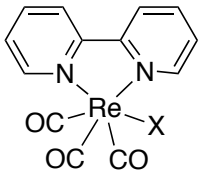
Complexes **14** and **15** (Figure 2.11) synthesized for photophysical studies were included in this study. The other complexes were synthesized by V. H. Ching. All the electrochemical experiments were carried out by V. H. Ching. The electrochemical behaviours are summarised in Table 2.3.[63]



3r: X = Cl, R = H, R' = $C_{12}H_{25}$
73a: X = Cl, R = H, R' = tolyl
73b: X = Cl, R = H, R' = tri(tert-butyl)phenyl
73c: X = Cl, R = H, R' = C_3H_6OH
14: X = Cl, R = OMe, R' = $C_{12}H_{25}$
15: X = Cl, R = NO_2, R' = $C_{12}H_{25}$
73d: X = Br, R = H, R' = $C_{12}H_{25}$



9: X = Cl
74: X = Br



75a: X = Cl
75b: X = Br

Figure 2.11 Molecular structures used in this study.

Table 2.3 Potentials of compounds.[63]

Complex	$E_{p\text{-reduction}}$ (V versus SCE)	$E_{p\text{-oxidation}}$ (V versus SCE)
3r	-1.67	1.46, 1.88 [a]
73a	-1.64	1.45, 1.88 [a]
73b	-1.69	1.46, 1.92 [a]
73c	-1.65	1.44, 1.88 [a]
14	-1.79	1.42, 1.85 [a]
15	-0.48, [a] -1.08	1.51, 1.91 [a]
73d	-1.59	1.42, 1.85 [a]
9	-1.42, -1.64 [a]	1.52, 1.91 [a]
74	-1.40, -1.64 [a]	1.52, 1.90 [a]
75a	-1.27, [a], -1.57	1.47, 1.89 [a]
75b	-1.28, [a] -1.55	1.32, 1.86 [a]

[a] $E_{1/2}$ values for reversible and quasi-reversible waves.

Rhenium(I) complexes based on either Pyta or Tapy ligand as well as classical bipyridine ligand as a reference have been synthesized and studied for their ability to catalyze the electro- and photoreduction of carbon dioxide (Figure 2.11). All the potentials in the following will be given against SCE. The influences on the catalytic activity of the normal versus inverse coordination and of functionalizing the pyridyl and triazolyl rings of the Pyta ligand were investigated. All

the Pyta rhenium(I) complexes **3r**, **73a – d**, **14** and **15** showed a first irreversible oxidation wave at ~1.45 V, which is assigned to Re(II)/Re(I) couple and a second oxidation wave at ~1.9 V, which is assigned to the oxidation of the ligand. The oxidation potentials are quite similar with that of Re(bpy)$(CO)_3$Cl complex. Comparing complexes **14** and **15**, complexes with electron-donating ligands showed slightly less positive oxidation potential (1.42, 1.85 V for complex **14** and 1.51, 1.91 V for complex **15**). The reduction waves of Pyta rhenium(I) complexes were more significantly influenced by the modification on the pyridine ring. For example, complex **14** showed reduction wave at -1.79V and complex **15** showed reduction wave at -1.08 V while complexes **73a – c** with functional groups on the 1 position of the triazole ring showed reduction waves at ca. -1.65 V which is close to that for complex **3r** (-1.76 V). This behaviour is in agreement with what was observed for the photophysical studies that the 1-position of the triazole ring is well electronically isolated. For complex **14**, an additional reversible signal at -0.5 V was assigned to the reversible reduction of the nitro group. Complex **3r** with Cl showed lower potential for reduction peak compared with that of complex **73d** with Br.

In agreement with the fact that the Tapy ligand is a poorer electron donating group than Pyta ligand,[63] the Tapy rhenium(I) complexes (complexes **15** and **73d**) showed anodic shift for the redox waves compared to their corresponding Pyta rhenium(I) complexes. CVs of Tapy rhenium(I) complexes also displayed an additional wave ca. -1.64 V, which is assigned to a further reduction of the complex.

Complexes **3r**, **73a**, **73b** and **14** showed catalytic activity towards CO_2 electroreduction. Complex **3r**, **73a**, **73b** and **14** showed catalytic peak current at -1.67, -1.64, -1.69 and -1.80 V, respectively in the presence of water. Also, the CVs of three complexes **3r**, **73a** and **73b** in the presence of water indicated displacement of coordinated halide by an aqua ligand. Controlled potential electrolysis (CPE) experiments in the presence of a proton source showed that CO is the major product of the electrocatalytic reaction and complex **73b** displaying the best stability (19 h) and selectivity for CO (~ 90% FE with water or TFE as proton source).

2.2.2 Catalytic activity of complex 16

The electrochemical behaviour of complex **16** was assessed in acetonitrile in the absence and presence of carbon dioxide. Preliminary experiments were also conducted by electrolysis.

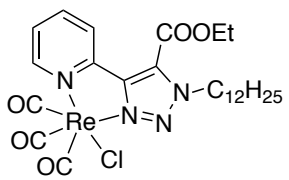


Figure 2.12 Molecular structure of complex **16**.

2.2.2.1 Electrochemical behavior of complex 16

Meanwhile, the electrochemical behaviour of complex **16** (Figure 2.13) at concentration of 1 mM was also well investigated by cyclic voltammetry at 100 mV/s in nitrogen-saturated acetonitrile in the presence of NBu_4PF_6 (0.1 M) as the supporting electrolyte, using a glassy carbon electrode. The reason for choosing acetonitrile as electrolyte solvent is that rhenium complexes are soluble in it and carbon dioxide is 8 times higher soluble in acetonitrile than in water. The cyclic voltammograms (CVs) are shown in Figure 2.13. The oxidation of the complex **16** (Figure 2.13-b) showed similar behaviour as mentioned before, first irreversible peaks at 1.44 V and quasi-reversible peak with $E_{1/2}$ ($E_{1/2} = (E_{pa}+E_{pc})/2$) of 1.86 V, which are assigned to the Re(II)/Re(I) couple and oxidation of the ligand, respectively.

The reduction of complex **16** (Figure 2.13-a) showed the classical first quasi-reversible reduction ($E_{1/2}$ = -1.40 V). This might be the reduction of –COOEt motif because in the CV of complex **3r** [Re(Pyta)$(CO)_3$Cl], there is no reversible reduction peak at this position. Furthermore, CV of complex **16** showed two reduction peaks at -1.69 V and -1.80 V which might be the reduction of Pyta part and the release of Cl^-, respectively. Though at low temperature, the radical anions of bipyridyl Re analogues are generally stable, they may still lose Cl^- at room temperature.[107] In the absence of a coordinating solvent, they may dimerize.[247] These may apply for complex **16** too.

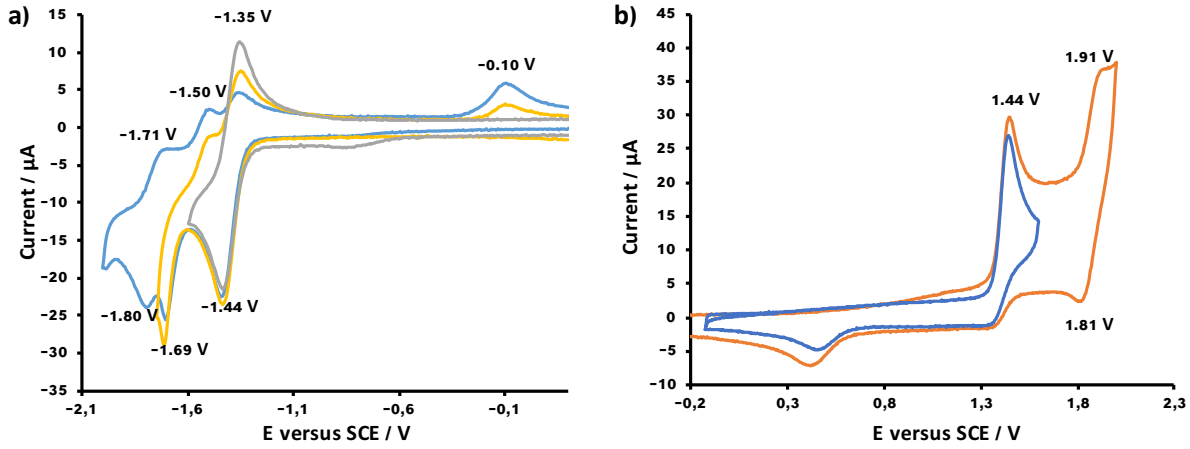


Figure 2.13 Cyclic voltammogram at glassy carbon electrode of 1 mM complex **16** in 0.1 M Bu_4NPF_6 acetonitrile under nitrogen. a) potential range from 0.2 V to -2 V and b) potential range from -0.2 V to 1.9 V. Scan rate 100 mV/s.

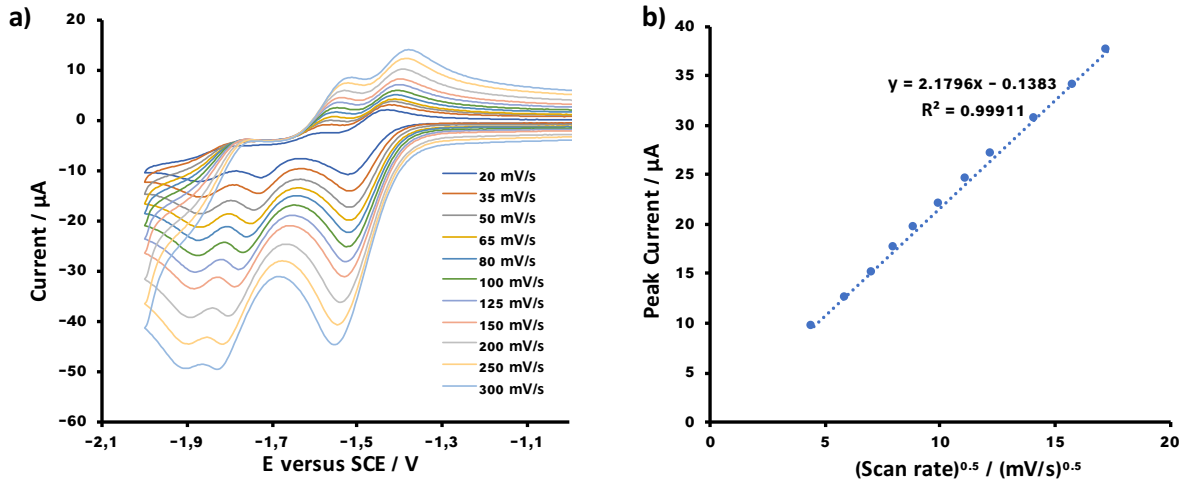


Figure 2.14 a) Evolution of CV of 1 mM complex **16** as a function of the scan rate at glassy carbon electrode in 0.1 M Bu_4NPF_6 acetonitrile under nitrogen. b) Plot of absolute value of the first cathodic peak (at around -1.5 V) current as a function of the $v^{1/2}$.

CV data can also provide information about electrochemical reaction rates. For example, when the kinetics is fast, the reaction is controlled by the diffusion of the species on the electrode surface. In this case, the peak current (*ip*) is proportional to the square root of the scan rate (*v*) and the relationship between these two parameters are described by Randles-Sevcik equation (equation 2.4), where n is the number of electrons transferred in the redox event, A (cm^2) is the electrode surface area, D (cm^2/s) is the diffusion coefficient of the oxidized analyte, and C (mol/cm^3) is the bulk concentration of the analyte.

$$ip = 0.446nFAC\left(\frac{nFvD}{RT}\right)^{\frac{1}{2}} \qquad \text{Equation 2.4}$$

For reversible systems, the anodic to cathodic peak separation is equal to (60/n) mV and is independent on the scan rate. Also, the ratio between cathodic to anodic peak current is equal to one.

To confirm that the electrochemical reaction is diffusion controlled, CVs at different scan rate were performed (Figure 2.14). The first reduction peak (at around -1.5 V) current displays a linear relation to the square root of the scan rate indicating that the active species are molecular in nature and that they function in a diffusion-controlled manner.

It can be noticed that in the case of electroactive adsorbed species and reversible system (immobilized at the electrode surface), where no diffusion in solution occurs, the peak current (*ip*) is proportional to the scan rate (*v*) and the relationship between these two parameters are described by equation 2.5, where n is the number of electrons transferred in the redox event, A (cm^2) is the electrode surface area, and Γ (mol/cm^2) is the surface coverage of the adsorbed species.

$$ip = \frac{n^2F^2}{4RT}vA\Gamma \qquad \text{Equation 2.5}$$

2.2.2.2 Catalytic activity of complex 16

Then the catalytic activity of complex **16** towards carbon dioxide electroreduction was assessed without and with proton sources (water or TFE)

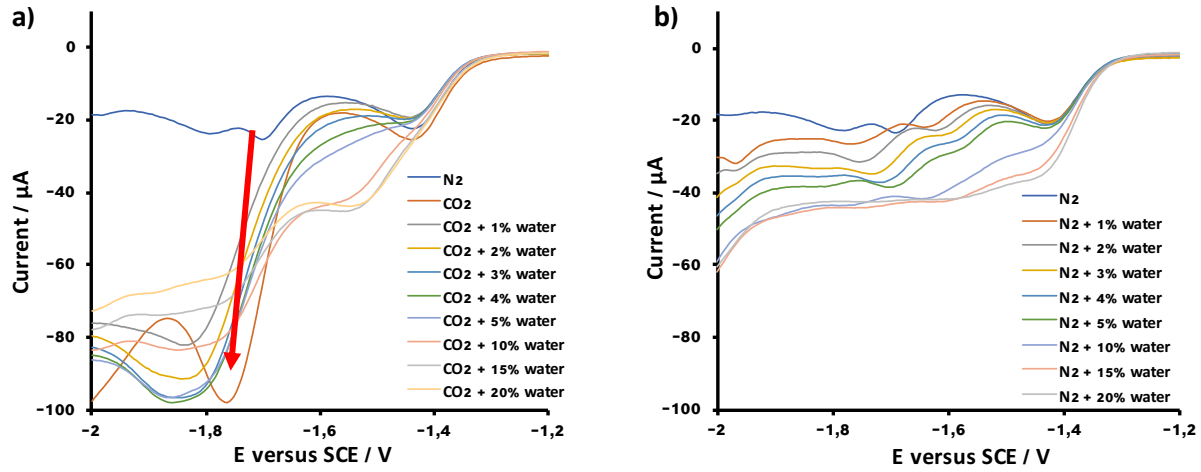


Figure 2.15 CVs of 1mM of complex **16** in 0.1 M NBu_4PF_6 acetonitrile solution under CO_2 (a) or nitrogen (b) with different percentage of water (v/v) concentration recorded at 100 mV/s using glassy carbon electrode at room temperature. Scan rate 100 mV/s.

Catalytic activity of electroreduction of carbon dioxide was first evaluated using CV under the same condition except for a carbon dioxide-saturated electrolyte. For an easier reading of the figure, only the forward scan is shown. A catalytic wave is observed under carbon dioxide at -1.78 V (Figure 2.15-a, orange line), with an increase of intensity of about four times intense than that under nitrogen atmosphere. Without adding proton source, the mechanism is proposed as below whereas water is from the nominally dry acetonitrile:[238]

$[Re(N\hat{}N)(CO)_3Cl] + e^- \rightarrow [Re(N\hat{}N^{\bullet-})(CO)_3Cl]$

$[Re(N\hat{}N^{\bullet-})(CO)_3Cl] + CO_2 \rightarrow [Re(N\hat{}N)(CO)_3(CO_2)] + Cl^-$

$[Re(N\hat{}N)(CO)_3(CO_2)] + e^- + H_2O \rightarrow [Re(N\hat{}N)(CO)_3(CO_2H)] + OH^-$; $OH^- + CO_2 \rightarrow CO_3^{2-} + H^+$

$[Re(N\hat{}N)(CO)_3(CO_2H)] + e^- \rightarrow [Re(N\hat{}N^{\bullet-})(CO)_3(CO_2H)]$

Usually, the addition of Brønsted acids can increases the catalytic current when using rhenium bipyridyl derivatives by stabilizing the rhenium-carbon dioxide intermediate through protonation as well as facilitating the cleavage CO.[192]

The addition of water did not increase the peak intensity a lot at around -1.8 V but at around -1.6 V when the amount of water is larger than 10 % (Figure 2.15-a). However, under the same condition but under nitrogen atmosphere, an increased peak intensity at about -1.6 V was observed (Figure 2.15-b), which may due to the addition of water rather than reduction of carbon dioxide.

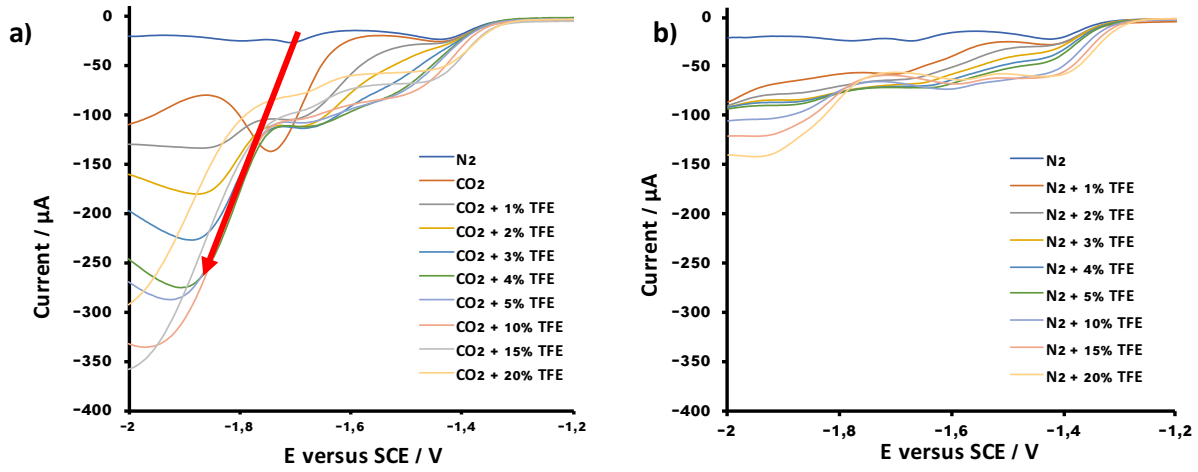


Figure 2.16 CVs of 1mM of complex **16** in 0.1 M NBu_4PF_6 acetonitrile solution under CO_2 (a) or nitrogen (b) with different percentage of triflouroethanol (v/v) concentration recorded at 100 mV/s using glassy carbon electrode at room temperature.

The addition of triflouroethanol showed a dramatic increase of peak intensity at -1.9 V as well as an increase in lower extent at around -1.6 V (Figure 2.16-a). With the same condition except under nitrogen atmosphere, it showed an increase of peak intensity at about -1.6 V (Figure 2.16-b), which may due to the addition of TFE. The increasing of the peak intensity is much larger than that with water, which is because trifluoroethanol is more acidic than water.[195]

2.2.2.3 Electrolysis using complex 16

To better evaluate the catalytic activity of complex **16**, preliminary controlled potential electrolysis was performed at -1.8 V versus SCE in 1mM complex **16** of 0.1 M NBu_4PF_6 acetonitrile solution with 5% water (v/v). The solution was saturated with carbon dioxide and when the electrolysis starts, the electrolysis system is well closed (Figure 2.17). The amount of produced carbon monoxide and hydrogen produced was determined using gas chromatography analysis (performed at College de France). The electrolysis for the blank solution was also performed under the same condition except for the addition of complex **16**. For both two conditions, the amount of the product (carbon monoxide and hydrogen), TON, TOF and FE were calculated and showed in Figure 2.18.

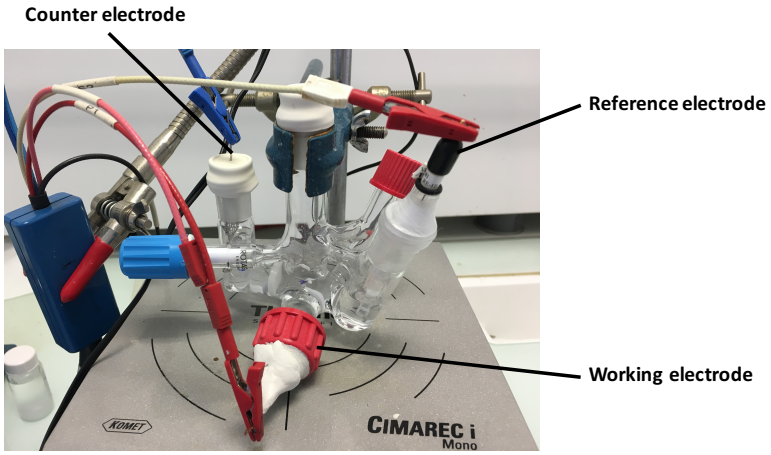


Figure 2.17 Photo of the set-up for controlled potential electrolysis.

The main products of electrolysis detected were carbon monoxide and hydrogen whatever the electrolysis conditions used. With 5% of water (v/v), the amount of carbon monoxide increased in 5 hours and then started to decrease. The amount of hydrogen increased slowly along the time. The amount of hydrogen produced with complex **16** is similar with that produced in the blank solution (Figure 2.18-a), indicating that with complex **16**, there is little amount of hydrogen produced. This result implied that complex **16** showed excellent selectivity for carbon dioxide reduction.

Unfortunately, the TON and TOF of complex **16** towards carbon monoxide are very low (0.39, 0.08 s^{-1}, respectively, Table 2.4) compared to that of complex **3r** (TON: 3.3[195]). The introduction of the EWG ester on the 1,2,3-triazole ring would decrease the charge density on Re centre, which may explain the fact that the TON is lower than that of complex **3r**. However, the TON is less than 1, which means that there is some chemical reaction occurs, for example the reduction of the ester group, which may consume the complex **16**.

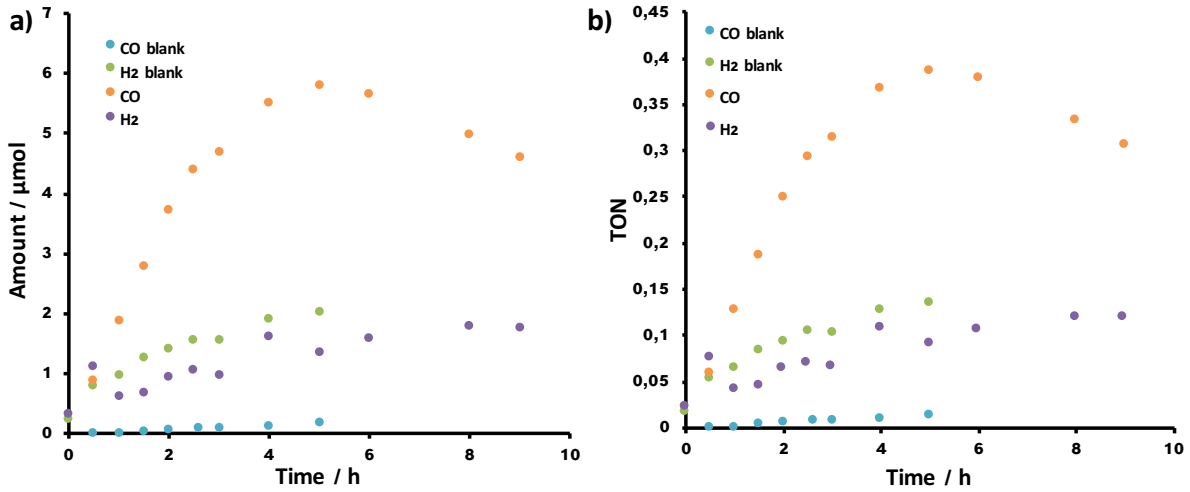


Figure 2.18 the amount of the product (carbon monoxide and hydrogen, a) and TON (b) with or without (blank) complex **16** solution (1 mM) in 0.1 M NBu_4PF_6 acetonitrile solution. Electrolysis performed at -1.8 V.

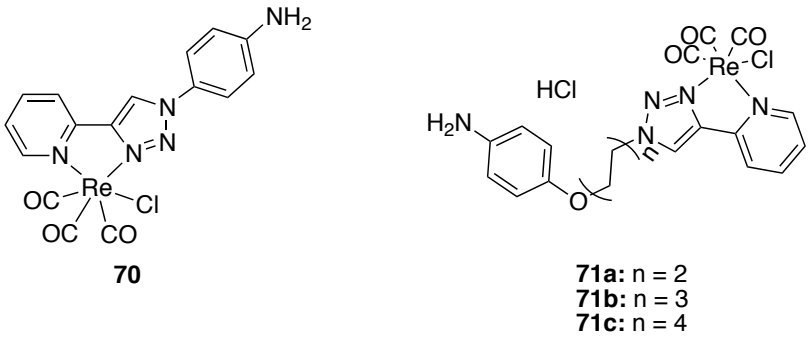
Table 2.4 Controlled potential electrolysis at -1.8 V for 2 and 5 hours: the amount of the product (carbon monoxide and hydrogen), TON, TOF and FE with or without (blank) complex **16** solution (1 mM) in 0.1 M NBu_4PF_6 acetonitrile solution.

	Time (h)	Amount of product (nmol)		TON		TOF (10^{-5} s^{-1})		Q (C)	FE (%)	
		CO	H_2	CO	H_2	CO	H_2		CO	H_2
Blank	2	79	1399	-	-	-	-	1.12	1.9	34
	5	183	2033	-	-	-	-	3.46	1.6	18
16	2	3732	953	0.249	0.06	3.5	0.9	3.99	18	5
	5	5787	1348	0.386	0.09	2.1	0.5	8.57	13	3

To further confirm the stability of the catalyst after electrolysis, the analysis of the solution directly after electrolysis need to be performed by using IR, NMR and other methods. Due to the limited time and difficult access to the GC instrument, the controlled potential electrolysis with or without the addition of trifluoroethanol were not performed.

2.3 Rhenium complexes towards electrochemical immobilisation on electrode

In this part, we designed rhenium(I) complexes for CO_2 reduction functionalized with an aniline motif for immobilisation on the electrode by electropolymerisation or by electroreduction of the corresponding diazonium salt (Figure 2.19). To investigate the impact of the distance between the catalyst and the electrode surface, different alkane lengths were chosen (0, 4, 6, 8 C length). However, due to the limited time, only complex **70** was investigated in detail.



70

71a: n = 2
71b: n = 3
71c: n = 4

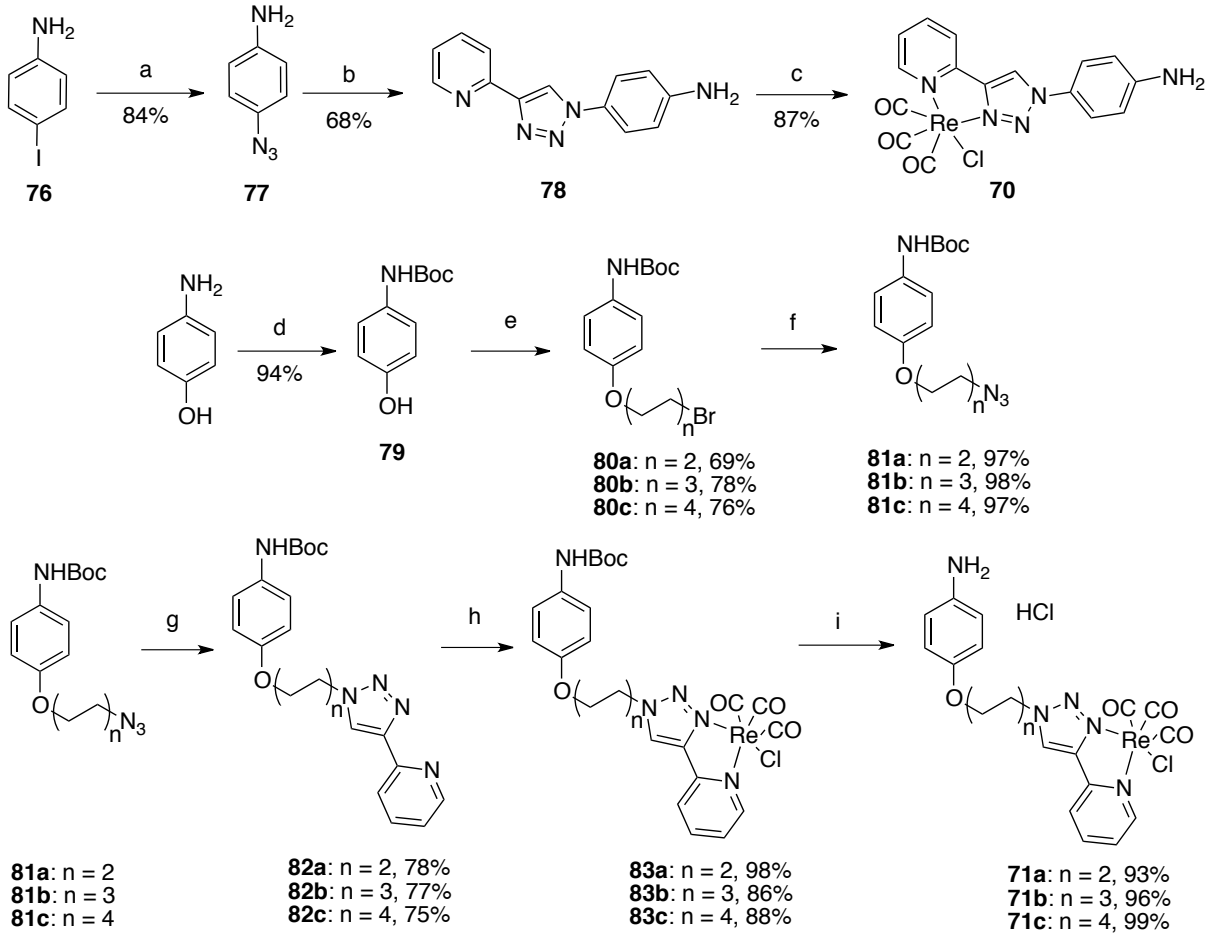
Figure 2.19 Molecular structures of complexes **70** – **71**.

2.3.1 Synthesis of the complexes

The synthesis of the complex **70** started from commercially available compound 4-iodoaniline. The azide precursor **77** was synthesized in 86% yield by the coupling reaction with sodium azide with a copper(I) catalyst (Scheme 2.4). Then the copper(I)-catalysed azide-alkyne cycloaddition (CuAAC) between the azide precursor **77** and 2-ethynylpridine under classical conditions was conducted and a washing step with N,N-diisopropylethylamine saturated aqueous solution was employed to trap copper and afford the ligand **78** in moderate yield. Complexation with rhenium(I) pentacarbonyl chloride afforded the target complex **70** in high yield (87%).

The synthesis of the complexes **71a – c** followed the same protocol (Scheme 3.2). Starting from the commercially available compound 4-aminophenol, Boc protecting group was introduced using di-*tert*-butyl dicarbonate as the reagent to protect the amino group in high yield (94 %). Then the etherification reaction between Boc protected compound **79** and the corresponding dibromoalkane under classical conditions using potassium carbonate afforded the products **80** in moderate yields (69 – 78 %). Afterwards, nucleophilic substitutions were conducted with sodium azide to form the compounds **81** in high yields (97 – 98%), followed by CuAAC reactions with 2-ethynylpyridine under classical conditions to give compounds **82** in moderate yields (75 – 78%). Compounds **83** were obtained in high yields by the complexation reaction between compounds **82** and rhenium(I) pentacarbonyl chloride in classical conditions. Finally, deprotection of the Boc group by trifluoroacetic acid (TFA) in dichloromethane (1/1, v/v) gave the desired complexes **71** in high yields (93 – 99%) with a purity of 90 – 97% determined by analytical reverse-phase HPLC. To regenerate the chloride complexes after exchange by TFA

during the reaction, the solvent was first removed and the crude complexes werer further treated concentrated hydrochloric acid in a dichloromethane solution before reevaporation.
All the final complexes were characterized by ^{1}H NMR, ^{13}C NMR, analytical HPLC and high-resolution mass spectrometry.



Scheme 2.4 Synthetic route of complexes **70 – 71**. Conditions: a: NaN_3 (2.0 equiv.), sodium ascorbate (6 mol%), CuI (12 mol%), N,N-diisopropylethylamine (DIEA) (15 mol%), DMF, water, room temperature, overnight; b: 2-ethynylpyridine (1.0 equiv.), sodium ascorbate (30 mol%), $CuSO_4 \cdot 5H_2O$ (10 mol%), tert-butanol, water, 70 °C, 12 hours; c: $Re(CO)_5Cl$ (1.0 equiv.), toluene, 120 °C, 12 hours; d: $(Boc)_2O$ (1.2 equiv.), methanol, 100 °C, overnight; e: corresponding dibromoalkane (3.0 equiv.), K_2CO_3 (3.0 equiv.), acetone, 60 °C, overnight; f: NaN_3 (2.0 equiv.), DMF, 80 °C, overnight; g: 2-ethynylpyridine (1.0 equiv.), $CuSO_4 \cdot 5H_2O$ (10 mol%), Sodium ascorbate (30 mol%), DCM, water,, room temperature, overnight; h: $Re(CO)_5Cl$ (1.0 equiv.), toluene, 80 °C, 2 hours; i: TFA, DCM, room temperature, monitored by TLC.

Meanwhile, we were able to get the single crystal structure of compound **82a** under slow evaporation of a solution in *d*-chloroform**.** The perspective drawing and the crystallographic data are shown in Figure 2.16 and Table appendix-1. The crystal structure of compound **82a** showed a head-tail arrangement of the Pyta ligand, that is, the pyridine ring was facing the triazole ring from another molecule and the triazole ring was facing the pyridine ring from

another same molecule. Weak π-π interactions occurred between them (3.7 Å), which might favour this confomation. The pyridine and triazole rings were slightly distorted with a dihedral angle of 166.81°. Moreover, one of the oxygen atoms on the carbamate moiety displayed weak N-H···O intermolecular interaction (2.31 Å) with the proton connected to the nitrogen atom of the carbamate moiety from another molecule.

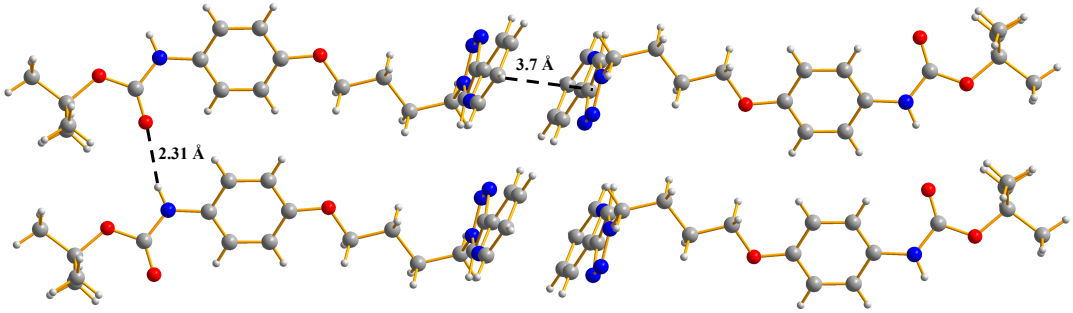


Figure 2.20 The perspective drawing of **82a**. White: hydrogen atom; gray: carbon atom; red: oxygen atom; blue: nitrogen atom.

2.3.2 Electrochemical characterisation

The electrochemical behaviour of all the complexes was investigated in argon-saturated acetonitrile with a concentration of 1 mM by cyclic voltammetry (CV) at 100 mV/s in the presence of Bu_4NPF_6 (0.1 M) as the supporting electrolyte, using a glassy carbon electrode (3 mm diameter). CVs of complex **70** and ligand **78** are shown in Figure 2.21-a. Complex **70** showed irreversible oxidation waves with the potentials of 1.24 V, 1.47 V and 1.94 V which were assigned to the oxidations of the amino group, Re(I)/Re(II), and Pyta ligand respectively A cathodic peak appeared at ~ 0.5 V can be attributed to electroactivity of the polymer formed at the electrode surface following aniline oxidation. Thus, every time before scanning towards oxidation direction, the electrode needs to be polished. An irreversible cathodic peak at E_p = -1.64 V, can be attributed to the reduction of the Pyta ligand.

For comparison, the electrochemical behaviour of the ligand **78** was also investigated by CV under the same condition (Figure 2.21-b). CVs of ligand **78** showed a large irreversible reduction peak at -2.47 V which is assigned to the reduction of the Pyta. Compared with that of complex **70** (-1.64 V), it was largely cathodically shifted. The irreversible oxidation peak at 1.0 V is attributed to oxidation of aniline while thereduction peak observed at ~ 0.5 V on the return scan can be attributed to the electroactivity of the polymer formed at the electrode surface *via* oxidation of aniline groups.

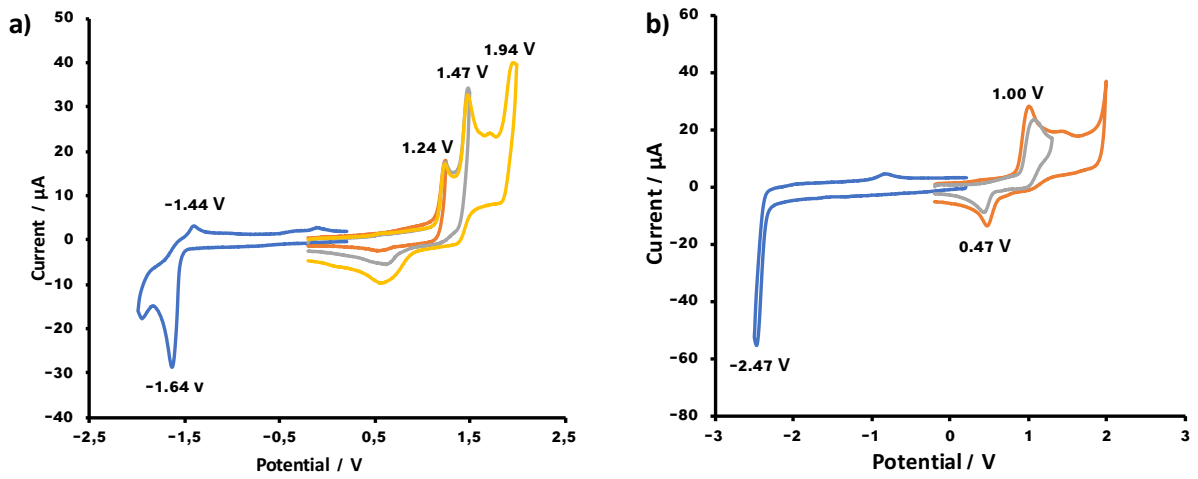


Figure 2.21 CVs of complex **70** (a) and ligand **78** (b). Condition: 1 mM compound in 0.1 M NBu_4PF_6 acetonitrile solution under nitrogen, glassy carbon electrode. Scan rate 100 mV/s.

2.3.3 Electrochemical immobilisation on the electrode

The aniline motif can either undergo electro-oxidation at the electrode surface or electro-grafting after *in situ* formation of corresponding diazonium salt to allow the immobilisation of the complex on the electrode surface. Both these two approaches are investigated.

2.3.3.1 Electro-polymerisation of the complex

First of all, the electro-polymerisation of the complex **70** on the electrode surface was studied through the possibility of the electro-polymerisation of its aniline group. The polymerisation is two-electron transfer procedure and head-to-tail product is formed for the polymerisation of aniline.[63] When there is functional group at the *para*- position of aniline, the oxidation procedure is related with one-electron transfer.[248] As shown before, the electro-oxidation potential of the aniline group for complex **70** is 1.24 V. The electro-polymerisation was first conducted in acetonitrile by cyclic voltammetry method in the potential range of -0.2 → 1.3 V in 1 mM complex **70** in 0.1 M NBu_4PF_6 solution for 20 cycles at 50 mV/s.

Figure 2.23-a showed the cyclic voltammograms obtained by cycling in a solution of complex **70**. The first cycle only showed one anodic peak at 1.24 V and two cathodic peaks at around 0.5 V, indicating the deposition of the polymerisation on the electrode surface. From the second cycles, the anodic peak at around 0.6 was observed, further confirming the electro-polymerisation of the aniline motif.[249] The intensity of these peaks did not increase after cycling. Then the modified electrode was rinsed three times using acetonitrile and sonicated for two minutes in acetonitrile to remove any physical-adsorbed complexes. The characterisation of the modified electrode was conducted using cyclic voltammetry in 0.1 M NBu_4PF_6 acetonitrile solution free of complex (Figure 2-22-b). The cathodic peak at around -1.7 V can be attributed to the reduction of complex **70**. However, the signal at -1.7 V was lost after several cycles with the scan rate of 100 mV/s, which can be attributed to the removal of the deposited layer.

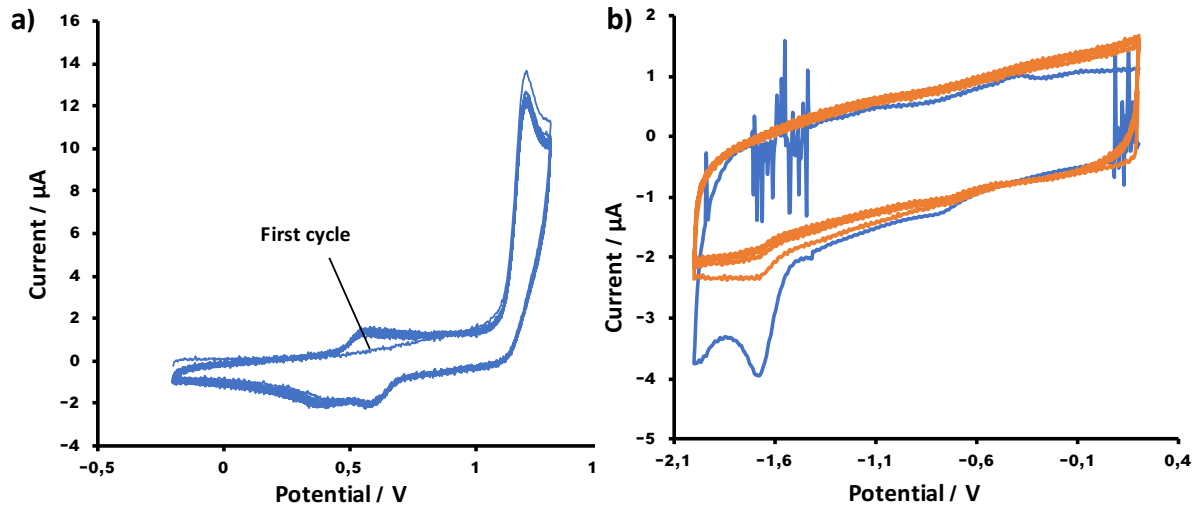


Figure 2.22 a) Cyclic voltammogram at glassy carbon electrode in a solution of complex **70** in acetonitrile with 0.1 M NBu_4PF_6, scan rate: 50 mV/s, 20 cycles. b) Cyclic voltammogram in acetonitrile with 0.1 M NBu_4PF_6 of glassy carbon electrode modified after the cyclic voltammetry in figure a, scan rate: 100 mV/s, blue line: first scan; orange line: second scan.

The electro-polymerisation through branching at the *ortho*-position of the aniline could probably lead to a larger number of the attached Re(I) motif compared to the commonly favoured growing in the *para*-position since in this way the *para*-group is eliminated.[250] The chronoamperometry method for polymerisation of the aniline is believed to increase the rate of *ortho*-coupling.[249,250] Thus, chronoamperometry method was also investigated for the electro-polymerisation of complex **70**. The potential of 1.3 V was used and the electrolysis last for 30 minutes (Figure 2.23-a). The current was around 3 µA, which was low and the current kept stable during the whole electrolysis. The resulted electrode was rinsed three times with acetonitrile and characterized using cyclic voltammetry in 0.1 M NBu_4PF_6 acetonitrile solution (Figure 2.23-b). The CVs of the modified electrode also showed an anodic peak at around -1.7 V, which is similar to that obtained using cyclic voltammetry electropolymerisation approach. However, similarly the modified electrode lost this anodic peak, indicating that the product deposited on the electrode surface is not stable under reduction condition in acetonitrile.

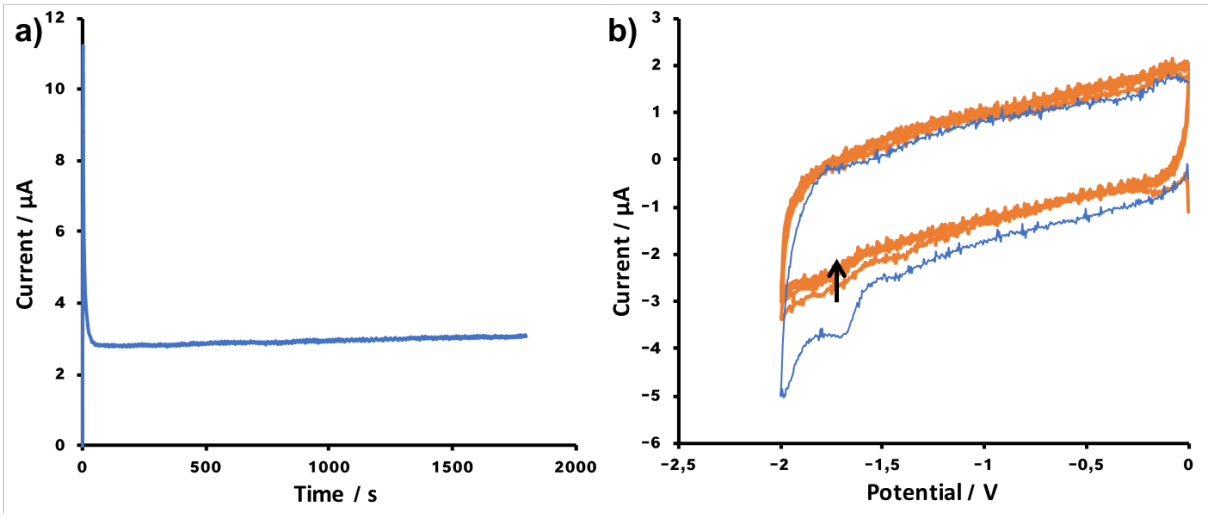


Figure 2.23 a) Chronoamperometry of complex **70**. Performed at 1.3 V for 30 minutes. b) CVs of modified electrode recorded in 0.1 M NBu_4PF_6 acetonitrile solution. Blue line: CVs from the first scan. Orange line: CVs from the second scan.

To improve the electropolymerisation, 2,4,6-collidine was used.[249] To 1 mM complex **70** in 0.1 M NBu_4PF_6 acetonitrile solution, 5 equiv. of 2,4,6-collidine was added and the mixture was degassed using nitrogen for 20 minutes. Then CVs were recorded in this solution with a scan rate of 50 mV/s (Figure 2.24-a). The oxidation peak shifted to positive direction, which is probably due to the formation of multilayer.[251,252] The electrode was rinsed three times with acetonitrile and CVs were recorded in 0.1 M NBu_4PF_6 acetonitrile solution using a scan rate of 100 mV/s (Figure 1.24-b). Similarly, a reduction peak at around -1.7 V was observed with higher current compared with grafting without 2,4,6-collidine. However, it disappeared after the first cycle.

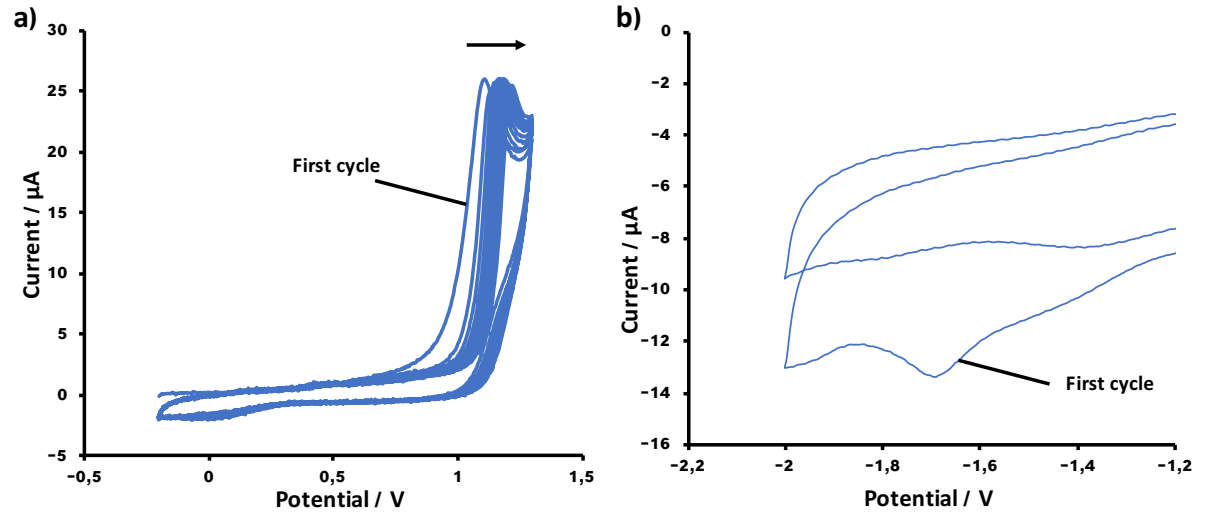


Figure 2.24 a) CVs of 1 mM complex **70** in 0.1 M NBu_4PF_6 acetonitrile solution in the presence of 5 equiv. of 2,4,6-collidine, scan rate: 50 mV/s. b) CVs of modified electrode in 0.1 M NBu_4PF_6 acetonitrile solution, scan rate: 100 mV/s.

The chronoamperometry method was also applied with 2,4,6-collidine under the same condition. The potential was 1.3 V and it last for 10 minutes (Figure 2.25-a). The current decreased, implying the covering of the electrode surface. The electrode was then rinsed three times with acetonitrile and CVs was recorded in 0.1 M NBu_4PF_6 acetonitrile solution (figure 2.25-b). A reduction peak was observed at around -1.7 V in the first cycle and then decreased a lot, which is similar as got using other grafting method.

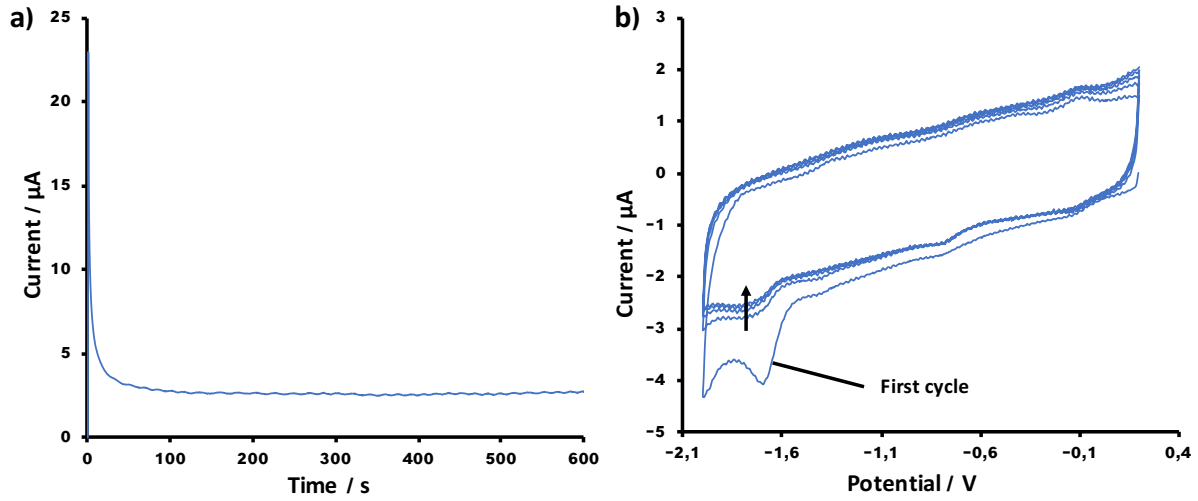
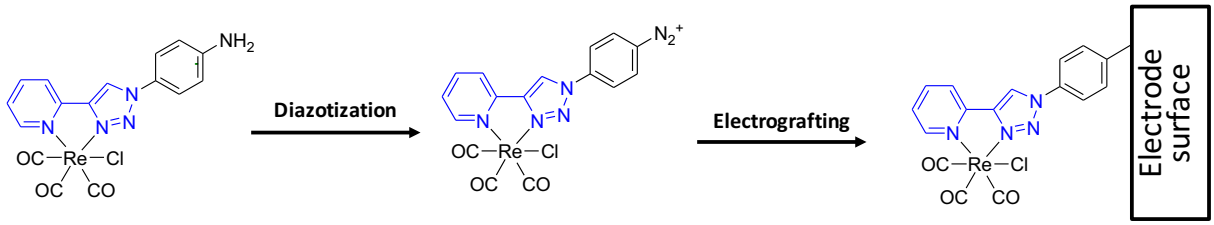


Figure 2.25 a) Chronoamperometry of 1 mM complex **70** in 0.1 M NBu_4PF_6 acetonitrile solution in the presence of 5 equiv. of 2,4,6-collidine for 10 minutes. b) CVs of modified electrode in 0.1 M NBu_4PF_6 acetonitrile solution, scan rate: 100 mV/s.

In all cases, the successful grafting of the complex **70** on the electrode surface was well observed. However, after cyclic voltammetry in acetonitrile (without complex) for several cycles at the scan rate of 100 mV/s, the electrode surface loses the electrochemical signals, indicating that the deposited layer is not stable under these conditions. However, the stability of the deposited polymers is rarely discussed in the literature for metal complexes.[251] Thus, it is not easy to make comparison regarding to the stability of the formed surface. It also offers difficulty to perform CO_2 reduction for the modified electrode. Thus, we tried to find another way to make the grafting of the electrode. The electro-reduction of the diazonium salt was chosen since *in situ* preparation of the diazonium salt from aniline is quite well-documented.[238]

2.3.3.2 Electrografting *via* the electroreduction of the corresponding diazonium salt

In this approach (Scheme 2.5), the aniline motif is first converted into diazonium salt using *tert*-butyl nitrite (tBuNO$_2$) as the reagent. Then, through electro-reduction of the diazonium salt, there is the formation of C-C bond with electrode surface, with the release of nitrogen. Since the diazotisation step is easy to perform, the diazonium salt can be prepared *in situ* and then electro-reduction can be performed directly without further separation nor purification.



Scheme 2.5 Assumed mechanism for electro-grafting of the diazonium salt.[253]

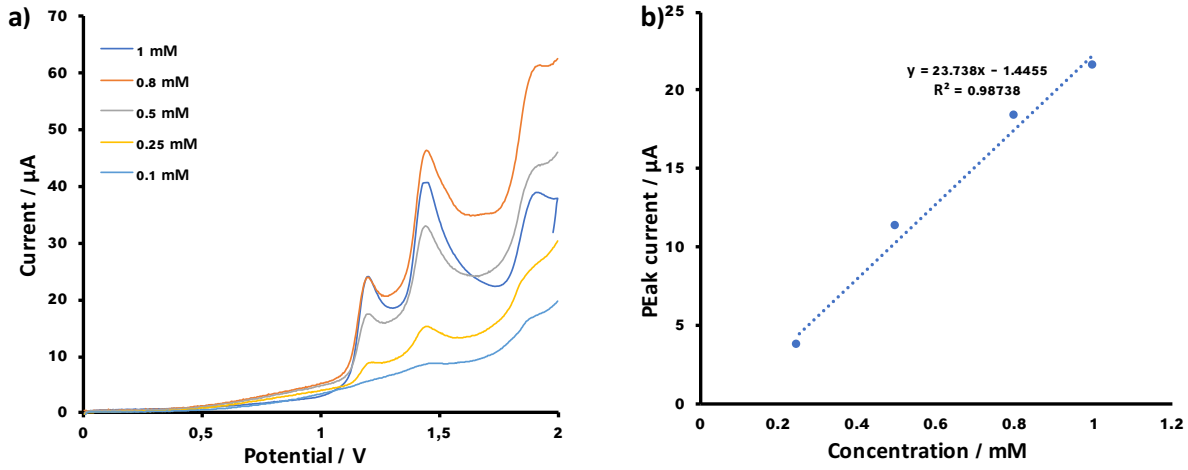


Figure 2.26 a) CVs of complex **70** (different concentration) in 0.1 M Bu_4NPF_6 acetonitrile under nitrogen. Glassy carbon electrode. b) Plot of cathodic peak (1.24 V) current as a function of the concentration.

First of all, concentration calibration curve was created by recording CVs of complex **70** at different concentrations (Figure 2.26). The diazonium salts solution were prepared from rhenium complexes **70** (1mM) in the presence of *t*$BuNO_2$ (10 equiv.) in 0.1 M NBu_4PF_6 nitrogen-saturated acetonitrile in the dark.[254] To monitor the reaction, CVs of the solution were recorded at stated times (Figure 2.27) to evaluate the decrease of the peak intensity of aniline oxidation (converted to diazonium during the reaction). The electrode was well polished every time before recording the CVs. After 1 hour, the concentration of the aniline motif in solution was lower than 0.1 mM (calculated using the concentration calibration curve), indicating the completion of the conversion. Also, the colour of the solution turned from pale yellow into yellow, indicating the existence of the diazonium in solution.

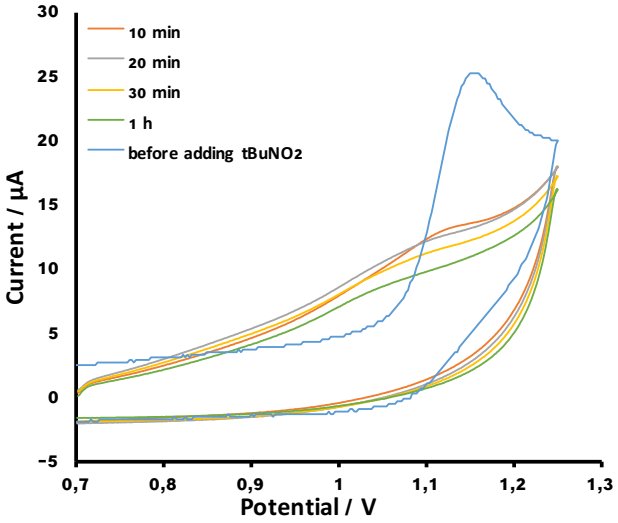


Figure 2.27 CVs of 1 mM complex **70** in 0.1 M NBu_4PF_6 acetonitrile solution after adding *t*$BuNO_2$ for stated time. Glassy carbon electrode, scan rate: 100 mV/s.

The glassy carbon electrode was functionalized through the reduction of the *in situ* generated diazonium cations from the complex **70** by 20 voltammetric cycles from 0 V versus OCP (open circuit potential) to -1 V with a scan rate of 50 mV/s (figure 2.28). On the first cycle, two broad irreversible peaks located at around 0 - 0.2 V were observed which can be attributed to the electrochemical reduction of diazonium cations to phenyl radicals, followed by a dramatic decrease of current intensity upon the following cycles which is due to the formation of a covalently linked layer blocking the electrode surface.[254]

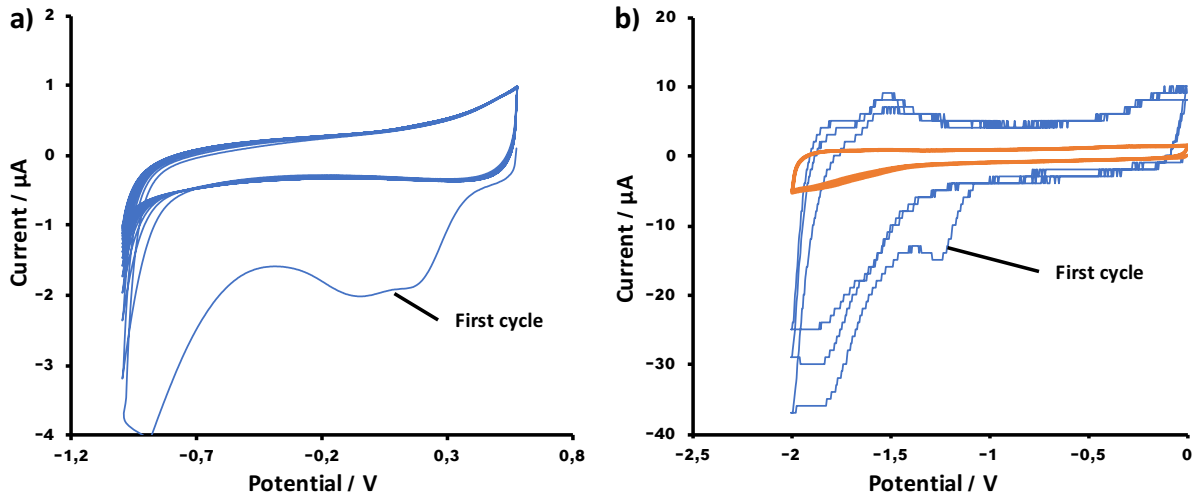


Figure 2.28 a) CVs at glassy carbon electrode of diazonium salt generated *in situ* from 1 mM complex **70** in 0.1 M NBu_4PF_6 acetonitrile solution, scan rate: 50 mV/s. b) CVs of modified glassy carbon electrode in 0.1 M NBu_4PF_6 acetonitrile solution with scan rate of 500 mV/s (blue line) or 100 mV/s (orange line).

The resulted electrode was rinsed three times with acetonitrile and CVs were recorded in 0.1 M NBu_4PF_6 acetonitrile solution (Figure 2.28-b). At high scan (500 mV/s), a quasi-reversible peak

was observed at around -1.7 V along with a pre-peak at around -1.3 V and the quasi-reversible peak was kept after several cycles but it disappeared when the second scan using the scan rate of 100 mV/s.

Since the modified electrode surface was not stable as we expected, another *in situ* diazonium synthesis approach was studied using sodium nitrite in the presence of hydrochloric acid.[255,256] The diazonium salt solutions were prepared from rhenium complexes **70** (1mM) in the presence of sodium nitrite (1.5 equiv.) in 0.1 M NBu_4PF_6 nitrogen-saturated mixture of acetonitrile and 1 M hydrochloric acid in water (96 : 4, v/v) in the dark.[257] The electrografting was conducted 1.5 hours after addition of sodium nitrite for completion of the reaction. The colour of the solution turned from pale yellow into yellow, indicating the occurring of the conversion.

The glassy carbon electrode was functionalized through the reduction of the *in situ* generated diazonium cations from the complex **70** by 20 voltammetric cycles from 0 V versus OCP to -0.5 V with a scan rate of 50 mV/s (figure 2.29-a). On the first cycle, one broad irreversible peaks located at around 0.1 V were observed which can be attributed to the reduction of diazonium cations to phenyl radicals, followed by a gradual decrease of current intensity upon the following cycles which is due to the formation of a covalently linked layer blocking the electrode surface.[254]

The resulted electrode was rinsed three times with acetonitrile and CVs were recorded in 0.1 M NBu_4PF_6 acetonitrile solution (Figure 2.29-b). The modified electrode was unstable upon cycling, which is similar as observed before. The trend of decrease of the current was smaller than that got using tBuNO$_2$, which may indicate that using this diazotisation procedure, the resulting grafting layer is more stable. This electrografting method is worth further exploration.

For electro-reduction of the diazonium salt approach, the *in situ* diazotisation step using both methods was successfully monitored and fulfilled. The electroreduction of the diazonium salt was investigated using cyclic voltammetry. The CVs showed successfully blocking the electrode surface. However, the modified electrode only showed stability with high scan rate and with moderate scan rate it is still not stable with cycling. This might be due to the slow procedure in high scan rate time scale. The stability of the surface using this approach is also seldom discussed in the literature. The stability of the modified electrode under reduction condition needs to be improved to study the further catalytic activity of modified electrode towards carbon dioxide electroreduction.

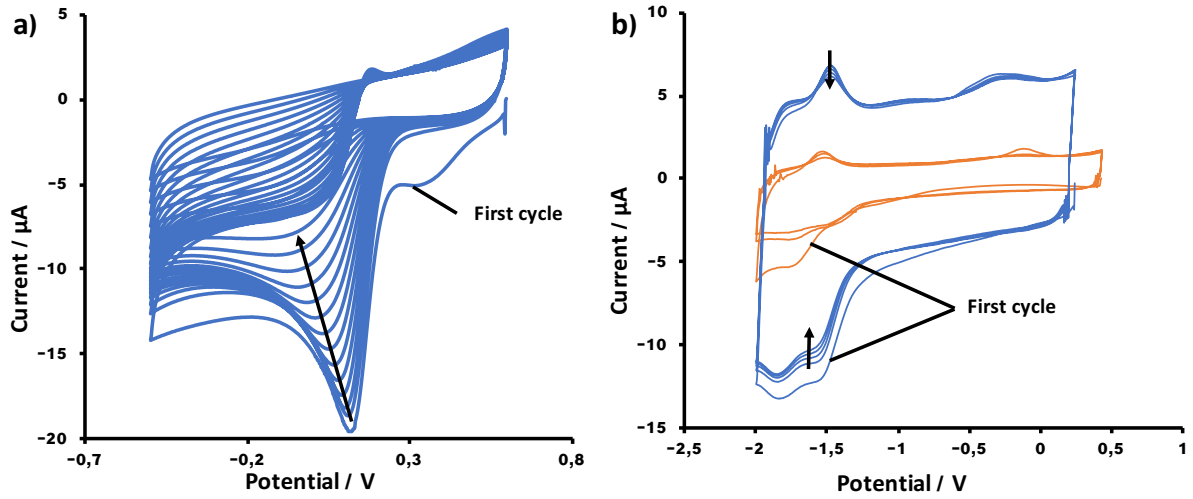


Figure 2.29 a) CVs at glassy carbon electrode of diazonium salt generated *in situ* from 1 mM complex **70** in a mixture of acetonitrile/1M HCl aqueous solution (96 : 4, v/v) containing 0.1 M NBu_4PF_6, scan rate: 50 mV/s. b) CVs of modified glassy carbon electrode in 0.1 M NBu_4PF_6 acetonitrile solution with scan rate of 500 mV/s (blue line) or 100 mV/s (orange line).

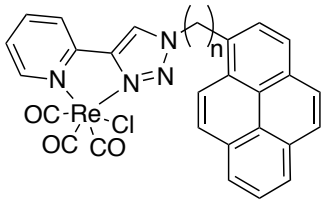
2.3.4 Summary

A new series of complexes with different chain lengths between the Re-Pyta-Cl moieties for carbon dioxide electroreduction catalysis and aniline moieties for electrografting on electrode was designed and synthesized. All the complexes were characterized by ^{1}H NMR, ^{13}C NMR, analytic HPLC and high-resolution mass spectrometry.

Due to the limited time, only complex **70** was investigated in detail. The electrochemical behaviour was first studied to have clue for the electro-grafting. The electro-oxidation of the aniline part and the electro-reduction of the *in situ* generated diazonium salt using *t*$BuNO_2$ or sodium nitrite were performed to modify the electrode surface. The former method is to perform the electro-polymerisation using the aniline part and deposit the polymer directly on the electrode surface. The later method is to form C-C covalent bond with the glassy carbon electrode surface. The grafting using either of them was successful. However, the modified electrode lost the electrochemical signals after several scans, which is not ideal for the further investigation of carbon dioxide reduction. The stability of the modified electrode under reduction condition needs to be improved by exploring different grafting ways. Meanwhile, the morphology of the grafted electrode surface needs to be characterized using electronic microscopy (AFM) and to directly confirm that there is rhenium atom on the electrode surface, X-ray photoelectron spectroscopy (XPS) experiments need to be performed. Meanwhile, the influence of the thickness of the grafted layer on the catalytic activities also needs to be investigated. The other three complexes are to be tested.

2.4 Rhenium complexes towards non-covalent immobilisation on electrode

Carbon nanotubes are an established platform for the immobilisation of molecular electrocatalysts.[255,256] The high surface area and excellent conductivity allows grafting various electrocatalytically active species while keeping good electron transfer properties.[258–261] The possibility of modification of carbon nanotubes using either covalent or noncovalent techniques is also an advantage.[262] Specially, the immobilisation of pyrene-modified catalysts through π-π interactions and Van der Waals interactions has been employed to graft Re,[263] Ir,[244] Fe,[246] Mn[243] based catalysts, and the latter three showed catalytic activity in aqueous solution. Using this method, the catalyst can be anchored on the electrode stably. This is a relatively new technique and there are less reports using this strategy. We designed rhenium(I) complexes for carbon dioxide reduction functionalized with a pyrene motif for non-covalent immobilisation on the electrode (Figure 2.30). To investigate the influence of the distance between the catalyst and the electrode surface, different alkane lengths were chosen (0, 1, 4 C length).

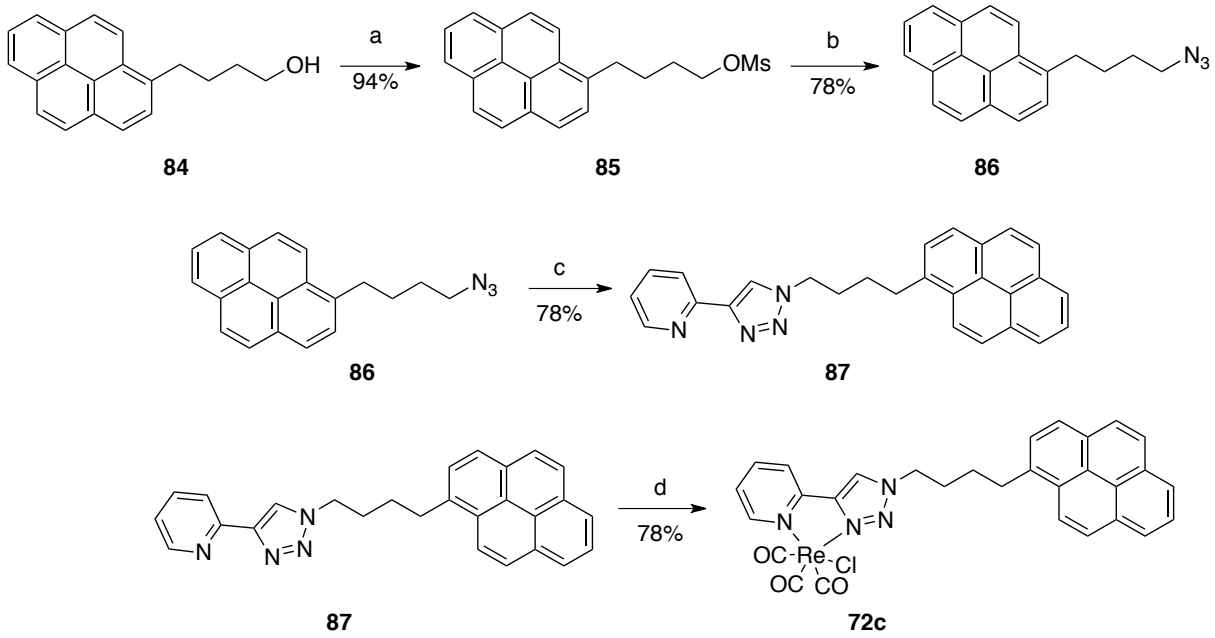


72a: n = 0
72b: n = 1
72c: n = 4

Figure 2.30 Molecular structures for complexes **72a** – **c**.

2.4.1 Synthesis of the complexes

The synthesis of complex **72c** started from commercial available compound 4-(pyren-1-yl)butan-1-ol. Treatment with methanesulfonyl chloride followed by nucleophilic substitution of the mesylated compound with sodium azide gave the azide precursor **86** in moderate yield (78%). Then a CuAAC reaction between precursor **86** and 2-ethynylpyridine under classical conditions afforded the ligand **87** in fair yield (78%). Finally, the complexation of compound **87** with rhenium(I) pentacarbonyl chloride in refluxing toluene gave the desired complex **72c** in 78% yield.



Scheme 2.6 Synthetic route for complex **72c**. Conditions: a: MsCl (1.5 equiv.), DIEA (3.5 equiv.), DCM, 0 °C ~ room temperature, overnight; b: NaN_3, DIEA, 80 °C, overnight; c: 2-ethynylpyridine (1.0 equiv.), sodium ascorbate (30 mol%), $CuSO_4 \cdot 5H_2O$ (10 mol%), DCM, water, room temperature, overnight; d: $Re(CO)_5Cl$ (1.0 equiv.), toluene, 120 °C, 1 hour.

Complexes **72a** and **72b** were synthesised by V. H. Ching. All the complexes were characterized using ^1H NMR, ^{13}C NMR, IR and high-resolution mass spectrometry. All the preliminary electrochemical behaviour was performed by Rosaria Pulcrano (internship Erasmus program)

2.4.2 Electrochemical characterisation in the absence/presence of CO_2

Since the complex **72a** has limited solubility in acetonitrile, the electrochemical behaviour of all the complexes was investigated in argon-saturated DMF with a concentration of 0.5 mM by cyclic voltammetry (CV) at 100 mV/s in the presence of Bu_4NPF_6 (0.1 M) as the supporting electrolyte, using a glassy carbon electrode (Figure 2.31). The potential window goes from -2 V to 0.5 V. Complexes **72a** and **72b** exhibited two reduction peaks. The first reduction peak around -1.6 V (complex **72a**: -1.6V; complex **72b**: -1.5 V; complex **72c**: -1.66 V) is referred to the reduction of Pyta ligand[241]. The second peak for complexes **72a** and **72b** around -2.0 V is assigned to the $Re^{+/0}$ couple[63].

The catalytic ability for carbon dioxide reduction was first evaluated under the same conditions except for the use of a carbon dioxide-saturated DMF solution. A catalytic wave is observed for complexes **72a** and **72c**, confirming the catalytic ability for carbon dioxide reduction. There is no obvious catalytic wave observed for complex **72b**.

Addition of the proton source 2,2,2-trifluoroethanol to the electrolyte solution increases the catalytic current, indicating the enhancement of the carbon dioxide reduction (Figure 2.31 d – f).

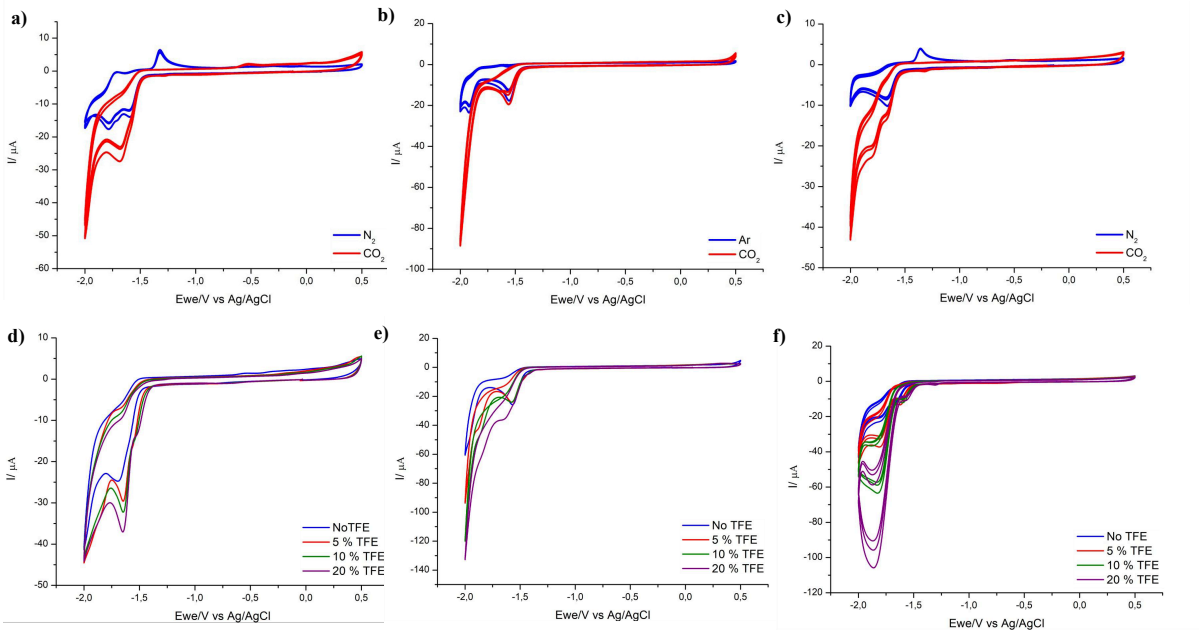
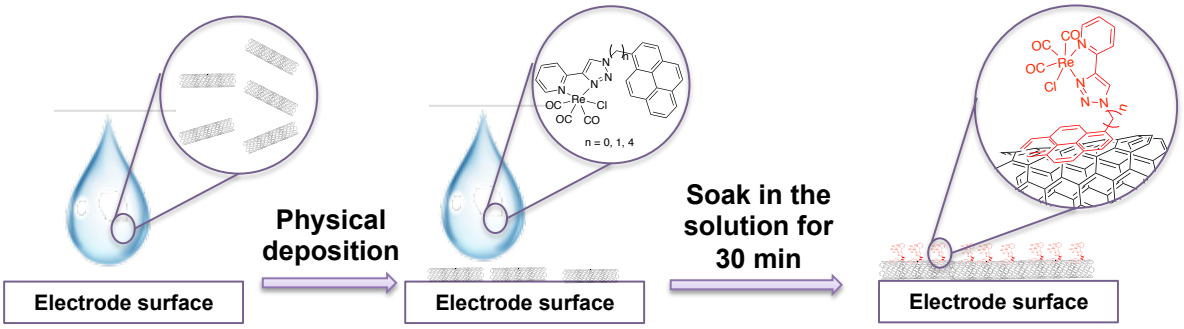


Figure 2.31 Cyclic voltammetry of complexes **72a** (a), **72b** (b), **72c** (c) in DMF with 0.1 M Bu_4NPF_6 under argon or CO_2. Blue line: argon-saturated solution; Red line: CO_2-saturated solution. Cyclic voltammetry of complexes **72a** (d), **72b** (e), **72c** (f) in CO_2-saturated DMF with 0.1 M Bu_4NPF_6 with 0% (blue), 5% (red), 10% (green), and 20% (purple) TFE.

2.4.3 Non-covalent immobilisation on the electrode and catalytic abilities

To fulfil the non-covalent immobilisation of the complexes on the electrode, the protocol is conducted as shown in Scheme 2.7. First, the commercially available single walled carbon nanotubes were dispersed in N-methyl-2-pyrrolidone (5 mg/mL) under sonication.[244] Then, 2 µL of the suspension was dropped on the glassy carbon electrode (dia. 3 mm) surface and the surface loading with single wall carbon nanotubes was well dried under argon flow. The modified electrode was soaked in a DMF solution of the corresponding pyrene complexes (1 mM). The resulting electrode was washed with DMF and acetonitrile to remove any residue and dried under argon flow. Now, the electrode surface was covered with single wall carbon nanotubes by physical adsorption and on the carbon nanotubes there attached rhenium(I) complex through π-π interaction.



Scheme 2.7 Schematic diagram of the non-covalent immobilisation method: 1. Drop a dispersion of nanotube on the electrode and dry it; 2. Soak the electrode getting from the 1st step into a solution of the complex for 30 minutes.

The bare electrode was first characterized using cyclic voltammetry in acetonitrile and 0.1 M Bu_4NPF_6 as electrolyte in the presence/absence of carbon dioxide (Figure 3.32-a). The cyclic voltammetry showed no obvious catalytic waves confirming no catalytic ability for carbon dioxide reduction. The electrode modified only with single walled carbon nanotubes was also characterized using the same protocol and showed similar results (Figure 3.32-b). An increase of the capacitive current could be observed showing the immobilisation of SWCNT at the surface of GC electrode.

The electrochemical behaviour of the electrodes modified with pyrene complexes **72a – c** was evaluated in the absence and presence of carbon dioxide. When the solution was saturated with carbon dioxide, a catalytic wave at around -1.4 V was observed for all the three complexes.

To further characterize the catalysed reaction, controlled potential electrolysis (CPE) of carbon dioxide-saturated acetonitrile with 0.1 M Bu_4NPF_6 was performed using pyrene complexes modified electrodes. The potential at -1.7 V was applied because the catalytic peak showed most intense at this potential. Both carbon monoxide and hydrogen were detected by gas chromatography during CPE for all the complex-grafted electrodes as well as for the single walled carbon nanotubes-grafted electrode. No formate was observed by ion-exchange chromatography. For all the three complexes, the current density remained roughly constant for 1 hour using these conditions leading to the increase of the charge passed over all electrolysis (Figure 3.33).

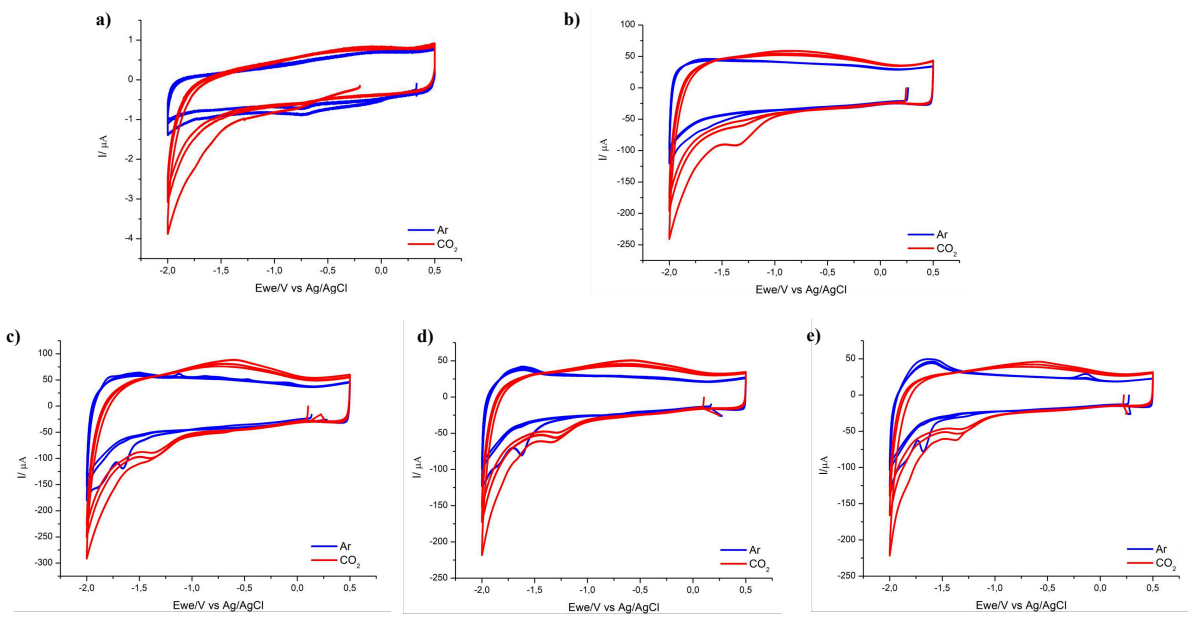


Figure 2.32 Cyclic voltammetry of blank electrode (a), electrode modified with single walled carbon nanotubes (b), electrode with single walled carbon nanotubes and **72a** (c), electrode with single walled carbon nanotubes and **72b** (d), and electrode with single walled carbon nanotubes and **72c** (e) in acetonitrile with 0.1 M Bu_4NPF_6 under argon or CO_2. Blue line: argon-saturated solution; Red line: CO_2-saturated solution.

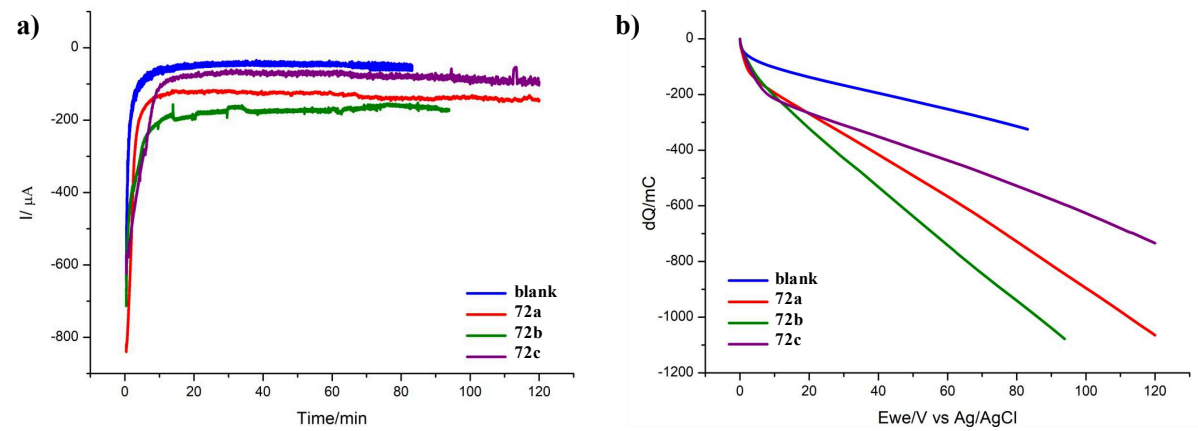


Figure 2.33 CPE (Current versus Time in CO_2-saturated acetonitrile, a) and CPE (Charge versus Time in CO_2-saturated acetonitrile, b) in CO_2-saturated acetonitrile using: single walled carbon nanotubes modified blank electrode (blue), electrode modified with complex **72a** (red), electrode modified with complex **72b** (green), electrode modified with complex **72c** (purple).

Faradaic efficiency (FE) values for CPE were summarized in Table 2.5. The results indicated that the total FY for the blank electrode only grafted with single walled carbon nanotubes was the highest among all of them (95%). However, it mainly produced H_2, which is understandable since the reduction of H^+ is easier than that of carbon dioxide. The total FE of electrodes modified with complexes **72a – c** varied from 28 – 47%, which is not really ideal compared to the literature in which the similar approach is applied.[241] Complexes **72a** and **72b** showed no

obvious selectivity towards the reduction of carbon dioxide while complex **72c** showed better selectively towards the reduction of carbon dioxide. This may due to the better screening effect caused by the longer chains. The repeatability of these results need to be checked.

Table 2.5 Controlled potential electrolysis[a] of complexes **72a – c** immobilized on SWCNT-modified glassy carbon electrodes.

Complex	µmol CO	µmol H_2	Q (C)	FE for CO	FE for H_2
Blank	0.20	0.60	-0.324	25%	70%
72a	0.60	0.70	-1.064	25%	22%
72b	0.30	0.48	-1.080	17%	11%
72c	1.03	0.48	-1.420	28%	13%

[a] grafted electrode in CO_2 saturated acetonitrile with 0.1 M Bu_4NPF_6 using a glassy carbon disk electrode (15 mm dia.) at room temperature. TON and TOF could not be evaluated since the amount of immobilised catalyst could not be measured.

2.4.4 Summary

In this part, we designed and synthesized a series of rhenium(I) tricarbonyl complexes functionalized with pyrene moieties for the non-covalent interaction with single walled carbon nanotubes and non-covalent modifications of electrodes. The distance between the active Re catalyst and the grafting unit was varied. All the complexes were characterized using ^{1}H NMR, ^{13}C NMR, and high-resolution mass spectrometry and electrochemistry (cyclic voltammetry). For the physical adsorption, single walled carbon nanotubes were first adsorbed on the glassy carbon electrode surface. By means of π-π interactions and Van der Waals interactions between pyrene and the single walled carbon nanotubes, the rhenium(I) complexes were then successfully grafted on the electrode. All the modified electrodes were able to catalyse carbon dioxide reduction. Complex **72c** with the longest flexible distance between pyrene and Pyta-Re moiety appeared more selective towards carbon dioxide reduction than H^+ reduction. However, a deeper characterisation of the modified electrodes with SWCNT and the complexes should be performed such as SEM, AFM, EDX and XPS experiments. The stability of the modified electrode also need to be confirmed. Meanwhile, the influence of the concentration of the catalyst attached on the carbon nanotubes and the use of different carbon nanotubes on the catalytic activity need to be investigated.

2.5 General conclusions and perspectives

As we have shown during the study of the photophysical properties, the 1- position of the triazole ring in Pyta framework is electronically well-isolated, the introduction of functional groups on this position will not affect either photophysical or electrochemical properties much. The modification on the pyridine ring has more effect on both photophysical and electrochemical properties.

For the catalytic ability for carbon dioxide electroreduction in homogenous phase, the introduction of bulky functional groups may be promising functional groups because they may inhibit the formation of Re-Re dimers which are not active for carbon dioxide electroreduction. The modification of ester group on the 5- position of the triazole showed good selectivity towards carbon dioxide reduction. The corresponding compound **16** was thus considered worth further investigation to improve the catalytic efficiency.

Different complexes were specifically synthesized to allow their immobilisation of the electrode surface to evaluate the electrocatalytic behaviour of such modified electrodes towards carbon dioxide reduction. Aniline derivatives were prepared, allowing for immobilisation *via* electropolymerisation or diazonium electrografting. The electro-grafting immobilisation of aniline groups on the glassy carbon electrode surface through electro-oxidation of the aniline to produce polymer or electro-reduction of in situ generated diazonium salt from aniline preliminarily showed success. However, using either method, the preliminary study tends to indicate that the modified electrode surface was not stable under reduction condition, which makes carbon dioxide reduction not easy. The stability of the electrode surface need to be improved and the further characterisation of the modified surface need to be explored by XPS and AFM, for example.

The non-covalent immobilisation through π-π and Van der Waals interaction employing carbon nanotubes as medium is another promising strategy because it is easy to modify the electrode surface with different catalysts. Also, the resulting grafted electrode is stable which means that the π-π and Van der Waals interactions between pyrene and carbon nanotubes are strong enough to perform further experiments. There has been previous report on the different catalytic mechanism using different loading of the catalyst on carbon nanotubes.[241,244] To better understand and explain the results, the mechanism is worth explored.

Other grafting method, for example, oxidative grafting, click chemical grafting and peptidic coupling using Pyta rhenium(I) complexes are under investigation.

2.6 Conclusion générale et perspectives

Comme nous l'avons montré lors de l'étude des propriétés photophysiques, la position 1- du noyau triazole dans la structure de Pyta est bien isolée électroniquement, l'introduction de groupes fonctionnels sur cette position n'affectera pas beaucoup les propriétés photophysiques ou électrochimiques. La modification sur le cycle pyridine a davantage d'effet sur les propriétés photophysiques et électrochimiques.

En ce qui concerne l'effet catalytique pour l'électroréduction du dioxyde de carbone en phase homogène, l'introduction de groupes fonctionnels volumineux peut être un groupe fonctionnel prometteur, car ils peuvent inhiber la formation de dimères Re-Re qui ne sont pas actifs pour l'électroréduction du dioxyde de carbone. La modification du groupe ester sur la position 5 du triazole a montré une bonne sélectivité envers la réduction de dioxyde de carbone. Le composé correspondant **16** a donc été considéré comme méritant des recherches supplémentaires pour améliorer l'efficacité catalytique.

Différents complexes ont été synthétisés spécifiquement pour permettre leur immobilisation à la surface d'électrodes afin d'évaluer le comportement électrocatalytique de telles électrodes modifiées vis-à-vis de la réduction de dioxyde de carbone. Des dérivés d'aniline ont été préparés, permettant une immobilisation par électropolymérisation ou électrogreffage de diazonium. L'immobilisation par électropolymérisation de groupes d'aniline sur carbone vitreux par électro-oxydation de l'aniline pour produire un polymère ou par électro-réduction du sel de diazonium généré *in situ* à partir de l'aniline est prometteuse. Cependant, en utilisant l'une ou l'autre méthode, l'étude préliminaire tend à indiquer que la surface de l'électrode modifiée n'est pas stable dans les conditions de réduction étudiées dans l'acétonitrile, ce qui rend l'étude de réduction du dioxyde de carbone difficile. La stabilité de la surface de l'électrode doit être améliorée et des caractérisations supplémentaires des électrodes modifiées doivent être explorées notamment par XPS et AFM, par exemple.

L'immobilisation non covalente par interaction π-π et Van der Waals utilisant des nanotubes de carbone comme électrode est une autre stratégie prometteuse, car il est facile de modifier la surface de l'électrode avec différents catalyseurs. En outre, l'électrode greffée obtenue est stable, ce qui signifie que les interactions π-π et Van der Waals entre le pyrène et les nanotubes de carbone sont suffisamment fortes pour permettre des expériences ultérieures. Des études antérieures ont été réalisées sur les différents mécanismes catalytiques en utilisant différentes quantités de catalyseur sur les nanotubes de carbone [83]. Pour mieux comprendre et expliquer les résultats, le mécanisme mérite d'être exploré.

D'autres méthodes de greffage, telles que le greffage par oxydation, par chimie clic ou par couplage peptidique utilisant des complexes de Pyta rhénium (I) sont à l'étude.

3. Rhenium(I) complexes as macrocyclic linkers in Keap1-Nrf2 peptidomimetics inhibitors

3.1 Introduction

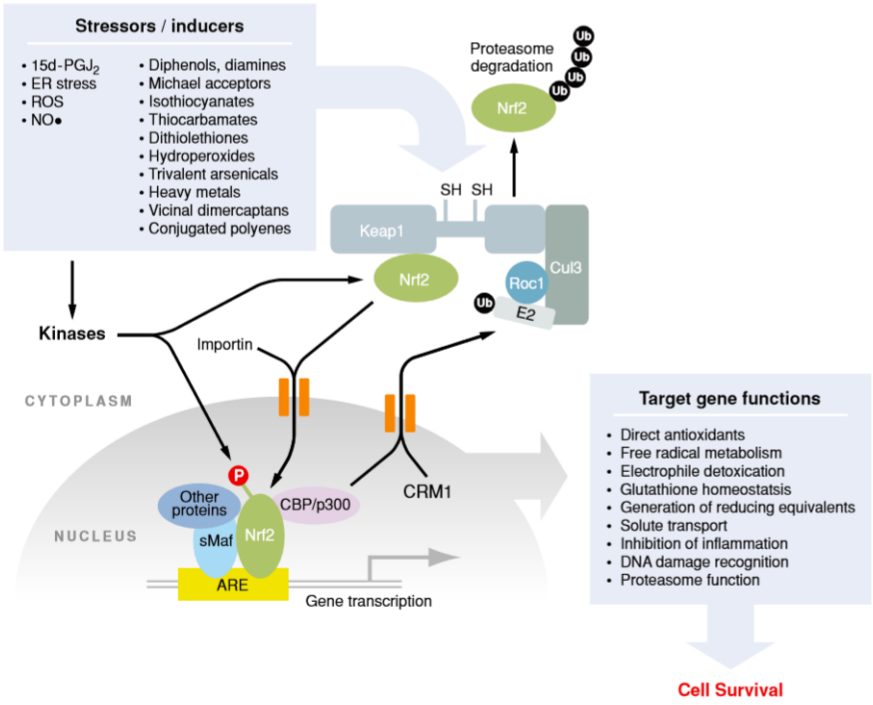
Protein-protein interactions (PPIs) play an important role in most of biological processes,[241] for example enzymatic reactions, subcellular localisation and binding. There are as many as ~650,000 pair-wise interactions for human PPIs.[264] The modulation of PPIs remains challenging and is one of the most important strategies towards next-generation therapeutics.[265] Modulators of PPIs are promising candidates in drug development.[65] In the context of protein-protein interactions, the term "hot-spot" refers to a residue or cluster of residues that makes a major contribution to the binding free energy. The hot-spot residues often represent a common feature of PPI interfaces.[65–67,266] In some cases, these hot-spot residues are part of a protein's segment adopting a well-defined secondary structure such as α-helix and β-turn upon interaction with the protein partner. Therefore, the design of PPI inhibitors based on hot-spot residues is considered as a useful strategy.[267,268] Secondary structure mimics, either small molecules or peptidomimetics are interesting tools. There are already small molecule inhibitors under clinical development[269] for some protein-protein interactions including the p53-MDM2/X[270], Keap1-Nrf2[271–275], PD-1/PD-L1[276–279] and Menin-MLL[280] protein-protein interactions. In this project, we are interested in designing secondary structure mimics centred on a rhenium tricarbonyl motif, acting as both secondary structure stabiliser and imaging core. The Keap1-Nrf2 PPI was chosen as a target, which is governed by a β-turn formed by Nrf2 upon interaction with Keap1.[281] We will first introduce this PPI and the peptide/peptidomimetics inhibitors described so far.

3.1.1 Regulation of Keap1-Nrf2 pathway

Nuclear factor erythroid 2-related factor 2, also known as Nrf2, is a basic-region leucine zipper (bZIP) transcription factor,[282] which is activated in response to oxidative stress.[283] The Nrf2 protein has 605 amino acids and includes six conserved Neh domains, Neh1 – Neh6. The Neh1 domain contains a bZIP motif, which is responsible for heterodimerisation with small MAF (muscle fascia fibrosarcoma) proteins. Its binding to antioxidant response element (ARE) in gene promoter regions activates gene expression.[284] Domains Neh3, Neh4 and Neh5 are able to bind to histone acetyltransferases to tune the Nrf2 transactivation activity. Neh6 mediates a Keap1-independent negative regulation of Nrf2. The Neh2 domain mediates the interaction with Keap1 Kelch domain *via* two binding sites,[278] a DLG-containing motif with amino acids from 17 – 32[285] and a ETGE-containing motif with amino acids from 77 – 82.[286,287] The binding towards Keap1 of the ETGE motif is 100-fold higher than that of DLG motif (binding constant 19×10^7 M^{-1} for ETGE motif and 0.1×10^7 M^{-1} for DLG motif).[288]

The human Keap1 protein, which exists as homodimers in mammalian cells, contains 624 amino acids and is divided into several domains, the N-terminal region (NTR), the broad-complex, tramtrack and bric-a-brac (BTB) domain which is essential for homodimerisation, the intervening region (IVR) which is rich in cysteines, double glycine repeats (DGR), a domain consisting of six Kelch motifs which is involved in binding with Neh2 domain of Nrf2, and the C-terminal region. The human Keap1 contains 27 cysteines, which act as redox sensors in the regulation of cellular homeostasis.

The Keap1-Nrf2 interaction is the main regulator of Nrf2 activity by targeting Nrf2 for ubiquitination and subsequent proteasome degradation (Scheme 3.1). Small molecules of endogenous and exogenous origins lead to activation of the transcription of Nrf2-regulated genes. These agents disrupt the association of Nrf2 with Keap1, leading to diminished rates of proteolysis of Nrf2 and enhanced nuclear accumulation. Phosphorylation of Nrf2 by a series of kinases also affects its fate and distribution. Interaction of Nrf2 with other transcription factors and proteins of the transcriptional complex allows for transactivation of ARE-responsive genes. Induction of these genes, which include prototypic conjugating and antioxidative genes, results in an adaptive response that enhances the resistance of cells to environmental stresses mediated by electrophiles and free radicals.[289] Thus, Nrf2-Keap1 interactions play important roles in both cancer and neurodegenerative disorders.[290]



Scheme 3.1 General scheme for the induction of gene expression through the Keap1-Nrf2-ARE signalling pathway.[68]

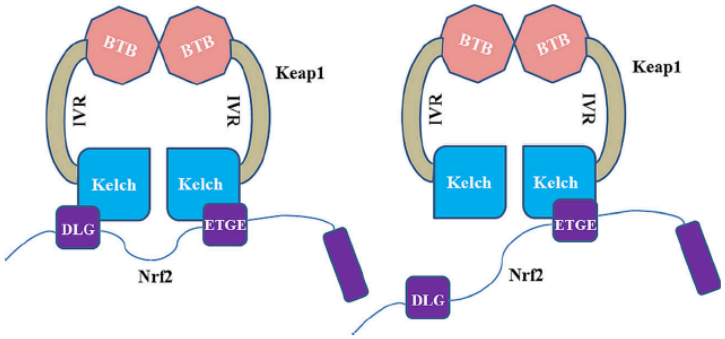


Figure 3.1 Binding model of Keap1/Nrf2.[295,296] It shows that these two sites are able to perform either two-site binding state or one-site binding state.

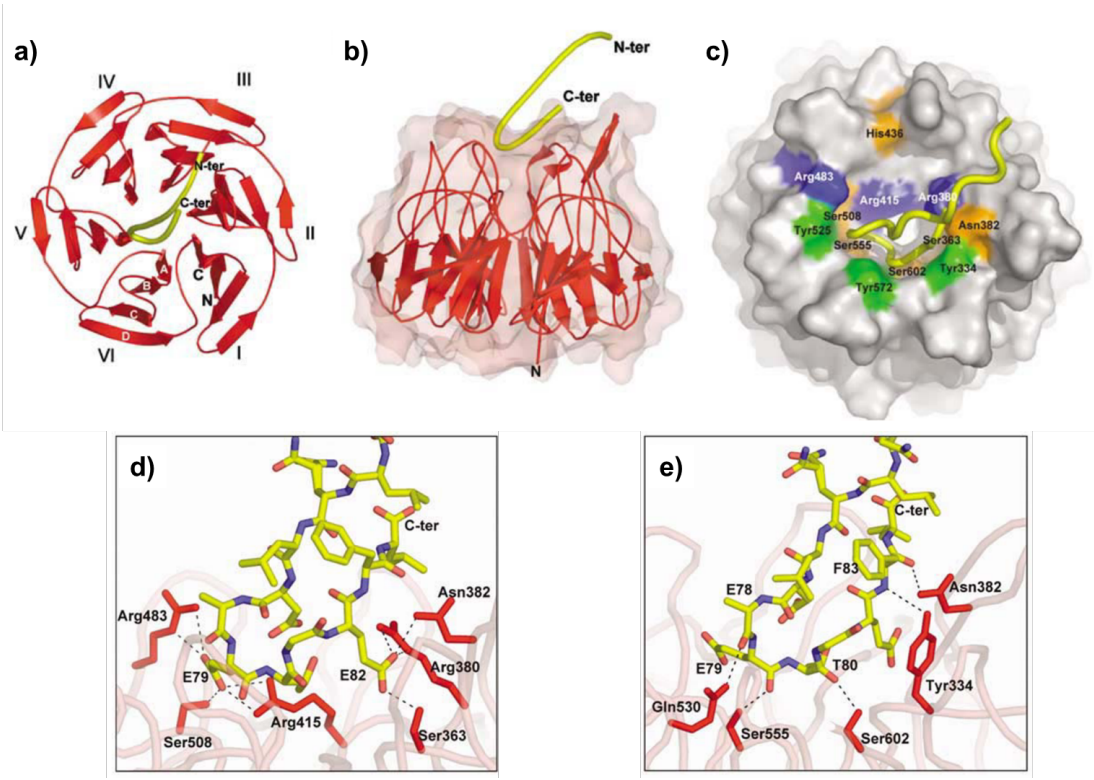


Figure 3.2 a) A ribbon diagram of the Kelch β-propeller (red) and bound Nrf2 peptide (yellow tube). The termini of the peptide are labelled N-ter and C-ter; those of the Kelch domain are labelled N and C. The six blades of the β-propeller are labelled I–VI and the four βl-strands found in each blade are labelled A–D (white font) on blade VI. b) Side view of the Kelch domain, with a surface representation of the β-propeller. c) A surface representation of the Kelch propeller (grey) and peptide (yellow tube). Selected residues are shown in blue (basic), orange (polar), and green (apolar). d) Contacts between the side chain atoms of the Nrf2 peptide and residues in the Kelch domain. e) Contacts between the backbone atoms of the peptide and residues of the Kelch domain.[68]

The ETGE and DLG motifs of Nrf2 can bind to the two Kelch domains of Keap1 homodimer respectively (Figure 3.1).[290] Under basal conditions, Keap1 self-associates *via* its BTB domain

to form homodimers. The two binding domains in Nrf2 (ETGE and DLG motif) are both indispensable for the Keap1-dependent repression on Nrf2. There are three models of mechanism of inhibition of the Keap1-Nrf2 PPI:[291,292] 1. In the Hinge-and-latch model, covalent modification of cysteine residues within the Keap1 IVR domain (especially Cys273 and Cys288) perturbs the oligomeric complex conformation and the low-affinity DLG motif dissociates from the Keap1 Kelch domain, thus disrupting the fixed arrangement of Nrf2 needed for ubiquitination;[279] 2. In the CuI3-dissociation model, covalent modification of cysteine residues in the BTB domain (especially Cys151) can decrease the association between Keap1 and Cul3 and thus encumber ubiquitination;[289,293] 3. In the conformation cycling model, cysteine modifications on Keap1 produces a dysfunctional closed state of the Keap1−Nrf2 complex in which both Neh2 domains are still bound to Keap1 but ubiquitination cannot take place.[294]

The interaction between Keap1 and Nrf2 was well investigated. L. J. Beamer, M. Hannink et al. determined the structure of the Kelch domain of Keap1 bound to a 16-mer peptide from Nrf2 peptide.[297] DxETGE motif is the principal Keap1 binding site in Nrf2. The binding pocket in Keap1 contains multiple charged and hydrophobic residues that contact the side chains of the two glutamate residues and the peptide backbone. The DxETGE motif contains a β-turn region stabilized by the aspartate and threonine residues. Threonine phosphorylation prevents binding of the Nrf2- derived peptide to Keap1 and phosphomimetic mutations enable Nrf2 to escape Keap1-mediated repression.

L. Hu *et al.* performed kinetic analyses of the interaction between Nrf2 residue 69 – 84 with different length (**Table 3.1**).[297] The minimal Nrf2 peptide sequence required for Keap1 binding is the 9-mer peptide LDEETGFEL and its binding affinity to Keap1 Kelch domain can be increased by 15x by removing the positive charge at the N-terminus with acetylation.

Table 3.1 Solution equilibrium dissociation constants ($K^{solution}_D$) of Nrf2 peptides as measured by a surface plasmon resonance-based solution competition assay.

Peptide sequence	**$K^{solution}_D$ (nM)**
H-EETGEFL-OH	>>1000
H-DEETGEFL-OH	>>1000
H-LDEETGEFL-OH	352
H-QLDEETGEFL-OH	27.3
H-LQLDEETGEFL-OH	31.3
H-QLQLDEETGEFL-OH	23.8
H-FAQLQLDEETGEFL-OH	22.5
H-AFFQLQLDEETGEFL-OH	23.9
Ac- LDEETGEFL-HH_2	21.4
H- LDEETGEFL-NH_2	355
Ac- LDEETGEFL-OH	23.1

3.1.2 Peptide inhibitors of the Keap1-Nrf2 interaction

3.1.2.1 Development of inhibitor screening techniques

Among high-throughput screening assays, fluorescence polarisation allows measurements of binding and dissociation of two molecules when one is small and fluorescently tagged. It has been widely used for diagnosis for more than 30 years and for drug screening more recently.[298] When a fluorescently labelled molecule is excited with plane polarized light, the emitted light has a degree of polarisation that is related to the molecular rotation. This phenomenon is called fluorescence polarisation. Large fluorescently-labelled molecules are relatively stationary or rotate slowly during excitation and lead to larger polarisation values of the emitted light in contrast to small fluorescently-labelled molecules which rotate fast and present low polarisation values of emitted light. For instance, when a fluorescein-labelled peptide binds to a large protein, the polarisation value is significantly increased. Thus, it is a useful technique for measuring equilibrium binding, nucleic acid hybridisation and enzymatic activity.[299]

The fluorescence polarisation (FP) assay has several advantages: it is homogeneous, and it does not need a separation step nor attachment to an immobilized phase. Polarisation values can be measured rapidly, repeatedly without destroying the samples. Fluorescence polarisation being independent on the concentration, concentrations as low picomolar concentrations can be used depending on the equipment's sensitivity.

Fluorescently tagged peptides as probes in fluorescence polarisation assays to screen for Keap1/Nrf2 inhibitors were developed. G. Wells *et al.* first reported a high-throughput fluorescence polarisation assay to screen Keap1/Nrf2 peptide inhibitors.[299] They investigated a series of fluorescein-labelled peptides based on high-affinity ETGE motif or on low-affinity DLG motif from the Neh2 domain of Nrf2 and they found that the FITC-β-DEETGEF-OH (FITC = fluorescein isothiocyanate, β = β-alanine.) showed an acceptable dissociation constant (95.7 nM) and large fluorescence polarisation signal, indicating the most suitable probe in the fluorescence polarisation assay due to larger signal-to-noise ratio. With the assay developed, 20 ETGE-containing peptides and 5 DLG-containing peptides were investigated. For the ETGE-containing peptides, the binding was more efficient as the length increased from 5-mer to 9-mer (LDEETGEFL) and the acetyl-capped N-terminus also helped to increase the binding ability.

L. Hu *et al.* also made efforts to optimize the fluorescently labelled peptide probes for fluorescence polarisation assay.[300] Since the binding of ETGE motif to Keap1 is much higher than that of DLG motif,[301] they tried different modifications on ETGE-containing peptides including peptide length, distance between the binding site and the fluorophore as well as different fluorophores and the 9-mer Nrf2 peptide FITC-LDEETGEFL-NH_2 had the best behaviour. They also ensured that the addition of DMSO (up to 10%) was tolerated for high-throughput applications. The resulted fluorescence polarisation assay was applied to screen 1810 compounds and 31 primary hits were identified.

Fluorescence or Förster resonance energy transfer (FRET) assays are another valuable method to study the Keap1/Nrf2 interaction and help to identify and design effective chemopreventive agents. FRET is a mechanism describing energy transfer between two light-sensitive molecules (chromophores). A donor chromophore, initially in its electronic excited state, may transfer energy to an acceptor chromophore through non-radiative dipole–dipole coupling. The efficiency depends on the overlap between the fluorescence emission spectra of the donor and the excitation spectrum of the acceptor. The energy transfer efficiency is a function of distance between the chromophores.[289] G. Wells et al. developed a steady-state FRET-based assay to identify inhibitors of the Keap1/Nrf2 protein-protein interaction.[302] The cyan fluorescent protein (CFP) was chosen as the donor fluorophore and was conjugated to an ETGE-containing 16-mer Nrf2 peptide [(6-His)-CFP-TEV-AFFAQLQLDEETGEFL] and the yellow fluorescent protein (YFP) was chosen as the acceptor fluorophore and was conjugated to the human Keap1 Kelch domain [(6-His)-YFP-TEV-(Kelch domain)]. When the single CFP-16mer peptide was excited at 435 nm, the CFP fluorophore emitted at 475 nm. When the two proteins are binding with each other, the two fluorophores are close enough (< 10 nm) for FRET to take place: when exciting the associated proteins at 435 nm, the YFP is excited and an emission centered at 527 nm occurs. The whole FRET system was stable over 24 hours.

3.1.2.2 Linear peptide inhibitors

Peptides and peptide mimics were developed and identified as Keap1-Nrf2 PPI inhibitors and helped building a detailed structure-activity relationship.

Since the molecular determinants of the Keap1/Nrf2 protein-protein interaction have been well investigated, there have been several linear peptide inhibitors developed for the Keap1/Nrf2 PPI. G. Wells *et al.* have made great efforts on the structure-activity relationships based on ETGE-containing peptides. Replacements of the different amino acids in the binding site influenced the binding activity towards Keap1 according to structure-activity relationship summarized in Figure 3.3.[303] They investigated a series of ETGE-containing peptides with modified C- or N- termini and reduced overall charge and among all of them, St-DPETGEL-OH peptide (St = stearic acid) showed potent activity *in vitro* (IC_{50} = 22 nM) compared to the St-DEETGEL-OH peptide (IC_{50} = 3710 nM). The replacement of glutamic acid to proline strongly enhanced the affinity towards Keap1. Furthermore, St-DPETGEL-OH peptide induced the expression of Nrf2 dependent gene products in cells.[300] They also developed a series of peptides with unnatural amino acids and the peptide Ac-D-Thp-ETGE-Cha-OH (Thp = thiazolidine-4-carboxylic acid, Cha = cyclohexylalanine) incorporating both a thioproline and a cyclohexylalanine residue showed improved binding ability (K_i = 13 nM).[74]

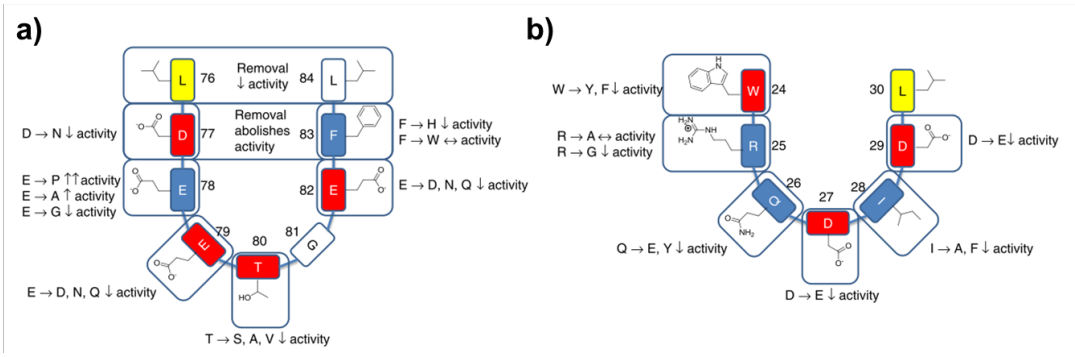


Figure 3.3.3 a) Summary of SAR data for the ETGE motif (residues 76–84). Point mutagenesis/ITC data from the mKelch–Nrf2 interaction is superimposed; b) Summary of SAR data for the DLG motif residues 24–30. red—amino acid change decreases binding (to <50% of control) to mKelch, yellow-intermediate decrease in binding (to between 25 and 50%), blue—no effect (to between 50 and 100% of control) or enhanced binding, white—not evaluated). [304]

B. Kuhlman developed a library of modified monobody-Keap1 complexes based on 10th type III domain of human fibronectin (FN3), an IgG-like β-sandwich protein that has three complementary determining regions (CDR)-like flexible loops (BC, DE and FG loops, Figure 3.4).[300] The Nrf2 peptide was grafted into the FG loop of FN3 and the FG and BC loops were optimized to enhance the affinity toward Keap1. These complexes are able to bind one loop of a monobody Keap1 and then use a neighboring loop in the monobody Keap1 to fill the rest of the pocket on Keap1.[305] Testing different sequences for BC and FG loops, they reported the first subnanomolar peptide inhibitor (RAYGYPS for BC loop and RDEETGEFHWP for FG loop) of the Keap1/Nrf2 interaction *in vitro*.

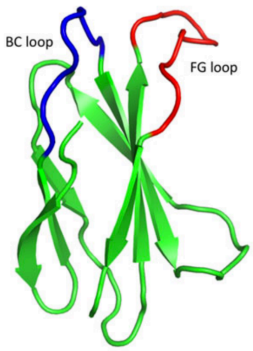


Figure 3.4 A crystal structure of 10th type III domain of human fibronectin with the FG loop coloured as red (used as the anchor loop in the design procedure) and the BC loop. [305]

ETGE motif based peptides were also conjugated to additional peptide sequences to improve the cell penetration of the resulting conjugate. For example, the HIV-1 targeting protein trans-activating transcriptional activator (TAT)[305] was conjugated with ETGE motif but the resulting TAT-DEETGE peptide showed no Nrf2 regulated gene expression in the injured brain of mice.[306] However, the introduction of a calpain cleavage site CAL between the TAT and the

DEETGE sequences (TAT-CAL-DEETGE) led to increased Nrf2 regulated gene expression and decreased blood-brain barrier (BBB) compromise. A similar peptide (DEETGE-CAL-TAT) was also developed which only showed effect on injured brain of mice.[72] Meanwhile, as a cell-penetrating peptide,[70] TAT was conjugated with a 14-mer ETGE peptide and the resulting peptide TAT-LQDEETGEFLPIQ was able to activate Nrf2 and its downstream target gene heme-oxygenase-1 (HO-1) in a dose-dependent manner in intact human THP-1 monocytes as well as inhibit the production of the pro-inflammatory cytokine TNF.[307]

A few Keap1/Nrf2 peptide inhibitors non-based on DLG or ETGE sequences were also described. S. Sogabe *et al.* has developed a new peptide inhibitor, which contains 4 amino acids (EWWW) indentified by phage-display screening.[71] L. Li, T. Zhang *et al.* have screened egg-derived peptides and they found out that DKK and DDW were able to exert antioxidant effects and protect cells against oxidative stress by inhibiting Keap1/Nrf2 interaction.[308] G. Wells *et al.* found that peptides derived from the nuclear protein prothymosin- α showed weak binding with Kelch domain while peptide derived from ubiquitin-binding protein sequestosome-1 (p62) showed similar binding affinity with DLG motif of Nrf2.[309]

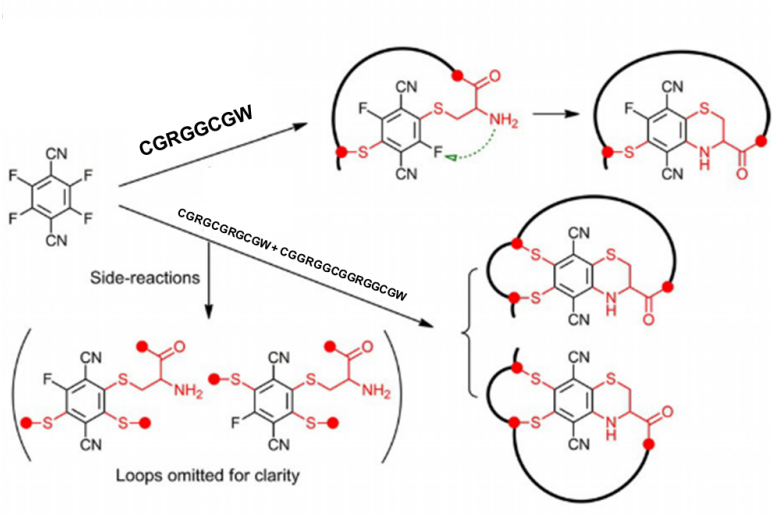
4.1.2.3 Cyclic peptide inhibitors

Without stabilisation by their protein domain, when they are free in solution and not interacting with their protein partner, peptides tend to lose their secondary structure and exist in a large/wide ensemble of conformational states in solution. These flexible structures result in relatively low target affinity upon binding due to the entropic effect.[300] In a nutshell, favorable events should lead, on the thermodynamical point of view, to a greater disorder. This is described with the equation: $\Delta G=\Delta H-T\Delta S$ ($-T\Delta S$ will be favorable if the reaction increases the disorder). If at the beginning the peptide is disorded, the binding procedure will be strongly disfavored since after binding the peptide is well organized. The pre-organisation of the peptide in a conformation appropriate to binding is a way to reduce this entropic penalty. This will favor ΔG of binding. Thus, it will be favorable if the conformation of the peptide is pre-organized. To improve the binding abilities, cyclic peptide inhibitors were developed for the Keap1/Nrf2 interaction.

Q.-D. You, Z.-Y. Jiang *et al.* have developed cyclic peptide inhibitors for the Keap1/Nrf2 interaction. Cyclized peptide (Ac-c[CLDPETGEYLC]-OH) using disulfide linkage with IC_{50} of 9.45 nM proved that the active conformation locking strategy is suitable for the design of Keap1/Nrf2 inhibitor.[75] Head-to-tail cyclic peptide c[GQLDPETGEFL] not only showed high potency in Nrf2 activation at the cellular level, but also exhibited effective anti-inflammatory effects in mouse RAW 264.7 cells.[310]

The cyclisation of CDEETEGC by introduction of a perfluoroarene, which is able to both stabilise the cyclic structure and enhance cell penetration, generated a peptide showing high affinity for Keap1 binding site with a K_i of 6.1 nM.[73] Recently, C. Wu *et al.* have developed a precisely regulated multiple cyclisation strategy to synthesise peptide macrocycles (Scheme 3.2).[311] This strategy relies on the efficient one-pot cyclisation of unprotected peptides with

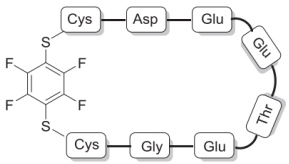
2,3,5,6-tetrafluoroterephthalonitrile (4F-2CN). They applied this peptide macrocycles as template for loop grafting to design inhibitors for Keap1-Nrf2 interaction and the best IC_{50} results is 208.6 nM with K_i of 149.1 nM using FP assay.



Scheme 3.2 Schematic illustration of the cyclisation of peptides with different lengths by 4F-2CN.[312]

Table 3.2 reported peptide sequences as Keap1-Nrf2 inhibitors.

Peptide sequences	**K_d (nM)**	**IC_{50} (nM)**	**K_i (nM)**	**Biophysical assay**	**Activity in cells**	**ref**
H-LDEETGEFL-OH	352	-	-	SPR	-	312
H-QLDEETGEFL-OH	27.3	-	-		-	
H-LQLDEETGEFL-OH	31.3	-	-		-	
H-QLQLDEETGEFL-OH	23.8	-	-		-	
H-FAQLQLDEETGEFL-OH	22.5	-	-		-	
H-AFFQLQLDEETGEFL-OH	23.9	-	-		-	
Ac-LDEETGEFL-NH_2	21.4	-	-		-	
Ac-LDEETGEFL-OH	23.1	-	-		-	
FITC-β-DEETGEF-OH	95.7	-	-	FP	-	298
FITC-β-LDEETGEFL-OH	53.8	-	-		-	
FAM-LDEETGEFLP-OH	51.0	-	-		-	
St-DPETGEL-OH	-	0.022	-	FP	-	300
Ac-DPETGE-Cha-OH	85	-	36	FP	-	74
Ac-D-Thp-ETGEL-OH	89	-	37	FP	-	

Ac-D-Thp-ETGE-Cha-OH	31	-	13	FP	-	
RAYGYPS-RDEETGEFHWP-FG loop	-	<3	-	ITC	-	304
	-	0.3	-	FP	-	
	-	0.3	-	SPR	-	
TAT-CAL-DEETGE	-	-	-	-	Increased gene expression	305
DEETGE-CAL-TAT	-	-	-	-	Sensitive to Ca^{2+} increase and allow injury-specific activation of Nrf2	72
TAT-LQDEETGEFLPIQ	-	-	-	-	inhibit the production of the pro-inflammatory cytokine TNF.	70
EWWW	-	30	-	TR-FRET	-	71
	77	-	-	SPR	-	
	10	-	-	ITC	-	
Ac-c[CLDPETGEYLC]-OH	-	9.45	-	FP	-	308
c[GQLDPETGEFL]	86.96	-	-	ITC	high potency in Nrf2 activation at the cellular level	310
	-	-	6.1	FP	-	73

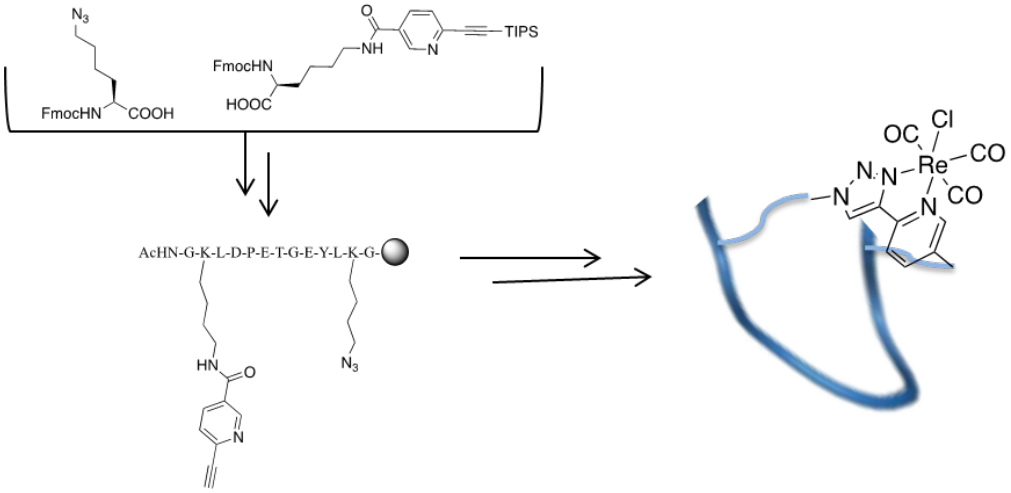
FITC = fluorescein isothiocyanate, β = β-alanine, Cha: cyclohexylalanine, Thp: thiazolidine-4-carboxylic acid, FAM: carboxyfluorescein.

3.1.3 Proposal of the project

As mentioned above, we aim at developing macrocyclic Nrf2 peptidomimetics with a Pyta rhenium tricarbonyl complex as macrocycle linker as Keap1/Nrf2 inhibitors. The cyclisation will be performed by a copper(I) catalysed azide-alkyne cycloaddition reaction CuAAC,

commonly used for peptides stapling and cyclisations, also generating the Pyta ligand, which will be further coordinated with rhenium (Scheme 3.3). The metal complex plays an important role, not only to stabilize the secondary structure of the metallopeptide (ß-turn) but also to act as a single core multimodal probe for imaging.

The sequence we chose here first is AcHN-GKLDPETGEYLKG-OH, in which the crucial 9mer LDPETGEYL was kept to ensure the protein-protein interaction. To avoid interrupting the ß-turn when interacting with Keap1, the unnatural amino acid was introduced bearing CuAAC reaction sites respectively at both end of this sequence. To avoid the steric hindrance, glycine was also added at both extremities. The acetyl capping was chosen to enhance the peptide affinity as mentioned above. Here, the synthesis of the unnatural amino acid was first investigated. Then, cyclisation and coordination on the resin were also explored.



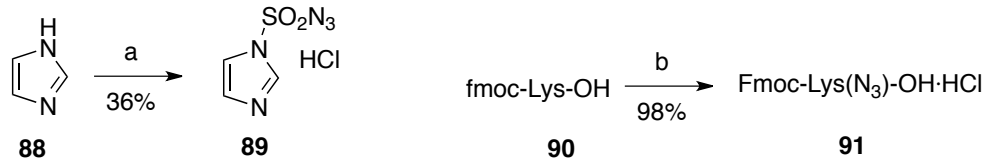
Scheme 3.3 Proposal of the project.

3.2 Synthesis of modified amino acids

To generate a Pyta ligand as macrocyclic linker, the introduction of two modified amino acids is needed: an azido-modified amino acid and 2-ethynylpyridyl-modified amino acid.

3.2.1 Synthesis of azido-modified amino acid

The preparation of azido-modified amino acids is well documented.[311] The azide group was introduced on Fmoc-Lys-OH by an azidation reaction using 1*H*-imidazole-1-sulfonyl azide hydrochloride **89** as azide reagent in high yield according to previous reports.[313–319] Sulfuryl chloride first reacted with sodium azide, followed by the addition of imidazole to offer desired compound **89** in moderate yield (36%). The moderate yield may be due to some loss in the recrystalisation step. Compound **89** is less explosive than other azide reagents, which makes this protocol safer for manipulation. Then Fmoc-lys-OH was reacted with compound **89** as azide transfer reagent and the modified amino acid **91** was obtained in high yield.



88 **89** **90** **91**

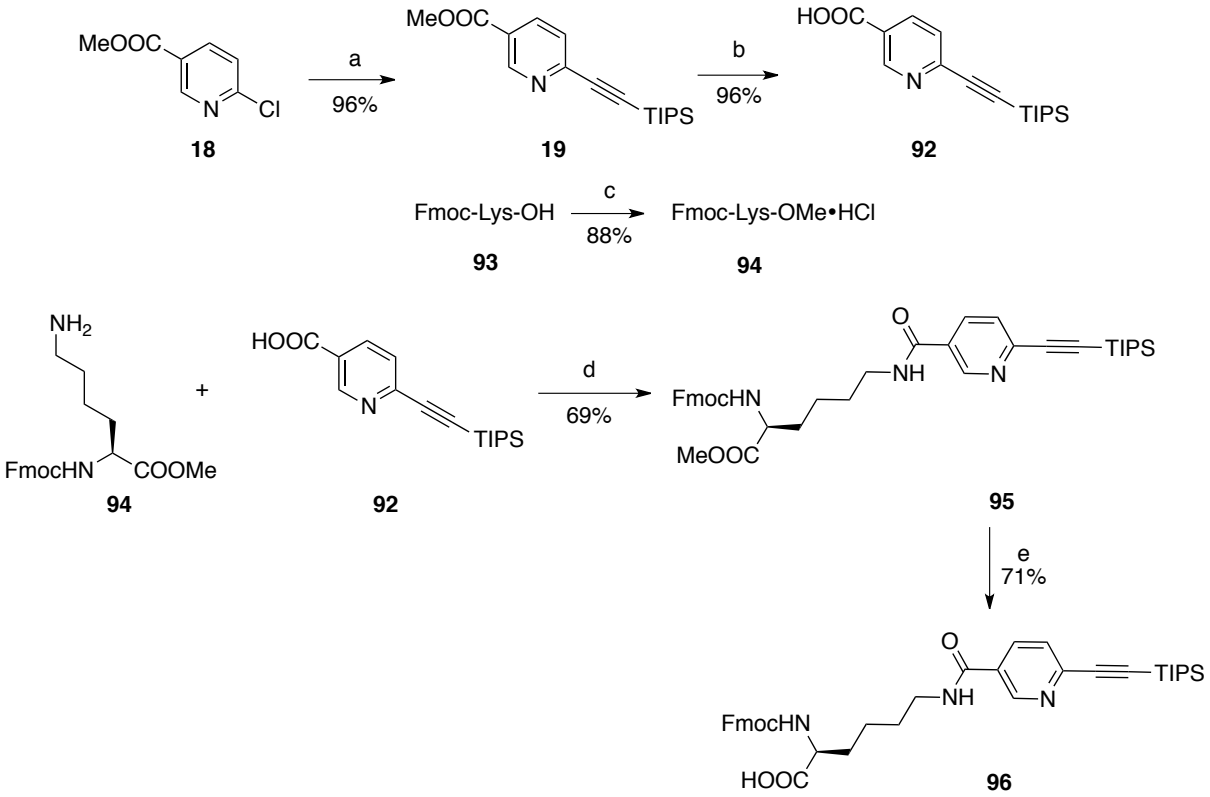
Scheme 3.4 Synthetic route for amino acid **91**. Conditions a: SO_2Cl_2 (1.0 equiv.), NaN_3 (1.0 equiv.), compound **88** (1.0 equiv.), acetonitrile (50 mL for 0.03 mol compound **88**), room temperature, overnight; b: compound **90** (1.0 equiv.), compound **89** (1.2 equiv.), $CuSO_4 \cdot 5H_2O$ (10 mol%), K_2CO_3 (2.7 equiv.), methanol (8 mL for 1.0 mmol compound **90**), room temperature, 12 hours.

3.2.2 Synthesis of 2-ethynylpyridyl-modified amino acid

3.2.2.1 Amidation approach

The introduction of an aliphatic alkynyl motif into an amino acid side chain has been well documented.[319] However, the introduction of a 2-ethynylpyridyl motif into an amino acid side chain has never been described. There are several ways to introduce a 2-ethynylpyridyl moiety on the side chain of an amino acid. One of the easiest ways is by using the side chain groups of natural amino acids as modification site. Here we used the L-lysine with an amino group on the side chain to introduce a 2-ethynylpyridyl moiety (Scheme 3.5). Compound **19** was synthesized using the same procedure as in chapter 1 (Page 25). Ester hydrolysis under basic conditions using lithium hydroxide afforded compound **92** in high yield (95%) without purification by column chromatography. The methyl ester of the Fmoc-protected L-lysine (Fmoc-Lys-OMe) **94** was used as the precursor **93**. The amidation reaction was conducted with compound **92** and compound **94**, using HBTU as coupling agent to give the modified amino acid **95** in moderate yield (69%) after column chromatography on silica gel. The methyl ester hydrolysis reaction of compound **95** is tricky because of the lability of the Fmoc protecting group under basic conditions. Calcium dichloride has been found to dramatically increase the lifetime of the Fmoc protecting group in alkaline *i*PrOH-water while having little effect on the hydrolytic processes.[316,320,329,330,321–328] We thus employed such conditions to generate **96**: sodium hydroxide in the presence of an excess of calcium dichloride. A small excess of sodium hydroxide dramatically decreased the yield. Thus, the use of one equivalent of sodium hydroxide need to be strictly controlled. The reaction was monitored using TLC and, after completion of the compound **95**, the solution was neutralized to pH ca. 5.0. The product **96** was further purified using preparative HPLC to afford the desired compound with a 71% yield. In this amidation strategy, the chiral center originates from the natural amino acid and is kept during the amidation and hydrolysis steps, with no need for chiral resolution. Meanwhile, by using different natural amino acid, it is easy to modulate and optimize the length. However, the introduction of an additional amide bond may also be a weakness point because the amide bond may be hydrolyzed. But the peptide will be sterically constrained and thus we hope it won't be

recognized by protease. It may also affect the conformation adopted by the macrocyclic linker and the photophysical properties of the corresponding complex.



Scheme 3.5 Synthetic route for compound **96.** Condition a: TIPSA (1.2 equiv.), $Pd(PPh_3)_2Cl_2$ (2 mol%), CuI (1 mol%), THF, Et_3N, room temperature, overnight; b: $LiOH{\cdot}H_2O$ (1.1 equiv.), THF, water, room temperature, 1 hour; c: SO_2Cl_2 (3.8 equiv.), methanol, room temperature, 2 hours; d: compound **94** (1.1 equiv.), compound **92** (1.0 equiv.), HBTU (1.2 equiv.), DIEA (3.0 equiv.), DMF, room temperature, overnight; d: $CaCl_2$ (20.0 equiv.), NaOH (1.0 equiv.), water, *i*-PrOH, 50 °C, 4 hours.

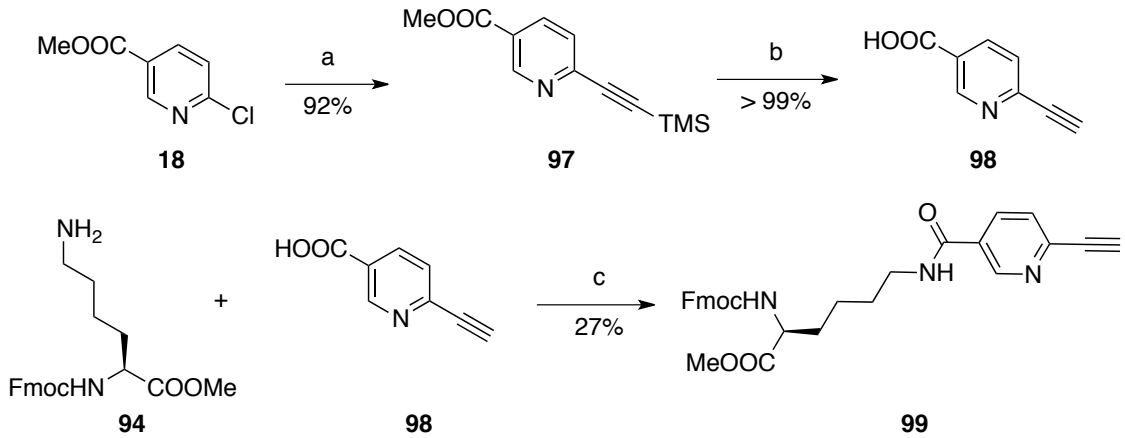
To confirm if the 2-ethynylpyridyl moiety without protecting group is stable under solid phase peptide synthesis and cleavage conditions, compound **98** was designed as a model compound. Compound **98** could not be obtained by a TIPS deprotection from intermediate **95** or **96** because of the lability of the Fmoc protecting group under treatment by TBAF.[331] The silyl protecting group has to be removed before the amidation step. We chose here the trimethylsilyl (TMS) protecting group instead of TIPS to synthesize the 2-ethynyl-5-hydroxycarbonylpyridine intermediate as a single hydrolysis in basic conditions would simultaneously hydrolyse the methyl ester and remove this silyl group. Thus, the synthesis of compound **99** (Scheme 3.6) started from commercially available compound **18** with a classical Sonogashira cross coupling reaction except for the use of trimethylsilylacetylene, in high yield (92%). Deprotection of both the TMS protecting group and the methyl ester using lithium hydroxide afforded precursor **98** in high yield (>99%) and good purity. The amidation reaction between compound **94** and **98** with HBTU as coupling agent offered the desired compound **99** in low yield (27%).

We then investigated the stability of amino acid **99** in key solid phase peptide synthesis (SPPS) reactions: Fmoc deprotection, capping with acetyl group and cleavage from the resin. We dissolved compound **99** (ca. 10 mg) in 0.5 mL of prepared solutions **1 – 3** respectively, evaporated and then directly monitored using ^{1}H NMR in acetone-d_3 (Figure 3.5):

Solution 1: 20% piperidine in NMP, stirred for 15 min (condition for deprotection of the Fmoc group);

Solution 2: 15% acetic anhydride in dichloromethane, stirred for 30 min (condition for capping with acetyl group);

Solution 3: 95 % trifluoroacetic acid, 2.5% water and 2.5% triisopropylsilane, stirred for 3 hours (condition for cleavage from the resin).



Scheme 3.6 Synthetic route for compound **99** Condition a: TMSA (1.2 equiv.), $Pd(PPh_3)_2Cl_2$ (2 mol%), CuI (1 mol%), THF, Et_3N, room temperature, overnight, start from 1 g; b: $LiOH{\cdot}H_2O$ (3,0 equiv.), THF, H_2O, room temperature, 10 minutes; c: HBTU (1.2 equiv.), DIEA (3,0 equiv.), DMF, room temperature, 2 days.

The ^{1}H NMR obtained after stirring compound **99** with **solution 1** (Figure 3.5-a) showed a shift of the proton signals of the Fmoc group, implying the removal of Fmoc, as expected. The proton for C=C may be overlapped with the board band near 6 ppm. The change of the other peaks showed that the compound is not stable in this condition.

The ^{1}H NMR obtained after stirring compound **99** with **solution 2** (Figure 3.5-b) showed similar proton signals as before stirring (Figure 3.5-d), indicating that compound **98** is stable under these conditions.

The ^{1}H NMR obtained after stirring compound **99** with **solution 3** (Figure 4.2-c) showed disappearance of ^{1}H signals and the appearance of the unstructured broad bands, indicating the total degradation of the compound.

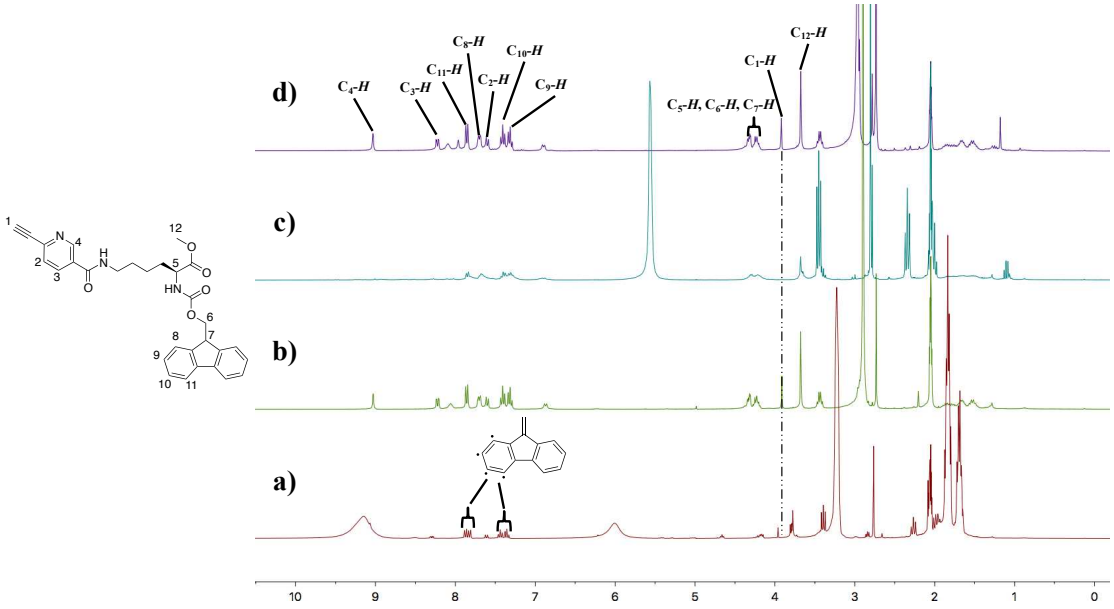
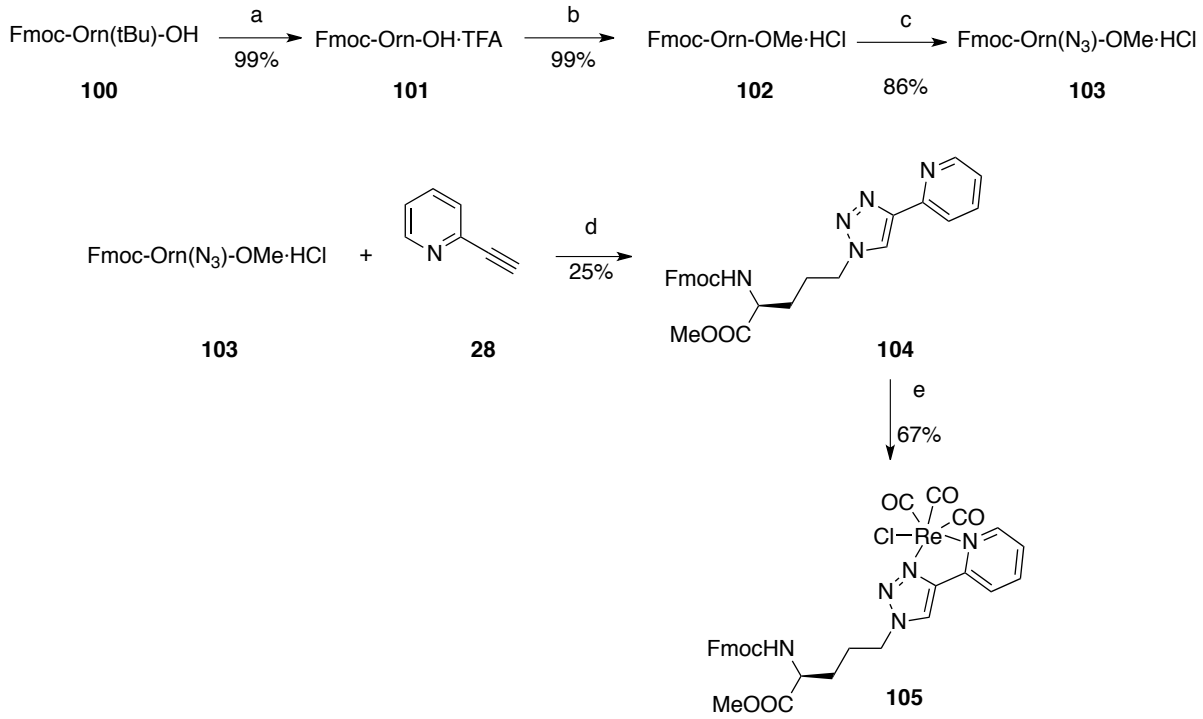


Figure 3.5 ^{1}H NMR of compound 99 in acetone-d_3 (d) and after stirring with solution 1 (a), solution 2 (b), and solution 3 (c).

To conclude, the compound bearing a terminal alkyne seems not to be stable under Fmoc deprotection conditions during the solid phase peptide synthesis procedure. This suggests that it is better to keep the triisopropylsilyl protecting group on the terminal alkyne during the solid phase peptide synthesis before the completion of peptide synthesis and it may be more convenient to conduct the CuAAC reaction on resin before the cleavage step.
Finally, we synthesized ligand **104** and the corresponding complex **105** to incorporate in the sequence of the control linear peptide to control the impact of cyclisation on affinity. The preliminary attempt of the CuAAC reaction between compound **94** and **28** was not successful. However, the CuAAC reaction between compound **103** and **28** occurred. Rigorously, lysine should have been used. The usage of ornithine instead of lysine is not expected to have any changes on photophysical properties. Meanwhile, this amino acid is also interesting to study incorporation of Re(Pyta) complex in peptides by SPPS.

The synthesis started from commercially available compound Fmoc-Orn(Boc)-OH **100**. The Boc deprotection using TFA and the following esterification ($SOCl_2$, MeOH) afforded compound **102** in high yield. The azide was introduced on compound **102** using azidation reaction described above to form the resulting compound **103**. Then the classical CuAAC condition was employed except that the mixed solvents of *t*BuOH, water and MeCN were used and this step gave the compound **104** in low yield (25%). The low yield may be due to the trapping of Cu(I) by amino acid which sometimes happens in bio-conjugated system thus decrease the catalytic activity of Cu(I) and reduce the progression of the reacion.[332,333] Meanwhile, the copper ion may also trap the final compound as a complex formation, which can be avoid by using a washing step with saturated EDTA. The yield may be increased using other ligand such as tris(3-hydroxypropyltriazolyl-methyl)amine (THPTA) to maintain active

Cu(I) species.[334] Then the classical complexation condition was conducted to produce the final complex **105** in moderate yield (67%).



Scheme 3.7 Synthetic route for compound **105**. Condition a: TFA, DCM, room temperature, 30 minutes; b: $SOCl_2$, MeOH, room temperature, 4 hours; c: compound **102** (1.2 equiv.), $CuSO_4 \cdot 5H_2O$ (10 mol%), K_2CO_3 (2.7 equiv.), methanol, room temperature, 12 hours; d: 2-ethynylpryidine (1.0 equiv.), $CuSO_4 \cdot 5H_2O$ (10 mol%), Sodium ascorbate (100 mol%), *t*BuOH, water, MeCN, room temperature, 6 hours; e: $Re(CO)_5Cl$ (1.0 equiv.), toluene, 120 °C, 4 hours.

The photophysical properties of complex **105** were investigated in acetonitrile at a concentration of 20 μM at 298 K (Figure 3.6) and complex **3r** (*fac*-[Re(Pyta)$(CO)_3$Cl]) was taken as reference. Complex **105** showed absorption centered at 333 nm, which is at the same position as that of complex **3r**. This band is assigned to a MLCT character. The absorption intensity of complex **105** is slightly stronger than that of complex **3r**. Complex **105** also showed unstructured absorption at higher energy waves, ca. 280 nm and it is much more intense than that of complex **3r**. This band is a mixture of intraligand charge transfer that has been discussed in chapter 1 and the absorption of Fmoc group. Complex **105** exhibited an emission centred at ~530 nm, similar to that of complex **3r**. The emission intensity of complex **105** is slightly weaker than that of complex **3r**. Both complexes showed similar absorption and emission behaviors.

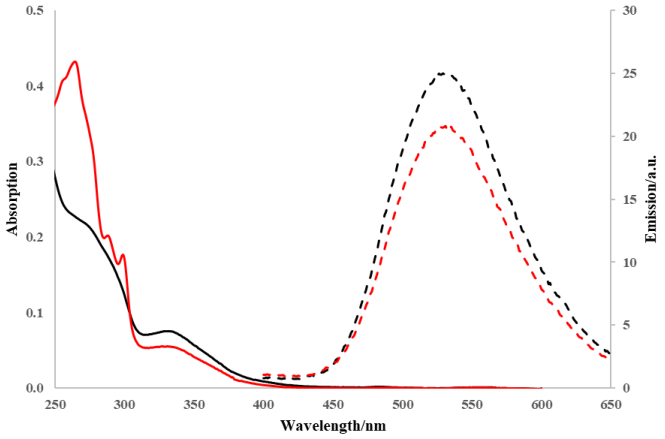
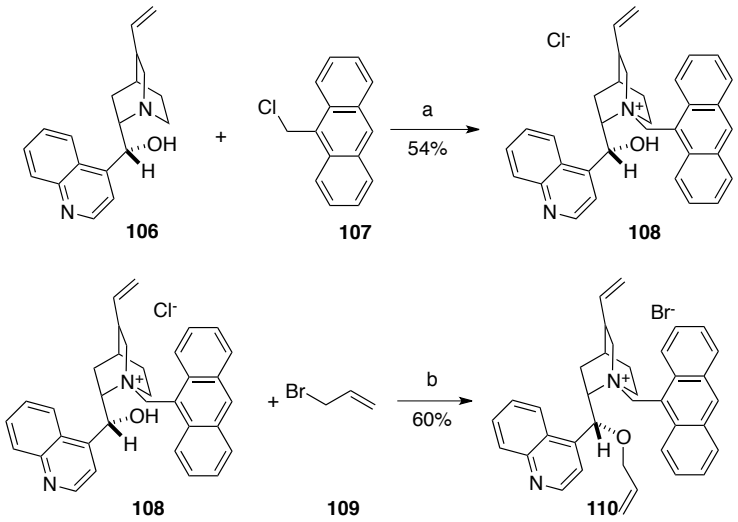


Figure 3.3.6 Absorption (solid line) and emission (dash line) spectra of complexes **3r** (*fac*-[Re(Pyta)(CO)$_3$Cl], black line) and **105** (red line).

3.2.2.2 Other approaches

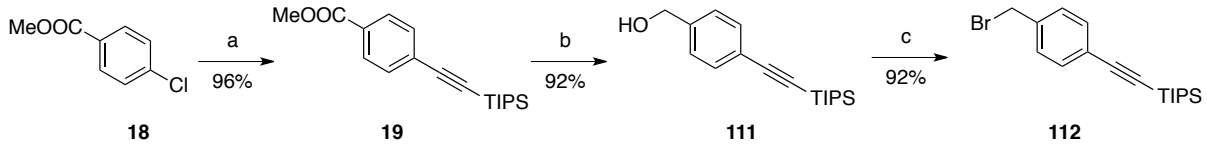
In parallel to the amidation approach, we explored other synthetic routes to introduce the 2-ethynylpyridyl moiety on an amino acid side chain. Among the various available methodological strategies for the synthesis of unnatural L-amino acids,[334] the enantioselective alkylation of glycine imines using asymmetric phase-transfer catalyst (PTC) derived from cinchona alkaloids, first reported by O'Donnell,[335–341] is promising to introduce desired functional groups onto α-amino acids scaffolds.[342]



Scheme 3.8 Synthetic route for the phase-transfer catalyst **112**. Condition a: compound **106** (1.0 equiv.), compound **107** (1.05 equiv.), toluene, 130 ºC, 24 hours; b: compound **108** (1.0 equiv.), compound **109** (3.0 equiv.), 50% aqueous NaOH (5.0 equiv.), DCM, room temperature, 4 hours.

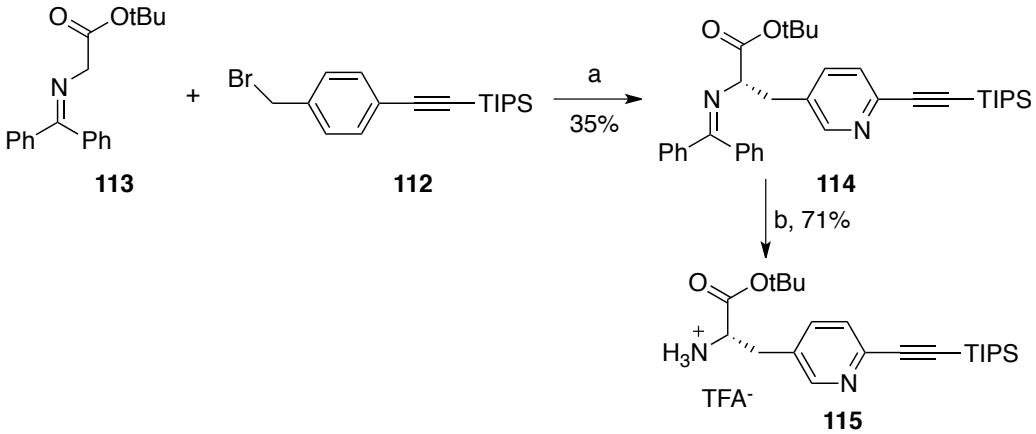
Catalyst **110** was chosen as PTC because the structure[343] as well as the mechanism of the catalysing procedure[344] have been well studied. The synthesis of the phase-transfer catalyst **110** (Scheme 3.8) started from the commercially available cinchona alkaloid **106**, with the

alkylation with 9-(chloromethyl)anthracene **107** in moderate yield (54%), followed by the etherification by nucleophilic substitution of 3-bromoprop-1-ene **109** in moderate yield (60%). The synthesis of 2-ethynyl-5-(bromomethyl)pyridine **112** was also developed (Scheme 3.9). Compound **19** was synthesized as described before (chapter 1, pages 25). Ester reduction of compound **18** using lithium aluminium hydride (LAH, 1M in tetrahydrofuran) in THF afforded the desired alcohol in high yield (92%). Bromination using N-bromosuccinimide (NBS) and triphenylphosphine[345] gave the brominated precursor **112** in high yield (>99%). However, it must be noted that this precursor is not stable and must be prepared and isolated freshly before its use in the phase transfer catalyzed reaction.



Scheme 3.9 Synthetic route for the precursor **112**. Condition a: TIPSA (1.2 equiv.), $Pd(PPh_3)_2Cl_2$ (2 mol%), CuI (1 mol%), THF, Et_3N, room temperature, overnight; b: LAH (1M in THF, 1.1 equiv.), THF, 0 °C ~ room temperature, 2 hours; c: PPh_3 (3.8 equiv.), NBS (3.8 equiv.), THF, room temperature, 24 hours.

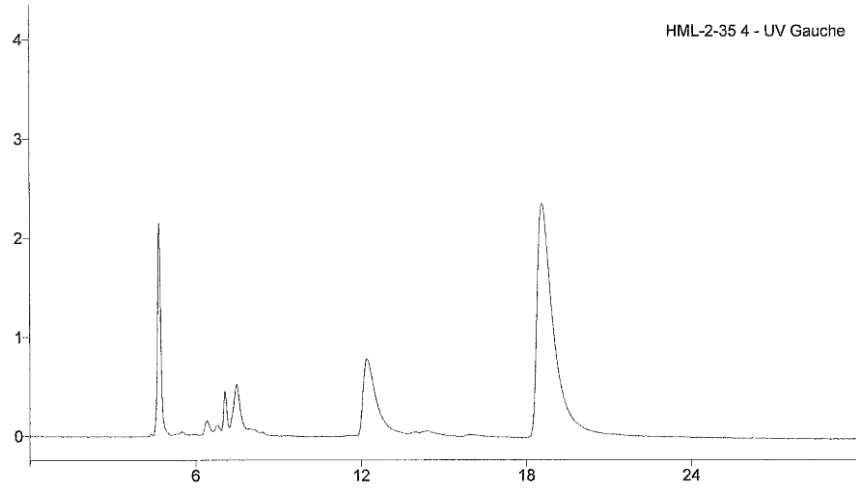
Finally, with the phase-transfer catalyst **110** and the precursor **112** in hand, the alkylation of compound **113** was conducted at -78 °C in the presence of a base in the conditions described[346] (Scheme 3.10). Compound **114** was successfully obtained in acceptable yield (35%) although a high purity could not be achieved by purification by column chromatography on silica gel. Then the hydrolysis of the imine under acidic conditions afforded the desired non-natural amino acid **115** in 71% yield after purification by preparative HPLC.



Scheme 3.10 Synthetic route for the non-natural amino acid **115**. Condition a: **113** (1.0 equiv.), **110** (0.1 equiv.), $CsOH \cdot H_2O$ (10.0 equiv.), **112** (1.5 equiv.) DCM, -78 °C, 7 hours; b: 1M HCl, diethyl ether, room temperature, overnight.

Chiral HPLC indicated an ratio of the two isomers of 21:79 for compound **115** (Figure 3.7), which is not satisfying. This may be due to the lack of precise temperature control during the

alkylation reaction without proper cryostat. The stability of the precursor **114** is another issue for gram scale synthesis and storage required for the modified amino acid.
Other strategies, such as the diastereoselective alkylation of a chiral Ni(II) complex for the synthesis of amino acids,[347] or the enantioselective reduction of C=C bonds[348,349] are also worth exploring.



Résultats d'intégration

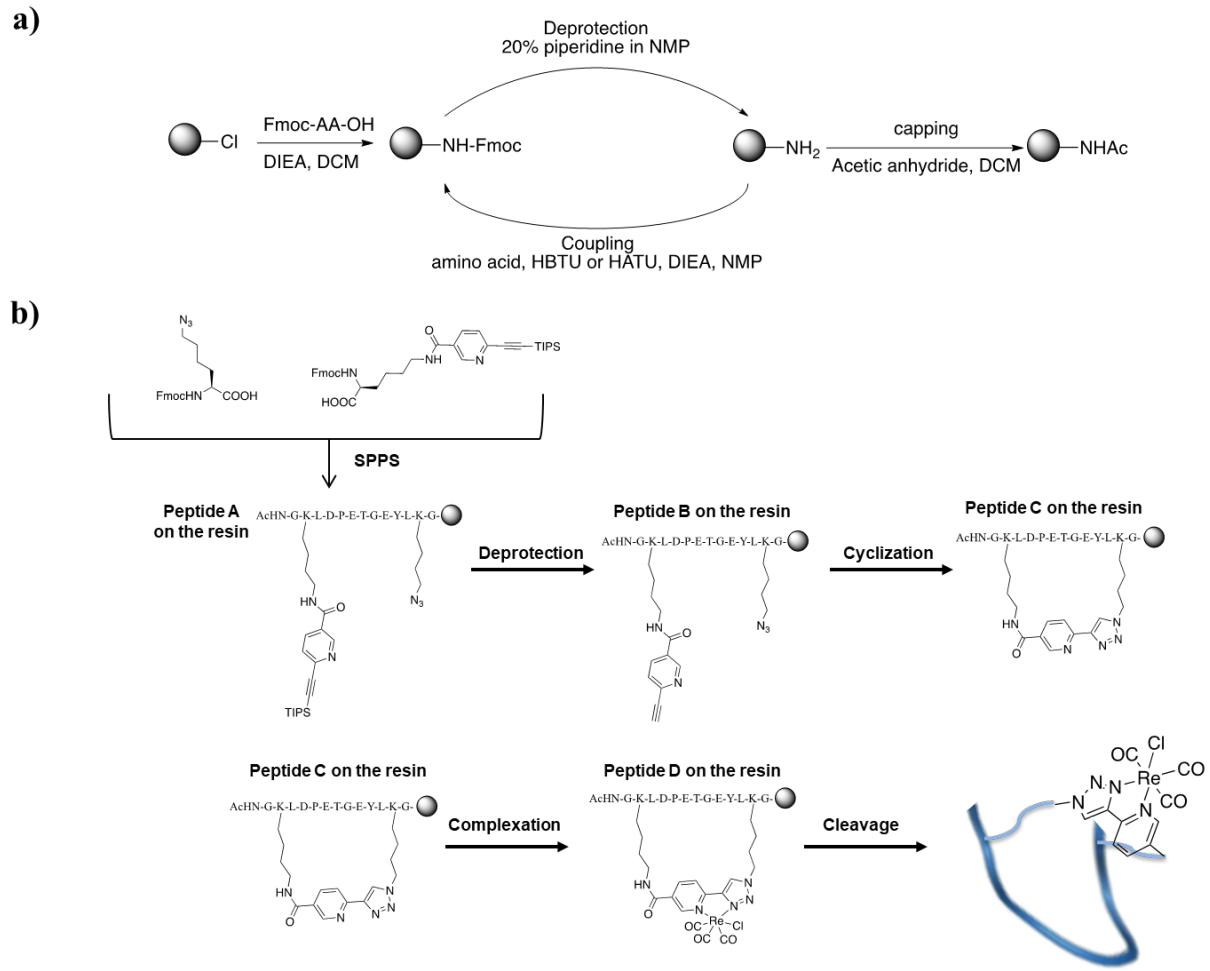
#	Nom du pic	Tr.	Aire	% Aire	Asymétrie (AIA)	Largeur (50%)	Plateaux (EP)
1		12,22	26,07	20,81	3,24	0,48	3596,41
2		18,58	99,22	79,19	3,07	0,59	5584,63
SOMME			125,28	100,00			

Figure 3.7 Chiral HPLC results for compound **115**.

3.3 Peptide mimics synthesis

3.3.1 Synthesis of linear peptides

The sequence (Ac-G-K(TIPS)-L-D-P-E-T-G-E-Y-L-K(N3)-G-OH) described in Scheme 3.11 was chosen in a first attempt. The sequence DPETGEYL was chosen due its high affinity for Keap1[350] and two glycine residues were added at the extremities to avoid the steric hindrance. The peptide was synthesized by solid phase peptide synthesis (SPPS) with Fmoc strategy (Scheme 3.11-a). Chlorotrityl chloride (CTC) resin was chosen because the peptide could be cleaved in mild acidic conditions keeping the protecting groups on the side chains. The first amino acid glycine was coupled using the Fmoc-protected amino acid (2 equiv.) and N,N-diisopropylethylamine (DIEA, 4 equiv.) in dichloromethane for 1 hour.



Scheme 3.11 Solid phase peptide synthesis procedure (a) and procedure for peptide mimics (b).

The coupling conditions were: N,N-diisopropylethylamine (DIEA, 6 equiv.), Fmoc-protected amino acid (3 equiv.), HBTU (3 equiv.) (HATU for Fmoc-Pro-OH) in NMP (1.0 mL for 200 mg resin) for 2 hours. The Fmoc group was deprotected using a 20% piperidine solution in NMP (1 × 1 min, 2 × 15 min). The N-terminal acetyl capping was carried out by treating the resin swelled in dichloromethane with acetic anhydride (10 equiv.) for 2 hours. All the coupling and deprotection steps were monitored by classical Kaiser test. For the deprotection after the coupling of proline, the Kaiser test showed red beads because the secondary amine on proline reacted with ninhydrin to produce 3-hydroxy-2-(pyrrolidin-1-yl)-1*H*-inden-1-one instead of blue compound 2-((3-hydroxy-1-oxo-1*H*-inden-2-yl)imino)-1*H*-indene-1,3(2*H*)-dione. The Kaiser test results of the coupling reactions of the two amino acids after Fmoc-Pro-OH showed a change from red to brown colour, indicating the completion of the coupling.

The loading of the resin, a very important parameter for on resin intramolecular cyclisation, was determined after the coupling of the first amino acid according to the previous literature[74] using the UV-Vis absorption of the Fmoc group. Here we prepared several batches of peptide

on resin with different loading abilities. It will be discussed along with the cyclisation conditions (synthesis of peptide **C**).

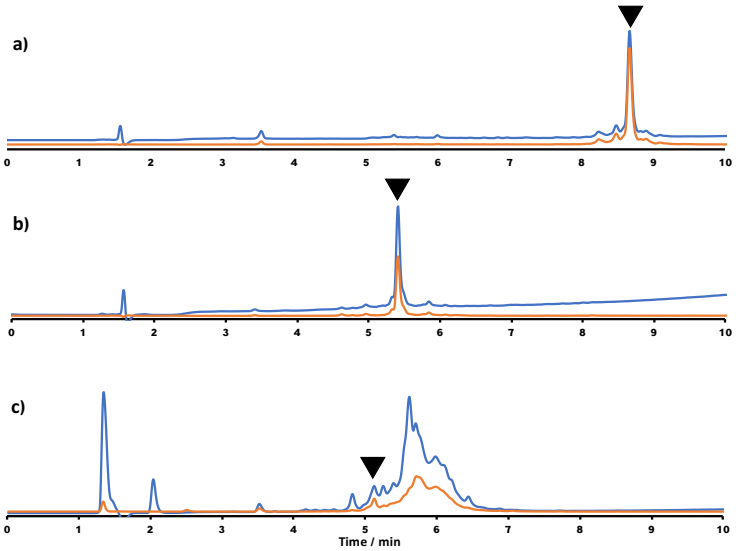


Figure 3.8 Analytic HPLC profiles for peptide **A** (a), **B** (b) and **C** (c) with absorption at 220 nm (blue line) and 280 nm (orange line), the peaks for corresponding product is marked with black triangle.

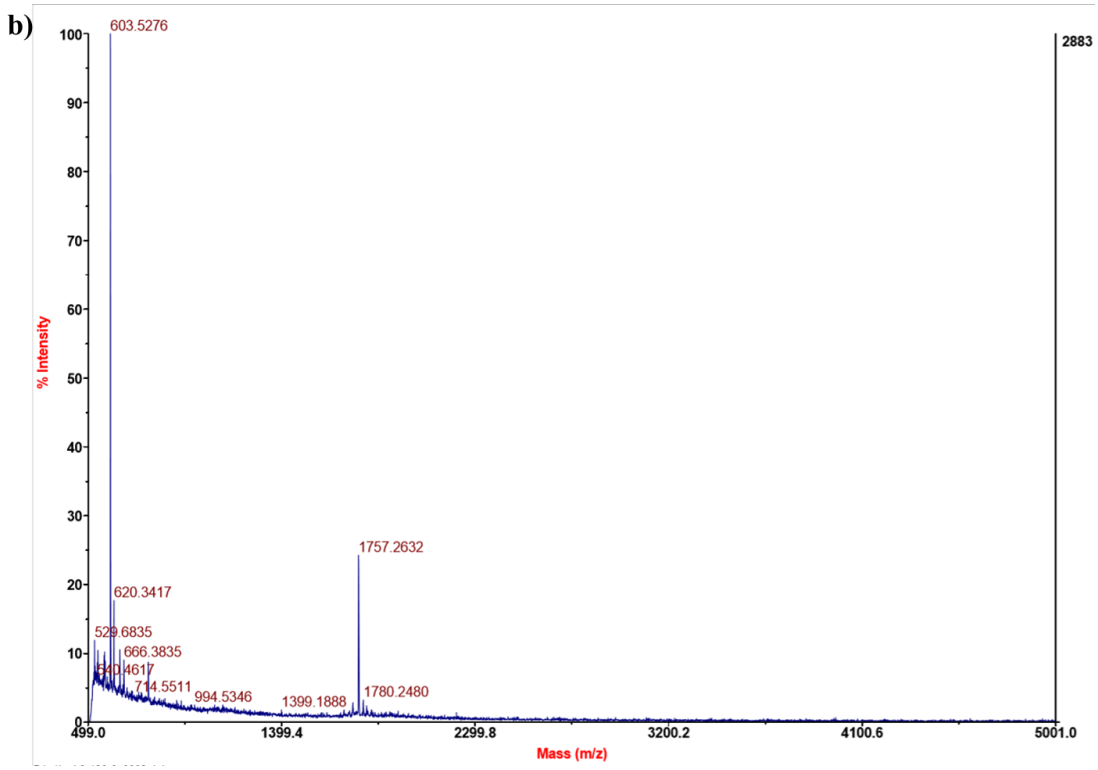


Figure 3.9 MALDI-ToF-MS spectrum of peptide **A**.

The linear peptide **A** was analyzed by analytical reversed-phase HPLC (Figure 3.8-a) and characterized by MALDI-ToF mass spectrometry after micro-cleavage (95% TFA, 2.5% water, 2.5% TIPS, 10 minutes) from the resin. The retention time was 8.67 minutes (5 to 100%

acetonitrile over 10 minutes) with 80% purity without further purification. The MALDI-ToF MS (Figure 3.9) showed a peak at m/z 1757.2632, confirming the presence of the right peptide. The deprotection of the TIPS group was performed on the resin, using a 0.1 M TBAF solution in DMF for 30 minutes to give the peptide **B** on the resin. The peptide **B** was also analysed by analytical reversed-phase HPLC (Figure 3.8-b) and characterized by MALDI-ToF mass spectrometry after a quick micro-cleavage (95% TFA, 2.5% water, 2.5% TIPS, 5 minutes) from the resin to limit the degradation of the ethynylpyridyl motif in these cleavage conditions. The retention time for peptide **B** (Figure 3.8-b) was 5.42 minutes (5 to 100% acetonitrile over 10 minutes) with a 76% purity without further purification. This is consistent with a more polar character for **B** compared to **A** in accordance with the removal of the non-polar TIPS group. The MALDI-ToF MS results (Figure 3.10) confirmed the existence of the expected peptide. Cyclisation attempts were performed on freshly deprotected resin batches.

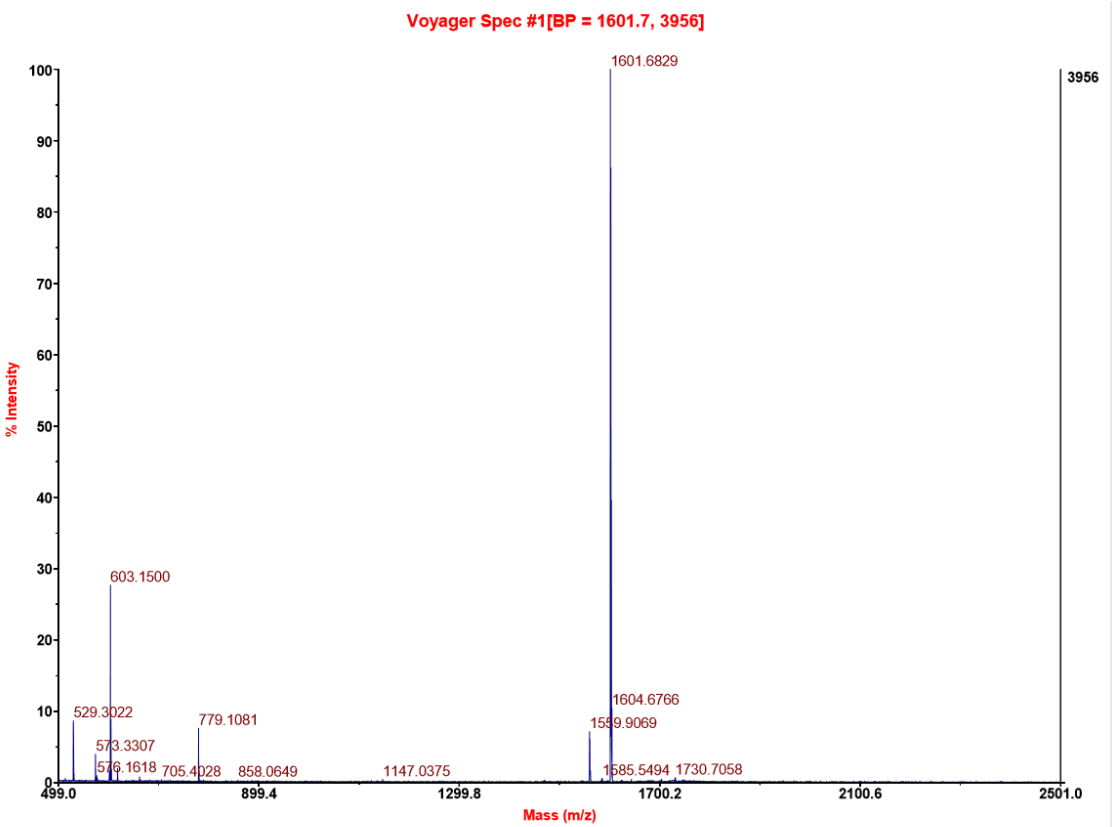


Figure 3.10 MALDI-ToF-MS spectrum of peptide **B**.

3.3.2 Synthesis of the cyclic peptide

Intramolecular cyclisations require diluted concentrations. An initial medium loading of the resin of 0.47 mmol/g was chosen to perform preliminary studies. Different conditions were screened:

Condition **1**: Sodium ascorbate (4.0 equiv.), copper(II) sulphate pentahydrate (1.0 equiv.), N,N-diisopropylethylamine (10.0 equiv.), DMF, room temperature;

Condition **2**: Copper(I) bromide (1.0 equiv.), sodium ascorbate (4.0 equiv.), N,N-diisopropylethylamine (10.0 equiv.), 2,6-lutidine (10.0 equiv.), DMF, room temperature.
A micro-cleavage was performed after reaction and analytical reversed-phase HPLC was used to monitor the reaction. According to the HPLC results, there was almost no conversion under condition **1**. The HPLC profile under condition **2** (Figure 3.8-c) showed the disappearance of the peak corresponding to peptide **B**, accompanied by the appearance of several small peaks and a broad unstructured peak at a retention time of ca. 6 minutes. Several fractions from analytical reversed-phase HPLC were collected for MALDI-ToF mass spectrometry. A fraction with the expected mass, which has a slightly shorter retention time on HPLC than peptide **B**, was identified. The faster elution from the column of the cyclized species may arise from its structuration in solution.
Meanwhile, since the azido group showed specific IR absorption at around 2095 cm^{-1}, we explored IR spectroscopy as a convenient way to monitor the cyclisation reaction on resin. The beads were directly used for IR experiments after washing with dichloromethane (3 times). Taking beads at 3 and 5 hours, we monitored the reaction under conditions 2 (Figure 3.11). After 3 hours, the small signal at 2095 cm^{-1} decreased. After 5 hours, this signal disappeared totally, indicating the complete conversion of the reaction.

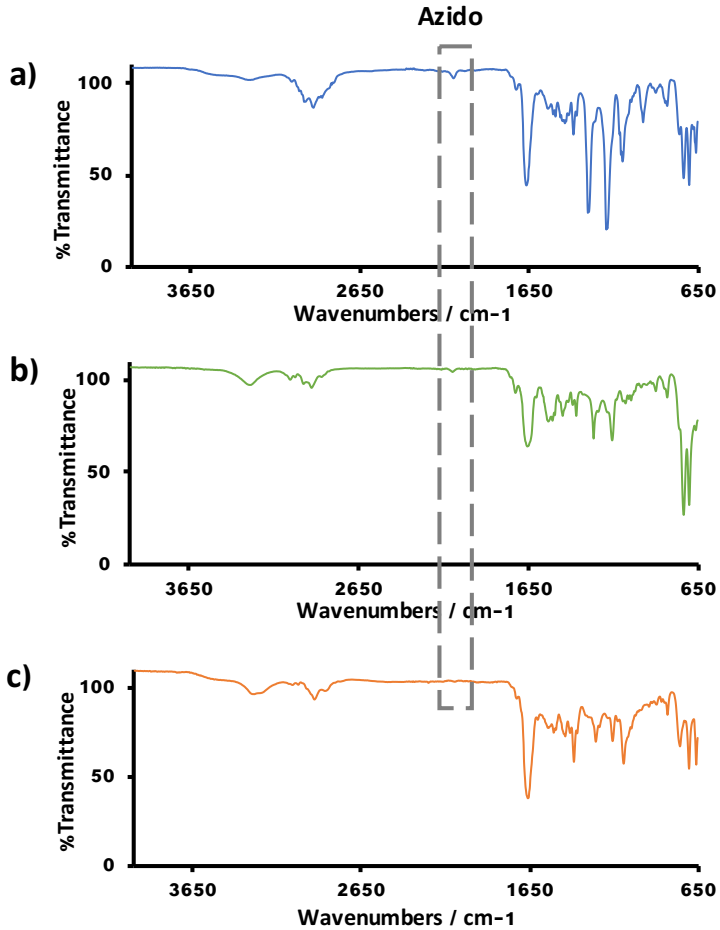


Figure 3.11 IR spectra for cyclisation under condition **2** after stated time. a) cleaved peptide B; b) after 3 hours; c) after 5 hours.

To further confirm the formation of the cyclic peptide, tandem MS technique was used (Figure 3.12). Tandem MS (or MS/MS, MSn)[351] is a technique used to break down selected ions (precursor ions) into fragments (product ions). The fragments reveal aspects of the chemical structure of the precursor ion. The analysis of the tandem MS results (Table 3.3) and the corresponding fragments identification, confirmed the structure of this isolated fraction as cyclic peptide **C**.

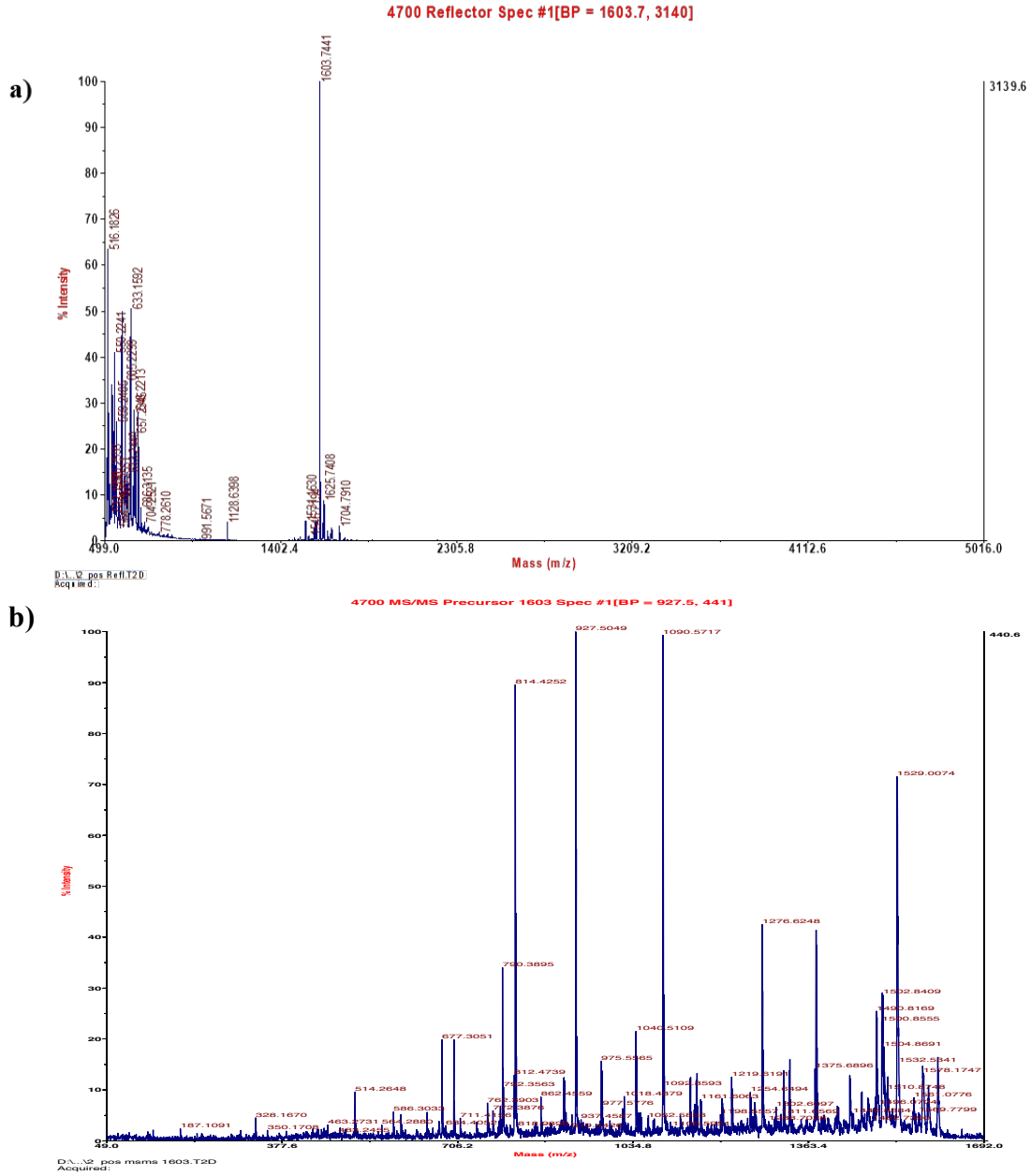
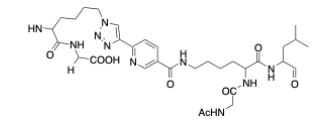
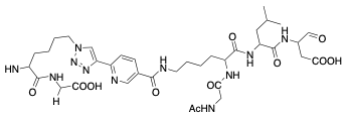
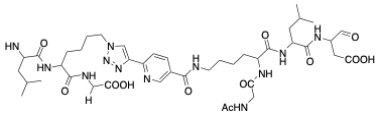
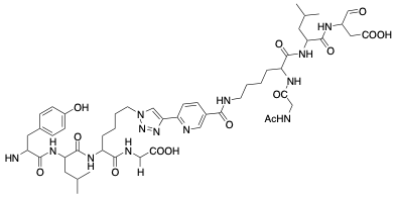
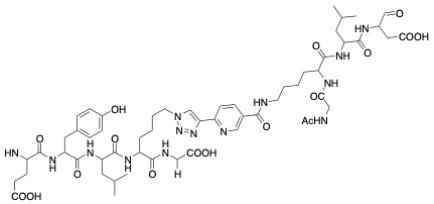
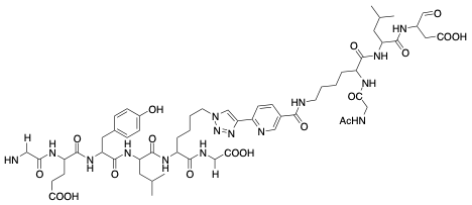
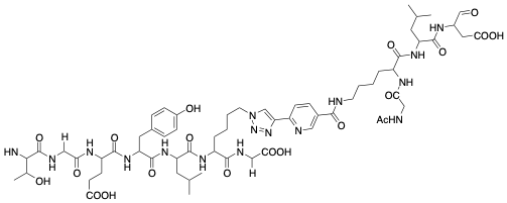
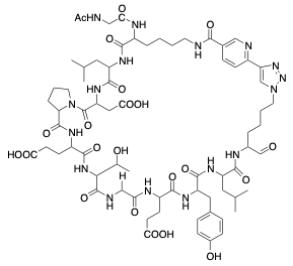


Figure 3.12 a) MALDI-ToF mass spectrum of the peptide **C** cleaved from resin and b) tandem mass spectrum of the peptide **C** cleaved from resin.

Table 3.3 Proposed structures for the fragments (positive mode).

Mass (m/z)	Proposed structure (with one positive charge)
699.3820	
814.4252	
927.5049	
1090.5717	
1219.6191	
1276.6248	
1377.6705	

1529.0074



Using a resin batch with a 0.47 mmol/g loading, we identified the cyclised peptide, but it only formed as a very minor product along with major side-products. The broad unstructured band observed on the HPLC profile might arise from intermolecular products formed due to the too high loading. The cyclisation reaction will be explored on batches of resin with lower loadings. Meanwhile, enough material can be isolated to perform preliminary evaluation of its affinity towards Keap1 compared to its linear counterpart.

3.4 Summary

In this chapter, we aim at developing macrocyclic Nrf2 peptidomimetics with *fac*-[Re(Pyta)$(CO)_3$Cl] complex as macrocycle linker as Keap1-Nrf2 inhibitors. Here we explored two approaches for the synthesis of 2-ethynylpyridyl functionalized amino acid and we successfully developed the synthesis *via* an amidation approach. A first linear peptide was successfully synthesized by SPPS. First cyclisation attempts have been performed and showed the formation of the desired cyclic peptide along with unidentified by-products, probably issued from intermolecular reactions. It proves nevertheless the feasibility of the approach. Despite the low efficiency of the cyclisation for now, we are still able to isolate enough material to study its interaction with Keap1 and compare with linear counterpart. This will be performed shortly using a FP assay set up in the laboratory.

Optimisations of the loading and cyclisation conditions are necessary. Meanwhile, the optimisation of the linker length needs to be taken into consideration. Two lysines might be too flexible and thus may not stabilize the β-turn. Direct synthesis of non-natural amino acids with shorter side chains is also preferable for their lower flexibility and higher robustness. Related strategies are currently under investigation in our group such as chiral Ni(II) complex for the synthesis of amino acids,[352] and enantioselective reduction of C=C bonds.[348,349]

3.5 Résumé

Dans ce chapitre, nous souhaitons développer des peptidomimes macrocycliques en tant qu'inhibiteurs de Keap1-Nrf2. Ces peptidomimes posséde le complexe *fac*-[Re(Pyta)$(CO)_3$Cl] comme agent « agrafe » pour fermer le macrocycle. Ici, nous avons exploré deux approches pour la synthèse d'acides aminés fonctionnalisés par la 2-éthynylpyridyle. Nous avons développé avec succès la synthèse de cet acide aminé par « amidation ». Un premier peptide linéaire incorporant cet acide aminé a été synthétisé avec succès par SPPS. Des premières tentatives de cyclisation ont été effectuées et ont montré la formation du peptide cyclique souhaité ainsi que de sous-produits non identifiés, probablement issus de réactions intermoléculaires. Cela prouve néanmoins la faisabilité de l'approche. Malgré la faible efficacité de la cyclisation pour le moment, nous sommes toujours en mesure d'isoler suffisamment de matériel pour étudier son interaction avec Keap1 et le comparer à son homologue linéaire. Ceci sera effectué sous peu en utilisant un dosage de PF mis en place dans le laboratoire.

Des optimisations des conditions, notamment, le taux de substitution de la résine, et des conditions expérimentales de cyclisation sont nécessaires. De plus, l'optimisation de la longueur de des chaînes latérales des acides aminés modifiés (azoture et ethynylpyridine) doit être entreprise. En effet, à l'heure actuelle, des dérivés de la lysine ont été utilisés et peuvent s'avérer être trop flexibles et ainsi réduire la stabilisationb du coude β. La synthèse d'acides aminés non naturels avec des chaînes latérales plus courtes est également préférable car ces acides aminés seront plus robustes. Des stratégies de synthèse sont actuellement à l'étude dans notre groupe pour la synthèse énantiosélective de ces acides aminés modifiés. L'utilisation d'un complexe chiral de Ni(II) pour la synthèse ainsi que la réduction énantiosélective de liaisons C=C sont explorées.

4. Experimental part

4.1 General information

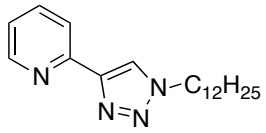
^{1}H and ^{13}C NMR spectra were recorded on a Bruker Avance 300 spectrometer using solvent residuals as internal references. The following abbreviations are used: singlet (s), doublet (d), doublet of doublets (dd), doublet of triplets (dt), triplet (t), doublet of triplets (td), quartet (q) and multiplet (m). Mass spectrometry services were performed at the ICMMO (Université Paris Sud, Orsay, France) and at UMR7201 (Institut Parisien de Chimie Moléculaire, IPCM). IR spectra were recorded on a Perkin-Elmer Spectrum 100 FT-IR spectrometer. Reactions were monitored by analytical thin-layer chromatography on commercially available precoated aluminium packed plates (Merck Kiesel gel 60F-254) with visualisation at 254 and 366 nm or using analytical reversed-phase HPLC (Agilent Technologies 1200 series. Column: PROTO 200 C18 with 3 μm particles from Higgins analystical Inc., 100 mm length and 4.6 mm internal diameter). Preparative HPLC was carried out with Agilent Technologies 1260 series machine (Column: Nucleodur C18 Htec. with 5 μm particles from Macherey-Nagel, 250 mm length and 16 mm internal diameter). Semi-preparative HPLC was carried out with Water 1525 Binary HPLC pump and Water 2487 Dual λ absorbance detector (Column: PROTO 200 C18 with 5 μm particles from Higgins analytical Inc., 150 mm length and 10 mm internal diameter). Preparative flash chromatography was carried out with Merck silica gel (Si 60, 40−63 μm). Reagents and chemicals were purchased from Sigma-Aldrich, Alfa Aesar, or Strem Chemicals and used without further purification. Dry solvents (dichloromethane, toluene, tetrahydrofuran, acetone and N, N-dimethylformamide, acetonitrile) were purchased from Sigma and used without further purification. All the reactions were conducted under an argon atmosphere unless otherwise stated. Though no problem was encountered in the handling of any of the azides used, these compounds are potentially explosive and should thus be manipulated with caution.

UV−vis absorption spectra were recorded on a Varian Cary 300 Bio spectrophotometer, luminescence emission spectra on a Jasco FP-8300 spectrofluorometer.

Crystallography: X-ray diffraction data were collected by using a Kappa X8 APPEX II Bruker diffractometer with graphite-monochro- mated Mo Kα radiation (λ = 0.710 73 Å). Crystals were mounted on a CryoLoop (Hampton Research) with Paratone-N (Hampton Research) as cryoprotectant and then flash-frozen in a nitrogen-gas stream at 100 K. The temperature of the crystal was maintained at the selected value (100 K) by means of a 700 series Cryostream cooling device to within an accuracy of ±1 K. The data were corrected for Lorentz polarisation and absorption effects. The structures were solved by direct methods using SHELXS-97 and refined against F2 by full- matrix least-squares techniques using SHELXL-97 with anisotropic displacement parameters for all non-hydrogen atoms. Hydrogen atoms were located on a difference Fourier map and introduced into the calculations as a riding model with isotropic thermal parameters. All calculations were performed by using the Crystal structure crystallographic software package WINGX.

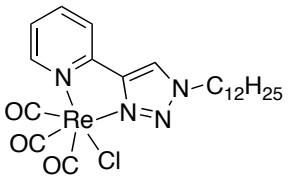
4.2 Synthesis for photophysical study

4.2.1 Synthesis of Rhenium complexes with modified Pyta ligands



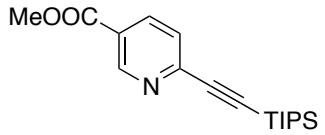
2-(1-Dodecyl-1*H*-1,2,3-triazol-4-yl)pyridine

2-Ethynylpyridine (0.5 mL, 5.0 mmol, 1.0 equiv.) and 1-azidododecane (1.2 g, 5.4 mmol, 1.1 equiv.) were dissolved in a mixture of dichloromethane (5.0 mL) and water (3.0 mL). Copper(II) sulfate pentahydrate (124 mg, 0.5 mmol, 0.1 equiv.) and sodium ascorbate (294 mg, 1.5 mmol, 0.3 equiv.) were added. The mixture was stirred at room temperature overnight. The mixture was diluted with dichloromethane and water. The organic phase was collected, dried over sodium sulfate, filtered and concentrated. The residue was purified by column chromatography on silica gel (cyclohexane : ethyl acetate = 1 : 1, v/v) to give the titled compound as a white solid (1.0 g, 66% yield). ^{1}H NMR (300 MHz, Chloroform-*d*) δ 8.58 (ddd, *J* = 4.9, 1.8, 1.0 Hz, 1H), 8.18 (dt, *J* = 8.0, 1.0 Hz, 1H), 8.12 (s, 1H), 7.77 (td, *J* = 7.6, 1.8 Hz, 1H), 7.22 (dd, *J* = 7.6, 4.9 Hz, 1H), 4.41 (t, *J* = 7.2 Hz, 2H), 2.06 – 1.82 (m, 2H), 1.39 – 1.14 (m, 18H), 0.92 – 0.81 (m, 3H). ^{13}C NMR (75 MHz, Chloroform-*d*) δ 150.6, 149.5, 148.5, 137.1, 122.9, 121.9, 120.4, 50.7, 32.0, 30.4, 29.7, 29.7, 29.5, 29.5, 29.2, 26.6, 22.8, 14.3. Characterisation in agreement with *Inorg. Chem.*, **2014**, *53*, 6204 − 6223.



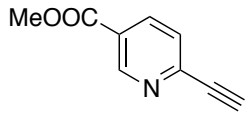
[2-(1-Dodecyl-1*H*-1,2,3-triazol-4-yl)pyridine]-chlorotricarbonylrhenium(I), **3r**

2-(1-Dodecyl-1*H*-1,2,3-triazol-4-yl)pyridine (250 mg, 0.8 mmol, 1.0 equiv.) was dissolved in toluene (15 mL). The mixture was heated at 120 °C and pentacarbonylchlororhenium(I) (286 mg, 0.8 mmol, 1.0 equiv.) was added. The mixture was stirred at 120 °C for 7 hours. After cooling to room temperature, the mixture was evaporated and the residue was purified by column chromatography on silica gel (cyclohexane : ethyl acetate = 3 : 7 → ethyl acetate, v/v) to give the titled compound as a pale yellow solid (454 mg, 93% yield). ^{1}H NMR (300 MHz, Chloroform-*d*) δ 9.01 (d, *J* = 5.6 Hz, 1H), 8.24 (s, 1H), 7.94 (t, *J* = 7.8 Hz, 1H), 7.76 (d, *J* = 7.8 Hz, 1H), 7.41 (td, *J* = 7.3, 5.6 Hz, 1H), 4.55 – 4.31 (m, 2H), 2.06 – 1.81 (m, 2H), 1.46 – 1.13 (m, 18H), 0.88 (t, *J* = 6.6 Hz, 3H). ^{13}C NMR (75 MHz, Chloroform-*d*) δ 197.3, 195.5, 189.2, 153.5, 149.4, 148.8, 139.3, 125.9, 123.2, 122.0, 52.6, 32.0, 30.1, 29.7, 29.6, 29.5, 29.1, 26.5, 22.8, 14.3. Characterisation in agreement with *Inorg. Chem.*, **2014**, *53*, 6204 − 6223.



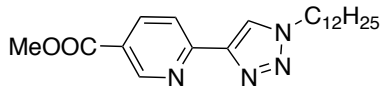
Methyl 6-((triisopropylsilyl)ethynyl)nicotinate, **19**

Methyl 6-chloronicotinate (2.0 g, 11.7 mmol, 1.0 equiv.) was dissolved in tetrahydrofuran (15 mL), followed by the addition of triethylamine (5 mL). The mixture was bubbled with argon for 10 minutes. Then bis(triphenylphosphine)palladium(II) dichloride (161 mg, 0.23 mmol, 0.02 equiv.), copper(I) iodide (23 mg, 0.12 mmol, 0.01 equiv.) and ethynyltriisopropylsilane (3.1 mL, 14.0 mmol, 1.2 equiv.) were added into the mixture in sequence. The mixture was stirred at room temperature overnight. Then the mixture was filtered and the filtrate was collected and concentrated. The residue was purified by column chromatography (cyclohexane : ethyl acetate = 10 : 1, v/v) on silica gel to give the titled compound as pale yellow liquid (3.6 g, 96% yield). ^{1}H NMR (300 MHz, Chloroform-*d*) δ 9.15 (dd, *J* = 2.2, 0.9 Hz, 1H), 8.23 (dd, *J* = 8.2, 2.2 Hz, 1H), 7.52 (dd, *J* = 8.2, 0.9 Hz, 1H), 3.94 (s, 3H), 1.14 (d, *J* = 3.4 Hz, 21H). ^{13}C NMR (75 MHz, Chloroform-*d*) δ 165.4, 151.1, 147.0, 137.2, 127.3, 124.8, 105.4, 95.7, 52.6, 18.8, 11.3. HRMS (ESI+): m/z calculated for $C_{18}H_{28}NO_2Si$: 318.1889 $[M + H]^+$; found: 318.1856.



Methyl 6-ethynylnicotinate, **20**

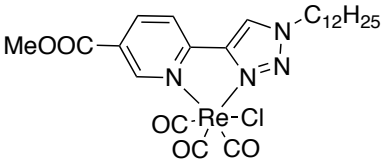
Methyl 6-((triisopropylsilyl)ethynyl)nicotinate (167 mg, 0.53 mmol, 1.0 equiv.) was dissolved in tetrahydrofuran (5 mL). The mixture was cooled to 0 °C, followed by the addition of tetra-*n*-butylammonium fluoride (1 M in THF, 0.5 mL, 0.50 mmol, 0.95 equiv.) dropwise. The mixture was stirred for 10 minutes and then was extracted by dichloromethane and water. The organic phase was collected, dried over sodium sulfate and concentrated. The residue was purified by column chromatography on silica gel (cyclohexane : ethyl acetate = 7 : 3, v/v) to give the titled compound as a pale yellow solid (69 mg, 81% yield). ^{1}H NMR (300 MHz, Chloroform-*d*) δ 9.18 (dd, *J* = 2.2, 0.9 Hz, 1H), 8.28 (dd, *J* = 8.1, 2.2 Hz, 1H), 7.56 (dd, *J* = 8.1, 0.9 Hz, 1H), 3.96 (s, 3H), 3.32 (s, 1H). ^{13}C NMR (75 MHz, Chloroform-*d*) δ 165.3, 151.2, 146.0, 137.4, 127.1, 125.4, 82.4, 80.1, 52.7, 17.8.



Methyl 6-(1-dodecyl-1*H*-1,2,3-triazol-4-yl)nicotinate, **22**

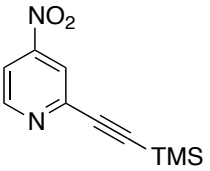
Methyl 6-ethynylnicotinate (50 mg, 0.30 mmol, 1.0 equiv.) and 1-azidododecane (70 mg, 0.33 mmol, 1.1 equiv.) were dissolved in a mixture of dichloromethane (2.0 mL) and water (1.0 mL). Copper(II) sulfate pentahydrate (7 mg, 0.03 mmol, 0.1 equiv.) and sodium ascorbate (18 mg, 0.09 mmol, 0.3 equiv.) were added and the mixture was stirred at room temperature overnight.

The mixture was diluted with dichloromethane and water. The organic phase was collected, dried over sodium sulfate, filtered and concentrated. The residue was purified by column chromatography on silica gel (cyclohexane : ethyl acetate = 7 : 3 → 1 : 1, v/v) to give the titled compound as a white solid (106 mg, 92% yield). ^{1}H NMR (300 MHz, Chloroform-*d*) δ 9.17 (dd, *J* = 2.1, 0.9 Hz, 1H), 8.37 (dd, *J* = 8.2, 2.1 Hz, 1H), 8.25 (dd, *J* = 8.2, 0.9 Hz, 1H), 8.20 (s, 1H), 4.42 (t, *J* = 7.2 Hz, 2H), 3.96 (s, 3H), 2.06 – 1.80 (m, 2H), 1.42 – 1.16 (m, H), 0.90 – 0.83 (m, 3H). ^{13}C NMR (75 MHz, Chloroform-*d*) δ 165.8, 154.0, 151.0, 147.7, 138.1, 124.9, 123.1, 119.6, 52.5, 50.8, 32.0, 30.4, 29.7, 29.6, 29.5, 29.5, 29.1, 26.6, 22.8, 14.3. HRMS (ESI+): m/z calculated for $C_{21}H_{32}N_4NaO_2$: 395.2423 $[M + Na]^+$; found: 395.2430.



[Methyl 6-(1-dodecyl-1*H*-1,2,3-triazol-4-yl)nicotinate]-chlorotricarbonylrhenium(I), **13**

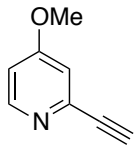
Methyl 6-(1-dodecyl-1*H*-1,2,3-triazol-4-yl)nicotinate (40 mg, 0.1 mmol, 1.0 equiv.) was dissolved in toluene (2 mL). The mixture was heated at 120 °C and pentacarbonylchlororhenium(I) (39 mg, 0.1 mmol, 1.0 equiv.) was added. The mixture was stirred at 80 °C for 2 hours. After cooling to room temperature, the yellow precipitate was collected, washed with cyclohexane and dried under vacuum to give the titled compound as a yellow solid (58 mg, 79% yield). ^{1}H NMR (300 MHz, Chloroform-*d*) δ 9.55 (dd, *J* = 1.9, 0.8 Hz, 1H), 8.54 (dd, *J* = 8.3, 1.9 Hz, 1H), 8.25 (s, 1H), 7.84 (dd, *J* = 8.3, 0.8 Hz, 1H), 4.63 – 4.36 (m, 2H), 4.05 (s, 3H), 2.03 (t, *J* = 7.3 Hz, 2H), 1.40 – 1.25 (m, 15H), 0.95 – 0.82 (m, 3H). ^{13}C NMR (75 MHz, Chloroform-*d*) δ 163.2, 154.7, 152.3, 148.1, 140.2, 128.1, 123.8, 121.4, 53.4, 52.8, 32.1, 30.0, 29.7, 29.6, 29.5, 29.0, 26.6, 22.8, 14.3. HRMS (ESI+): m/z calculated for $C_{24}H_{32}ClN_4NaO_5Re$: 701.1516 $[M + Na]^+$; found: 701.1508. IR: ν_{max}/cm^{-1} 2021,1886 (CO).



4-Nitro-2-((trimethylsilyl)ethynyl)pyridine

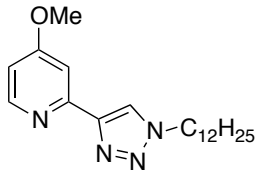
2-Bromo-4-nitropyridine (100 mg, 0.49 mmol, 1.0 equiv.) was dissolved in N,N-dimethylformamide (1 mL), followed by the addition of triethylamine (139 uL, 1.0 mmol, 2.0 equiv.). The mixture was bubbled with argon for 10 minutes. Then bis(triphenylphosphine)palladium(II) dichloride (7 mg, 0.01 mmol, 0.02 equiv.), copper(I) iodide (1 mg, 0.004 mmol, 0.008 equiv.) and ethynyltrimethylsilane (83 uL, 0.59 mmol, 1.2 equiv.) were added into the mixture in sequence. The mixture was heated at 60 °C overnight. Then the mixture was filtered and the filtrate was collected and concentrated. The residue was purified by column chromatography (cyclohexane : ethyl acetate = 9 : 1, v/v) on silica gel to

afford the titled compound as pale yellow solid (44 mg, 41% yield). ^{1}H NMR (300 MHz, Chloroform-*d*) δ 8.86 (dd, *J* = 5.4, 0.7 Hz, 1H), 8.15 (dd, *J* = 2.2, 0.7 Hz, 1H), 7.95 (dd, *J* = 5.4, 2.2 Hz, 1H), 0.30 (s, 9H). Characterisation in agreement with *J. Am. Chem. Soc.*, **2016**, *138*, 9853 − 9863.



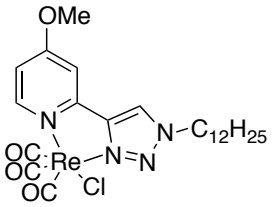
2-Ethynyl-4-methoxypyridine, **24**

4-Nitro-2-((trimethylsilyl)ethynyl)pyridine (44 mg, 0.2 mmol, 1.0 equiv.) was dissolved in methanol, followed by the addition of potassium carbonate (137 mg, 1.0 mmol, 5.0 equiv.). The mixture was stirred at room temperature for 4 hours. The mixture was filtered, the filtrate was diluted with dichloromethane and water and extracted with dichloromethane. The organic phase was dried over sodium sulfate, filtered and concentrated to afford the titled product as a white solid (21 mg, 81% yield). ^{1}H NMR (300 MHz, Chloroform-*d*) δ 8.39 (dd, *J* = 5.8, 0.5 Hz, 1H), 7.01 (dd, *J* = 2.6, 0.5 Hz, 1H), 6.80 (dd, *J* = 5.8, 2.6 Hz, 1H), 3.85 (s, 3H), 3.12 (s, 1H). Characterisation in agreement with *J. Am. Chem. Soc.*, 2016, *138*, 9853 − 9863.



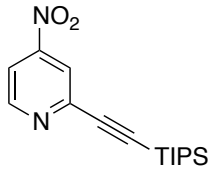
2-(1-Dodecyl-1*H*-1,2,3-triazol-4-yl)-4-methoxypyridine, **26**

2-Ethynyl-4-methoxypyridine (21.0 mg, 0.16 mmol, 1.0 equiv.) and 1-azidododecane (36.0 mg, 0.17 mmol, 1.05 equiv.) were dissolved in a mixture of dichloromethane (1.0 mL) and water (0.6 mL). Copper(II) sulfate pentahydrate (4.0 mg, 0.016 mmol, 0.1 equiv.) and sodium ascorbate (9.0 mg, 0.048 mmol, 0.3 equiv.) were added, and the mixture was stirred at room temperature for 23 hours. The mixture was diluted with dichloromethane and water and decanted. The organic phase was dried over sodium sulfate, filtered and concentrated. The residue was purified by column chromatography (ethyl acetate) on silica gel to afford the titled compound as a white solid (30 mg, 55% yield). R_f = 0.71 (ethyl acetate). ^{1}H NMR (300 MHz, Chloroform-*d*) δ 8.37 (d, *J* = 5.8 Hz, 1H), 8.21 (s, 1H), 7.76 (d, *J* = 2.6 Hz, 1H), 6.78 (dd, *J* = 5.8, 2.6 Hz, 1H), 4.40 (t, *J* = 7.2 Hz, 2H), 3.94 (s, 3H), 1.99 – 1.90 (m, 2H), 1.51−1.10 (m, 18H), 0.86 (t, *J* = 6.0 Hz, 3H). ^{13}C NMR (75 MHz, Chloroform-*d*) δ 166.9, 151.8, 150.0, 147.8, 122.4, 110.5, 105.3, 55.6, 50.7, 32.0, 30.4, 29.7, 29.6, 29.5, 29.45, 29.1, 26.6, 22.8, 14.2. HRMS (ESI+): m/z calculated for $C_{20}H_{33}N_4O$: 345.2654 $[M + H]^+$; found: 345.2652.



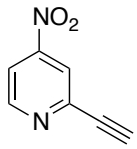
[2-(1-Dodecyl-1*H*-1,2,3-triazol-4-yl)-4-methoxypyridine]-chlorotricarbonylrhenium(I), **14**

2-(1-Dodecyl-1*H*-1,2,3-triazol-4-yl)-4-methoxypyridine (24 mg, 0.07 mmol, 1.0 equiv.) wad dissolved in toluene (3 mL). The mixture was heated at 120 °C. Pentacarbonylchlororhenium(I) (25 mg, 0.07 mmol, 1.0 equiv.) was added and the mixture was heated at 120 °C overnight. The mixture was cooled to room temperature, evaporated and the residue was purified by column chromatography on silica gel (ethyl acetate) to afford the titled compound as a pale yellow solid (42 mg, 92% yield). ^{1}H NMR (300 MHz, Chloroform-*d*) δ 8.70 (d, *J* = 6.4 Hz, 1H), 8.41 (s, 1H), 7.35 (d, *J* = 2.7 Hz, 1H), 6.86 (dd, *J* = 6.4, 2.7 Hz, 1H), 4.39−4.23 (m, 1H), 4.14−3.98 (m, 1H), 3.91 (s, 3H), 1.93−1.82 (m, 2H), 1.46−1.16 (m, 18H), 0.87 (t, *J* = 7.5 Hz, 3H). ^{13}C NMR (75 MHz, Chloroform-*d*) δ167.8, 153.8, 151.3, 149.1, 124.4, 113.1, 107.3, 57.4, 52.3, 32.0, 30.1, 29.7, 29.6, 29.5, 29.4, 29.0, 26.5, 22.8, 14.3. HRMS (ESI+): m/z calculated for $C_{23}H_{32}ClN_4NaO_4Re$: 673.1567 $[M + Na]^+$; found 673.1538. IR: ν_{max}/cm^{-1} 2019, 1885 (CO).



4-Nitro-2-((triisopropylsilyl)ethynyl)pyridine

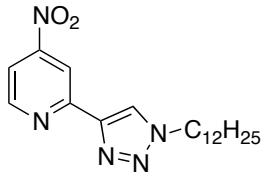
2-Bromo-4-nitropyridine (150 mg, 0.7 mmol, 1.0 equiv.) was dissolved in N,N-dimethylformamide (2 mL), followed by the addition of triethylamine (209 uL, 1.4 mmol, 2.0 equiv.). The mixture was bubbled with argon for 10 minutes. Then bis(triphenylphosphine)palladium(II) dichloride (11 mg, 0.015 mmol, 0.02 equiv.), copper(I) iodide (2 mg, 0.008 mmol, 0.01 equiv.) and ethynyltriisopropylsilane (200 uL, 0.9 mmol, 1.2 equiv.) were added into the mixture in sequence. The mixture was heated at 60 °C overnight. The mixture was filtered and the filtrate concentrated. The residue was purified by column chromatography on silica gel (cyclohexane : ethyl acetate = 9 : 1, v/v) to afford the titled compound as pale yellow liquid (100 mg, 44% yield), which was used directly in the next step.



2-Ethynyl-4-nitropyridine, **25**

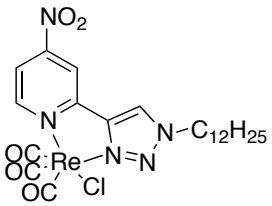
4-Nitro-2-((triisopropylsilyl)ethynyl)pyridine (100 mg, 0.3 mmol, 1.0 equiv.) was dissolved in tetrahydrofuran (2 mL) and the mixture was cooled to 0 °C. Tetra-n-butylammonium fluoride

(1 M in tetrahydrofuran, 0.3 mL, 0.3 mmol, 0.95 equiv.) was added and the mixture was stirred at 0 °C for 30 minutes. The mixture was diluted with water and extracted with dichloromethane. The organic phase was dried over sodium sulfate, filtered and concentrated. The residue was purified by column chromatography on silica gel (cyclohexane : ethyl acetate = 7 : 3, v/v) to afford the titled compound as a pale yellow solid (37 mg, 76% yield). ^{1}H NMR (300 MHz, Chloroform-*d*) δ 8.90 (dd, *J* = 5.4, 0.8 Hz, 1H), 8.19 (dd, *J* = 2.1, 0.8 Hz, 1H), 8.01 (dd, *J* = 5.4, 2.1 Hz, 1H), 3.36 (s, 1H). Characterisation in agreement with *J. Am. Chem. Soc.*, **2016**, *138*, 9853 − 9863.



2-(1-Dodecyl-1*H*-1,2,3-triazol-4-yl)-4-nitropyridine, **27**

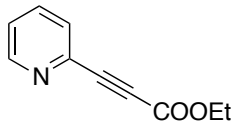
2-Ethynyl-4- nitropyridine (37 mg, 0.25 mmol, 1.0 equiv.) and 1-azidododecane (58 mg, 0.28 mmol, 1.1 equiv.) were dissolved in a mixture of dichloromethane (2.0 mL) and water (1.5 mL). Copper(II) sulfate pentahydrate (8 mg, 0.03 mmol, 0.1 equiv.) and sodium ascorbate (16 mg, 0.08 mmol, 0.3 equiv.) were added, and the mixture was stirred at room temperature for 16 hours. The mixture was diluted with water and extracted with dichloromethane. The organic phase was dried over sodium sulfate, filtered and concentrated. The residue was purified by column chromatography on silica gel (cyclohexane : ethyl acetate = 7 : 3, v/v) to afford the titled compound as a white solid (79.0 mg, 88% yield). R_f = 0.39 (cyclohexane : ethyl acetate = 7 : 3, v/v). ^{1}H NMR (300 MHz, Chloroform-*d*) δ 8.89 (d, *J* = 2.2 Hz, 1H), 8.85 (d, *J* = 5.4 Hz, 1H), 8.21 (s, 1H), 7.93 (dd, *J* = 5.4, 2.2 Hz, 1H), 4.45 (t, *J* = 7.2 Hz, 2H), 2.15 – 1.93 (m, 2H), 1.52−1.11 (m, 18H), 0.87 (t, *J* = 6.0 Hz, 3H). ^{13}C NMR (75 MHz, Chloroform-*d*) 154.9, 153.6, 151.6, 146.7, 123.0, 115.0, 113.0, 50.9, 32.0, 30.4, 29.7, 29.6, 29.5, 29.46, 29.1, 26.6, 22.8, 14.25. HRMS (ESI+): m/z calculated for $C_{19}H_{29}N_5NaO_2$: 382.2219 [M + Na]$^+$; found 382.2222.



[2-(1-Dodecyl-1*H*-1,2,3-triazol-4-yl)-4-nitropyridine]-chlorotricarbonylrhenium(I), **15**

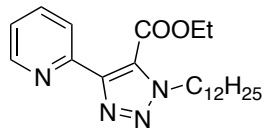
2-(1-Dodecyl-1*H*-1,2,3-triazol-4-yl)-4-nitropyridine (30 mg, 0.08 mmol, 1.0 equiv.) wad dissolved in toluene (3 mL). The mixture was heated at 120 °C. Pentacarbonylchlororhenium(I) (30 mg, 0.08 mmol, 1.0 equiv.) was added and the mixture was heated at 120 °C overnight. The mixture was cooled to room temperature, concentrated under reduced pressure and the residue purified by column chromatography on silica gel (ethyl acetate : cyclohexane = 1: 1, v/v) to afford the titled compound as an orange solid (56 mg, 99% yield). ^{1}H NMR (300 MHz,

Acetone-d_6) δ 9.42 (dd, J = 6.1, 0.7 Hz, 1H), 9.39 (s, 1H), 9.00 (dd, J = 2.4, 0.7 Hz, 1H), 8.35 (dd, J = 6.1, 2.4 Hz, 1H), 4.76 (t, J = 7.2 Hz, 2H), 2.21−2.06 (m, 2H), 1.53−1.13 (m, 18H), 0.86 (t, J = 6.0 Hz, 3H). ^{13}C NMR (75 MHz, Acetone-d_6) δ 156.6, 156.2, 153.3, 148.6, 127.5, 119.7, 116.6, 53.1, 32.6, 30.4, 30.2, 30.1, 30.06, 29.6, 26.9, 23.3, 14.35. HRMS (ESI+): m/z calculated for $C_{22}H_{29}ClN_5NaO_5Re$: 688.1312 $[M + Na]^+$; found 688.1285. IR: ν_{max}/cm^{-1} 2023, 1897 (CO).



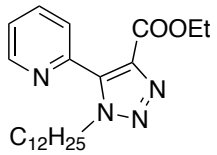
Ethyl 3-(pyridin-2-yl)propiolate, **29**

To a solution of 2-ethynylpyridine (0.5 mL, 0.5 mmol, 1.0 equiv.) in THF (distilled, 10 mL) was added *n*-butyllithium (1.0 M in hexane, 1.7 mL, 3.4 equiv.) at -75 °C. The mixture was stirred at -75 °C for 30 min. Then ethyl chloroformiate (0.262 mL, 2.75 mmol, 5.5 equiv.) was added at -75 °C. The mixture was stirred at -75 °C for 1.5 hours and then at room temperature for 2 days. Then water was added and the mixture was extracted with ethyl acetate. The organic phase was dried over sodium sulfate, filtered and concentrated. The residue was purified by column chromatography on silica gel (ethyl acetate : cyclohexane = 1 : 9, v/v) to afford the titled product as a pale yellow solid (299 mg, 68% yield). R_f = 0.26 (ethyl acetate: cyclohexane = 1 :4, v/v). ^{1}H NMR (300 MHz, Chloroform-*d*) δ 8.66 (d, J = 4.8 Hz, 1H), 7.72 (t, J = 7.8 Hz, 1H), 7.59 (d, J = 7.8 Hz, 1H), 7.35 (dd, J = 7.8, 4.8 Hz, 1H), 4.31 (q, J = 7.1 Hz, 2H), 1.35 (t, J = 7.1 Hz, 3H). ^{13}C NMR (75 MHz, Chloroform-*d*) δ 153.6, 150.7, 140.8, 136.4, 128.7, 124.7, 83.9, 79.4, 62.5, 14.2.



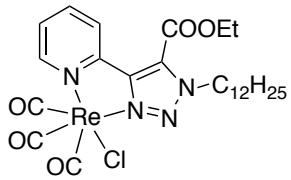
Ethyl 1-dodecyl-4-(pyridin-2-yl)-1*H*-1,2,3-triazole-5-carboxylate, **31**

Ethyl 3-(pyridin-2-yl)propiolate (200 mg, 1.14 mmol, 1.0 equiv.) and 1-azidododecane (724 mg, 3.43 mmol, 3.0 equiv.) were dissolved in toluene (5 mL). The mixture was heated at 120 °C for 12 hours. The mixture was concentrated and the residue was purified by column chromatography on silica gel (ethyl acetate : dichloromethane = 1:9 → 1:1, v/v) to afford the titled compound as a pale yellow oil (110 mg, 25% yield). R_f = 0.41 (ethyl acetate: dichloromethane = 1 :4, v/v). ^{1}H NMR (300 MHz, Chloroform-*d*) δ 8.65 (d, J = 4.9 Hz, 1H), 7.87 (d, J = 7.6 Hz, 1H), 7.79 (t, J = 7.6 Hz, 1H), 7.30 (dd, J = 7.6, 4.9 Hz, 1H), 4.64 (t, J = 7.5 Hz, 2H), 4.36 (q, J = 7.2 Hz, 2H), 1.90 – 1.82 (m, 2H), 1.43 – 1.19 (m, 21H), 0.87 (t, J = 7.5 Hz, 3H). ^{13}C NMR (75 MHz, Chloroform-*d*) δ 159.9, 150.1, 149.4, 148.9, 136.4, 126.3, 123.5, 123.4, 62.2, 50.8, 32.1, 30.6, 29.8, 29.7, 29.6, 29.5, 29.2, 26.6, 22.8, 14.3, 13.0. HRMS (ESI+): m/z calculated for $C_{22}H_{34}N_4NaO_2$: 409,2579 $[M + Na]^+$; found: 409.2566.



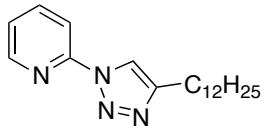
Ethyl 1-dodecyl-5-(pyridin-2-yl)-1*H*-1,2,3-triazole-4-carboxylate, **32**

The isomer was isolated as a white solid (303 mg, 69%). ^{1}H NMR (300 MHz, Chloroform-*d*) δ 8.64 (d, *J* = 4.8 Hz, 1H), 7.86 (d, *J* = 7.8 Hz, 1H), 7.82 – 7.73 (m, 1H), 7.29 (dd, *J* = 7.8, 4.8 Hz, 1H), 4.63 (t, *J* = 7.4 Hz, 2H), 4.35 (q, *J* = 7.1 Hz, 2H), 1.92 (t, *J* = 7.4 Hz, 2H), 1.45 – 1.05 (m, 21H), 0.87 (t, *J* = 6.4 Hz, 3H). ^{13}C NMR (75 MHz, Chloroform-*d*) δ 159.9, 150.0, 149.4, 148.8, 136.4, 126.3, 123.5, 123.4, 62.2, 50.7, 32.0, 30.5, 29.7, 29.6, 29.5, 29.5, 29.2, 26.6, 22.8, 14.2, 13.9. HRMS (ESI+): m/z calculated for $C_{22}H_{34}N_4NaO_2$: 409,2579 $[M + Na]^+$; found: 409.2549.



[Ethyl 1-dodecyl-4-(pyridin-2-yl)-1*H*-1,2,3-triazole-5-carboxylate]-chlorotricarbonylrhenium(I), **16**

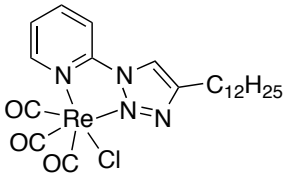
Ethyl 1-dodecyl-4-(pyridin-2-yl)-1*H*-1,2,3-triazole-5-carboxylate (110 mg, 0.28 mmol, 1.0 equiv.) was dissolved in toluene (4 mL) and the mixture was heated at 120 °C. Then pentacarbonylchlororhenium(I) (103 mg, 0.28 mmol, 1.0 equiv.) was added and the mixture was stirred at 120 °C for 1 hour. After cooling to room temperature, the solvent was evaporated and the residue was purified by column chromatography on silica gel (dichloromethane : ethyl acetate = 9 : 1, v/v) to afford the titled compound as a yellow solid (169 mg, 87% yield). R_f = 0.20 (dichloromethane). ^{1}H NMR (300 MHz, Chloroform-*d*) δ 9.11 (d, *J* = 5.5 Hz, 1H), 8.94 (d, *J* = 8.2 Hz, 1H), 8.04 (dd, *J* = 8.2, 7.7 Hz, 1H), 7.49 (dd, *J* = 7.7, 5.5 Hz, 1H), 4.86 – 4.71 (m, 2H), 4.59 – 4.65 (m, 2H), 2.00 (m, 2H), 1.53 (t, *J* = 7.2 Hz, 3H), 1.46 – 1.22 (m, 18H), 0.88 (t, *J* = 7.5 Hz, 3H). ^{13}C NMR (75 MHz, Chloroform-*d*) δ 197.3, 195.4, 189.1, 157.1, 154.0, 150.0, 148.8, 139.3, 127.5, 126.9, 125.4, 64.2, 53.9, 32.0, 30.5, 29.7, 29.6, 29.5, 29.1, 26.6, 22.8, 14.2. IR: ν_{max}/cm^{-1} 2024, 1918, 1887 (CO). HPLC (75 to 100% ACN in 10 min): rt 7.51 minutes (>95%). HRMS (ESI+): m/z calculated for $C_{25}H_{34}ClN_4NaO_5Re$: 715,1673 $[M + H]^+$; found: 715.1649.



2-(4-Dodecyl-1*H*-1,2,3-triazol-1-yl)pyridine

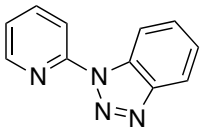
2-Azidopyridine (500 mg, 4.2 mmol, 1.0 equiv.) and tetradec-1-yne (1.1 mL, 4.6 mmol, 1.1 equiv.) were dissolved in toluene (28 mL). Copper(I) trifluoromethanesulfonate benzene

complex (100 mg, 0.4 mmol, 0.1 equiv.) was added and the mixture was stirred at 120 °C overnight. The mixture was diluted with dichloromethane and water. The organic phase was collected, dried over sodium sulfate, filtered and concentrated. The residue was purified by column chromatography on silica gel (cyclohexane : ethyl acetate = 1 : 1, v/v) to give the titled compound as a pale yellow solid (831 mg, 66% yield). ^{1}H NMR (300 MHz, Chloroform-*d*) δ 8.48 (s, 1H), 8.31 (s, 1H), 8.19 (d, *J* = 8.2 Hz, 1H), 7.89 (td, *J* = 7.9, 1.7 Hz, 1H), 7.32 (dd, *J* = 7.6, 4.8 Hz, 1H), 2.80 (t, *J* = 7.6 Hz, 2H), 1.84 – 1.60 (m, 2H), 1.25 (s, 16H), 1.00 – 0.74 (m, 3H). Characterisation in agreement with *Inorg. Chem.*, **2014**, *53*, 6204 − 6223.



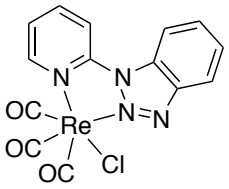
[2-(4-Dodecyl-1*H*-1,2,3-triazol-1-yl)pyridine]-chlorotricarbonylrhenium(I), **9**

2-(1-Dodecyl-1*H*-1,2,3-triazol-4-yl)pyridine (250 mg, 0.8 mmol, 1.0 equiv.) was dissolved in toluene (15 mL). The mixture was heated at 120 °C and pentacarbonylchlororhenium(I) (286 mg, 0.8 mmol, 1.0 equiv.) was added. The mixture was stirred at 120 °C for 7 hours. After cooling to room temperature, the mixture was evaporated and the residue was purified by column chromatography on silica gel (cyclohexane : ethyl acetate = 3 : 7, v/v) to give the titled compound as a yellow solid (450 mg, 92% yield). ^{1}H NMR (300 MHz, Chloroform-*d*) δ 8.89 (d, *J* = 5.4 Hz, 1H), 8.12 (m, 2H), 7.74 (d, *J* = 8.1 Hz, 1H), 7.47 (dd, *J* = 5.7, 7.2 Hz, 1H), 2.75 (m, 2H), 1.66 – 1.68 (m, 2H), 1.23 (m, 18H), 0.81 (t, *J* = 6.9 Hz, 3H). Characterisation in agreement with *Inorg. Chem.*, **2014**, *53*, 6204 − 6223.



1-(Pyridin-2-yl)-1*H*-benzo[*d*][1,2,3]triazole

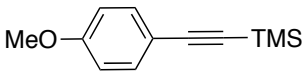
Thiobarbituric acid (1.0 g, 6.9 mmol, 1.0 equiv.) was dissolved in MeOH (3.9 mL). To the resulting solution 1-bromobutane (748 µL, 6.9 mmol, 1.0 equiv.) and Et_3N (968 µL, 6.9 mmol, 1.0 equiv.) were added. The reaction mixture was stirred under reflux for 24 h under argon then cold H_2O (20 mL) was added. The precipitate formed was collected by filtration under vacuum and dried to give crude 6-hydroxy-2-(butylthio)pyrimidin-4(3H)-one as a white precipitate (708.7 mg, 51% yield). The crude product was used for subsequent reactions with no further purification. R*f* (dicholomethane : methanol 4:1, v/v) = 0.80. ^{1}H NMR (300 MHz, Chloroform-*d* : Methanol-d_4 = 5:1, v/v) δ 5.21 (s, 1H), 3.07 (t, *J* = 7.2 Hz, 2H), 1.69 – 1.47 (m, 2H), 1.34 (q, *J* = 7.5 Hz, 2H), 0.83 (t, *J* = 6.0 Hz, 3H).



[1-(Pyridin-2-yl)-1*H*-benzo[*d*][1,2,3]triazole]-chlorotricarbonylrhenium(I), **16**

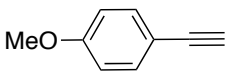
1-(Pyridin-2-yl)-1*H*-benzo[*d*][1,2,3]triazole (30 mg, 0.15 mmol, 1.0 equiv.) was dissolved in toluene (2 mL). The mixture was heated at 110 ˚C and pentacarbonylchlororhenium(I) (54 mg, 0.15 mmol, 1.0 equiv.) was added. The mixture was stirred at 110 ˚C for 4 hours. After cooling to room temperature, the mixture was evaporated and the residue was purified by column chromatography on silica gel (cyclohexane : ethyl acetate = 3 : 7, v/v) to give the titled compound as a bright yellow solid (67 mg, 87% yield). ^{1}H NMR (300 MHz, Chloroform-*d*) δ 9.10 (dd, *J* = 5.6, 1.2 Hz, 1H), 8.78 (d, *J* = 8.4 Hz, 1H), 8.58 (d, *J* = 8.8 Hz, 1H), 8.59 - 8.54 (m, 1H), 8.35 (d, *J* = 8.4 Hz, 1H), 7.99 (t, *J* = 7.8 Hz, 1H), 7.79 (q, *J* = 8.0 Hz, 2H). ^{13}C NMR (75 MHz, Acetone-d_6) δ: 153.9, 143.7, 133.0, 128.4, 126.1, 121.8, 114.6, 112.7. IR: ν_{max}/cm^{-1} 2027, 1906, 1891 (CO). HRMS (ESI+): m/z calculated for $C_{14}H_8ClN_4NaO_3Re$: 524.9726 $[M+Na]^+$; found 524.9716.

4.2.2 Synthesis of Rhenium complexes bearing acetylide ligands



((4-Methoxyphenyl)ethynyl)trimethylsilane, **35a**

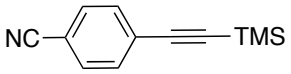
1-Iodo-4-methoxybenzene (1.0 g, 4.3 mmol, 1.0 equiv.) was dissolved in tetrahydrofuran (15 mL), followed by the addition of triethylamine (5 mL). The mixture was bubbled with argon for 10 minutes. Then bis(triphenylphosphine)palladium(II) dichloride (147 mg, 0.2 mmol, 0.05 equiv.), copper(I) iodide (41 mg, 0.2 mmol, 0.05 equiv.) and ethynyltrimethylsilane (750 μL, 5.1 mmol, 1.2 equiv.) were added into the mixture in sequence. The mixture was stirred at room temperature overnight. The mixture was filtered and the filtrate concentrated. The residue was purified by column chromatography on silica gel (cyclohexane) to afford the titled compound as a pale yellow solid. (807 mg, 93% yield). ^{1}H NMR (300 MHz, Chloroform-*d*) δ 7.40 (d, *J* = 8.9 Hz, 2H), 6.82 (d, *J* = 8.9 Hz, 2H), 3.81 (s, 3H), 0.24 (s, 9H). Characterisation in agreement with *Org. Biomol. Chem.*, 2011, *9*, 78 – 80.



1-Ethynyl-4-methoxybenzene, **36a**

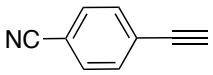
((4-Methoxyphenyl)ethynyl)trimethylsilane (200 mg, 1.0 mmol, 1.0 equiv.) was dissolved in a mixture of tetrahydrofuran (5 mL) and methanol (5 mL), followed by the addition of potassium carbonate (291 mg, 3.0 mmol, 3.0 equiv.). The mixture was stirred at room temperature for 30 minutes. The mixture was filtered and the filtrate was concentrated. The residue was purified

by column chromatography on silica gel (dichloromethane : cyclohexane = 2 : 1, v/v) to give the titled compound as a yellow solid (21 mg, 55% yield). ^{1}H NMR (300 MHz, Chloroform-*d*) δ 7.43 (d, *J* = 8.9 Hz, 2H), 6.84 (d, *J* = 8.9 Hz, 2H), 3.81 (s, 3H), 2.99 (s, 1H). Characterisation in agreement with *Org. Lett.*, **2013**, *15*, 936 – 939.



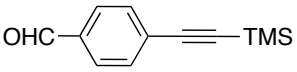
4-((Trimethylsilyl)ethynyl)benzonitrile, **35b**

4-Bromobenzonitrile (1.0 g, 5.5 mmol, 1.0 equiv.) was dissolved in tetrahydrofuran (15 mL), followed by the addition of triethylamine (5 mL). The mixture was bubbled with argon for 10 minutes. Then bis(triphenylphosphine)palladium(II) dichloride (193 mg, 0.3 mmol, 0.05 equiv.), copper(I) iodide (52 mg, 0.3 mmol, 0.05 equiv.) and ethynyltrimethylsilane (933 μL, 6.6 mmol, 1.2 equiv.) were added into the mixture in sequence. The mixture was stirred at room temperature overnight. Then the mixture was filtered and the filtrate was collected and concentrated. The residue was purified by column chromatographyon silica gel (cyclohexane: dichloromethane = 1 : 1, v/v) to give the titled compound as a yellow solid (457 mg, 42% yield). ^{1}H NMR (300 MHz, Chloroform-*d*) δ 7.67 – 7.40 (m, 4H), 0.26 (s, 9H). Characterisation in agreement with *J. Org. Chem.* **2008**, *73*, 2912 – 2915.



4-Ethynylbenzonitrile, **36b**

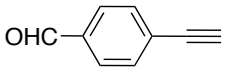
4-((Trimethylsilyl)ethynyl)benzonitrile (200 mg, 1.0 mmol, 1.0 equiv.) was dissolved in a mixture of tetrahydrofuran (5 mL) and methanol (5 mL), followed by the addition of potassium carbonate (297 mg, 3.0 mmol, 3.0 equiv.). The mixture was stirred at room temperature for 30 minutes. The mixture was filtered and the filtrate was concentrated. The residue was purified by column chromatography on silica gel (dichloromethane) to give the titled compound as a white solid (92 mg, 72% yield). ^{1}H NMR (300 MHz, Chloroform-*d*) δ 7.65 – 7.54 (m, 4H), 3.30 (s, 1H). ^{13}C NMR (75 MHz, Chloroform-*d*) δ 132.8, 132.2, 127.1, 118.4, 112.5, 82.0, 81.7.



4-((Trimethylsilyl)ethynyl)benzaldehyde, **35c**

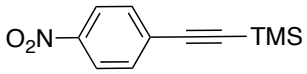
4-Bromobenzaldehyde (100 mg, 0.54 mmol, 1.0 equiv.) was dissolved in tetrahydrofuran (3 mL), followed by the addition of triethylamine (0.5 mL). The mixture was bubbled with argon for 10 minutes. Then bis(triphenylphosphine)palladium(II) dichloride (19 mg, 0.03 mmol, 0.05 equiv.), copper(I) iodide (5 mg, 0.03 mmol, 0.05 equiv.) and ethynyltrimethylsilane (92 μL, 0.65 mmol, 1.2 equiv.) were added into the mixture in sequence. The mixture was stirred at room temperature overnight. Then the mixture was filtered and the filtrate was collected and concentrated. The residue was purified by column chromatography on silica gel (cyclohexane: dichloromethane = 1 : 1, v/v) to give the titled compound as a white solid (90 mg, 83% yield).

^{1}H NMR (300 MHz, Chloroform-*d*) δ 10.00 (s, 1H), 7.82 (d, *J* = 8.3 Hz, 2H), 7.60 (d, *J* = 8.3 Hz, 2H), 0.27 (s, 9H).



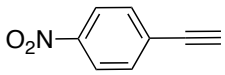
4-Ethynylbenzaldehyde, **36c**

4-((Trimethylsilyl)ethynyl)benzaldehyde (90 mg, 0.45 mmol, 1.0 equiv.) was dissolved in a mixture of tetrahydrofuran (2 mL) and methanol (2 mL), followed by the addition of potassium carbonate (86 mg, 0.90 mmol, 2.0 equiv.). The mixture was stirred at room temperature for 30 minutes. The mixture was filtered and the filtrate was concentrated. The residue was purified by column chromatography on silica gel (dichloromethane) to give the titled compound as a white solid (13 mg, 23% yield). ^{1}H NMR (300 MHz, Chloroform-*d*) δ 10.02 (s, 1H), 7.85 (d, *J* = 8.6 Hz, 1H), 7.64 (d, *J* = 8.6 Hz, 2H), 3.29 (s, 1H). ^{13}C NMR (75 MHz, $CDCl_3$) δ 191.5, 136.1, 132.9, 129.6, 128.5, 82.8, 81.2.



Trimethyl((4-nitrophenyl)ethynyl)silane, **35d**

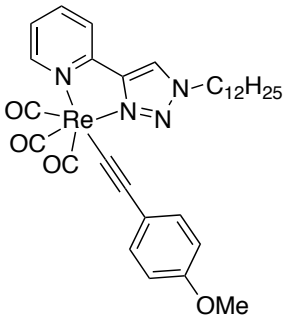
1-Bromo-4-nitrobenzene (1.0 g, 5.0 mmol, 1.0 equiv.) was dissolved in tetrahydrofuran (15 mL), followed by the addition of triethylamine (5 mL). The mixture was bubbled with argon for 10 minutes. Then bis(triphenylphosphine)palladium(II) dichloride (174 mg, 0.2 mmol, 0.05 equiv.), copper(I) iodide (47 mg, 0.2 mmol, 0.05 equiv.) and ethynyltrimethylsilane (839 μL, 5.9 mmol, 1.2 equiv.) were added into the mixture in sequence. The mixture was stirred at room temperature overnight. The mixture was filtered and the filtrate was concentrated. The residue was purified by column chromatography on silica gel (cyclohexane: dichloromethane = 1 : 1, v/v) to give the titled compound as a white solid (194 mg, 18% yield). ^{1}H NMR (300 MHz, Chloroform-*d*) δ 8.17 (d, *J* = 9.0 Hz, 2H), 7.59 (d, *J* = 9.0 Hz, 2H), 0.27 (s, 9H). Characterisation in agreement with *Tetrahedron*, **2010**, *66*, 4230 – 4242.



1-Ethynyl-4-nitrobenzene, **35d**

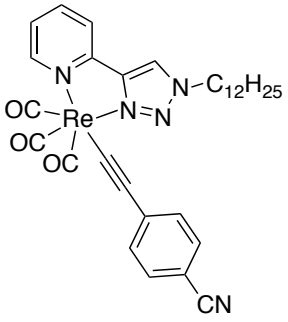
Trimethyl((4-nitrophenyl)ethynyl)silane (194 mg, 0.9 mmol, 1.0 equiv.) was dissolved in a mixture of tetrahydrofuran (5 mL) and methanol (5 mL), followed by the addition of potassium carbonate (261 mg, 2.6 mmol, 3.0 equiv.). The mixture was stirred at room temperature for 30 minutes. The mixture was filtered and the filtrate was concentrated. The residue was purified by column chromatography on silica gel (dichloromethane) to give the titled compound as a yellow solid (124 mg, 95% yield). ^{1}H NMR (300 MHz, Chloroform-*d*) δ 8.31 – 8.08 (m, 2H), 7.64 (d, *J* = 8.8 Hz, 2H), 3.36 (s, 1H). Characterisation in agreement with *Tetrahedron*, **2010**, *66*, 4230 – 4242.

General procedure 1: [2-(1-Dodecyl-1*H*-1,2,3-triazol-4-yl)pyridine]-chlorotricarbonylrhenium(I) (1.0 equiv.), silver trifluoromethanesulfonate (1.1 equiv.) and the corresponding ligand (1.1 equiv.) were added into a vial, followed by the addition of tetrahydrofuran (0.04 M) and triethylamine (4.0 equiv.). The resulting mixture was stirred at room temperature for 24 hours protected from light, evaporated in vacuum and the residue was purified by column chromatography on silica gel (cyclohexane: ethyl acetate = 1 : 1, v/v) to afford the expected product.



[2-(1-Dodecyl-1*H*-1,2,3-triazol-4-yl)pyridine][1-ethynyl-4-methoxybenzene]-tricarbonylrhenium(I), **33a**

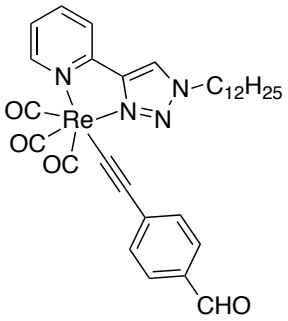
Prepared following the general procedure 1 starting from ((4-methoxyphenyl)ethynyl)trimethylsilane (50 mg, 0.38 mmol) and obtained as a yellow solid (37 mg, 14% yield). ^{1}H NMR (300 MHz, Chloroform-*d*) δ 9.06 (dt, *J* = 5.4, 1.2 Hz, 1H), 8.10 (s, 1H), 7.89 (td, *J* = 7.8, 1.6 Hz, 1H), 7.72 – 7.60 (m, 1H), 7.35 (dd, *J* = 7.3, 5.4 Hz, 1H), 6.89 (d, *J* = 8.8 Hz, 2H), 6.55 (d, *J* = 8.8 Hz, 1H), 4.59 – 4.32 (m, 2H), 3.67 (s, 3H), 2.09 – 1.87 (m, 2H), 1.47 – 1.13 (m, 18H), 0.88 (t, *J* = 6.3 Hz, 3H). ^{13}C NMR (75 MHz, Chloroform-*d*) δ 153.7, 149.4, 148.6, 138.0, 134.9, 132.7, 125.4, 122.4, 121.4, 120.6, 113.3, 55.3, 52.5, 32.1, 30.1, 29.8, 29.7, 29.5, 29.1, 26.5, 22.8, 14.3. IR: ν_{max}/cm^{-1} 2006, 1881 (CO).



[2-(1-Dodecyl-1*H*-1,2,3-triazol-4-yl)pyridine][4-ethynylbenzonitrile]-tricarbonylrhenium(I), **33b**

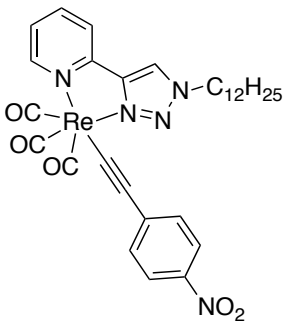
Prepared following the general procedure 1 starting from 4-ethynylbenzonitrile (50 mg, 0.39 mmol) and obtain as a yellow solid (123 mg, 44% yield). ^{1}H NMR (300 MHz, Chloroform-*d*) δ 9.10 (d, *J* = 5.6 Hz, 1H), 8.08 (s, 1H), 7.99 (td, *J* = 7.8, 1.5 Hz, 1H), 7.77 (d, *J* = 7.8 Hz, 1H), 7.44 – 7.37 (m, 1H), 7.31 – 7.27 (m, 2H), 7.00 (d, *J* = 8.4 Hz, 2H), 4.59 – 4.43 (m, 2H), 2.13 – 2.01 (m, 2H), 1.39 – 1.16 (m, 16H), 0.97 – 0.73 (m, 3H). ^{13}C NMR (75 MHz, $CDCl_3$) δ 197.8,

196.4, 192.4, 153.7, 149.4, 148.6, 138.5, 134.4, 133.0, 132.0, 131.4, 125.6, 122.3, 121.5, 119.7, 107.3, 105.7, 52.6, 32.0, 30.1, 29.7, 29.6, 29.5, 29.0, 26.5, 22.8, 14.3. IR: ν_{max}/cm^{-1} 2088, 2004, 1886 (CO).



[2-(1-Dodecyl-1*H*-1,2,3-triazol-4-yl)pyridine] [4-ethynylbenzaldehyde]-tricarbonylrhenium(I), **33c**

Prepared following the general procedure 1 starting from 4-ethynylbenzaldehyde (50 mg, 0.38 mmol) and obtain as a yellow solid (152 mg, 60% yield).^{1}H NMR (300 MHz, Chloroform-*d*) δ 9.80 (s, 1H), 9.10 (dd, *J* = 5.6, 1.4 Hz, 1H), 8.09 (s, 1H), 7.98 (td, *J* = 7.8, 1.4 Hz, 1H), 7.77 (d, *J* = 7.8 Hz, 1H), 7.52 (d, *J* = 8.3 Hz, 1H), 7.41 (dd, *J* = 7.5, 5.6 Hz, 1H), 7.06 (d, *J* = 8.3 Hz, 2H), 4.63 – 4.40 (m, 2H), 2.13 – 1.93 (m, 2H), 1.49 – 1.21 (m, 16H), 0.96 – 0.76 (m, 3H). ^{13}C NMR (75 MHz, Chloroform-*d*) δ 197.8, 196.5, 192.5, 191.7, 153.7, 149.3, 148.6, 138.6, 134.8, 134.8, 132.7, 132.0, 129.4, 125.6, 122.4, 121.6, 106.7, 52.6, 32.0, 30.1, 29.7, 29.6, 29.5, 29.0, 26.5, 22.8, 14.3. IR: ν_{max}/cm^{-1} 2087, 2004,1889 (CO).

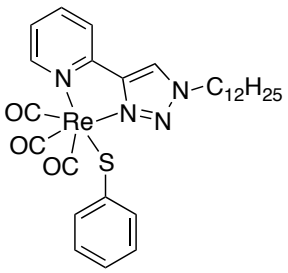


[2-(1-Dodecyl-1*H*-1,2,3-triazol-4-yl)pyridine] [1-ethynyl-4-nitrobenzene]-tricarbonylrhenium(I), **33d**

Prepared following the general procedure 1 starting from 1-ethynyl-4-nitrobenzene (50 mg, 0.34 mmol) and obtain as a yellow solid (129 mg, 52% yield). 1H NMR (300 MHz, Chloroform-d) δ 9.08 (dd, J = 5.6, 1.6 Hz, 1H), 8.11 (s, 1H), 7.99 (td, J = 7.8, 1.6 Hz, 1H), 7.86 (d, J = 9.0 Hz, 2H), 7.82 – 7.73 (m, 1H), 7.41 (dd, J = 7.7, 5.6 Hz, 1H), 7.02 (d, J = 9.0 Hz, 2H), 4.64 – 4.37 (m, 2H), 2.16 – 1.87 (m, 2H), 1.44 – 1.18 (m, 18H), 0.95 – 0.78 (m, 3H). 13C NMR (75 MHz, Chloroform-*d*) δ 197.6, 192.5, 153.8, 149.4, 148.6, 144.3, 138.6, 137.4, 135.4, 131.95, 125.7, 123.2, 122.2, 121.5, 106.2, 52.6, 32.0, 30.1, 29.7, 29.6, 29.5, 29.0, 26.5, 22.8, 14.3. IR: ν_{max}/cm^{-1} 2088, 2005, 1885 (CO).

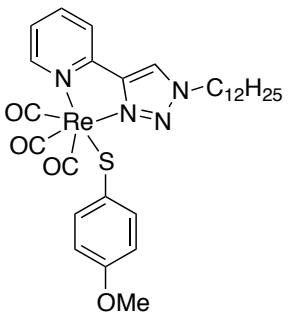
4.2.3 Synthesis of Rhenium complexes with arenethiolate ligands

General procedure 2: [2-(1-Dodecyl-1*H*-1,2,3-triazol-4-yl)pyridine]-chlorotricarbonylrhenium(I) or [2-(4-Dodecyl-1*H*-1,2,3-triazol-1-yl)pyridine]-chlorotricarbonylrhenium(I) (1.0 eq) was added into a vial, followed by a tetrahydrofuran (0.04 M). Silver trifluoromethanesulfonate (1.1 eq) was added in the dark. The mixture was stirred at room temperature protected from light for 2 hours. The mixture was filtered and the residue was washed with tetrahydrofuran (3 mL). The collected solution was introduced into another vial, followed by the corresponding ligand (1.0 eq) and triethylamine (4.0 eq). The resulting mixture was stirred at room temperature for 24 hours, evaporated in vacuum and the residue was purified by column chromatography on silica gel (cyclohexane: ethyl acetate = 3 :7, v/v) to afford the expected product.



[2-(1-Dodecyl-1*H*-1,2,3-triazol-4-yl)pyridine][benzenethiolate]-tricarbonylrhenium(I), **37a**

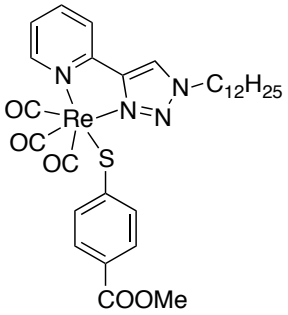
Prepared following the general procedure 2 starting from [2-(1-Dodecyl-1*H*-1,2,3-triazol-4-yl)pyridine]-chlorotricarbonylrhenium(I) (50 mg, 0.08 mmol) and obtain as a yellow solid (25 mg, 45% yield). ^{1}H NMR (300 MHz, Acetone-d_6) δ 8.91 (d, J = 5.6 Hz, 1H), 8.80 (s, 1H), 8.18 – 8.06 (m, 1H), 7.98 (d, J = 7.8 Hz, 1H), 7.60 – 7.49 (m, 1H), 6.81 – 6.62 (m, 5H), 4.61 (t, J = 7.2 Hz, 2H), 1.51 – 1.16 (m, 18H), 0.87 (t, J = 6.5 Hz, 3H).^{13}C NMR (75 MHz, Acetone-d_6) δ 153.8, 149.9, 148.8, 144.8, 140.0, 135.2, 130.2, 128.3, 127.6, 126.6, 125.2, 123.3, 122.9, 52.8, 32.6, 30.6, 30.3, 30.2, 30.13, 30.05, 29.7, 27.0, 23.3, 14.4. HRMS (ESI+): m/z calculated for $C_{28}H_{35}N_4NaO_3ReS$: 717.1885 $[M + Na]^+$; found: 717.1878. IR: ν_{max}/cm^{-1} 2013, 1891 (CO).



[2-(1-Dodecyl-1*H*-1,2,3-triazol-4-yl)pyridine]-[4-methoxybenzenethiolate]-tricarbonylrhenium(I), **37b**

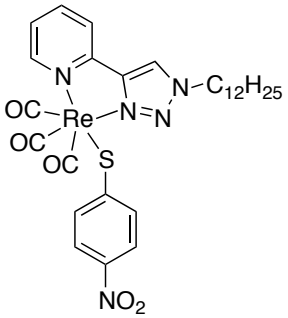
Prepared following the general procedure 2 starting from [2-(1-Dodecyl-1*H*-1,2,3-triazol-4-yl)pyridine]-chlorotricarbonylrhenium(I) (50 mg, 0.08 mmol) and obtain as a yellow solid (12

mg, 20% yield). ^{1}H NMR (300 MHz, Acetone-d_6) δ 8.99 – 8.91 (m, 2H), 8.23 – 8.14 (m, 1H), 8.14 – 8.07 (m, 1H), 7.66 – 7.54 (m, 1H), 7.48 – 7.37 (m, 2H), 7.09 – 6.98 (m, 2H), 4.64 (t, J = 7.2 Hz, 2H), 3.78 (s, 3H), 1.50 – 1.14 (m, 18H), 0.92 – 0.81 (m, 3H). ^{13}C NMR (75 MHz, Acetone-d_3) δ 157.4, 153.8, 149.8, 139.9, 136.1, 134.2, 126.6, 125.1, 122.8, 113.3, 55.4, 52.7, 32.6, 27.1, 23.3, 14.4. HRMS (ESI+): m/z calculated for $C_{29}H_{37}N_4NaO_4ReS$: 747.1991 [M + Na]$^+$; found: 747.1977. IR: ν_{max}/cm^{-1} 2013,1897 (CO).



[2-(1-Dodecyl-1*H*-1,2,3-triazol-4-yl)pyridine]- [methyl-4-carboxylatebenzenethiolate]-tricarbonylrhenium(I), **37c**

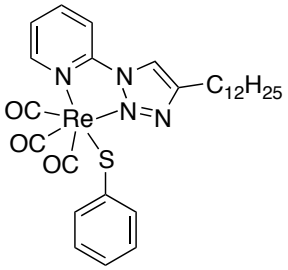
Prepared following the general procedure 2 starting from [2-(1-Dodecyl-1*H*-1,2,3-triazol-4-yl)pyridine]-chlorotricarbonylrhenium(I) (50 mg, 0.08 mmol) and obtain as an orange solid (29 mg, 48% yield). ^{1}H NMR (300 MHz, Acetone-d_6) δ 8.99 – 8.91 (m, 2H), 8.23 – 8.14 (m, 1H), 8.14 – 8.07 (m, 1H), 7.66 – 7.54 (m, 1H), 7.48 – 7.37 (m, 2H), 7.09 – 6.98 (m, 2H), 4.64 (d, J = 7.2 Hz, 2H), 3.78 (s, 3H), 1.50 – 1.14 (m, 18H), 0.92 – 0.81 (m, 3H). ^{13}C NMR (75 MHz, Acetone-d_6) δ 167.4, 155.3, 154.0, 150.0, 149.1, 140.5, 134.2, 128.7, 126.9, 125.6, 124.6, 123.2, 52.9, 51.8, 32.6, 30.6, 30.3, 29.7, 27.0, 23.3, 14.4. HRMS (ESI+): m/z calculated for $C_{30}H_{37}N_4NaO_5ReS$: 775.1940 [M + Na]$^+$; found: 775.1933. IR: ν_{max}/cm^{-1} 2015, 1897 (CO).



[2-(1-Dodecyl-1*H*-1,2,3-triazol-4-yl)pyridine]- [4-nitrobenzenethiolate]-tricarbonylrhenium(I), **37d**

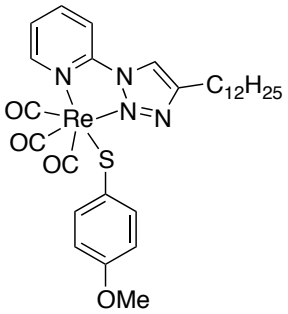
Prepared following the general procedure 2 starting from [2-(1-Dodecyl-1*H*-1,2,3-triazol-4-yl)pyridine]-chlorotricarbonylrhenium(I) (50 mg, 0.08 mmol) and obtain as an orange solid (32 mg, 54% yield). ^{1}H NMR (300 MHz, Acetone-d_6) δ 9.06 – 8.99 (m, 2H), 8.30 – 8.14 (m, 2H), 7.74 – 7.68 (m, 2H), 7.68 – 7.60 (m, 1H), 7.29 – 7.17 (m, 2H), 4.68 (t, J = 7.2 Hz, 2H), 1.42 – 1.19 (m, 18H), 0.92 – 0.81 (m, 3H). ^{13}C NMR (75 MHz, Acetone-d_6) δ 161.1, 154.2, 150.1, 149.3, 143.7, 140.8, 133.9, 127.7, 127.1, 126.0, 125.3, 123.4, 122.8, 53.0, 32.6, 30.6, 30.2, 29.6,

27.0, 23.3, 14.4. HRMS (ESI+): m/z calculated for $C_{28}H_{34}N_5NaO_5ReS$: 762.1736 $[M + Na]^+$; found: 762.1707. IR: ν_{max}/cm^{-1} 2018, 1904 (CO).



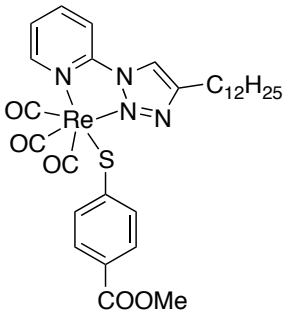
[2-(4-Dodecyl-1*H*-1,2,3-triazol-1-yl)pyridine] [benzenethiolate]-tricarbonylrhenium(I), **38a**

Prepared following the general procedure 2 starting from [2-(4-Dodecyl-1*H*-1,2,3-triazol-1-yl)pyridine]-chlorotricarbonylrhenium(I) (50 mg, 0.08 mmol) and obtain as an orange solid (21 mg, 37% yield). ^{1}H NMR (300 MHz, Acetone-d_6) δ 8.90 (d, J = 4.9 Hz, 1H), 8.80 (s, 1H), 8.37 – 8.25 (m, 1H), 8.04 (d, J = 8.4 Hz, 1H), 7.73 – 7.62 (m, 1H), 6.77 (t, J = 7.1 Hz, 1H), 6.69 – 6.51 (m, 4H), 1.85 – 1.68 (m, 2H), 1.56 – 1.17 (m, 18H), 0.93 – 0.82 (m, 3H). ^{13}C NMR (75 MHz, Acetone-d_6) δ 153.3, 152.7, 147.7, 142.5, 135.3, 133.4, 127.9, 126.8, 123.9, 122.1, 114.8, 32.6, 30.4, 30.3, 29.4, 26.1, 23.3, 14.4. HRMS (ESI+): m/z calculated for $C_{28}H_{35}N_4NaO_3ReS$: 717.1885 $[M + Na]^+$; found: 717.1875. IR: ν_{max}/cm^{-1} 2019, 1904 (CO).



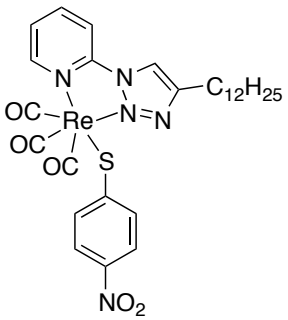
[2-(4-Dodecyl-1*H*-1,2,3-triazol-1-yl)pyridine] [4-methoxybenzenethiolate]-tricarbonylrhenium(I), **38b**

Prepared following the general procedure 2 starting from [2-(4-Dodecyl-1*H*-1,2,3-triazol-1-yl)pyridine]-chlorotricarbonylrhenium(I) (50 mg, 0.08 mmol) and obtain as an orange solid (20 mg, 35% yield). ^{1}H NMR (300 MHz, Acetone-d_6) δ 8.95 (d, J = 5.6 Hz, 1H), 8.84 (s, 1H), 8.42 – 8.29 (m, 1H), 8.07 (d, J = 8.4 Hz, 1H), 7.78 – 7.66 (m, 1H), 6.38 (d, J = 8.2 Hz, 2H), 6.25 (d, J = 8.2 Hz, 2H), 3.67 (d, J = 1.8 Hz, 3H), 1.90 – 1.76 (m, 2H), 1.56 – 1.26 (m, 18H), 0.97 – 0.86 (m, 3H). ^{13}C NMR (75 MHz, Acetone-d_6) δ 159.5, 153.7, 153.0, 148.2, 144.3, 143.3, 134.5, 127.2, 122.9, 122.8, 115.3, 32.6, 30.4, 30.3, 30.0, 29.8, 29.4, 26.1, 23.3, 14.4. HRMS (ESI+): m/z calculated for $C_{28}H_{34}N_5NaO_5ReS$: 762.1736 $[M + Na]^+$; found: 762.1728. IR: ν_{max}/cm^{-1} 2019, 1909 (CO).



[2-(4-Dodecyl-1*H*-1,2,3-triazol-1-yl)pyridine] [methyl-4-carboxylatebenzenethiolate]-tricarbonylrhenium(I), **38c**

Prepared following the general procedure 2 starting from [2-(4-Dodecyl-1*H*-1,2,3-triazol-1-yl)pyridine]-chlorotricarbonylrhenium(I) (50 mg, 0.08 mmol) and obtain as an orange solid (34 mg, 56% yield). ^{1}H NMR (300 MHz, Acetone-d_6) δ 9.00 – 8.90 (m, 2H), 8.45 – 8.33 (m, 1H), 8.22 (d, J = 8.4 Hz, 1H), 7.79 – 7.68 (m, 1H), 7.37 (d, J = 8.4 Hz, 2H), 6.89 (d, J = 8.4 Hz, 2H), 3.79 (s, 3H), 1.83 – 1.66 (m, 2H), 1.34 – 1.25 (m, 18H), 0.93 – 0.82 (m, 3H).^{13}C NMR (75 MHz, Acetone-d_6) δ 167.3, 153.7, 153.5, 152.8, 148.0, 143.0, 134.7, 128.8, 127.0, 125.3, 122.5, 115.0, 51.9, 32.6, 30.4, 30.3, 30.0, 29.8, 29.4, 26.1, 23.3, 14.4. HRMS (ESI+): m/z calculated for $C_{30}H_{37}N_4NaO_5ReS$: 775.1940 $[M + Na]^+$; found: 775.1921. IR: ν_{max}/cm^{-1} 2018, 1894 (CO).



[2-(4-Dodecyl-1*H*-1,2,3-triazol-1-yl)pyridine] [4-nitrobenzenethiolate]-tricarbonylrhenium(I), **38d**

Prepared following the general procedure 2 starting from [2-(4-Dodecyl-1*H*-1,2,3-triazol-1-yl)pyridine]-chlorotricarbonylrhenium(I) (50 mg, 0.08 mmol) and obtain as a yellow solid (22 mg, 37% yield). ^{1}H NMR (300 MHz, Acetone-d_6) δ 9.05 (s, 1H), 9.01 (d, J = 5.6 Hz, 0H), 8.51 – 8.39 (m, 1H), 8.32 (d, J = 8.4 Hz, 1H), 7.84 – 7.72 (m, 1H), 7.66 (d, J = 9.0 Hz, 1H), 7.12 (d, J = 9.0 Hz, 1H), 1.75 (d, J = 7.5 Hz, 2H), 1.49 – 1.17 (m, 18H), 0.93 – 0.82 (m, 3H). ^{13}C NMR (75 MHz, Acetone-d_6) δ 157.9, 153.3, 152.6, 147.6, 142.35, 136.1, 132.7, 126.7, 121.8, 114.7, 113.7, 55.4, 32.6, 26.1, 23.3, 14.4. HRMS (ESI+): m/z calculated for $C_{29}H_{38}N_4O_4ReS$: 725.2171 $[M + H]^+$; found: 725.2149. IR: ν_{max}/cm^{-1} 2023, 1913 (CO).

4.2.4 Luminescence quantum yield determination

Emission spectra were recorded at two concentrations and for three different excitation wavelengths (at the absorption maximum λ^{max}_{abs} and around λ^{max}_{abs} - 10 and λ^{max}_{abs} + 10). The

average integrated emission area *F* for the six measurements is used to determine the quantum yield in the equation

$$\emptyset s = \emptyset r \left(\frac{Ar}{As}\right)\left(\frac{Fs}{Fr}\right)\left(\frac{ns^2}{nr^2}\right)$$

where the subscripts s and r refer to the sample and the standard reference solution, respectively, n is the refractive index of the solvents, F is the integrated emission intensity, A is the absorbance at the excitation wavelength (A< 0.1), and ∅ is the luminescence quantum yield. Quinine sulfate in 0.1 N sulfuric acid was used as the standard with a known emission quantum yield of 0.546 (λ_{ex} 330–350 nm).

4.2.5 DFT calculations

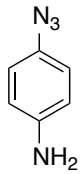
The calculations were performed using the Gaussian 09 program package. Geometries of all complexes were optimized for the singlet states with the DFT method using the hybrid B3LYP functional and the 6-311G** basis set for all atoms except rhenium, for which the LANL2DZ basis set was used. Vibrational harmonic frequency analysis of the optimized geometries was used to ensure that there were true local minima with no imaginary frequencies. The solvent effect was simulated using the polarizable continuum model (PCM) for acetonitrile. The intensities of the ten lowest-energy electronic transitions were calculated using the TD-DFT method with the B3LYP functional, and the solvent effect was simulated using the polarizable continuum model (PCM) for acetonitrile.

4.2.6 Electrochemistry

Cyclic voltammetry was performed with a classical three-electrode single compartment cell at room temperature, using a microcarbon fiber electrode (33 μm dia., IJ Cambria Scientific Ltd., U.K.), a Pt wire counter electrode, and a Ag/AgCl wire pseudoreference electrode. The experiments were performed using a VSP Potentiostat (Bio-Logic, France). Fc/Fc+ (0.46 V vs saturated calomel electrode (SCE)) was used as an internal standard. The working electrode was polished with 1200 grit and then 2400 grit SiC papers, and at the start of each experiment with 3 and 0.3 μm diamond pastes followed by extensive rinsing and sonication with ultrapure water and ethanol. MeCN solutions containing 0.1 M Bu_4NPF_6 as the supporting electrolyte were deaerated with Ar or saturated with CO2 for at least 10 min before cyclic voltammograms (CVs) were recorded.

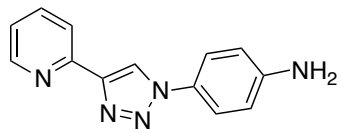
4.3 Synthesis for catalysts for CO_2 electroreduction

4.3.1 Synthesis of catalysts for covalent immobilisation method



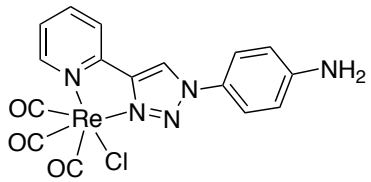
4-Azidoaniline, **77**

4-Iodoaniline (1.0 g, 4.57 mmol, 1.0 equiv.) was dissolved in a mixture of dimethyl sulfoxide (10 mL) and water (2 mL), followed by the addition of NaN_3 (594 mg, 9.13 mmol, 2.0 equiv.), sodium ascorbate (53 mg, 0.27 mmol, 0.06 equiv.), copper(I) iodide (88 mg, 0.46 mmol, 0.12 equiv.) and N^1,N^2-dimethylethane-1,2-diamine (74 μL, 0.69 mmol, 0.15 equiv.). The mixture was stirred at room temperature overnight. The mixture was diluted with water and extracted by ethyl acetate. The organic phase was dried over sodium sulfate, filtered and concentrated. The residue was purified by column chromatography on silica gel (dichloromethane : ethyl acetate = 4 : 1, v/v) to afford the titled compound as a brown solid (513 mg, 84% yield). ^{1}H NMR (300 MHz, Chloroform-*d*) δ 6.84 (d, *J* = 8.7 Hz, 2H), 6.67 (d, *J* = 8.7 Hz, 2H), 3.64 (s, 2H). ^{13}C NMR (75 MHz, Chloroform-*d*) δ 143.9, 130.3, 120.1, 116.4, 77.6, 77.2, 76.7.



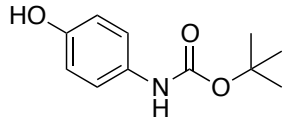
4-(4-(Pyridin-2-yl)-1*H*-1,2,3-triazol-1-yl)aniline, **78**

2-Ethynylpyridine (188 μL, 1.86 mmol, 1.0 equiv.) and 4-azidoaniline (150 mg, 1.86 mmol, 1.0 equiv.) were dissolved in *tert*-butanol (10 mL), followed by the addition of an aqueous solution (3 mL) of sodium ascorbate (111 mg, 0.56 mmol, 0.3 equiv.) and an aqueous solution (3 mL) of copper sulfate pentahydrate (47 mg, 0.19 mmol, 0.1 equiv.). The mixture was heated at 70 ^{o}C for 12 hours, followed by extraction by water and dichloromethane. The organic phase was dried over sodium sulfate, filtered and concentrated. The residue was purified by column chromatography on silica gel (cyclohexane : ethyl acetate = 3:1, v/v) to afford the titled compound as a pale yellow solid (301 mg, 68% yield). ^{1}H NMR (300 MHz, Chloroform-*d*) δ 8.60 (d, *J* = 4.9 Hz, 1H), 8.45 (s, 1H), 8.23 (d, *J* = 7.8 Hz, 1H), 7.75 – 7.83 (m, 1H), 7.57 – 7.49 (m, 2H), 7.26 – 7.21 (m, 1H), 6.77 (d, *J* = 8.8 Hz, 2H), 3.94 (s, 2H). ^{13}C NMR (75 MHz, Chloroform-*d*) δ 150.3, 149.5, 148.6, 147.4, 137.1, 128.6, 123.0, 122.3, 120.5, 120.2, 115.4.



[4-(4-(Pyridin-2-yl)-1*H*-1,2,3-triazol-1-yl)aniline]-chlorotricarbonylrhenium(I), **70**

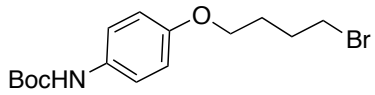
4-(4-(Pyridin-2-yl)-1*H*-1,2,3-triazol-1-yl)aniline (100 mg, 0.42 mmol, 1.0 equiv.) was dissolved in toluene (5 mL) and the solution was heated at 120 °C. Then pentacarbonylchlororhenium(I) (152 mg, 0.42 mmol, 1.0 equiv.) was added and the mixture was heated at 120 °C for 12 hours. After cooling to room temperature, the suspension was filtered and the residue washed with toluene and dried under vacuum to afford the titled compound as a pale yellow solid (201 mg, 87% yield). ^{1}H NMR (300 MHz, dimethyl sulfoxide-d_6) δ 9.70 (s, 1H), 8.99 (d, J = 5.5 Hz, 1H), 8.30 – 8.38 (m, 1H), 8.26 (d, J = 7.7 Hz, 1H), 7.71 – 7.64 (m, 1H), 7.62 (d, J = 8.8 Hz, 2H), 6.76 (d, J = 8.8 Hz, 2H), 5.82 (s, 2H).^{13}C NMR (75 MHz, Dimethyl sulfoxide-d_6) δ 197.6, 196.8, 189.6, 153.1, 150.9, 148.8, 148.7, 140.8, 126.6, 124.3, 123.3, 122.6, 122.3, 113.9. HPLC (5 to 100% ACN in 10 min): rt 7.00 minutes (>95%). IR: ν_{max}/cm^{-1} 2023, 1932, 1990, 1883 (CO).



tert-Butyl (4-hydroxyphenyl)carbonate, **79**

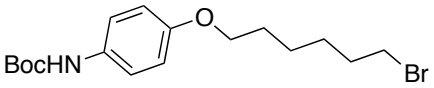
4-Aminophenol (500 mg, 4.60 mmol, 1 equiv.) was dissolved in methanol (15 mL), followed by the addition of di-tert-butyl dicarbonate (1.3 mL, 5.52 mmol, 1.2 equiv.). The mixture was stirred at 100 °C overnight. Then the mixture was cooled to room temperature, diluted with water and extracted with dichloromethane. The organic phase was dried over sodium sulfate, filtered and concentrated. The residue was purified by column chromatography on silica gel (dichloromethane:ethyl acetate 9:1, v/v) to afford 1 as a white solid (908 mg, 94% yield). ^{1}H NMR (300 MHz, Chloroform-*d*) δ 7.17 (d, J = 8.8 Hz, 2H), 6.73 (d, J = 8.8 Hz, 2H), 6.33 (s, 1H), 1.51 (s, 9H). Characterisation in agreement with *Tetrahedron*, 2006, *62*, 11599 – 11607.

General procedure 3: The corresponding dibromoalkane (3.0 equiv.) was dissolved in acetone (0.3 M). Then potassium carbonate (3.0 equiv.) and *tert*-butyl (4-hydroxyphenyl)carbamate (1.0 equiv.) were added into the mixture. The mixture was heated at 60 °C overnight. Then the reaction mixture was cooled to room temperature and filtered. The filtrate was dried over sodium sulfate, filtered and concentrated. The residue was purified by column chromatography on silica gel (cyclohexane : ethyl acetate = 19:1, v/v).



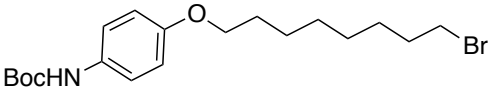
tert-Butyl (4-(4-bromobutoxy)phenyl)carbonate, **80a**

Prepared following the general procedure 3 starting from 1,4-dibromobutane (344 μL, 2.88 mmol) and obtained as a white solid (227 mg, 69% yield). R_f = 0.34 (cyclohexane : ethyl acetate = 10:1, v/v). ^{1}H NMR (300 MHz, Methanol-d_4) δ 5.72 (d, J = 9.0 Hz, 2H), 5.29 (d, J = 9.0 Hz, 2H), 2.43 (t, J = 6.1 Hz, 2H), 1.98 (t, J = 6.6 Hz, 2H), 0.55 – 0.42 (m, 2H), 0.42 – 0.30 (m, 2H), -0.04 (s, 9H). ^{13}C NMR (75 MHz, Methanol-d_4) δ 156.3, 155.8, 133.5, 121.9, 115.7, 80.6, 68.4, 34.1, 30.8, 29.1, 28.7. HRMS (ESI+): m/z calculated for $C_{15}H_{22}BrNNaO_3$: 366.0675 $[M + Na]^+$; found: 366.0674.



tert-Butyl (4-((6-bromohexyl)oxy)phenyl)carbamate, **80b**

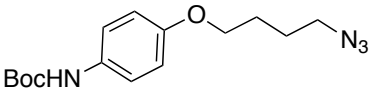
Prepared following the general procedure 3 starting from 1,6-dibromohexane (444 μL, 2.88 mmol) and obtain as a white solid (271 mg, 76% yield). R_f = 0.29 (cyclohexane : ethyl acetate = 10:1, v/v). ^{1}H NMR (300 MHz, Methanol-d_4) δ 7.25 (d, J = 9.0 Hz, 2H), 6.82 (d, J = 9.0 Hz, 2H), 3.93 (t, J = 6.3 Hz, 2H), 3.46 (t, J = 6.7 Hz, 2H), 1.94 – 1.82 (m, 2H), 1.82 – 1.71 (m, 2H), 1.50 (s, 13H). ^{13}C NMR (75 MHz, Methanol-d_4) δ 156.4, 155.8, 133.4, 121.9, 115.7, 80.6, 69.1, 34.3, 33.9, 30.3, 29.0, 28.7, 26.4. HRMS (ESI+): m/z calculated for $C_{17}H_{26}BrNNaO_3$: 394.0988 $[M + Na]^+$; found: 394.0978.



tert-Butyl (4-((8-bromooctyl)oxy)phenyl)carbamate, **80c**

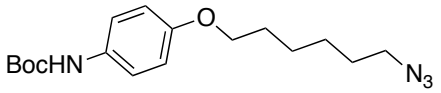
Prepared following the general procedure 1 starting from 1,8-dibromooctane (530 μL, 2.88 mmol) and obtain as a white solid (299 mg, 78% yield). R_f = 0.35 (cyclohexane : ethyl acetate = 10:1, v/v). ^{1}H NMR (300 MHz, Methanol-d_4) δ 7.25 (d, J = 9.0 Hz, 2H), 6.81 (d, J = 9.0 Hz, 2H), 3.92 (t, J = 6.4 Hz, 2H), 3.44 (t, J = 6.7 Hz, 2H), 1.93 – 1.80 (m, 2H), 1.80 – 1.67 (m, 2H), 1.62 – 1.27 (m, 17H). ^{13}C NMR (75 MHz, Methanol-d_4) δ 156.5, 155.8, 133.4, 121.9, 115.7, 80.6, 69.3, 34.4, 34.0, 30.4, 30.3, 29.8, 29.1, 28.8, 27.1. HRMS (ESI+): m/z calculated for $C_{19}H_{30}BrNNaO_3$: 422.1301$[M + Na]^+$; found: 422.1305.

General procedure 4: The corresponding compound **80** (1.0 equiv.) and sodium azide (2.0 equiv.) were dissolved in N,N-dimethylformamide (0.06 M). The mixture was heated at 80 ˚C overnight. Then it was cooled to room temperature. The mixture was diluted with water and extracted with dichloromethane. The organic phase was dried over sodium sulfate, filtered and concentrated to give the titled compound.



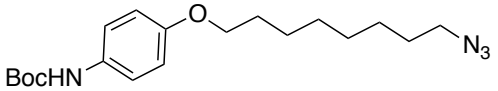
tert-Butyl (4-(4-azidobutoxy)phenyl)carbamate, **81a**

Prepared following the general procedure 4 starting from *tert*-Butyl (4-(4-bromobutoxy)phenyl)carbonate (227 mg, 0.66 mmol) and obtain as a yellow solid (189 mg, 94% yield). R_f = 0.42 (dichloromethane). ^{1}H NMR (300 MHz, Dimethyl sulfoxide-d_6) δ 9.09 (s, 1H), 7.33 (d, *J* = 9.0 Hz, 2H), 6.82 (d, *J* = 9.0 Hz, 2H), 3.92 (t, *J* = 5.9 Hz, 2H), 3.39 (t, *J* = 6.5 Hz, 2H), 1.79 – 1.60 (m, 4H), 1.46 (s, 9H). ^{13}C NMR (75 MHz, Dimethyl sulfoxide-d_6) δ 153.7, 152.9, 132.6, 119.6, 114.4, 78.6, 67.0, 50.4, 28.2, 26.0, 25.1. HRMS (ESI+): m/z calculated for $C_{15}H_{22}N_4NaO_3$: 329.1584 $[M + Na]^+$; found 329.1588.



tert-butyl (4-((6-azidohexyl)oxy)phenyl)carbamate, **81b**

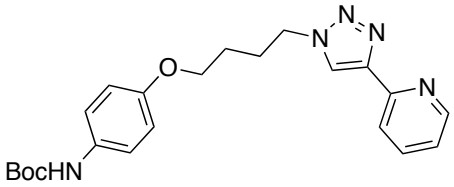
Prepared following the general procedure 4 starting from *tert*-Butyl (4-((6-bromohexyl)oxy)phenyl)carbamate (100 mg, 0.27 mmol) and obtain as a pale yellow solid (88 mg, 98% yield). R_f = 0.31 (dichloromethane). ^{1}H NMR (300 MHz, Acetone-d_6) δ 7.44 (d, *J* = 9.0 Hz, 2H), 6.85 (d, *J* = 9.0 Hz, 2H), 3.95 (t, *J* = 6.4 Hz, 2H), 3.35 (t, *J* = 6.8 Hz, 2H), 1.85 – 1.70 (m, 2H), 1.70 – 1.57 (m, 2H), 1.57 – 1.40 (m, 13H). ^{13}C NMR (75 MHz, Acetone-d_6) δ 155.6, 153.9, 133.7, 120.6, 115.4, 79.6, 68.6, 52.0, 28.6, 27.2, 26.4. HRMS (ESI+): m/z calculated for $C_{17}H_{26}N_4NaO_3$: 357.1897 $[M + Na]^+$; found 357.1893.



tert-Butyl (4-((8-azidooctyl)oxy)phenyl)carbamate, **81c**

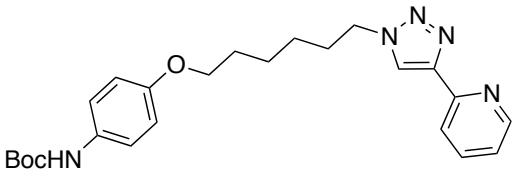
Prepared following the general procedure 4 starting from *tert*-Butyl (4-(8-bromooxtyl)phenyl)carbonate (299 mg, 0.75 mmol) and obtain as a yellow solid (263 mg, 97% yield). R_f = 0.22 (dichloromethane). ^{1}H NMR (300 MHz, Dimethyl sulfoxide-d_6) δ 9.08 (s, 1H), 7.32 (d, *J* = 9.0 Hz, 2H), 6.80 (d, *J* = 9.0 Hz, 2H), 3.88 (t, *J* = 6.4 Hz, 2H), 3.29 (d, *J* = 6.4 Hz, 2H), 1.72 – 1.61 (m, 2H), 1.58 – 1.48 (m, 2H), 1.45 (s, 9H), 1.42 – 1.26 (m, 8H). ^{13}C NMR (75 MHz, Dimethyl sulfoxide-d_6) δ 153.9, 152.9, 132.5, 119.6, 114.4, 78.6, 67.5, 50.6, 28.7, 28.6, 28.5, 28.2, 28.2, 26.1, 25.4. HRMS (ESI+): m/z calculated for $C_{19}H_{30}N_4NaO_3$: 385.2210 $[M + Na]^+$; found 385.2211.

General procedure 5: The corresponding compound **81** (1.0 equiv.) and 2-ethynylpyridine (1.0 equiv.) were dissolved in a mixture of dichloromethane (0.08 M) and water (1/2 volume of dichloromethane). Then copper sulfate pentahydrate (0.3 equiv.) and sodium ascorbate (0.1 equiv.) were added and the mixture was stirred at room temperature overnight. The mixture was diluted with water and extracted with dichloromethane. The organic phase was dried over sodium sulfate, filtered and concentrated. The residue was purified by column chromatography on silica gel (dichloromethane : ethyl acetate 1:1 → ethyl acetate, v/v) to afford the titled compound.



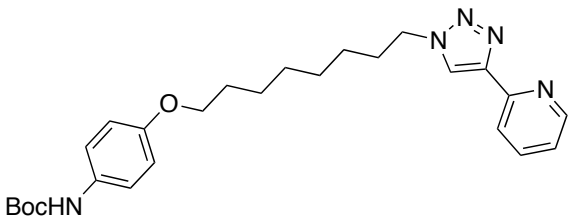
tert-Butyl (4-(4-(4-(pyridin-2-yl)-1*H*-1,2,3-triazol-1-yl)butoxy)phenyl)carbamate, **82a**

Prepared following the general procedure 5 starting from *tert*-Butyl (4-(4-azidobutoxy)phenyl)carbamate (143 mg, 0.33 mmol) and obtain as a pale yellow solid (151 mg, 78% yield). R_f = 0.40 (dichloromethane : ethyl acetate = 1:1, v/v). ^{1}H NMR (300 MHz, Methanol-d_4) δ 8.57 (d, J = 5.0 Hz, 1H), 8.44 (s, 1H), 8.06 (d, J = 7.7 Hz, 1H), 7.87 – 7.93 (m, 1H), 7.36 (dd, J = 7.7, 5.0 Hz, 1H), 7.24 (d, J = 9.0 Hz, 2H), 6.82 (d, J = 9.0 Hz, 2H), 4.57 (t, J = 7.1 Hz, 2H), 3.98 (t, J = 6.1 Hz, 2H), 2.24 – 2.08 (m, 2H), 1.89 – 1.67 (m, 2H), 1.50 (s, 9H). ^{13}C NMR (75 MHz, Methanol-d_4) δ 156.2, 155.7, 151.1, 150.4, 148.7, 138.9, 133.6, 124.5, 124.2, 121.8, 121.6, 115.7, 80.6, 68.4, 51.3, 28.7, 28.2, 27.4. HRMS (ESI+): m/z calculated for $C_{22}H_{27}N_5NaO_3$: 432.2006 $[M + Na]^+$; found 432.2009.



tert-Butyl (4-((6-(4-(pyridin-2-yl)-1*H*-1,2,3-triazol-1-yl)hexyl)oxy)phenyl)carbamate, **82b**

Prepared following the general procedure 5 starting from *tert*-butyl (4-((6-azidohexyl)oxy)phenyl)carbamate (109 mg, 0.33 mmol) and obtain as a pale yellow solid (111 mg, 77% yield). R_f = 0.29 (dichloromethane : ethyl acetate = 1:1, v/v). ^{1}H NMR (300 MHz, Methanol-d_4) δ 8.57 (d, J = 4.9 Hz, 1H), 8.41 (s, 1H), 8.06 (d, J = 7.8 Hz, 1H), 7.88 – 7.94 (m, 1H), 7.36 (dd, J = 7.8, 4.9 Hz, 1H), 7.23 (d, J = 9.0 Hz, 2H), 6.79 (d, J = 9.0 Hz, 2H), 4.50 (t, J = 7.0 Hz, 2H), 3.91 (t, J = 6.3 Hz, 2H), 1.97 – 2.03 (m, 2H), 1.84 – 1.68 (m, 2H), 1.63 – 1.36 (m, 13H). ^{13}C NMR (75 MHz, Methanol-d_4) δ 156.4, 155.8, 151.1, 150.4, 148.6, 138.9, 133.4, 124.5, 124.1, 121.8, 121.5, 115.7, 80.6, 69.1, 51.5, 31.2, 30.2, 28.8, 27.2, 26.6. HRMS (ESI+): m/z calculated for $C_{24}H_{31}N_5NaO_3$: 460.2325$[M + Na]^+$; found 460.2307. HRMS (ESI+): m/z calculated for $C_{24}H_{32}N_5O_3$: 438.2300$[M + H]^+$; found 438.2480.

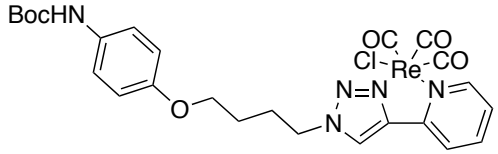


tert-Butyl (4-((8-(4-(pyridin-2-yl)-1*H*-1,2,3-triazol-1-yl)octyl)oxy)phenyl)carbamate, **82c**

Prepared following the general procedure 5 starting from *tert*-butyl (4-((8-azidooctyl)oxy)phenyl)carbamate (162 mg, 0.45 mmol) and obtain as a white solid (157 mg, 75% yield). Follow the general procedure 3. Yield: 75%, white solid. R_f = 0.35

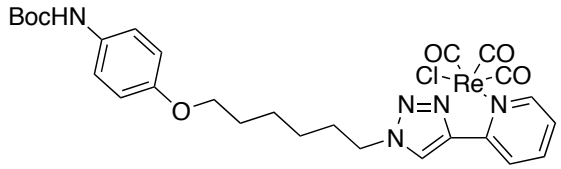
(dichloromethane : ethyl acetate = 1:1, v/v). ^{1}H NMR (300 MHz, Methanol-d_4) δ 8.61 – 8.52 (m, 1H), 8.41 (s, 1H), 8.07 (d, J = 7.8 Hz, 1H), 7.87 – 7.93 (m, 1H), 7.36 (dd, J = 7.8, 5.0 Hz, 1H), 7.24 (d, J = 9.0 Hz, 2H), 6.79 (d, J = 9.0 Hz, 2H), 4.48 (t, J = 7.0 Hz, 2H), 3.90 (t, J = 6.4 Hz, 2H), 2.05 – 1.92 (m, 2H), 1.78 – 1.65 (m, 2H), 1.53 – 1.33 (m, 17H). ^{13}C NMR (75 MHz, Methanol-d_4) δ 156.5, 155.8, 151.1, 150.4, 148.6, 138.9, 133.4, 124.5, 124.1, 121.9, 121.6, 115.7, 69.2, 51.6, 31.2, 30.4, 30.2, 29.9, 28.8, 27.4, 27.0. HRMS (ESI+): m/z calculated for $C_{26}H_{35}N_5NaO_3$: 488.2631 $[M + Na]^+$; found 488.2631.

General procedure 6: The corresponding compound **82** (1.0 equiv.) was dissolved in toluene (0.03 M). The mixture was heated at 80 °C and pentacarbonylchlororhenium(I) (1.0 equiv.) was added. The mixture was stirred at 80 °C for 2 hours. Then it was cooled to room temperature and concentrated. The residue was purified by column chromatography on silica gel (dichloromethane : acetone 4:1, v/v) to afford the titled compound.



[*tert*-Butyl(4-(4-(4-(pyridin-2-yl)-1*H*-1,2,3-triazol-1-yl)butoxy)phenyl)carbamate]-chlorotricarbonylrhenium(I), **83a**

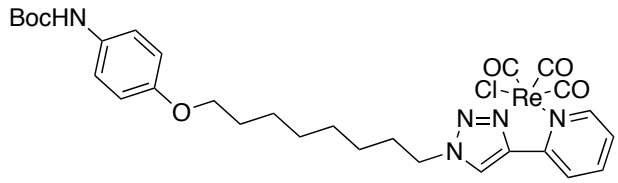
Prepared following the general procedure 6 starting from *tert*-butyl (4-((4-azidobutyl)oxy)phenyl)carbamate (50 mg, 0.12 mmol) and obtain as a yellow solid (85 mg, 98% yield). R_f = 0.40 (dichloromethane : acetone = 4:1, v/v). ^{1}H NMR (300 MHz, Dimethyl sulfoxide-d_6) δ 9.29 (s, 1H), 9.10 (s, 1H), 8.96 (d, J = 5.6 Hz, 1H), 8.32 – 8.23 (m, 2H), 7.64 (dd, J = 6.6, 5.6 Hz, 1H), 7.31 (d, J = 9.0 Hz, 2H), 6.82 (d, J = 9.0 Hz, 2H), 4.70 (t, J = 7.2 Hz, 2H), 3.95 (t, J = 6.4 Hz, 2H), 2.17 – 2.05 (m, 2H), 1.83 – 1.71 (m, 2H), 1.45 (s, 9H). ^{13}C NMR (75 MHz, Dimethyl sulfoxide-d_6) δ 197.7, 196.8, 189.6, 153.7, 153.0, 152.9, 148.7, 148.2, 140.6, 132.6, 126.4, 125.8, 122.6, 119.6, 114.5, 78.7, 66.8, 51.4, 28.2, 26.1, 25.7. HRMS (ESI+): m/z calculated for $C_{25}H_{27}ClN_5NaO_6Re$: 738.1105 $[M + Na]^+$; found 738.1076. IR: n_{max}/cm^{-1} 2021, 1882 (CO).



[*tert*-Butyl (4-((6-(4-(pyridin-2-yl)-1*H*-1,2,3-triazol-1-yl)hexyl)oxy)phenyl)carbamate]-chlorotricarbonylrhenium(I), **83b**

Prepared following the general procedure 6 starting from *tert*-butyl (4-((6-(4-(pyridin-2-yl)-1*H*-1,2,3-triazol-1-yl)hexyl)oxy)phenyl)carbamate (123 mg, 0.28 mmol) and obtain as a yellow solid (178 mg, 86% yield). R_f = 0.57 (dichloromethane : acetone = 4:1, v/v). ^{1}H NMR (300 MHz, Dimethyl sulfoxide-d_6) δ 9.27 (s, 1H), 8.96 (d, J = 5.6 Hz, 1H), 8.39 – 8.20 (m, 2H), 7.64

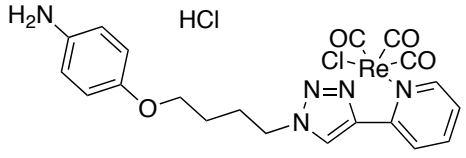
(dd, *J* = 6.6, 5.6 Hz, 1H), 7.30 (d, *J* = 9.0 Hz, 2H), 6.79 (d, *J* = 9.0 Hz, 2H), 4.63 (t, *J* = 7.2 Hz, 2H), 3.88 (t, *J* = 6.4 Hz, 2H), 2.05 – 1.89 (m, 2H), 1.75 – 1.61 (m, 2H), 1.49 – 1.40 (m, 4H). ^{13}C NMR (75 MHz, Dimethyl sulfoxide-d_6) δ 197.7, 196.8, 189.6, 153.9, 153.0, 152.9, 152.9, 148.7, 148.2, 140.6, 132.5, 132.4, 126.4, 125.7, 122.6, 119.7, 114.4, 78.7, 67.4, 51.6, 29.0, 28.5, 28.2, 25.4, 24.9. HRMS (ESI+): m/z calculated for $C_{27}H_{31}ClN_5NaO_6Re$: 766.1418 $[M + Na]^+$; found 766.1430. IR: ν_{max}/cm^{-1} 2020, 1882 (CO).



[*tert*-Butyl (4-((8-(4-(pyridin-2-yl)-1*H*-1,2,3-triazol-1-yl)octyl)oxy)phenyl)carbamate]-chlorotricarbonylrhenium(I), **83c**

Prepared following the general procedure 6 starting from *tert*-butyl (4-((8-(4-(pyridin-2-yl)-1*H*-1,2,3-triazol-1-yl)octyl)oxy)phenyl)carbamate (50 mg, 0.11 mmol) and obtain as a yellow solid (75 mg, 88% yield). R_f = 0.45 (dichloromethane : acetone = 4:1, v/v). ^{1}H NMR (300 MHz, Dimethyl sulfoxide-d_6) δ 9.28 (s, 1H), 9.09 (s, 1H), 8.97 (d, *J* = 5.7 Hz, 1H), 8.33 – 8.24 (m, 2H), 7.64 (dd, *J* = 5.7, 3.0 Hz, 1H), 7.32 (d, *J* = 9.0 Hz, 2H), 6.80 (d, *J* = 9.0 Hz, 2H), 4.62 (t, *J* = 7.2 Hz, 2H), 3.87 (t, *J* = 6.4 Hz, 2H), 1.95 (m, 2H), 1.73 – 1.61 (m, 2H), 1.49 – 1.31 (m, 8H). ^{13}C NMR (75 MHz, Dimethyl sulfoxide-d_6) δ 197.7, 196.8, 189.6, 153.9, 153.0, 152.9, 148.8, 148.2, 140.6, 132.5, 126.4, 125.7, 122.6, 119.7, 114.4, 78.6, 67.5, 51.6, 29.1, 28.7, 28.5, 28.2, 28.2, 25.6, 25.4. HRMS (ESI+): m/z calculated for $C_{29}H_{35}ClN_5NaO_6Re$: 794.1731 $[M + Na]^+$; found 794.1716. IR: ν_{max}/cm^{-1} 2015, 1887, 1865 (CO).

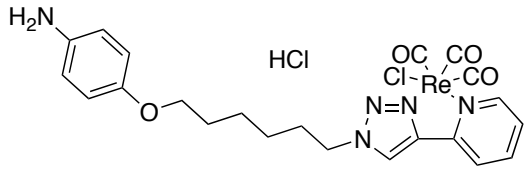
General procedure 7: The corresponding complex **83** (1.0 equiv.) was dissolved in dichloromethane (0.06 M). Then trifluoroacetic acid (1/2 volume of dichloromethane) was added slowly. After completion as monitored by thin layer chromatography, the mixture was concentrated and redissolved in dichloromethane (0.06 M). The mixture was stirred with an addition of hydrochloric acid (37%) (1/8 volume of dichloromethane) for 30 minutes. The solvent was evaporated to afford the titled complex.



[4-(4-(4-(Pyridin-2-yl)-1*H*-1,2,3-triazol-1-yl)butoxy)aniline]-chlorotricabonylrhenium(I) hydrochloride, **71a**

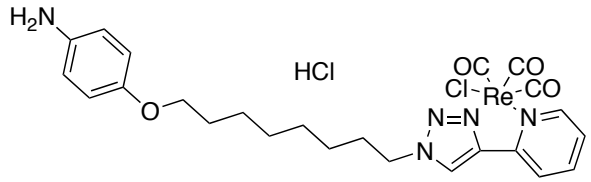
Prepared following the general procedure 7 starting from [*tert*-butyl(4-(4-(4-(pyridin-2-yl)-1*H*-1,2,3-triazol-1-yl)butoxy)phenyl)carbamate]-chlorotricarbonylrhenium(I) (85 mg, 0.12 mmol) and obtain as a yellow solid (71 mg, 93% yield). ^{1}H NMR (300 MHz, Dimethyl sulfoxide-d_6)

δ 10.12 (s, 2H), 9.35 (s, 1H), 8.96 (d, *J* = 5.4 Hz, 1H), 8.40 – 8.21 (m, 2H), 7.82 – 7.57 (m, 1H), 7.42 – 7.21 (m, 2H), 7.13 – 6.96 (m, 2H), 4.71 (t, *J* = 7.2 Hz, 2H), 4.04 (t, *J* = 6.2 Hz, 2H), 2.19 – 2.01 (m, 2H), 1.87 – 1.70 (m, 2H). ^{13}C NMR (75 MHz, Dimethyl sulfoxide-d_6) δ 197.6, 196.8, 189.6, 157.9, 153.0, 148.7, 148.2, 140.7, 126.4, 125.9, 124.3, 124.2, 122.6, 115.4, 67.1, 51.3, 26.1, 25.5. HRMS (ESI+): m/z calculated for $C_{20}H_{19}ClN_5NaO_4Re$: 638.0581 $[M + Na]^+$; found: 638.0561. IR: ν_{max}/cm^{-1} 2020, 1877 (CO). HPLC (5 to 100% ACN in 10 min): rt 6.711 minutes (>95%).



[4-((6-(4-(Pyridin-2-yl)-1*H*-1,2,3-triazol-1-yl)hexyl)oxy)aniline]-chlorotricarbonylrhenium(I) hydrochloride, **71b**

Prepared following the general procedure 7 starting from [*tert*-butyl (4-((6-(4-(pyridin-2-yl)-1*H*-1,2,3-triazol-1-yl)hexyl)oxy)phenyl)carbamate]- chlorotricarbonylrhenium(I) (178 mg, 0.24 mmol) and obtain as a yellow solid (156 mg, 96% yield). Follow the general procedure 5. Yield: 96%, yellow solid. ^{1}H NMR (300 MHz, Dimethyl sulfoxide-d_6) δ 9.80 (s, 2H), 9.31 (s, 1H), 8.96 (d, *J* = 5.5 Hz, 1H), 8.35 – 8.22 (m, 4H), 7.62 – 7.66 (m, 1H), 7.23 (d, *J* = 8.3 Hz, 2H), 6.99 (d, *J* = 8.3 Hz, 1H), 4.63 (t, *J* = 7.4 Hz, 2H), 3.95 (t, *J* = 6.5 Hz, 2H), 2.04 – 1.86 (m, 2H), 1.81 – 1.62 (m, 2H), 1.58 – 1.30 (m, 4H). ^{13}C NMR (75 MHz, Dimethyl sulfoxide-d_6) δ 157.7, 153.0, 148.7, 148.2, 140.7, 126.4, 125.7, 124.8, 123.9, 122.6, 115.4, 67.7, 51.5, 29.0, 28.3, 25.4, 24.8. HRMS (ESI+): m/z calculated for $C_{22}H_{24}ClN_5O_4Re$: 644.1069 $[M + H]^+$; found 644.1071. IR: ν_{max}/cm^{-1} 2020, 1878 (CO). HPLC (5 to 100% ACN in 10 min): rt 7.12 minutes (86%).

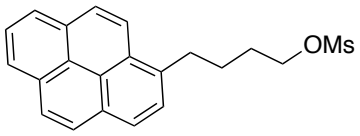


[4-((8-(4-(Pyridin-2-yl)-1*H*-1,2,3-triazol-1-yl)octyl)oxy)aniline]-chlorotricarbonylrhenium(I) hydrochloride, **71c**

Prepared following the general procedure 7 starting from [*tert*-butyl (4-((8-(4-(pyridin-2-yl)-1*H*-1,2,3-triazol-1-yl)octyl)oxy)phenyl)carbamate]- chlorotricarbonylrhenium(I) (92 mg, 0.12 mmol) and obtain as a pale brown solid (96 mg, >99% yield). ^{1}H NMR (300 MHz, Dimethyl sulfoxide -d_6) δ 10.10 (s, 2H), 9.33 (s, 1H), 8.96 (d, *J* = 5.5 Hz, 1H), 8.35 – 8.22 (m, 2H), 7.62 – 7.66 (m, 1H), 7.28 (d, *J* = 9.0 Hz, 2H), 7.00 (d, *J* = 9.0 Hz, 2H), 4.62 (t, *J* = 7.2 Hz, 2H), 3.94 (t, *J* = 6.5 Hz, 2H), 2.05 – 1.80 (m, 2H), 1.80 – 1.54 (m, 2H), 1.50 – 1.10 (m, 8H). ^{13}C NMR (75 MHz, Dimethyl sulfoxide -d_6) δ 197.7, 196.8, 189.6, 158.0, 153.0, 148.7, 148.2, 140.7, 126.4, 125.8, 124.2, 122.6, 115.3, 67.8, 51.6, 29.0, 28.5, 28.5, 28.2, 25.5, 25.3. HRMS (ESI+): m/z calculated or $C_{24}H_{27}ClN_5NaO_4Re$: 694.1207 $[M + Na]^+$; found 694.1189; HRMS (ESI+):

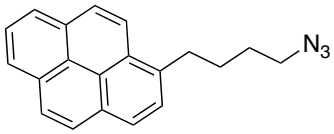
m/z calculated for $C_{24}H_{28}ClN_5O_4Re$: 672.1387 $[M + H]^+$; found 672.1369. IR: ν_{max}/cm^{-1} 2020, 1882 (CO). HPLC (5 to 100% ACN in 10 min): rt 7.52 minutes (81%).

4.3.2 Synthesis of catalysts for non-covalent immobilisation method



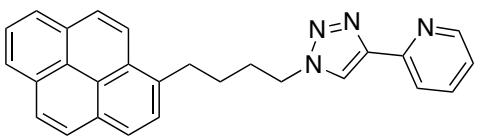
4-(Pyren-1-yl)butyl methanesulfonate, **85**

4-(Pyren-1-yl)butan-1-ol (500 mg, 1.8 mmol, 1.0 equiv.) was added into a mixture of N,N-diisopropylethylamine (640 mg, 6.3 mmol, 3.5 equiv.) and dichloromethane (15 mL). Methanesulfonyl chloride (209 μL, 2.7 mmol, 1.5 equiv.) was added at 0 °C. The mixture was stirred overnight at room temperature. The mixture was extracted by dichloromethane and saturated aqueous sodium bicarbonate solution. The organic phase was dried over sodium sulfate, filtered and concentrated. The residue was purified by column chromatography on silica gel (dichloromethane : cyclohexane = 1:1, v/v) to afford the titled compound as a pale yellow solid (598 mg, 94% yield). ^{1}H NMR (300 MHz, Chloroform-*d*$_6$) δ 8.25 (d, *J* = 9.2 Hz, 1H), 8.19 – 8.16 (m, 2H), 8.12 (d, *J* = 8.5 Hz, 2H), 8.06 – 7.96 (m, 3H), 7.86 (d, *J* = 7.8 Hz, 1H), 4.27 (t, *J* = 6.0 Hz, 2H), 3.40 (t, *J* = 7.2 Hz, 2H), 2.95 (s, 3H), 2.06 – 1.83 (m, 4H). Characterisations in agreement with *J. Am. Chem. Soc.* **1998**, *120*, 3289 – 3294.



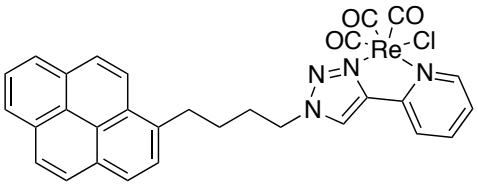
1-(4-Azidobutyl)pyrene, **86**

4-(Pyren-1-yl)butyl methanesulfonate (598 mg, 1.7 mmol, 1.0 equiv.) and NaN_3 (177 mg, 2.7 mmol, 1.6 equiv.) were added in N,N-diisopropylethylamine (5 mL). The mixture was heated at 80 °C overnight. The mixture was cooled to room temperature, diluted with water and extracted with dichloromethane. The organic phase was dried over sodium sulfate, filtered and concentrated to afford the titled compound as a white solid (396 mg, 78% yield). ^{1}H NMR (300 MHz, Chloroform-*d*) δ 8.26 (d, *J* = 9.2 Hz, 1H), 8.21 – 8.14 (m, 2H), 8.12 (d, *J* = 8.5 Hz, 2H), 8.05 – 7.95 (m, 3H), 7.86 (d, *J* = 7.8 Hz, 1H), 3.48 – 3.26 (m, 4H), 2.03 – 1.89 (m, 2H), 1.83 – 1.71 (m, 2H). ^{13}C NMR (75 MHz, Chloroform-*d*) δ 136.2, 131.6, 131.0, 130.0, 128.7, 127.6, 127.5, 127.3, 126.8, 126.0, 125.2, 125.1, 125.1, 125.0, 124.9, 123.3, 51.5, 33.1, 29.0, 28.9.



2-(1-(4-(Pyren-1-yl)butyl)-1*H*-1,2,3-triazol-4-yl)pyridine, **87**

1-(4-Azidobutyl)pyrene (100 mg, 0.33 mmol, 1.0 equiv.) and 2-ethynylpyridine (34 uL, 0.33 mmol, 1.0 equiv.) were dissolved in a mixture of dichloromethane (2 mL) and water (2 mL), followed by the addition of copper sulfate pentahydrate (8 mg, 0.033 mmol, 0.1 equiv.) and sodium ascorbate (20 mg, 0.1 mmol, 0.3 equiv.). The mixture was stirred at room temperature overnight. The mixture was extracted by dichloromethane and water. The organic phase was dried over sodium sulfate, filtered and concentrated. The residue was purified by column chromatography on silica gel (dichloromethane : ethyl acetate = 9 : 1, v/v) to afford the titled product as a white solid (103 mg, 78% yield). ^{1}H NMR (300 MHz, Chloroform-*d*) δ 8.55 (d, *J* = 4.9 Hz, 1H), 8.23 (d, *J* = 9.3 Hz, 1H), 8.19 – 8.06 (m, 6H), 8.05 – 7.95 (m, 3H), 7.84 (d, *J* = 7.8 Hz, 1H), 7.73 – 7.79 (m, 1H), 7.17 – 7.23 (m, 1H), 4.46 (t, *J* = 7.0 Hz, 2H), 3.41 (t, *J* = 7.4 Hz, 2H), 2.20 – 2.04 (m, 2H), 2.02 – 1.90 (m, 2H). ^{13}C NMR (75 MHz, Chloroform-*d*) δ 150.4, 149.5, 148.6, 137.0, 135.7, 131.5, 131.0, 130.1, 128.7, 127.6, 127.4, 126.89, 126.0, 125.3, 125.1, 125.0, 124.9, 123.2, 122.9, 121.9, 120.4, 50.5, 32.9, 30.2, 28.5. HRMS (ESI+): m/z calculated for $C_{27}H_{23}N_4$: 403.1923 $[M + H]^+$; found: 403.1898.



[2-(1-(4-(Pyren-1-yl)butyl)-1*H*-1,2,3-triazol-4-yl)pyridine]-chlorotricarbonylrhenium(I), **72c**
2-(1-(4-(Pyren-1-yl)butyl)-1*H*-1,2,3-triazol-4-yl)pyridine (70 mg, 0.17 mmol, 1.0 equiv.) was dissolved in toluene (5 mL) and the solution was heated at 120 °C. Pentacarbonylchlororhenium(I) (63 mg, 0.17 mmol, 1.0 equiv.) was added and the mixture was heated at 120 °C for 1 hour. After cooling to room temperature, the solvent was evaporated and the residue was purified by column chromatography on silica gel (dichloromethane : ethyl acetate = 9 : 1, v/v) to afford the titled product as pale yellow solid (93 mg 78% yield). ^{1}H NMR (300 MHz, Dimethyl sulfoxide-d_6) δ 9.23 (s, 1H), 8.96 (d, *J* = 5.6 Hz, 1H), 8.36 (d, *J* = 9.3 Hz, 1H), 8.29 – 8.16 (m, 6H), 8.14 – 8.09 (m, 2H), 8.01 – 8.06 (m, 1H), 7.97 (d, *J* = 7.8 Hz, 1H), 7.63 (dd, *J* = 7.5, 5.6 Hz, 1H), 4.72 (t, *J* = 7.1 Hz, 2H), 3.49 – 3.41 (m, 2H), 2.20 – 2.04 (m, 2H), 1.97 – 1.73 (m, 2H). ^{13}C NMR (75 MHz, Dimethyl sulfoxide-d_6) δ 197.6, 196.8, 189.5, 152.9, 148.7, 148.2, 140.5, 136.2, 130.9, 130.4, 129.3, 128.1, 127.4, 127.3, 126.5, 126.4, 126.1, 125.7, 124.9, 124.7, 124.2, 124.1, 123.4, 122.5, 51.4, 31.8, 29.1, 28.0. IR: ν_{max}/cm^{-1} 2016, 1913, 1878, 1860 (CO).

4.3.3 Electrochemistry

Cyclic voltammetry was performed with a classical three-electrode single compartment cell at room temperature, using a glassy carbon electrode (3 mm dia., Origalys, France), a Pt wire counter electrode, and a saturated Ag/AgCl/KCl electrode (Biologic, France). The experiments were performed using a 263A EGG Potentiostat (PAR Research). The working electrode was

polished with 1200 grit, then 2400 grit and 4000 grit papers followed by extensive rinsing and sonication with ultrapure water and ethanol. MeCN solutions containing 0.1 M Bu_4NPF_6 as the supporting electrolyte were deaerated with Ar or saturated with CO_2 for at least 10 min before cyclic voltammograms (CVs) were recorded.

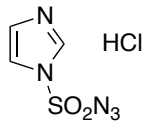
Controlled-potential electrolysis experiments were performed at room temperature in a custom-built, gas-tight two-compartment electrochemical cell. The cathodic compartment, which contained a fitting for a 15 mm diameter glassy carbon disk working electrode, was separated from the anodic compartment *via* a glass frit of fine porosity. The counter electrode was a platinum wire grid (10 × 40 mm), and the reference electrode was a saturated Ag/AgCl/KCl electrode that is separated from the solution by a Vycor tip. MeCN solutions containing 0.1 M Bu_4NPF_6 as the supporting electrolyte were saturated with CO_2 for at least 15 min prior to bulk electrolysis and was stirred rigorously during the experiment. Typically, the solution volume of the cathodic compartment was 15 mL with a headspace volume of 28.6 mL.

4.3.4 Chemical Analysis

H_2 and CO evolution were monitored by gas chromatography during bulk electrolysis and photocatalysis by periodically sampling 50 μL of the headspace. Measurements for H_2 were performed by gas chromatography on a Shimadzu GC-2014 equipped with a Quadrex column, a thermal conductivity detector, and using N_2 as a carrier gas. CO was measured using a Shimadzu GC- 2010 Plus gas chromatography, fitted with a Restek Shin Carbon column, helium carrier gas, a methanizer, and a flame ionisation detector. Gas chromatography calibration curves were made by sampling known volumes of CO and H_2 gas, respectively. Formate concentration was determined using a Metrohm 883 Basic IC plus ionic exchange chromatography instrument, using a Metrosep A Supp 5 column and a conductivity detector. A typical measurement consists of sampling 200 μL of the reaction mixture, which is diluted 100-fold in deionized 18 MΩ water, followed by a 20 μL injection into the instrument.

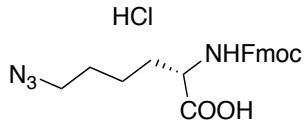
4.4 Synthesis for Keap1-Nrf2 peptidomimetics inhibitors

4.4.1 Synthesis of azido-modified amino acid



[1]*H*-Imidazole-1-sulfonyl azide hydrochloride, **89**

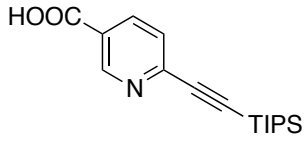
Sodium azide (2.0 g, 0.03 mol, 1.0 equiv.) was dispersed in acetonitrile (50 mL). Sulfuryl chloride (2.4 mL, 0.03 mol, 1.0 equiv.) was added at 0 °C and the mixture was stirred at room temperature overnight. Imidazole (2.0 g, 0.03 mol, 1.0 equiv.) was added and the mixture was stirred for 3 hours. The mixture was diluted with ethyl acetate and water. The organic phase was separated, further washed with a saturated sodium bicarbonate aqueous solution, dried over sodium sulfate, filtered and concentrated to give a pale yellow oil. An ethanolic solution of hydrogen chloride (2.5 mL acetyl chloride in 12.5 mL ethanol) was added to the oil resulting in the formation of a white solid. The solid was filtered, washed with cold ethanol and dried in vacuum to give the titled compound as a white solid (2.2 g, 36% yield). ^{1}H NMR (300 MHz, Deuterium Oxide) δ 9.54 – 9.20 (m, 1H), 8.05 (dd, *J* = 4.2, 2.2 Hz, 1H), 7.79 – 7.54 (m, 1H). Characterisations in agreement with *Org. Lett.*, **2017**, *9*, 3797 – 3800.



Fmoc-Lys-(*S*)-2-((((9*H*-fluoren-9-yl)methoxy)carbonyl)amino)-6-azidohexanoic acid hydrochloride – Fmoc-Lys(N_3)-OH.HCl, **91**

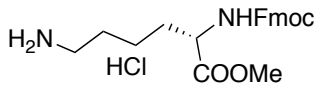
(*S*)-2-((((9*H*-Fluoren-9-yl)methoxy)carbonyl)amino)-6-aminohexanoic acid hydrochloride (400 mg, 1.0 mmol, 1.0 equiv.), copper(II) sulfate pentahydrate (24 mg, 0.1 mmol, 0.1 equiv.) and potassium carbonate (400 mg, 2.7 mmol, 2.7 equiv.) were added into methanol (8 mL). 1*H*-Imidazole-1-sulfonyl azide hydrochloride (252 mg, 1.2 mmol, 1.2 equiv.) was added and the mixture was stirred at room temperature overnight. The mixture was evaporated; the residue was dispersed in water and neutralized by 37% HCl solution. The mixture was extracted with ethyl acetate, the organic phase was dried over sodium sulfate, filtered and concentrated. The residue was purified by preparative HPLC (column, 50 to 65% acetonitrile over 10 minutes) to give the titled product as a pale yellow solid (203 mg, 47% yield). ^{1}H NMR (300 MHz, Acetone-d_6) δ 7.86 (d, *J* = 7.5 Hz, 2H), 7.77 – 7.65 (m, 2H), 7.41 (t, *J* = 7.5 Hz, 2H), 7.32 (t, *J* = 7.5 Hz, 2H), 6.78 (d, *J* = 8.3 Hz, 1H), 4.34 (d, *J* = 7.2 Hz, 2H), 4.30 – 4.20 (m, 2H), 3.37 (t, *J* = 6.6 Hz, 2H), 1.97 – 1.86 (m, 1H), 1.86 – 1.74 (m, 1H), 1.70 – 1.60 (m, 2H), 1.60 – 1.47 (m, 2H). HPLC (5 to 100% ACN in 10 min): rt 8.73 minutes (>95%). Characterisations in agreement with *Chem. Commun.,* **2011**, *47*, 2589 – 2591.

4.4.2 Synthesis of 2-ethynylpyridyl-modified amino acid using amidation



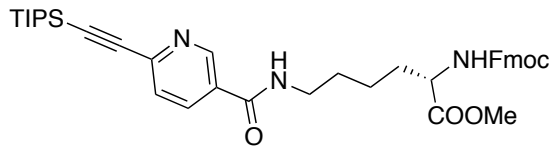
6-((Triisopropylsilyl)ethynyl)nicotinic acid, **92**

Methyl 6-((triisopropylsilyl)ethynyl)nicotinate (790 mg, 2.5 mmol, 1.0 equiv.) was dissolved in a mixture of tetrahydrofuran (15 mL) and water (7 mL). Lithium hydroxide monohydrate (113 mg, 2.68 mmol, 1.1 equiv.) was added and the mixture was stirred at room temperature for an hour. An aqueous 1M HCl solution was added to tune the pH to pH 1. The mixture was diluted with water and ethyl acetate. The organic phase was collected, dried over sodium sulfate, filtered and concentrated to give the titled product as a white solid (723 mg, 96% Yield). ^{1}H NMR (300 MHz, Acetone-d$_6$) δ 8.63 – 8.45 (m, 1H), 7.80 (dd, *J* = 8.1, 2.1 Hz, 1H), 7.21 (dd, *J* = 8.1, 0.8 Hz, 1H), 0.66 (s, 21H). ^{13}C NMR (75 MHz, Acetone-*d*$_6$) δ 156.1, 141.0, 135.5, 128.0, 117.8, 116.2, 96.1, 83.7, 8.8, 1.0.



***N*$_\alpha$**-9-Fluorenylmethoxycarbonyl-L-lysine methyl ester hydrochloride Fmoc-Lys-OMe·HCl, **94**

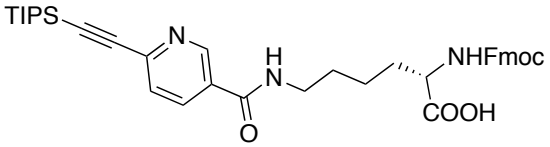
***N*$_\alpha$**-9-Fluorenylmethoxycarbonyl-L-lysine hydrochloride (200 mg, 0.5 mmol, 1.0 equiv.) was dissolved in methanol (10 mL). Thionyl chloride (136 uL, 1.9 mmol, 3.8 equiv.) was added slowly and the mixture was stirred at room temperature for 2 hours. The mixture was concentrated and poured into diethyl ether to form a white precipitate. The precipitate was filtered and dried under vacuum to give the titled compound as a white solid (80 mg, 88% yield). ^{1}H NMR (300 MHz, Methanol-*d*$_4$) δ 7.80 (d, *J* = 7.4 Hz, 2H), 7.67 (t, *J* = 6.6 Hz, 2H), 7.40 (t, *J* = 7.4 Hz, 2H), 7.31 (t, *J* = 7.4 Hz, 2H), 4.56 (s, 1H), 4.50 – 4.29 (m, 2H), 4.28 – 4.12 (m, 2H), 3.72 (s, 3H), 2.91 (t, *J* = 7.6 Hz, 2H), 1.93 – 1.78 (m, 1H), 1.78 – 1.56 (m, 3H), 1.56 – 1.36 (m, 2H). ^{13}C NMR (75 MHz, Methanol-*d*$_4$) δ 152.1, 149.0, 147.0, 138.5, 136.9, 130.9, 129.6, 119.3, 63.2, 61.1, 43.2, 36.4, 31.7.



(*S*)-Methyl 2-((((9*H*-fluoren-9-yl)methoxy)carbonyl)amino)-6-(6-((triisopropylsilyl)ethynyl)nicotinamido)hexanoate, **95**

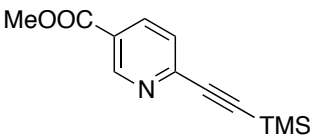
6-((Triisopropylsilyl)ethynyl)nicotinic acid (500 mg, 1.7 mmol, 1.0 equiv.) was dissolved in dimethylformamide (10 mL), followed by the addition of HBTU (750 mg, 2.0 mmol, 1.2 equiv.). The mixture was stirred at room temperature for 30 minutes. Then ***N*$_\alpha$**-9-fluorenylmethoxycarbonyl-L-lysine methyl ester hydrochloride (759 mg, 1.8 mmol, 1.1 equiv.)

and N, N-diisopropylethylamine (818 uL, 5.0 mmol, 3.0 equiv.) were added and the resulting mixture was stirred overnight. The mixture was concentrated and the residue was taken up in dichloromethane and water. The organic phase was collected, dried over sodium sulfate, filtered and concentrated. The residue was purified by column chromatography on silica gel (ethyl acetate : cyclohexane = 3 : 7 → 1 : 1, v/v) to give the titled product as a white solid (731 mg, 69% yield). ^{1}H NMR (300 MHz, Chloroform-*d*) δ 8.95 (s, 1H), 8.07 (d, *J* = 8.0 Hz, 1H), 7.74 (dd, *J* = 7.7, 1.0 Hz, 2H), 7.61 – 7.51 (m, 2H), 7.43 (d, *J* = 8.0 Hz, 1H), 7.38 (d, *J* = 7.4 Hz, 2H), 7.30 (t, *J* = 7.4 Hz, 2H), 6.74 (t, *J* = 5.8 Hz, 1H), 5.52 (t, *J* = 6.0 Hz, 1H), 4.46 – 4.28 (m, 3H), 4.19 (t, *J* = 6.9 Hz, 1H), 3.74 (s, 3H), 3.45 (q, *J* = 6.5 Hz, 2H), 1.97 – 1.80 (m, 2H), 1.79 – 1.60 (m, 2H), 1.53 – 1.36 (m, 2H), 1.13 (d, *J* = 3.2 Hz, 21H). ^{13}C NMR (75 MHz, Chloroform-*d*) δ 173.0, 165.3, 156.3, 148.2, 145.6, 143.9, 143.8, 141.4, 135.4, 129.0, 127.8, 127.4, 127.2, 125.1, 120.1, 105.3, 94.7, 67.2, 53.6, 52.6, 47.3, 39.8, 32.5, 28.8, 22.7, 18.8, 11.3.



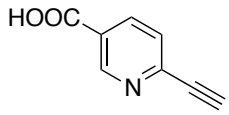
(*S*)-2-((((9*H*-Fluoren-9-yl)methoxy)carbonyl)amino)-6-(6-((triisopropylsilyl)ethynyl)nicotinamido)hexanoic acid, **96**

Calcium chloride (2.6 mg, 15.6 mmol, 20.0 equiv.) and sodium hydroxide (31 mg, 0.8 mmol, 1.0 equiv.) were dissolved in water (20 mL). The mixture was heated at 50 °C. A solution of (*S*)-methyl 2-((((9*H*-fluoren-9-yl)methoxy)carbonyl)amino)-6-(6-((triisopropylsilyl)ethynyl)nicotinamido)hexanoate (500 mg, 0.8 mmol, 1.0 equiv.) in isopropyl alcohol (40 mL) was slowly added to the mixture. The resulting mixture was heated at 50 °C for 4 hours. After cooling to room temperature, acetic acid was added to the mixture until pH 5. The mixture was diluted with ethyl acetate and water. The organic phase as collected, dried over sodium sulfate, filtered and concentrated. The residue was purified by preparative HPLC (75 to 100% acetonitrile over 30 minutes, rt 18.56 minutes) to give the titled compound as a pale yellow solid (348 mg, 71% yield). ^{1}H NMR (300 MHz, Chloroform-*d*) δ 9.14 (s, 1H), 8.46 (dd, *J* = 8.2, 1.8 Hz, 1H), 7.89 (s, 1H), 7.71 (dt, *J* = 7.4, 0.9 Hz, 2H), 7.62 (d, *J* = 8.2 Hz, 1H), 7.54 (dd, *J* = 7.4, 3.3 Hz, 2H), 7.36 (t, *J* = 7.4 Hz, 2H), 7.31 – 7.22 (m, 2H), 5.72 (d, *J* = 7.7 Hz, 1H), 4.51 – 4.39 (m, 1H), 4.39 – 4.27 (m, 2H), 4.16 (t, *J* = 6.9 Hz, 1H), 3.60 – 3.36 (m, 2H), 1.95 – 1.76 (m, 2H), 1.76 – 1.57 (m, 2H), 1.57 – 1.36 (m, 2H), 1.21 – 1.03 (m, 21H). ^{13}C NMR (75 MHz, Chloroform-*d*) δ 175.2, 163.6, 156.3, 144.3, 143.9, 143.7, 141.4, 141.2, 140.5, 131.0, 128.8, 127.9, 127.2, 125.2, 120.1, 100.2, 67.2, 53.8, 47.3, 39.9, 31.5, 27.9, 22.1, 18.6, 11.2. HPLC (75 to 100% ACN in 10 min): rt 5.49 minutes (>95%).



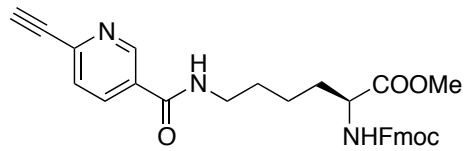
Methyl 6-((trimethylsilyl)ethynyl)nicotinate, **97**

Methyl 6-chloronicotinate (100 mg, 0.46 mmol, 1.0 equiv.) was dissolved in tetrahydrofuran (2 mL), followed by the addition of triethylamine (0.1 mL). The mixture was bubbled with argon for 10 minutes. Then bis(triphenylphosphine)palladium(II) dichloride (16 mg, 0.023 mmol, 5 mol %.), copper(I) iodide (4 mg, 0.023 mmol, 5 mol %) and ethynyltrimethylsilane (0.1 mL, 0.69 mmol, 1.5 equiv.) were added into the mixture in sequence. The mixture was stirred at room temperature overnight. Then the mixture was filtered and the filtrate was collected and concentrated. The residue was purified by column chromatography (dicholoromethane : methonal = 100 : 1, v/v) on silica gel to give the titled compound as pale yellow solid (88 mg, 83% yield). ^{1}H NMR (300 MHz, Chloroform-*d*) δ 9.16 (s, 1H), 8.28 (d, *J* = 8.4 Hz, 1H), 7.55 (d, *J* = 8.1 Hz, 1H), 3.96 (s, 3H), 0.29 (s, 9H).



6-Ethynylnicotinic acid, **98**

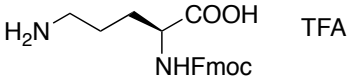
Methyl 6-((triisopropylsilyl)ethynyl)nicotinate (200 mg, 0.86 mmol, 1.0 equiv.) was dissolved in a mixture of tetrahydrofuran (5 mL) and water (2.5 mL). Lithium hydroxide monohydrate (171 mg, 4.1 mmol, 3.0 equiv.) was added and the mixture was stirred at room temperature for 10 minutes. An aqueous 1M HCl solution was added to tune the pH to pH 5. The mixture was diluted with water and dichloromethane. The organic phase was collected, dried over sodium sulfate, filtered and concentrated to give the titled product as a pale yellow solid (130 mg, > 99% Yield). ^{1}H NMR (300 MHz, Chloroform-*d*) δ 9.26 (d, *J* = 2.2 Hz, 1H), 8.34 (dd, *J* = 8.1, 2.1 Hz, 1H), 7.60 (d, *J* = 8.2 Hz, 1H), 3.37 (s, 1H). Characterisations in agreement with EP0879814, 1998-11-25.



(*S*)-Methyl 2-((((9*H*-fluoren-9-yl)methoxy)carbonyl)amino)-6-(6-ethynylnicotinamido)hexanoate, **99**

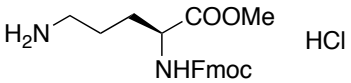
6-Ethynylnicotinic acid (148 mg, 1.0 mmol, 1.0 equiv.) was dissolved in dimethylformamide (10 mL), followed by the addition of HBTU (379 mg, 1.0 mmol, 1.0 equiv.). The mixture was stirred at room temperature for 30 minutes. Then ***N*$_\alpha$**-9-fluorenylmethoxycarbonyl-L-lysine methyl ester hydrochloride (461 mg, 1.1 mmol, 1.1 equiv.) and N, N-diisopropylethylamine (0.6 mL) were added and the resulting mixture was stirred overnight. The mixture was concentrated and the residue was taken up in dichloromethane and water. The organic phase was collected, dried over sodium sulfate, filtered and concentrated. The residue was purified by column chromatography on silica gel (ethyl acetate) to give the titled product as a pale yellow solid (139 mg, 27% yield). ^{1}H NMR (300 MHz, Chloroform-*d*) δ 8.96 (s, 1H), 8.11 (d, *J* = 8.2 Hz, 1H), 7.75 (dd, *J* = 7.5, 2.8 Hz, 2H), 7.58 (d, *J* = 7.4 Hz, 2H), 7.46 (d, *J* = 8.0 Hz, 1H), 7.40

(t, *J* = 7.6 Hz, 2H), 7.32 (d, *J* = 7.4 Hz, 2H), 6.48 (s, 1H), 5.45 (d, *J* = 8.3 Hz, 1H), 4.48 – 4.30 (m, 3H), 4.20 (t, *J* = 6.9 Hz, 1H), 3.76 (s, 3H), 3.28 (s, 1H), 1.94 – 1.80 (m, 2H), 1.78 – 1.68 (m, 2H), 1.55 – 1.39 (m, 2H).



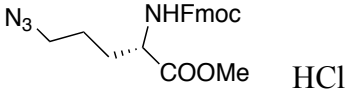
(*S*)-2-((((9*H*-Fluoren-9-yl)methoxy)carbonyl)amino)-5-aminopentanoic acid, **101**

(*S*)-2-((((9*H*-Fluoren-9-yl)methoxy)carbonyl)amino)-5-((*tert*-butoxycarbonyl)amino)pentanoic acid (2.0 g, 4.4 mmol) was dissolved in a mixture of dichloromethane (20 mL) and trifluoroacetic acid (20 mL). The mixture was stirred at room temperature for an hour. Then the solvent was removed to give the titled compound asa pale yellow solid (2.0 g, > 99%). ^{1}H NMR (300 MHz, Methanol-d_4) δ 7.84 – 7.77 (m, 2H), 7.67 (t, *J* = 6.6 Hz, 2H), 7.45 – 7.35 (m, 2H), 7.31 (td, *J* = 7.4, 1.2 Hz, 2H), 4.49 – 4.39 (m, 1H), 4.39 – 4.28 (m, 1H), 4.27 – 4.10 (m, 2H), 3.04 – 2.87 (m, 2H), 2.03 – 1.83 (m, 1H), 1.84 – 1.68 (m, 3H). Characterisations in agreement with *J. Pept. Sci.,* **2010**, *16*, 10 – 14.



(S)-methyl 2-((((9H-fluoren-9-yl)methoxy)carbonyl)amino)-5-aminopentanoate hydrochloride, **102**

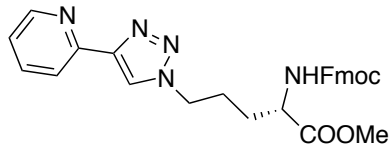
(*S*)-2-((((9*H*-Fluoren-9-yl)methoxy)carbonyl)amino)-5-aminopentanoic acid (1.2 g, 2.7 mmol, 1.0 equiv.) was dissolved in methanol (50 mL). Thionyl chloride (0.7 mL, 10.3 mmol, 3.8 equiv.) was added slowly and the mixture was stirred at room temperature for 2 hours. The mixture was concentrated and poured into diethyl ether to form a white precipitate. The precipitate was filtered and dried under vacuum to give the titled compound as a white solid (504 mg, 46% yield). ^{1}H NMR (300 MHz, Methanol-d_4) δ 7.80 (d, *J* = 7.3 Hz, 2H), 7.67 (t, *J* = 6.3 Hz, 2H), 7.45 – 7.36 (m, 2H), 7.32 (t, *J* = 7.5 Hz, 2H), 4.50 – 4.39 (m, 1H), 4.39 – 4.27 (m, 1H), 4.22 (t, *J* = 6.7 Hz, 2H), 3.73 (s, 3H), 2.95 (t, *J* = 7.3 Hz, 2H), 2.01 – 1.82 (m, 1H), 1.82 – 1.61 (m, 3H). Characterisations in agreement with *J. Comb. Chem.,* **2000**, *2*, 370 – 377.



(*S*)-Methyl 2-((((9*H*-fluoren-9-yl)methoxy)carbonyl)amino)-5-azidopentanoate hydrochloride, Fmoc-Orn(N_3)-OMe HCl, **103**

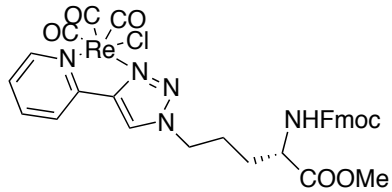
(*S*)-2-((((9*H*-Fluoren-9-yl)methoxy)carbonyl)amino)-6-aminopentanoic acid hydrochloride (404 mg, 1.0 mmol, 1.0 equiv.), copper(II) sulfate pentahydrate (24 mg, 0.1 mmol, 0.1 equiv.) and potassium carbonate (400 mg, 2.7 mmol, 2.7 equiv.) were added into methanol (8 mL). 1*H*-Imidazole-1-sulfonyl azide hydrochloride (252 mg, 1.2 mmol, 1.2 equiv.) was added and the mixture was stirred at room temperature overnight. The mixture was evaporated, the residue was dispersed in water and neutralized by 37% HCl solution. The mixture was extracted with

ethyl acetate, the organic phase was dried over sodium sulfate, filtered and concentrated. The residue was purified by preparative HPLC (column, 50 to 65% acetonitrile over 10 minutes) to give the titled product as a pale yellow solid (371 mg, 86% yield). ^{1}H NMR (300 MHz, Acetone-d_6) HPLC (5 to 100% ACN in 10 min): rt 8.94 minutes (>95%). Characterisations in agreement with *Chem. Commun.,* **2011**, *47*, 2589 – 2591.



(*S*)-Methyl 2-((((9*H*-fluoren-9-yl)methoxy)carbonyl)amino)-5-(4-(pyridin-2-yl)-1*H*-1,2,3-triazol-1-yl)pentanoate, **104**

(*S*)-Methyl 2-((((9*H*-fluoren-9-yl)methoxy)carbonyl)amino)-5-azidopentanoate hydrochloride (93 mg, 0.22 mmol, 1.0 equiv.) was dissolved in a mixture of *tert*-butyl alcohol (2 mL), water (2 mL) and acetonitrile (2 mL), followed by the addition of 2-ethynylpyridine (22 uL, 0.22 mmol, 1.0 equiv.), copper sulfate pentahydrate (5 mg, 0.02 mmol, 0.1 equiv.) and sodium ascorbate (44 mg, 0.22 mmol, 1.0 equiv.). The mixture was heated at 40 °C for 6 hours. The mixture was cooled to room temperature and extracted by dichloromethane and 0.1 M ethylenediaminetetraacetic acid aqueous solution. The organic phase was dried over sodium sulfate, filtered and concentrated. The residue was purified by preparative HPLC (5 – 100 % acetonitrile over 10 minutes, rt. 4.0 minutes) to afford the titled product as a white solid (26 mg, 25% yield). ^{1}H NMR (300 MHz, Chloroform-*d*) δ 8.57 (dd, *J* = 4.9, 1.8 Hz, 1H), 8.19 (d, *J* = 6.0 Hz, 2H), 7.80 (td, *J* = 7.8, 1.8 Hz, 1H), 7.75 (d, *J* = 6.0 Hz, 2H), 7.59 (d, *J* = 7.3 Hz, 2H), 7.39 (td, *J* = 7.3, 1.6 Hz, 2H), 7.35 – 7.27 (m, 2H), 7.26 – 7.20 (m, 1H), 5.47 (d, *J* = 8.2 Hz, 1H), 4.59 – 4.33 (m, 5H), 4.20 (t, *J* = 6.7 Hz, 1H), 3.73 (s, 3H), 2.37 – 2.09 (m, 2H), 2.11 – 1.98 (m, 1H), 1.79 – 1.60 (m, 1H).

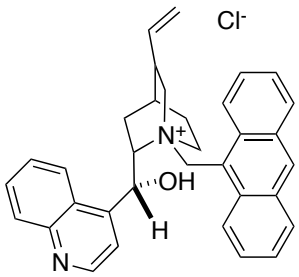


[(*S*)-Methyl 2-((((9*H*-fluoren-9-yl)methoxy)carbonyl)amino)-5-(4-(pyridin-2-yl)-1*H*-1,2,3-triazol-1-yl)pentanoate] -chlorotricarbonylrhenium(I), **105**

[(*S*)-Methyl 2-((((9*H*-fluoren-9-yl)methoxy)carbonyl)amino)-5-(4-(pyridin-2-yl)-1*H*-1,2,3-triazol-1-yl)pentanoate] (26 mg, 0.05 mmol, 1.0 equiv.) was dissolved in toluene (2 mL). The mixture was heated at 120 °C, followed by the addition of pentacarbonylchlororhenium(I) (20 mg, 0.05 mmol, 1.0 equiv.). The mixture was heated at 120 °C for 4 hours. Then the mixture was cooled to room temperature, dried under reduced pressure and purified by column chromatography on silica gel (acetone : dichloromethane = 4 : 1, v/v) to give the titled compound as a yellow solid (29 mg, 67% yield). ^{1}H NMR (300 MHz, Chloroform-*d*) δ 8.98 (d,

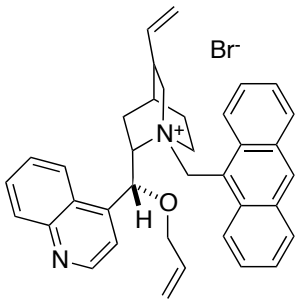
J = 5.5 Hz, 1H), 8.27 (d, *J* = 6.7 Hz, 1H), 7.91 (t, *J* = 7.9 Hz, 1H), 7.80 – 7.64 (m, 3H), 7.64 – 7.50 (m, 2H), 7.40 (td, *J* = 7.4, 2.1 Hz, 3H), 7.35 – 7.27 (m, 2H), 5.54 (t, *J* = 8.8 Hz, 1H), 4.53 – 4.35 (m, 5H), 4.21 (t, *J* = 6.8 Hz, 1H), 3.78 (s, 3H), 2.12 – 1.80 (m, 2H), 1.80 – 1.57 (m, 2H). ^{13}C NMR (75 MHz, Chloroform-*d*) δ 197.3, 195.8, 189.1, 172.1, 156.3, 153.4, 149.3, 148.9, 148.9, 143.9, 143.8, 143.7, 143.6, 141.4, 141.4, 139.5, 128.0, 128.0, 127.3, 127.3, 126.0, 125.2, 122.3, 120.2, 67.2, 53.1, 51.6, 47.3, 29.7, 26.0.

4.4.3 Synthesis of 2-ethynylpyridyl-modified amino acid using other strategy



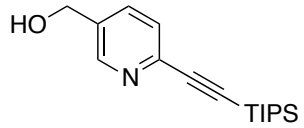
(1*S*,2*S*,4*S*)-1-(anthracen-9-ylmethyl)-2-((*R*)-hydroxy(quinolin-4-yl)methyl)-5-vinylquinuclidin-1-ium chloride, **108**

(1*R*)-quinolin-4-yl((1*S*,2*S*,4*S*)-5-vinylquinuclidin-2-yl)methanol (372 mg, 1.26 mmol, 1.0 equiv.) and 9-(chloromethyl)anthracene (300 mg, 1.32 mmol, 1.05 equiv.) were dissolved in toluene (4 mL). The mixture was heated at 130 °C for 24 hours. The mixture was cooled to room temperature and filtered. The collected solid was recrystallized in dichloromethane to give the titled product as a light yellow solid (353 mg, 54% yield). ^{1}H NMR (300 MHz, Chloroform-*d*) δ 9.05 (d, *J* = 8.4 Hz, 1H), 8.93 (d, *J* = 8.6 Hz, 1H), 8.86 (d, *J* = 4.7 Hz, 1H), 8.65 (d, *J* = 9.1 Hz, 1H), 8.29 (s, 1H), 8.12 (d, *J* = 4.7 Hz, 1H), 7.97 (s, 1H), 7.78 (d, *J* = 8.6 Hz, 1H), 7.62 (d, *J* = 8.0 Hz, 1H), 7.57 (d, *J* = 8.4 Hz, 1H), 7.41 – 7.31 (m, 1H), 7.25 – 7.14 (m, 4H), 7.11 – 7.02 (m, 2H), 6.86 (d, *J* = 13.4 Hz, 1H), 6.62 (d, *J* = 13.4 Hz, 1H), 5.39 (dd, *J* = 10.4, 5.9 Hz, 1H), 5.33 – 5.20 (m, 1H), 4.91 (dd, *J* = 10.4, 1.5 Hz, 1H), 4.81 – 4.58 (m, 2H), 4.08 (d, *J* = 12.6 Hz, 1H), 2.58 (dd, *J* = 12.6, 10.4 Hz, 1H), 2.40 (t, *J* = 11.9 Hz, 1H), 2.13 (s, 1H), 1.85 – 1.64 (m, 3H), 1.18 – 1.03 (m, 1H), 1.03 – 0.90 (m, 1H). Characterisations in agreement with *Org. Syn*, **2003,** *80*, 38 – 45.



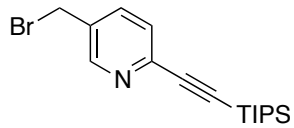
(1*S*,2*S*,4*S*)-2-((*R*)-(allyloxy)(quinolin-4-yl)methyl)-1-(anthracen-9-ylmethyl)-5-vinylquinuclidin-1-ium bromide, **110**

(1*S*,2*S*,4*S*)-1-(anthracen-9-ylmethyl)-2-((*R*)-hydroxy(quinolin-4-yl)methyl)-5-vinylquinuclidin-1-ium chloride (50 mg, 0.1 mmol, 1.0 equiv.) was dissolved in dichloromethane (1 mL), followed by the addition of 3-bromoprop-1-ene (26 uL, 0.3 mmol, 3.0 equiv.) and 50% aqueous sodium hydroxide (50 uL, 0.5 mmol, 5.0 equiv.). The mixture was stirred vigorously at room temperature for 4 hours. Then the mixture was diluted with 1 mL water and was stirred for 5 minutes. After separation of the phases, the organic phase was collected, dried over sodium sulfate and filtered. Ethyl ether was added to produce some pale yellow precipitation and the mixture was stirred for 1 hour. The solid was collected by filtration, washed with diethyl ether and dried under vacuum to give the titled compound as a pale yellow solid (36 mg, 60% yield). ^{1}H NMR (300 MHz, Chloroform-*d*) δ 9.79 (s, 1H), 9.13 – 9.00 (m, 1H), 8.65 (s, 1H), 8.35 – 8.18 (m, 2H), 8.12 (d, *J* = 8.1 Hz, 1H), 8.04 (d, *J* = 8.6 Hz, 1H), 7.95 – 7.79 (m, 2H), 7.66 – 7.49 (m, 3H), 6.74 (s, 1H), 6.38 – 6.20 (m, 1H), 6.07 – 5.80 (m, 2H), 5.72 – 5.45 (m, 3H), 5.20 (d, *J* = 17.0 Hz, 1H), 5.07 (d, *J* = 10.2 Hz, 1H), 4.66 – 4.42 (m, 2H), 4.42 – 4.27 (m, 1H), 3.09 – 2.86 (m, 1H), 2.85 – 2.58 (m, 1H), 2.36 (s, 1H), 2.28 – 1.83 (m, 7H), 1.64 – 1.32 (m, 3H). Characterisations in agreement with *Org. Syn*, **2003,** *80*, 38 – 45.



(6-((Triisopropylsilyl)ethynyl)pyridin-3-yl)methanol, **111**

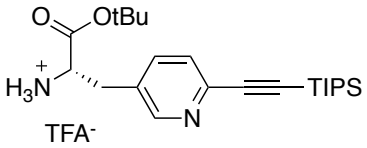
Lithium aluminium hydride (1 M in tetrahydrofuran, 0.37 mL, 1.1 equiv.) was suspended in tetrahydrofuran (0.5 mL) at 0 °C. A solution of methyl 6-((triisopropylsilyl)ethynyl)nicotinate (108 mg, 0.34 mmol, 1.0 equiv.) in tetrahydrofuran (1.5 mL) was added slowly and the mixture was stirred for 2 hours being allowed to warm up to room temperature. Then water (14 μL), aqueous 15% sodium hydroxide solution (14 uL), and water (42 uL) were added in sequence at 0 °C. The mixture was filtered over celite, the filtrate was dried over sodium sulfate, filtered and concentrated to give the titled product as a pale yellow liquid (90 mg, 92% yield). ^{1}H NMR (300 MHz, Chloroform-*d*) δ 8.55 (d, *J* = 2.2 Hz, 1H), 7.67 (dd, *J* = 8.0, 2.2 Hz, 1H), 7.47 (d, *J* = 8.0 Hz, 1H), 4.74 (s, 2H), 1.15 (s, 21H).



5-(Bromomethyl)-2-((triisopropylsilyl)ethynyl)pyridine, **112**

(6-((Triisopropylsilyl)ethynyl)pyridin-3-yl)methanol (93 mg, 0.32 mmol, 1.0 equiv.) was added in tetrahydrofuran (10 mL). Triphenylphosphine (318 mg, 1.21 mmol, 3.8 equiv.) was added and the mixture was stirred for 5 minutes. N-bromosuccinimide (215 mg, 1.21 mmol, 3.8 equiv.) was added and the mixture was stirred at room temperature for 24 hours. The mixture was diluted with water and dichloromethane. The organic phase was collected, dried over sodium sulfate, filtered and concentrated. The residue was purified by column chromatography

on silica gel (cyclohexane : ethyl acetate = 10 : 1, v/v) to give the titled product as a yellow liquid (94 mg, > 99% yield). ^{1}H NMR (300 MHz, Chloroform-*d*) δ 8.58 (dd, *J* = 2.4, 0.8 Hz, 1H), 7.67 (dd, *J* = 8.1, 2.4 Hz, 1H), 7.45 (dd, *J* = 8.1, 0.8 Hz, 1H), 4.46 (s, 2H), 1.24 – 0.90 (m, 21H).



(*R*)-*tert*-Butyl 2-amino-3-(4-((triisopropylsilyl)ethynyl)phenyl)propanoate, **115**

tert-Butyl 2-((diphenylmethylene)amino)acetate (50 mg, 0.17 mmol, 1.0 equiv.) and (1*S*,2*S*,4*S*)-2-((*R*)-(allyloxy)(quinolin-4-yl)methyl)-1-(anthracen-9-ylmethyl)-5-vinylquinuclidin-1-ium bromide (10 mg, 0.017 mmol, 0.1 equiv.) were dissolved in dichloromethane (2 mL). The mixture was cooled to -78 °C, cesium hydroxide monohydrate (285 mg, 17.00 mmol, 10 equiv.) was added and the resulting mixture was stirred at -78 °C for 30 minutes. A solution of 5-(bromomethyl)-2-((triisopropylsilyl)ethynyl)pyridine (67 mg, 0.25 mmol, 1.5 equiv.) in dichloromethane (3 mL) was added dropwise at -78 °C. The mixture was stirred at -78 °C for 7 hours and then left stirring overnight at room temperature. The mixture was diluted with diethyl ether and water. The organic phase was collected, dried over sodium sulfate, filtered and concentrated. The residue was purified by column chromatography on aluminium oxide (neutral, dichloromethane : cyclohexane = 1:9→1:4→2:1, v/v) to give (*R*)-*tert*-Butyl 2-((diphenylmethylene)amino)-3-(4-((triisopropylsilyl)ethynyl)phenyl)propanoate, (compound **114)** as a white solid (58 mg, 35% yield). (*R*)-*tert*-Butyl 2-((diphenylmethylene)amino)-3-(4-((triisopropylsilyl)ethynyl)phenyl)propanoate (70 mg, 0.12 mmol, 1.0 equiv.) was dissolved in diethyl ether (2 mL). An aqueous 1M HCl solution (1.5 mL) was added and the mixture was stirred at room temperature overnight. The mixture was concentrated and the residue was purified by preparative HPLC (X-Bridge, 5-100% acetonitrile over 10 minutes) to give the titled compound as a white solid (60 mg, 71% yield). ^{1}H NMR (300 MHz, Chloroform-*d*) δ 8.54 (s, 1H), 7.82 (d, *J* = 8.0 Hz, 1H), 7.58 – 7.46 (m, 1H), 4.30 – 4.12 (m, 1H), 3.47 – 3.20 (m, 2H), 1.37 (s, 9H), 1.27 – 0.85 (m, 21H). ^{13}C NMR (75 MHz, $CDCl_3$) δ 167.3, 148.9, 140.4, 139.9, 131.3, 128.5, 102.9, 97.0, 85.3, 54.0, 33.4, 27.8, 18.7, 11.3. HPLC (5 to 100% ACN in 10 min): rt 9.52 minutes (>95%). ee: 0.58 (chiral HPLC).

4.4.4 Peptide synthesis

Linear peptides were synthesized using manual Fmoc solid phase peptide synthesis using 2-chlorotrityl chloride resin (1.3 – 1.8 mmol/g loading). The resin was swelled in dichloromethane for 30 minutes before use.

Fmoc-Gly-OH, Fmoc-Leu(tBu)-OH, Fmoc-Tyr(tBu)-OH, Fmoc-Glu(tBu)-OH, Fmoc-Thr(tBu)-OH, fmoc-Pro-OH, Fmoc-Asp(tBu)-OH were commercially available and obtained

from Iris. Fmoc-TK-OH (compound **96**) and Fmoc-K(N_3)-OH (compound **92**) were obtained as described above.

The first amino acid was coupled on the resin using Fmoc-protected amino acid (2 eq) and N,N-diisopropylethylamine (4 eq) in dichloromethane for 1 hour. The resin loading was monitored by quantification of free dibenzofulvene using UV absorbance at 294 nm as described below.

The following protocol was used for the successive amino acid couplings: N,N-diisopropylethylamine (6 eq) was added to a solution of the Fmoc-protected amino acid (3 eq) and HBTU (3 eq) (HATU for Fmoc-Pro-OH) in NMP (1.0 mL for 200 mg resin). This pre-activated mixture was then added to the resin and shaken for 2 hours.

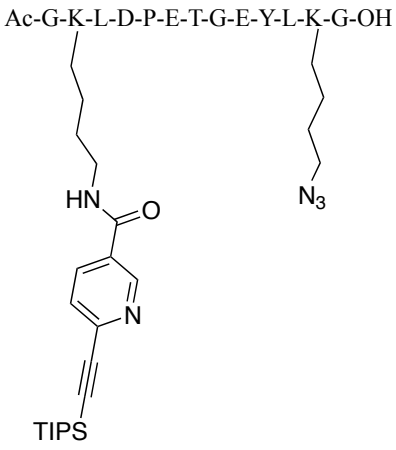
Fmoc deprotection was carried out with 20% piperidine in NMP (1 × 1 min, 2 × 15 min). After coupling and deprotection steps the resin was washed with DCM and NMP. N-terminal acetyl capping was carried out by treating the resin swelled in dichloromethane with acetic anhydride (10 equiv) for 2 hours.

The deprotection of TIPS was carried out by adding tetra-n-butylammonium fluoride (diluted from 1.0 M in tetrahydrofuran to 0.1 M with N,N-dimethylformamide) to the swelled resin and shaking for 30 minutes. After every step, the beads were washed with NMP for 3 times and then DCM for 3 times.

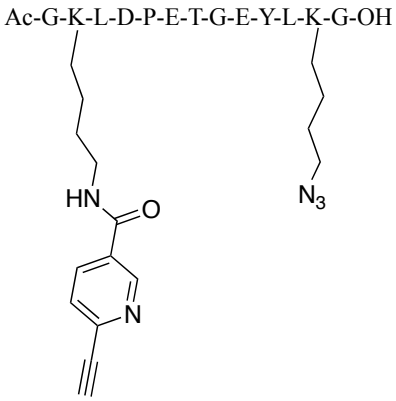
The intramolecular cyclisation reaction was carried out by adding N,N-diisopropylethylamine (10.0 eq), 2,6-lutidine (10.0 eq), a N,N-dimethylformamide solution of sodium ascorbate (4.0 eq) and an acetonitrile solution of copper(I) bromide (1.0 eq) to the swelled resin and shaking for 5 hours. The reaction was monitored by IR spectroscopy (on resin) and analytical HPLC (after cleavage, 5 to 100% acetonitrile over 10 minutes). The resin was subsequently washed with NMP, 0.05 M diethyldithiocarbamate sodium salt in NMP, water, NMP and dichloromethane.

The peptide was cleaved and deprotected using 2.5% triisopropylsilane, 2.5% water and 95% TFA for 2 hours. The solvent was removed under a stream of air and the residue triturated with diethyl ether before purification by HPLC and lyophilisation.

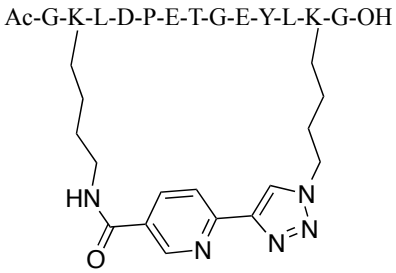
Analytical samples of intermediate peptides were obtained from cleavage of a small portion of the resin and subsequent purification by prep-HPLC and freeze-drying.



HPLC (5 to 100% ACN in 10 min): rt 8.67 minutes. MALDI-TOF-MS(-) m/z calcd for $C_{81}H_{121}N_{18}O_{24}Si$: 1757.8570 $[M-H]^-$; found: 1757.2632.



HPLC (5 to 100% ACN in 10 min): rt 5.42 minutes. MALDI-TOF-MS(-) m/z calcd for $C_{72}H_{101}N_{18}O_{24}$: 1601.7236 $[M-H]^-$; found: 1601.9735.



HPLC (5 to 100% ACN in 10 min): rt 5.10 minutes. MALDI-TOF-MS(+) m/z calcd for $C_{72}H_{103}N_{18}O_{24}$: 1603.7393 $[M+H]^+$; found: 1603.7441.

4.4.5 Quantification of Fmoc loading

The protocol was modified according to *Lett. Pept. Sci.* **2002**, *9*, 203 – 206.
A precise amount of the resin *m* (mg) was soaked in 2% DBU in dimethylformamide solution (2 mL) and the mixture was shaken for 1 hour. Then the solution was diluted with acetonitrile as *n* times which is suitable for UV-Vis experiment. The absorbance of the diluted solution at 294 nm was recorded as *A*. Then the following formula was applied to calculate the Fmoc loading ability *L* (mmol/g) for the resin.

$$L = \frac{0.1137 \times A \times n}{m}$$

References

[1] Sahara, G.; Ishitani, O. *Inorg. Chem.* **2015**, *54* (11), 5096–5104.
[2] Doherty, M. D.; Grills, D. C.; Muckerman, J. T.; Polyansky, D. E.; Fujita, E. *Coord. Chem. Rev.* **2010**, *254* (21–22), 2472–2482.
[3] Grice, K. A.; Kubiak, C. P. In *Advances in Inorganic Chemistry*; Aresta, M., van Eldik, R., Eds.; Academic Press, 2014; Vol. 66, pp 163–188.
[4] Rohacova, J.; Ishitani, O. *Dalt. Trans.* **2017**, *46* (28), 8899–8919.
[5] Hu, Y.-X.; Zhao, G.-W.; Dong, Y.; Lü, Y.-L.; Li, X.; Zhang, D.-Y. *Dye. Pigment.* **2017**, *137*, 569–575.
[6] Zhao, G. W.; Zhao, J. H.; Hu, Y. X.; Zhang, D. Y.; Li, X. *Synth. Met.* **2016**, *212*, 131–141.
[7] Martínez-Máñez, R.; Sancenón, F. *J. Fluoresc.* **2005**, *15* (3), 267–285.
[8] Lo, K. K.-W. *Acc. Chem. Res.* **2015**, *48* (12), 2985–2995.
[9] Chang, K.-C.; Sun, S.-S.; Lees, A. J. *Inorganica Chim. Acta* **2012**, *389*, 16–28.
[10] Ramdass, A.; Sathish, V.; Babu, E.; Velayudham, M.; Thanasekaran, P.; Rajagopal, S. *Coord. Chem. Rev.* **2017**, *343*, 278–307.
[11] Sun, S.-S.; Lees, A. J. *Coord. Chem. Rev.* **2002**, *230* (1), 171–192.
[12] Yip, A. M.-H.; Lo, K. K.-W. *Coord. Chem. Rev.* **2018**, *361*, 138–163.
[13] Hostachy, S.; Policar, C.; Delsuc, N. *Coord. Chem. Rev.* **2017**, *351*, 172–188.
[14] Lo, K. K.-W.; Zhang, K. Y.; Li, S. P.-Y. *Eur. J. Inorg. Chem.* **2011**, *2011* (24), 3551–3568.
[15] Chen, K.; Cui, M. *Medchemcomm* **2017**, *8* (7), 1393–1407.
[16] Cattaneo, M.; Fagalde, F.; Katz, N. E. *Inorg. Chem.* **2006**, *45* (17), 6884–6891.
[17] Lam, M. H. W.; Lee, D. Y. K.; Man, K. W.; Lau, C. S. W. *J. Mater. Chem.* **2000**, *10* (8), 1825–1828.
[18] Hung, C.-Y.; Singh, A. S.; Chen, C.-W.; Wen, Y.-S.; Sun, S.-S. *Chem. Commun.* **2009**, No. 12, 1511.
[19] Louie, M.-W.; Liu, H.-W.; Lam, M. H.-C.; Lau, T.-C.; Lo, K. K.-W. *Organometallics* **2009**, *28* (15), 4297–4307.
[20] Li, M.-J.; Ko, C.-C.; Duan, G.-P.; Zhu, N.; Yam, V. W.-W. *Organometallics* **2007**, *26* (25), 6091–6098.
[21] Zhang, F.; Cheng, X.; Cui, H.; Jia, H.; Li, Z. *J. Lumin.* **2018**, *194*, 467–473.
[22] Liu, L.; Yang, Y.; Feng, J. *Sensors Actuators B Chem.* **2017**, *253*, 310–316.
[23] Yang, X.; Li, Y. *Spectrochim. Acta Part A Mol. Biomol. Spectrosc.* **2016**, *153*, 746–753.
[24] Zhang, J.; Cui, Y.; Gao, B.; Hu, G.; Jiang, Q. *Sensors Actuators B Chem.* **2016**, *223*, 806–819.
[25] Xu, X.; Deng, A.; Xiang, Y. *J. Lumin.* **2015**, *160*, 151–157.
[26] Wang, C. *J. Lumin.* **2014**, *145*, 531–538.
[27] Xu, G.; Lu, M.; Huang, C.; Wang, Y.; Ge, S. *Spectrochim. Acta Part A Mol. Biomol. Spectrosc.* **2014**, *123*, 369–375.
[28] Huynh, L.; Wang, Z.; Yang, J.; Stoeva, V.; Lough, A.; Manners, I.; Winnik, M. A. *Chem. Mater.* **2005**, *17* (19), 4765–4773.
[29] Sacksteder, L.; Demas, J. N.; DeGraff, B. A. *Anal. Chem.* **1993**, *65* (23), 3480–3483.
[30] Palmioli, A.; Aliprandi, A.; Septiadi, D.; Mauro, M.; Bernardi, A.; De Cola, L.; Panigati, M. *Org. Biomol. Chem.* **2017**, *15* (7), 1686–1699.
[31] Raszeja, L. J.; Siegmund, D.; Cordes, A. L.; Güldenhaupt, J.; Gerwert, K.; Hahn, S.; Metzler-Nolte, N. *Chem. Commun.* **2017**, *53* (5), 905–908.
[32] Caspar, J. V; Meyer, T. J. *J. Phys. Chem.* **1983**, *87* (6), 952–957.
[33] Wrighton, M.; David, L. *J. Am. Chem. Soc.* **1974**, *96* (4), 998–1003.

[34] Chisholm, M. H.; Kelly, R. L.; Cotton, F. A.; Extine, M. W. *J. Am. Chem. Soc.* **1978**, *100* (7), 2257–2259.
[35] Lo, K. K. W.; Tsang, K. H. K.; Hui, W. K.; Zhu, N. *Inorg. Chem.* **2005**, *44* (17), 6100–6110.
[36] Lo, K. K. W.; Tsang, K. H. K.; Zhu, N. *Organometallics* **2006**, *25* (13), 3220–3227.
[37] Lo, K. K. W.; Tsang, K. H. K. *Organometallics* **2004**, *23* (12), 3062–3070.
[38] Giordano, P. J.; Wrighton, M. S. *J. Am. Chem. Soc.* **1979**, *101* (11), 2888–2897.
[39] Suntrup, L.; Klenk, S.; Klein, J.; Sobottka, S.; Sarkar, B. *Inorg. Chem.* **2017**, *56* (10), 5771–5783.
[40] Piletska, K. O.; Domasevitch, K. V; Gusev, A. N.; Shul'gin, V. F.; Shtemenko, A. V. *Polyhedron* **2015**, *102*, 699–704.
[41] Klemens, T.; Świtlicka-Olszewska, A.; Machura, B.; Grucela, M.; Schab-Balcerzak, E.; Smolarek, K.; Mackowski, S.; Szlapa, A.; Kula, S.; Krompiec, S.; et al. *Dalt. Trans.* **2016**, *45* (4), 1746–1762.
[42] Norouzi-Arasi, H.; Pal, A. K.; Nag, S.; Chartrand, D.; Hanan, G. S. *Chem. Commun.* **2016**, *52* (82), 12159–12162.
[43] Worl, L. A.; Duesing, R.; Chen, P.; Ciana, L. Della; Meyer, T. J. *J. Chem. Soc. Dalt. Trans.* **1991**, *0*, 849–858.
[44] Obata, M.; Kitamura, A.; Mori, A.; Kameyama, C.; Czaplewska, J. A.; Tanaka, R.; Kinoshita, I.; Kusumoto, T.; Hashimoto, H.; Harada, M.; et al. *Dalt. Trans.* **2008**, 3292–3300.
[45] Huang, R.; Langille, G.; Gill, R. K.; Li, C. M. J.; Mikata, Y.; Wong, M. Q.; Yapp, D. T.; Storr, T. *J. Biol. Inorg. Chem.* **2013**, *18* (7), 831–844.
[46] Wolff, M.; Munoz, L.; François, A.; Carrayon, C.; Seridi, A.; Saffon, N.; Picard, C.; Machura, B.; Benoist, E. *Dalt. Trans.* **2013**, *42* (19), 7019–7031.
[47] Huff, G. S.; Lo, W. K. C. C.; Horvath, R.; Turner, J. O.; Sun, X.-Z. Z.; Weal, G. R.; Davidson, H. J.; Kennedy, A. D. W. W.; McAdam, C. J.; Crowley, J. D.; et al. *Inorg. Chem.* **2016**, *55* (23), 12238–12253.
[48] Bertrand, H. C.; Clède, S.; Guillot, R.; Lambert, F.; Policar, C. *Inorg. Chem.* **2014**, *53* (12), 6204–6223.
[49] Clède, S.; Policar, C. *Chem. - A Eur. J.* **2015**, *21* (3), 942–958.
[50] Policar, C.; Waern, J. B.; Plamont, M.-A.; Clède, S.; Mayet, C.; Prazeres, R.; Ortega, J.-M.; Vessières, A.; Dazzi, A. *Angew. Chemie Int. Ed.* **2010**, *50* (4), 860–864.
[51] Hostachy, S.; Masuda, M.; Miki, T.; Hamachi, I.; Sagan, S.; Lequin, O.; Medjoubi, K.; Somogyi, A.; Delsuc, N.; Policar, C. *Chem. Sci.* **2018**, *9* (19), 4483–4487.
[52] Clède, S.; Lambert, F.; Sandt, C.; Gueroui, Z.; Réfrégiers, M.; Plamont, M. A.; Dumas, P.; Vessières, A.; Policar, C. *Chem. Commun.* **2012**, *48* (62), 7729–7731.
[53] Clède, S.; Lambert, F.; Sandt, C.; Kascakova, S.; Unger, M.; Harté, E.; Plamont, M. A.; Saint-Fort, R.; Deniset-Besseau, A.; Gueroui, Z.; et al. *Analyst* **2013**, *138* (19), 5627–5638.
[54] Clède, S.; Lambert, F.; Sandt, C.; Gueroui, Z.; Delsuc, N.; Dumas, P.; Vessières, A.; Policar, C. *Biotechnol. Adv.* **2013**, *31* (3), 393–395.
[55] Clède, S.; Lambert, F.; Saint-Fort, R.; Plamont, M. A.; Bertrand, H.; Vessières, A.; Policar, C. *Chem. - A Eur. J.* **2014**, *20* (28), 8714–8722.
[56] Clède, S.; Delsuc, N.; Laugel, C.; Lambert, F.; Sandt, C.; Baillet-Guffroy, A.; Policar, C. *Chem. Commun.* **2015**, *51* (13), 2687–2689.
[57] Lamy, E.; Nadjo, L.; Saveant, J. M. *J. Electroanal. Chem. Interfacial Electrochem.* **1977**, *78* (2), 403–407.
[58] Schwarz, H. A.; Dodson, R. W. *J. Phys. Chem.* **1989**, *93* (1), 409–414.
[59] Francke, R.; Schille, B.; Roemelt, M. *Chem. Rev.* **2018**, *118* (9), 4631–4701.

[60] Fisher, B. J.; Eisenberg, R. *J. Am. Chem. Soc.* **1980**, *102* (24), 7361–7363.
[61] Qiao, J.; Liu, Y.; Hong, F.; Zhang, J. *Chem. Soc. Rev.* **2014**, *43* (2), 631–675.
[62] Hawecker, J.; Lehn, J.-M.; Ziessel, R. *J. Chem. Soc. Chem. Commun.* **1984**, *984* (6), 328–330.
[63] Ching, H. Y. V.; Wang, X.; He, M.; Perujo Holland, N.; Guillot, R.; Slim, C.; Griveau, S.; Bertrand, H. C.; Policar, C.; Bedioui, F.; et al. *Inorg. Chem.* **2017**, *56* (5), 2966–2976.
[64] Feng, D.-M.; Zhu, Y.-P.; Chen, P.; Ma, T.-Y. *Catalysts* **2017**, *7* (12), 373.
[65] Milroy, L.-G.; Grossmann, T. N.; Hennig, S.; Brunsveld, L.; Ottmann, C. *Chem. Rev.* **2014**, *114* (9), 4695–4748.
[66] Nevola, L.; Giralt, E. *Chem. Commun.* **2015**, *51* (16), 3302–3315.
[67] Hill, T. A.; Shepherd, N. E.; Diness, F.; Fairlie, D. P. *Angew. Chemie Int. Ed.* **2014**, *53* (48), 13020–13041.
[68] Deshmukh, P.; Unni, S.; Krishnappa, G.; Padmanabhan, B. *Biophys. Rev.* **2017**, *9* (1), 41–56.
[69] Shih-Ching, L.; Xuchu, L.; Micheal T, H.; Lesa J, B.; Mark Hannink. *EMBO J.* **2006**, *25* (16), 3605–3617.
[70] Tu, J.; Zhang, X.; Zhu, Y.; Dai, Y.; Li, N.; Yang, F.; Zhang, Q.; Brann, D. W.; Wang, R. *J. Neurosci.* **2015**, *35* (44), 14727–14739.
[71] Steel, R.; Cowan, J.; Payerne, E.; O'Connell, M. A.; Searcey, M. *ACS Med. Chem. Lett.* **2012**, *3* (5), 407–410.
[72] Zhao, J.; Redell, J. B.; Moore, A. N.; Dash, P. K. *Biochem. Biophys. Res. Commun.* **2011**, *407* (3), 501–506.
[73] Lu, M. C.; Jiao, Q.; Liu, T.; Tan, S. J.; Zhou, H. S.; You, Q. D.; Jiang, Z. Y. *Eur. J. Med. Chem.* **2018**, *143*, 1578–1589.
[74] Hancock, R.; Schaap, M.; Pfister, H.; Wells, G. *Org. Biomol. Chem.* **2013**, *11* (21), 3553–3557.
[75] Houk, K. N.; Leach, A. G.; Kim, S. P.; Zhang, X. *Angew. Chemie Int. Ed.* **2003**, *42* (40), 4872–4897.
[76] Verdine, G. L.; Hilinski, G. J. In *Methods in Enzymology*; Elsevier Inc., 2012; Vol. 503, pp 3–33.
[77] Elgrishi, N.; Chambers, M. B.; Wang, X.; Fontecave, M. *Chem. Soc. Rev.* **2017**, *46* (3), 761–796.
[78] Yamazaki, Y.; Takeda, H.; Ishitani, O. *J. Photochem. Photobiol. C Photochem. Rev.* **2015**, *25*, 106–137.
[79] Happ, B.; Winter, A.; Hager, M. D.; Schubert, U. S. *Chem. Soc. Rev.* **2012**, *41* (6), 2222–2255.
[80] Zhao, G.-W. W.; Zhao, J.-H. H.; Hu, Y.-X. X.; Zhang, D.-Y. Y.; Li, X. *Synth. Met.* **2016**, *212*, 131–141.
[81] Lam, S.-T.; Yam, V. W.-W. *Chem. – A Eur. J.* **2010**, *16* (38), 11588–11593.
[82] Liu, Z.; He, W.; Guo, Z. *Chem. Soc. Rev.* **2013**, *42* (4), 1568–1600.
[83] Coogan, M. P.; Fernández-Moreira, V. *Chem. Commun.* **2014**, *50* (4), 384–399.
[84] Leonidova, A.; Gasser, G. *ACS Chem. Biol.* **2014**, *9* (10), 2180–2193.
[85] Ong, Y. C.; Roy, S.; Andrews, P. C.; Gasser, G. *Chem. Rev.* **2019**, *119* (2), 730–796.
[86] Scattergood, P. A.; Sinopoli, A.; Elliott, P. I. P. P. *Coord. Chem. Rev.* **2017**, *350*, 136–154.
[87] Scattergood, P. A.; Elliott, P. I. P. *Dalt. Trans.* **2017**, *46* (47), 16343–16356.
[88] Elliott, I. P. P. In *Organometallic Chemistry: Volume 39*; The Royal Society of Chemistry, 2014; Vol. 39, pp 1–25.
[89] Van Hilst, Q. V. C. C.; Lagesse, N. R.; Preston, D.; Crowley, J. D. *Dalt. Trans.* **2018**, *47* (4), 997–1002.

[90] Meldal, M.; Tornøe, C. W. *Chem. Rev.* **2008**, *108* (8), 2952–3015.
[91] Kolb, H. C.; Finn, M. G.; Sharpless, K. B. *Angew. Chemie Int. Ed.* **2001**, *40* (11), 2004–2021.
[92] Mohapatra, S.; Bhanja, C.; Jena, S.; Chakroborty, S.; Nayak, S. *Synth. Commun.* **2013**, *43* (15), 1993–2007.
[93] Bollinger, F. W.; Tuma, L. D. *Synlett* **1996**, *1996* (05), 407–413.
[94] Stufkens, D. J.; Vlček, A. *Coord. Chem. Rev.* **1998**, *177* (1), 127–179.
[95] Cannizzo, A.; Blanco-Rodríguez, A. M.; Nahhas, A. El; Šebera, J.; Záliš, S.; Vlček, A.; Chergui, M. *J. Am. Chem. Soc.* **2008**, *130* (28), 8967–8974.
[96] El Nahhas, A.; Consani, C.; Blanco-Rodríguez, A. M.; Lancaster, K. M.; Braem, O.; Cannizzo, A.; Towrie, M.; Clark, I. P.; Záliš, S.; Chergui, M.; et al. *Inorg. Chem.* **2011**, *50* (7), 2932–2943.
[97] Striplin, D. R.; Crosby, G. A. *Coord. Chem. Rev.* **2001**, *211* (1), 163–175.
[98] Kluba, C. A.; Mindt, T. L. *Molecules* **2013**, *18* (3), 3206–3226.
[99] Banerjee, S. R.; Maresca, K. P.; Francesconi, L.; Valliant, J.; Babich, J. W.; Zubieta, J. *Nucl. Med. Biol.* **2005**, *32* (1), 1–20.
[100] Seridi, A.; Wolff, M.; Boulay, A.; Saffon, N.; Coulais, Y.; Picard, C.; MacHura, B.; Benoist, E. *Inorg. Chem. Commun.* **2011**, *14* (1), 238–242.
[101] Mindt, T. L.; Struthers, H.; Brans, L.; Anguelov, T.; Schweinsberg, C.; Maes, V.; Tourwé, D.; Schibli, R. *J. Am. Chem. Soc.* **2006**, *128* (47), 15096–15097.
[102] Struthers, H.; Spingler, B.; Mindt, T. L.; Schibli, R. *Chem. - A Eur. J.* **2008**, *14* (20), 6173–6183.
[103] Mindt, T. L.; Müller, C.; Melis, M.; Jong, M. De; Schibli, R. *Bioconj. Chem.* **2008**, *19* (8), 1689–1695.
[104] Kim, E. M.; Joung, M. H.; Lee, C. M.; Jeong, H. J.; Lim, S. T.; Sohn, M. H.; Kim, D. W. *Bioorganic Med. Chem. Lett.* **2010**, *20* (14), 4240–4243.
[105] Mindt, T. L.; Schweinsberg, C.; Brans, L.; Hagenbach, A.; Abram, U.; Tourwé, D.; Garcia-Garayoa, E.; Schibli, R. *ChemMedChem* **2009**, *4* (4), 529–539.
[106] Anderson, C. B.; Elliott, A. B. S.; Lewis, J. E. M.; McAdam, C. J.; Gordon, K. C.; Crowley, J. D. *Dalt. Trans.* **2012**, *41* (48), 14625–14632.
[107] Lo, W. K. C.; Huff, G. S.; Cubanski, J. R.; Kennedy, A. D. W.; McAdam, C. J.; McMorran, D. A.; Gordon, K. C.; Crowley, J. D. *Inorg. Chem.* **2015**, *54* (4), 1572–1587.
[108] Boulay, A.; Seridi, A.; Zedde, C.; Ladeira, S.; Picard, C.; Maron, L.; Benoist, E. *Eur. J. Inorg. Chem.* **2010**, No. 32, 5058–5062.
[109] Wang, J.; Delavaux-Nicot, B.; Wolff, M.; Mallet-Ladeira, S.; Métivier, R.; Benoist, E.; Fery-Forgues, S. *Dalt. Trans.* **2018**, *47* (24), 8087–8099.
[110] Fernández, E.; Rodríguez, G.; Hostachy, S.; Clède, S.; Cócera, M.; Sandt, C.; Lambert, F.; de la Maza, A.; Policar, C.; López, O. *Colloids Surfaces B Biointerfaces* **2015**, *131*, 102–107.
[111] Kim, T. Y.; Elliott, A. B. S.; Shaffer, K. J.; John McAdam, C.; Gordon, K. C.; Crowley, J. D. *Polyhedron* **2013**, *52*, 1391–1398.
[112] Elliott, A. B. S.; Lewis, J. E. M.; Van Der Salm, H.; McAdam, C. J.; Crowley, J. D.; Gordon, K. C. *Inorg. Chem.* **2016**, *55* (7), 3440–3447.
[113] Lewis, J. E. M.; Elliott, A. B. S.; McAdam, C. J.; Gordon, K. C.; Crowley, J. D. *Chem. Sci.* **2014**, *5* (5), 1833–1843.
[114] Northrop, B. H.; Yang, H.-B. B.; Stang, P. J. *Chem. Commun.* **2008**, 5896–5908.
[115] Connell, T. U.; Hayne, D. J.; Ackermann, U.; Tochon-Danguy, H. J.; White, J. M.; Donnelly, P. S. *J. Label. Compd. Radiopharm.* **2014**, *57* (4), 262–269.
[116] Sacksteder, L. A.; Brown, E. A.; Demas, J. N.; Zipp, A. P.; Streich, J.; DeGraff, B. A. *Inorg. Chem.* **1990**, *29* (21), 4335–4340.

[117] François, A.; Auzanneau, C.; Le Morvan, V.; Galaup, C.; Godfrey, H. S.; Marty, L.; Boulay, A.; Artigau, M.; Mestre-Voegtlé, B.; Leygue, N.; et al. *Dalt. Trans.* **2014**, *43* (2), 439–450.
[118] Jindabot, S.; Teerachanan, K.; Thongkam, P.; Kiatisevi, S.; Khamnaen, T.; Phiriyawirut, P.; Charoenchaidet, S.; Sooksimuang, T.; Kongsaeree, P.; Sangtrirutnugul, P. *J. Organomet. Chem.* **2014**, *750*, 35–40.
[119] Chattopadhyay, B.; Vera, C. I. R.; Chuprakov, S.; Gevorgyan, V. *Org. Lett.* **2010**, *12* (9), 2166–2169.
[120] Zhang, Q.; Wang, X.; Cheng, C.; Zhu, R.; Liu, N.; Hu, Y. *Org. Biomol. Chem.* **2012**, *10* (14), 2847–2854.
[121] Schulze, B.; Schubert, U. S. *Chem. Soc. Rev.* **2014**, *43* (8), 2522–2571.
[122] Mole, T. K.; Arter, W. E.; Marques, I.; Félix, V.; Beer, P. D. *J. Organomet. Chem.* **2015**, *792*, 206–210.
[123] Anderson, C. B.; Elliott, A. B. S.; McAdam, C. J.; Gordon, K. C.; Crowley, J. D. *Organometallics* **2013**, *32* (3), 788–797.
[124] Yam, V. W.-W. W.; Wong, K. M.-C. C.; Chong, S. H.-F. F.; Lau, V. C.-Y. Y.; Lam, S. C.-F. F.; Zhang, L.; Cheung, K.-K. K. *J. Organomet. Chem.* **2003**, *670* (1–2), 205–220.
[125] Oberholzer, M.; Probst, B.; Bernasconi, D.; Spingler, B.; Alberto, R. *Eur. J. Inorg. Chem.* **2014**, *2014* (19).
[126] Chong, S. H.-F.; Lam, S. C.-F.; Ko, C.-C.; Yam, V. W.-W. *J. Clust. Sci.* **2004**, *15* (3), 301–314.
[127] Packheiser, R.; Lohan, M.; Bräuer, B.; Justaud, F.; Lapinte, C.; Lang, H. *J. Organomet. Chem.* **2008**, *693* (17), 2898–2902.
[128] Chung, W.-K. K.; Wong, K. M.-C. C.; Lam, W. H.; Zhu, X.; Zhu, N.; Kwok, H.-S. S.; Yam, V. W.-W. W. *New J. Chem.* **2013**, *37* (6), 1753–1767.
[129] Chong, S. H.-F.; Lam, S. C.-F.; Yam, V. W.-W.; Zhu, N.; Cheung, K.-K. *Organometallics* **2004**, *23*, 4924–4933.
[130] Lam, S. C.-F.; Yam, V. W.-W.; Wong, K. M.-C.; Cheng, E. C.-C.; Zhu, N. *Organometallics* **2005**, *24* (17), 4298–4305.
[131] Wong, K. M.-C.; Lam, S. C.-F.; Ko, C.-C.; Zhu, N.; Roué, S.; Lapinte, C.; Fathallah, S.; Costuas, K.; Kahlal, S.; Halet, J.-F. *Inorg. Chem.* **2003**, *42* (22), 7086–7097.
[132] Yam, V. W.-W.; Lo, W.-Y.; Zhu, N. *Chem. Commun.* **2003**, No. 19, 2446–2447.
[133] Fraser, M. G.; Blackman, A. G.; Irwin, G. I. S.; Easton, C. P.; Gordon, K. C. *Inorg. Chem.* **2010**, *49* (11), 5180–5189.
[134] Van Der Salm, H.; Fraser, M. G.; Horvath, R.; Turner, J. O.; Greetham, G. M.; Clark, I. P.; Towrie, M.; Lucas, N. T.; George, M. W.; Gordon, K. C. *Inorg. Chem.* **2014**, *53* (24), 13049–13060.
[135] Hevia, E.; Pérez, J.; Riera, V.; Miguel, D. *Organometallics* **2002**, *21* (9), 1966–1974.
[136] Chen, Y.; Zhang, L.; Chen, Z. *Acta Crystal.* **2002**, *58* (10), m590–m591.
[137] Yam, V. W.-W.; Chong, S. H.-F.; Ko, C.-C.; Cheung, K.-K. *Organometallics* **2000**, *19* (24), 5092–5097.
[138] Yam, V. W.-W.; Wong, K. M.-C.; Cheung, K.-K. *Organometallics* **1997**, *16*.
[139] Tarran, W. A.; Freeman, G. R.; Murphy, L.; Benham, A. M.; Kataky, R.; Williams, J. A. G. *Inorg. Chem.* **2014**, *53* (11), 5738–5749.
[140] Steel, H. L.; Allinson, S. L.; Andre, J.; Coogan, M. P.; Platts, J. A. *Chem. Commun.* **2015**, *51* (57), 11441–11444.
[141] Wang, D.; Yang, Y.; Huang, R.; Wang, L.; Wan, H. *J. Chem. Res.* **2016**, *40* (11), 645–647.
[142] Yang, Y.; Hu, W.; Ye, X.; Wang, D.; Shi, X. *Adv. Synth. Catal.* **2016**, *358* (16), 2583–2588.

[143] Wang, F.; Wu, X. Y.; Yu, R. M.; Zhao, Z. G.; Lu, C. Z. *J. Coord. Chem.* **2009**, *62* (20), 3296–3305.
[144] Richardson, C.; Steel, P. J. *Dalt. Trans.* **2003**, No. 5, 992–1000.
[145] Costa, I.; Montalti, M.; Pallavicini, P.; Perotti, A.; Prodi, L.; Zaccheroni, N. *J. Organomet. Chem.* **2000**, *593–594*, 267–273.
[146] Frisch, M. J.; Trucks, G. W.; Schlegel, H. B.; Scuseria, G. E.; Robb, M. A.; Cheeseman, J. R.; Scalmani, G.; Barone, V.; Mennucci, B.; Petersson, G. A.; et al. Gaussian, Inc.: Wallingford CT 2009.
[147] Wong, K. M.-C.; Yam, V. W.-W. *Coord. Chem. Rev.* **2007**, *251* (17), 2477–2488.
[148] Yam, V. W.-W.; Kam-Wing Lo, K.; Man-Chung Wong, K. *J. Organomet. Chem.* **1999**, *578* (1), 3–30.
[149] Hissler, M.; McGarrah, J. E.; Connick, W. B.; Geiger, D. K.; Cummings, S. D.; Eisenberg, R. *Coord. Chem. Rev.* **2000**, *208* (1), 115–137.
[150] Wang, W.; Yang, H.-B. *Chem. Commun.* **2014**, *50* (40), 5171–5186.
[151] Zhou, G. J.; Wong, W. Y. *Chem. Soc. Rev.* **2011**, *40* (5), 2541–2566.
[152] Blons, C.; Amgoune, A.; Bourissou, D. *Dalt. Trans.* **2018**, *47* (31), 10388–10393.
[153] Ford, P. C.; Cariati, E.; Bourassa, J. *Chem. Rev.* **1999**, *99* (12), 3625–3648.
[154] Chan, C.-W.; Cheng, L.-K.; Che, C.-M. *Coord. Chem. Rev.* **1994**, *132*, 87–97.
[155] Ko, C.-C.; Yam, V. W.-W. *Acc. Chem. Res.* **2018**, *51* (1), 149–159.
[156] Yam, V. W. W.; Lau, V. C. Y.; Cheung, K. K. *Organometallics* **1995**, *14* (6), 2749–2753.
[157] Yam, V. W.-W.; Lau, V. C.-Y.; Cheung, K.-K. *Organometallics* **1996**, *15* (6), 1740–1744.
[158] Hissler, M.; Connick, W. B.; Geiger, D. K.; McGarrah, J. E.; Lipa, D.; Lachicotte, R. J.; Eisenberg, R. *Inorg. Chem.* **2000**, *39* (3), 447–457.
[159] Yam, V. W.-W.; Tang, R. P.-L.; Wong, K. M.-C.; Cheung, K.-K. *Organometallics* **2001**, *20* (22), 4476–4482.
[160] Whittle, C. E.; Weinstein, J. A.; George, M. W.; Schanze, K. S. *Inorg. Chem.* **2001**, *40* (16), 4053–4062.
[161] Mel, M. Y.; Butin, K. P. **2003**, *52* (5), 1150–1156.
[162] Yam, V.-W.; Chong, S. H.-F.; Cheung, K.-K. *Chem. Commun.* **1998**, 2121–2122.
[163] Yam, V.-W.; Chong, S.-F.; Wong, K.-C.; others. *Chem. Commun.* **1999**, 1013–1014.
[164] Liu, R.; Zhou, D.; Azenkeng, A.; Li, Z.; Li, Y.; Glusac, K. D.; Sun, W. *Chem. - A Eur. J.* **2012**, *18* (36), 11440–11448.
[165] He, M.; Ching, H. Y. V.; Policar, C.; Bertrand, H. C. *New J. Chem.* **2018**, *42* (14), 11312–11323.
[166] Yu, H.; Li, M.; Liu, G.; Geng, J.; Wang, J.; Ren, J.; Zhao, C.; Qu, X. *Chem. Sci.* **2012**, *3* (11), 3145.
[167] G. R. Stephenson. In *Bioorganometallics: Biomolecules, labeling, Medicine*; G. Jaouen, Ed.; Wiley-VCH, Weinheim, 2006; pp 215–262.
[168] Gabrielsson, A.; Busby, M.; Matousek, P.; Towrie, M.; Hevia, E.; Cuesta, L.; Perez, J.; Záliš, S.; Vlček, A. *Inorg. Chem.* **2006**, *45* (24), 9789–9797.
[169] Compton, R. N.; Reinhardt, P. W.; Cooper, C. D. *J. Chem. Phys.* **1975**, *63* (9), 3821–3827.
[170] Qiao, J.; Liu, Y.; Hong, F.; Zhang, J. *Chem. Soc. Rev.* **2014**, *43* (2), 631–675.
[171] Bard, A. J.; Parsons, R.; Jordan, J. CRC press, 1985.
[172] Sun, Z.; Talreja, N.; Tao, H.; Texter, J.; Muhler, M.; Strunk, J.; Chen, J. *Angew. Chemie - Int. Ed.* **2018**, *57* (26), 7610–7627.
[173] Li, R.; Zhang, W.; Zhou, K. *Adv. Mater.* **2018**, *30* (35), 1705512.
[174] Ran, J.; Jaroniec, M.; Qiao, S.-Z. *Adv. Mater.* **2018**, *30* (7), 1704649.
[175] Takeda, H.; Ishitani, O. *Coord. Chem. Rev.* **2010**, *254* (3), 346–354.

[176] Morimoto, T.; Ishitani, O. *Acc. Chem. Res.* **2017**, *50* (11), 2673–2683.
[177] Takeda, H.; Koike, K.; Morimoto, T.; Inumaru, H.; Ishitani, O. In *Inorganic Photochemistry*; Eldik, R. van, Stochel, G. B. T.-A. in I. C., Eds.; Academic Press, 2011; Vol. 63, pp 137–186.
[178] Sato, S.; Ishitani, O. *Coord. Chem. Rev.* **2015**, *282–283*, 50–59.
[179] Sahara, G.; Ishitani, O. *Inorg. Chem.* **2015**, *54* (11), 5096–5104.
[180] Fujita, E.; Brunschwig, B. S. *Electron Transfer in Chemistry*. April 14, 2008.
[181] Sutin, N.; Creutz, C.; Fujita, E. *Comments Inorg. Chem.* **1997**, *19* (2), 67–92.
[182] Doherty, M. D.; Grills, D. C.; Muckerman, J. T.; Polyansky, D. E.; Fujita, E. *Coord.Chem. Rev.* **2010**, *254* (21), 2472–2482.
[183] Zhao, G.; Huang, X.; Wang, X.; Wang, X. *J. Mater. Chem. A* **2017**, *5* (41), 21625–21649.
[184] Costentin, C.; Savéant, J. M.; Tard, C. *ACS Energy Lett.* **2018**, *3* (3), 695–703.
[185] Costentin, C.; Robert, M.; Savéant, J. M. *Acc. Chem. Res.* **2015**, *48* (12), 2996–3006.
[186] Bonin, J.; Maurin, A.; Robert, M. *Coord. Chem. Rev.* **2017**, *334*, 184–198.
[187] Takeda, H.; Cometto, C.; Ishitani, O.; Robert, M. *ACS Catal.* **2017**, *7* (1), 70–88.
[188] Costentin, C.; Drouet, S.; Robert, M.; Savéant, J. M. *J. Am. Chem. Soc.* **2012**, *134* (27), 11235–11242.
[189] Hawecker, J.; Lehn, J.-M.; Ziessel, R. *J. Chem. Soc. Chem. Commun.* **1984**, *984* (6), 328–330.
[190] Sullivan, B. P.; Bolinger, C. M.; Conrad, D.; Vining, W. J.; Meyer, T. J. *J. Chem. Soc. Chem. Commun.* **1985**, No. 20, 1414–1416.
[191] Breikss, A. I.; Abruña, H. D. *J. Electroanal. Chem.* **1986**, *201* (2), 347–358.
[192] Christensen, P.; Hamnett, A.; Muir, A. V. G.; Timney, J. A. *J. Chem. Soc. Dalt. Trans.* **1992**, No. 9, 1455–1463.
[193] Grice, K. A.; Gu, N. X.; Sampson, M. D.; Kubiak, C. P. *Dalt. Trans.* **2013**, *42* (23), 8498–8503.
[194] Scheiring, T.; Klein, A.; Kaim, W. *J. Chem. Soc., Perkin Trans. 2* **1997**, 2569–2571.
[195] Wong, K. Y.; Chung, W. H.; Lau, C. P. *J. Electroanal. Chem.* **1998**, *453* (1–2), 161–170.
[196] Smieja, J. M.; Kubiak, C. P. *Inorg. Chem.* **2010**, *49* (20), 9283–9289.
[197] Benson, E. E.; Grice, K. A.; Smieja, J. M.; Kubiak, C. P. *Polyhedron* **2013**, *58*, 229–234.
[198] Kalläne, S. I.; van Gastel, M. *J. Phys. Chem. A* **2016**, *120* (38), 7465–7474.
[199] Clark, M. L.; Cheung, P. L.; Lessio, M.; Carter, E. A.; Kubiak, C. P. *ACS Catal.* **2018**, *8* (3), 2021–2029.
[200] Machan, C. W.; Chabolla, S. A.; Kubiak, C. P. *Organometallics* **2015**, *34* (19), 4678–4683.
[201] Newkome, G. R.; Patri, A. K.; Holder, E.; Schubert, U. S. *European J. Org. Chem.* **2004**, No. 2, 235–254.
[202] Teesdale, J. J.; Pistner, A. J.; Yap, G. P. A.; Ma, Y. Z.; Lutterman, D. A.; Rosenthal, J. *Catal. Today* **2014**, *225*, 149–157.
[203] Machan, C. W.; Chabolla, S. A.; Yin, J.; Gilson, M. K.; Tezcan, F. A.; Kubiak, C. P. *J. Am. Chem. Soc.* **2014**, *136* (41), 14598–14607.
[204] Portenkirchner, E.; Schlager, S.; Apaydin, D.; Oppelt, K.; Himmelsbach, M.; Egbe, D. A. M.; Neugebauer, H.; Knör, G.; Yoshida, T.; Sariciftci, N. S. *Electrocatalysis* **2015**, *6* (2), 185–197.
[205] Portenkirchner, E.; Oppelt, K.; Ulbricht, C.; Egbe, D. A. M.; Neugebauer, H.; Knör, G.; Sariciftci, N. S. *J. Organomet. Chem.* **2012**, *716*, 19–25.
[206] Whang, D. R.; Apaydin, D. H.; Park, S. Y.; Sariciftci, N. S. *J. Catal.* **2018**, *363*, 191–196.
[207] Sung, S.; Kumar, D.; Gil-Sepulcre, M.; Nippe, M. *J. Am. Chem. Soc.* **2017**, *139* (40), 13993–13996.

[208] Yang, W.; Sinha Roy, S.; Pitts, W. C.; Nelson, R. L.; Fronczek, F. R.; Jurss, J. W. *Inorg. Chem.* **2018**, *57* (15), 9564–9575.
[209] Stanton, C. J.; Machan, C. W.; Vandezande, J. E.; Jin, T.; Majetich, G. F.; Schaefer, H. F.; Kubiak, C. P.; Li, G.; Agarwal, J. *Inorg. Chem.* **2016**, *55* (6), 3136–3144.
[210] Calzaferri, G.; Hädener, K.; Li, J. *J. Photochem. Photobiol. A Chem.* **1992**, *64* (2), 259–262.
[211] Vollmer, M. V.; Machan, C. W.; Clark, M. L.; Antholine, W. E.; Agarwal, J.; Schaefer, H. F.; Kubiak, C. P.; Walensky, J. R. *Organometallics* **2015**, *34* (1), 3–12.
[212] Valenti, G.; Panigati, M.; Boni, A.; D'Alfonso, G.; Paolucci, F.; Prodi, L.; D'Alfonso, G.; Paolucci, F.; Prodi, L.; D'Alfonso, G.; et al. *Inorganica Chim. Acta* **2014**, *417*, 270–273.
[213] Donghi, D.; D'Alfonso, G.; Mauro, M.; Panigati, M.; Mercandelli, P.; Sironi, A.; Mussini, P.; D'Alfonso, L. *Inorg. Chem.* **2008**, *47* (10), 4243–4255.
[214] Sinha, S.; Berdichevsky, E. K.; Warren, J. J. *Inorganica Chim. Acta* **2017**, *460*, 63–68.
[215] Nganga, J. K.; Samanamu, C. R.; Tanski, J. M.; Pacheco, C.; Saucedo, C.; Batista, V. S.; Grice, K. A.; Ertem, M. Z.; Angeles-Boza, A. M. *Inorg. Chem.* **2017**, *56* (6), 3214–3226.
[216] Neyhouse, B. J.; White, T. A. *Inorganica Chim. Acta* **2018**, *479*, 49–57.
[217] Liang, Y.; Nguyen, M. T.; Holliday, B. J.; Jones, R. A. *Inorg. Chem. Commun.* **2017**, *84*, 113–117.
[218] Qiao, X.; Li, Q.; Schaugaard, R. N.; Noffke, B. W.; Liu, Y.; Li, D.; Liu, L.; Raghavachari, K.; Li, L. shi. *J. Am. Chem. Soc.* **2017**, *139* (11), 3934–3937.
[219] Schaugaard, R. N.; Raghavachari, K.; Li, L. *Inorg. Chem.* **2018**, *57* (17), 10548–10556.
[220] Elgrishi, N.; Griveau, S.; Chambers, M. B.; Bedioui, F.; Fontecave, M. *Chem. Commun.* **2015**, *51* (14), 2995–2998.
[221] Kramer, W. W.; McCrory, C. C. L. *Chem. Sci.* **2016**, *7* (4), 2506–2515.
[222] Rosser, T. E.; Windle, C. D.; Reisner, E. *Angew. Chemie Int. Ed.* **2016**, *55* (26), 7388–7392.
[223] Maurin, A.; Robert, M. *Chem. Commun.* **2016**, *52* (81), 12084–12087.
[224] Walsh, J. J.; Neri, G.; Smith, C. L.; Cowan, A. J. *Chem. Commun.* **2014**, *50* (84), 12698–12701.
[225] Rosser, T. E.; Reisner, E. *ACS Catal.* **2017**, *7* (5), 3131–3141.
[226] Lin, S.; Diercks, C. S.; Zhang, Y.-B.; Kornienko, N.; Nichols, E. M.; Zhao, Y.; Paris, A. R.; Kim, D.; Yang, P.; Yaghi, O. M.; et al. *Science (80-.).* **2015**, *349* (6253), 1208–1213.
[227] Bullock, R. M.; Das, A. K.; Appel, A. M. *Chem. – A Eur. J.* **2017**, *23* (32), 7626–7641.
[228] Cabrera, C. R.; Abruña, H. D. *J. Electroanal. Chem. Interfacial Electrochem.* **1986**, *209* (1), 101–107.
[229] O'Toole, T. R.; Sullivan, B. P.; Bruce, M. R.-M.; Margerum, L. D.; Murray, R. W.; Meyer, T. J. *J. Electroanal. Chem. Interfacial Electrochem.* **1989**, *259* (1), 217–239.
[230] Cecchet, F.; Alebbi, M.; Bignozzi, C. A.; Paolucci, F. *Inorganica Chim. Acta* **2006**, *359* (12), 3871–3874.
[231] Oyarzún, D. P.; Chardon-Noblat, S.; Linarez Pérez, O. E.; López Teijelo, M.; Zúñiga, C.; Zarate, X.; Shott, E.; Carreño, A.; Arratia-Perez, R. *Chem. Phys. Lett.* **2018**, *694*, 40–47.
[232] Chiang, C. K.; Fincher, C. R.; Park, Y. W.; Heeger, A. J.; Shirakawa, H.; Louis, E. J.; Gau, S. C.; MacDiarmid, A. G. *Phys. Rev. Lett.* **1977**, *39* (17), 1098–1101.
[233] Zhanaidarova, A.; Ostericher, A. L.; Miller, C. J.; Jones, S. C.; Kubiak, C. P. *Organometallics* **2018**, acs.organomet.8b00547.
[234] Cosnier, S.; Deronzier, A.; Moutet, J. *J. Mol. Catal.* **1988**, *45*, 381–391.
[235] Cheung, K. C.; Guo, P.; So, M. H.; Lee, L. Y. S.; Ho, K. P.; Wong, W. L.; Lee, K. H.; Wong, W. T.; Zhou, Z. Y.; Wong, K. Y. *J. Organomet. Chem.* **2009**, *694* (17), 2842–

2845.
[236] Sun, C.; Prosperini, S.; Quagliotto, P.; Viscardi, G.; Yoon, S. S.; Gobetto, R.; Nervi, C. *Dalt. Trans.* **2016**, *45* (37), 14678–14688.
[237] Pinson, J.; Podvorica, F. *Chem. Soc. Rev.* **2005**, *34* (5), 429–439.
[238] Sun, C.; Rotundo, L.; Garino, C.; Nencini, L.; Yoon, S. S.; Gobetto, R.; Nervi, C. *ChemPhysChem* **2017**, *18* (22), 3219–3229.
[239] Oh, S.; Gallagher, J. R.; Miller, J. T.; Surendranath, Y. *J. Am. Chem. Soc.* **2016**, *138* (6), 1820–1823.
[240] Rezaei, B.; Mokhtarianpour, M.; Ensafi, A. A.; Hadadzadeh, H.; Shakeri, J. *Polyhedron* **2015**, *101*, 160–164.
[241] Reuillard, B.; Ly, K. H.; Rosser, T. E.; Kuehnel, M. F.; Zebger, I.; Reisner, E. *J. Am. Chem. Soc.* **2017**, *139* (41), 14425–14435.
[242] Huan, T. N.; Prakash, P.; Simon, P.; Rousse, G.; Xu, X.; Artero, V.; Gravel, E.; Doris, E.; Fontecave, M. *ChemSusChem* **2016**, *9* (17), 2317–2320.
[243] Maurin, A.; Robert, M. *J. Am. Chem. Soc.* **2016**, *138* (8), 2492–2495.
[244] Blakemore, J. D.; Gupta, A.; Warren, J. J.; Brunschwig, B. S.; Gray, H. B. *J. Am. Chem. Soc.* **2013**, *135* (49), 18288–18291.
[245] Hu, X.-M.; Rønne, M. H.; Pedersen, S. U.; Skrydstrup, T.; Daasbjerg, K. *Angew. Chemie Int. Ed.* **2017**, *56* (23), 6468–6472.
[246] Kang, P.; Zhang, S.; Meyer, T. J.; Brookhart, M. *Angew. Chem. Int. Ed.* **2014**, *53* (33), 8709–8713.
[247] Johnson, F. P.; George, M. W.; Hartl, F.; Turner, J. J. *Organometallics* **1996**, *15* (15), 3374–3387.
[248] Sequoia, E.; Genies, E. M.; Tsintavis, C. *J. Electroanal. Chem.* **1985**, *195*, 109–128.
[249] Bacon, J.; Adams, R. N. *J. Am. Chem. Soc.* **1968**, *90* (24), 6596–6599.
[250] Girard, C.; Bedioui, F.; Elamari, H.; Nyokong, T.; Griveau, S.; Coates, M. *J. Electroanal. Chem.* **2012**, *670*, 79–84.
[251] Sandroni, M.; Volpi, G.; Fiedler, J.; Buscaino, R.; Viscardi, G.; Milone, L.; Gobetto, R.; Nervi, C. *Catal. Today* **2010**, *158* (1–2), 22–28.
[252] Buriez, O.; Labbé, E.; Pigeon, P.; Jaouen, G.; Amatore, C. *J. Electroanal. Chem.* **2008**, *619–620* (1–2), 169–175.
[253] He, L.; Qiu, G.; Gao, Y.; Wu, J. *Org. Biomol. Chem.* **2014**, *12* (36), 6965–6971.
[254] Baranton, S.; Bélanger, D. *Electrochim. Acta* **2008**, *53* (23), 6961–6967.
[255] Pinson, J.; Delamar, M.; Desbat, B.; Hitmi, R.; Savéant, J.-M.; Allongue, P.; Fagebaume, O. *J. Am. Chem. Soc.* **2002**, *119* (1), 201–207.
[256] Karsi, N.; Vautrin-Ul, C.; Chehimi, M. M.; Podvorica, F.; Pinson, J.; Chaussé, A. *Chem. Mater.* **2002**, *14* (1), 392–400.
[257] Bourdillon, C.; Delamar, M.; Demaille, C.; Hitmi, R.; Moiroux, J.; Pinson, J. *J. Electroanal. Chem.* **1992**, *336* (1–2), 113–123.
[258] Aoi, S.; Mase, K.; Ohkubo, K.; Fukuzumi, S. *Chem. Commun.* **2015**, *51* (50), 10226–10228.
[259] Wei, P.-J.; Yu, G.-Q.; Naruta, Y.; Liu, J.-G. *Angew. Chemie Int. Ed.* **2014**, *53* (26), 6659–6663.
[260] Elouarzaki, K.; Le Goff, A.; Holzinger, M.; Thery, J.; Cosnier, S. *J. Am. Chem. Soc.* **2012**, *134* (34), 14078–14085.
[261] Le, A.; Artero, V.; Jousselme, B.; Tran, P. D.; Métayé, R.; Fihri, A.; Palacin, S.; Fontecave, M. **2018**, *326* (5958), 1384–1387.
[262] De Volder, M. F. L.; Tawfick, S. H.; Baughman, R. H.; Hart, A. J. *Science (80-.).* **2013**, *339* (6119), 535–539.
[263] Karousis, N.; Tagmatarchis, N.; Tasis, D. *Chem. Rev.* **2010**, *110* (9), 5366–5397.

[264] Zhuang, C.; Miao, Z.; Sheng, C.; Zhang, W. *Curr. Med. Chem.* **2014**, *21*, 1861–1870.
[265] Stumpf, M. P. H.; Thorne, T.; de Silva, E.; Stewart, R.; An, H. J.; Lappe, M.; Wiuf, C. *Proc. Natl. Acad. Sci.* **2008**, *105* (19), 6959 LP – 6964.
[266] Berg, T. *Angew. Chemie Int. Ed.* **2017**, *56* (40), 12048–12050.
[267] Moreira, I. S.; Fernandes, P. A.; Ramos, M. J. *Proteins Struct. Funct. Bioinforma.* **2007**, *68* (4), 803–812.
[268] Geppert, T.; Hoy, B.; Wessler, S.; Schneider, G. *Chem. Biol.* **2011**, *18* (3), 344–353.
[269] Guo, W.; Wisniewski, J. A.; Ji, H. *Bioorg. Med. Chem. Lett.* **2014**, *24* (11), 2546–2554.
[270] Arkin, M. R.; Wells, J. A. *Nat. Rev. Drug Discov.* **2004**, *3* (4), 301–317.
[271] Zhang, B.; Golding, B. T.; Hardcastle, I. R. *Future Med. Chem.* **2015**, *7* (5), 631–645.
[272] Millard, M.; Pathania, D.; Grande, F.; Xu, S.; Neamati, N. *Curr. Pharm. Des.* **2011**, *17* (6), 536–559.
[273] Weber, L. *Expert Opin. Ther. Pat.* **2010**, *20* (2), 179–191.
[274] Zhao, Y.; Aguilar, A.; Bernard, D.; Wang, S. *J. Med. Chem.* **2015**, *58* (3), 1038–1052.
[275] Patel, S.; Player, M. R. *Expert Opin. Investig. Drugs* **2008**, *17* (12), 1865–1882.
[276] Zhuang, C.; Wu, Z.; Xing, C.; Miao, Z. *Medchemcomm* **2017**, *8* (2), 286–294.
[277] Wells, G. *Biochem. Soc. Trans.* **2015**, *43* (4), 674 LP – 679.
[278] Zhuang, C.; Miao, Z.; Sheng, C.; Zhang, W.; Zhang, C. S. and W.; Sheng, C.; Zhang, W. *Curr. Med. Chem.* **2014**, *21* (16), 1861–1870.
[279] Pallesen, J. S.; Tran, K. T.; Bach, A. *J. Med. Chem.* **2018**, *61* (18), 8088–8103.
[280] Yang, J.; Hu, L. *Med. Res. Rev.* **2018**, doi: 10.1002/med/21530.
[281] Cierpicki, T.; Grembecka, J. *Future Med. Chem.* **2014**, *6* (4), 447–462.
[282] Itoh, K.; Wakabayashi, N.; Katoh, Y.; Ishii, T.; Igarashi, K.; Engel, J. D.; Yamamoto, M. *Genes Dev.* **1999**, *13* (1), 76–86.
[283] Moi, P.; Chan, K.; Asunis, I.; Cao, A.; Kan, Y. W. *Proc. Natl. Acad. Sci.* **1994**, *91* (21), 9926–9930.
[284] Reuter, S.; Gupta, S. C.; Chaturvedi, M. M.; Aggarwal, B. B. *Free Radic. Biol. Med.* **2010**, *49* (11), 1603–1616.
[285] Itoh, K.; Chiba, T.; Takahashi, S.; Ishii, T.; Igarashi, K.; Katoh, Y.; Oyake, T.; Hayashi, N.; Satoh, K.; Hatayama, I.; et al. *Biochem. Biophys. Res. Commun.* **1997**, *236* (2), 313–322.
[286] McMahon, M.; Thomas, N.; Itoh, K.; Yamamoto, M.; Hayes, J. D. *J. Biol. Chem.* **2004**, *279* (30), 31556–31567.
[287] Katoh, Y.; Itoh, K.; Yoshida, E.; Miyagishi, M.; Fukamizu, A.; Yamamoto, M. *Genes to Cells* **2002**, *6* (10), 857–868.
[288] Kobayashi, M.; Itoh, K.; Suzuki, T.; Osanai, H.; Nishikawa, K.; Katoh, Y.; Takagi, Y.; Yamamoto, M. *Genes to Cells* **2002**, *7* (8), 807–820.
[289] Tong, K. I.; Katoh, Y.; Kusunoki, H.; Itoh, K.; Tanaka, T.; Yamamoto, M. *Mol. Cell. Biol.* **2006**, *26* (8), 2887–2900.
[290] Kensler, T. W.; Wakabayashi, N.; Biswal, S. *Annu. Rev. Pharmacol. Toxicol.* **2007**, *47* (1), 89–116.
[291] Padmanabhan, B.; Tong, K. I.; Ohta, T.; Nakamura, Y.; Scharlock, M.; Ohtsuji, M.; Kang, M.-I.; Kobayashi, A.; Yokoyama, S.; Yamamoto, M. *Mol. Cell* **2006**, *21* (5), 689–700.
[292] Tong, K. I.; Padmanabhan, B.; Kobayashi, A.; Shang, C.; Hirotsu, Y.; Yokoyama, S.; Yamamoto, M. *Mol. Cell. Biol.* **2007**, *27* (21), 7511–7521.
[293] Magesh, S.; Chen, Y.; Hu, L. *Med. Res. Rev.* **2012**, *32* (4), 687–726.
[294] Zhang, D. D.; Lo, S.-C.; Cross, J. V; Templeton, D. J.; Hannink, M. *Mol. Cell. Biol.* **2004**, *24* (24), 10941–10953.
[295] Baird, L.; Llères, D.; Swift, S.; Dinkova-Kostova, A. T. *Proc. Natl. Acad. Sci.* **2013**, *110*

(38), 15259–15264.
[296] Baird, L.; Swift, S.; Llères, D.; Dinkova-Kostova, A. T. *Biotechnol. Adv.* **2014**, *32* (6), 1133–1144.
[297] Shih-Ching, L.; Xuchu, L.; Micheal T, H.; Lesa J, B.; Mark Hannink; Lo, S. C.; Li, X.; Henzl, M. T.; Beamer, L. J.; Hannink, M.; et al. *EMBO J.* **2006**, *25* (15), 3605–3617.
[298] Chen, Y.; Inoyama, D.; Kong, A. N. T.; Beamer, L. J.; Hu, L. *Chem. Biol. Drug Des.* **2011**, *78* (6), 1014–1021.
[299] Burke, T. J.; Loniello, K. R.; Beebe, J. a; Ervin, K. M. *Comb. Chem. High Throughput Screen.* **2003**, *6* (3), 183–194.
[300] Hancock, R.; Bertrand, H. C.; Tsujita, T.; Naz, S.; El-Bakry, A.; Laoruchupong, J.; Hayes, J. D.; Wells, G. *Free Radic. Biol. Med.* **2012**, *52* (2), 444–451.
[301] Borja-Cacho, D.; Matthews, J.; Inoyama, D.; Chen, Y.; Huang, X.; Beamer, L. J.; Kong, A.-N. T.; Hu, L. *J. Biomol. Screen.* **2011**, *17* (4), 435–447.
[302] Deniz, A. A.; Dahan, M.; Grunwell, J. R.; Ha, T.; Faulhaber, a E.; Chemla, D. S.; Weiss, S.; Schultz, P. G. *Proc. Natl. Acad. Sci. U. S. A.* **1999**, *96* (7), 3670–3675.
[303] Schaap, M.; Hancock, R.; Wilderspin, A.; Wells, G. *Protein Sci.* **2013**, *22* (12), 1812–1819.
[304] Georgakopoulos, N. D.; Talapatra, S. K.; Gatliff, J.; Kozielski, F.; Wells, G. *ChemBioChem* **2018**, 1810–1816.
[305] Guntas, G.; Lewis, S. M.; Mulvaney, K. M.; Cloer, E. W.; Tripathy, A.; Lane, T. R.; Major, M. B.; Kuhlman, B. *Protein Eng. Des. Sel.* **2015**, *29* (1), 1–9.
[306] Debaisieux, S.; Rayne, F.; Yezid, H.; Beaumelle, B. *Traffic* **2011**, *13* (3), 355–363.
[307] Ziegler, A.; Nervi, P.; Dürrenberger, M.; Seelig, J. *Biochemistry* **2005**, *44* (1), 138–148.
[308] Sogabe, S.; Sakamoto, K.; Kamada, Y.; Kadotani, A.; Fukuda, Y.; Sakamoto, J. ichi. *Biochem. Biophys. Res. Commun.* **2017**, *486* (3), 620–625.
[309] Li, L.; Liu, J. J.; Nie, S.; Ding, L.; Wang, L.; Liu, J. J.; Liu, W.; Zhang, T. *RSC Adv.* **2017**, *7* (56), 34963–34971.
[310] Lu, M. C.; Chen, Z. Y.; Wang, Y. Lou; Jiang, Y. L.; Yuan, Z. W.; You, Q. D.; Jiang, Z. Y. *RSC Adv.* **2015**, *5* (105), 85983–85987.
[311] Steel, R. J.; O'Connell, M. A.; Searcey, M. *Bioorganic Med. Chem. Lett.* **2018**, *28* (16), 2728–2731.
[312] Wang, J.; Zha, M.; Fei, Q.; Liu, W.; Zhao, Y.; Wu, C. *Chem. - A Eur. J.* **2017**, *23* (60), 15150–15155.
[313] Pehere, A. D.; Abell, A. D. *Org. Lett.* **2012**, *14* (5), 1330–1333.
[314] Jamali, H.; Khan, H. A.; Stringer, J. R.; Chowdhury, S.; Ellman, J. A. *J. Am. Chem. Soc.* **2015**, *137* (10), 3616–3621.
[315] Pícha, J.; Buděšínský, M.; Macháčková, K.; Collinsová, M.; Jiráček, J. *J. Pept. Sci.* **2017**, *23* (3), 202–214.
[316] Testa, C.; Scrima, M.; Grimaldi, M.; D'Ursi, A. M.; Dirain, M. L.; Lubin-Germain, N.; Singh, A.; Haskell-Luevano, C.; Chorev, M.; Rovero, P.; et al. *J. Med. Chem.* **2014**, *57* (22), 9424–9434.
[317] Le Chevalier Isaad, A.; Barbetti, F.; Rovero, P.; D'Ursi, A. M.; Chelli, M.; Chorev, M.; Papini, A. M. *European J. Org. Chem.* **2008**, *2008* (31), 5308–5314.
[318] Rhodes, A. J.; Deming, T. J. *ACS Macro Lett.* **2013**, *2* (5), 351–354.
[319] Byrne, C.; McEwan, P. A.; Emsley, J.; Fischer, P. M.; Chan, W. C. *Chem. Commun.* **2011**, *47* (9), 2589–2591.
[320] Metaferia, B. B.; Rittler, M.; Gheeya, J. S.; Lee, A.; Hempel, H.; Plaza, A.; Stetler-Stevenson, W. G.; Bewley, C. A.; Khan, J. *Bioorganic Med. Chem. Lett.* **2010**, *20* (24), 7337–7340.
[321] Lau, Y. H.; De Andrade, P.; Quah, S. T.; Rossmann, M.; Laraia, L.; Sköld, N.; Sum, T.

J.; Rowling, P. J. E.; Joseph, T. L.; Verma, C.; et al. *Chem. Sci.* **2014**, *5* (5), 1804–1809.
[322] Tahoori, F.; Balalaie, S.; Sheikhnejad, R.; Sadjadi, M.; Boloori, P. *Amino Acids* **2014**, *46* (4), 1033–1046.
[323] Bonnet, R.; Lavergne, T.; Gennaro, B.; Spinelli, N.; Defrancq, E. *Chem. Commun.* **2015**, *51* (23), 4850–4853.
[324] Liu, Y.; Zhang, L.; Wan, J.; Li, Y.; Xu, Y.; Pan, Y. *Tetrahedron* **2008**, *64* (47), 10728–10734.
[325] Scrima, M.; Le Chevalier-Isaad, A.; Rovero, P.; Papini, A. M.; Chorev, M.; D'Ursi, A. M. *European J. Org. Chem.* **2010**, No. 3, 446–457.
[326] Tran, P. T.; Larsen, C. Ø.; Røndbjerg, T.; De Foresta, M.; Kunze, M. B. A.; Marek, A.; Løper, J. H.; Boyhus, L. E.; Knuhtsen, A.; Lindorff-Larsen, K.; et al. *Chem. - A Eur. J.* **2017**, *23* (14), 3490–3495.
[327] Scrima, M.; Grimaldi, M.; Di Marino, S.; Testa, C.; Rovero, P.; Papini, A. M.; Chorev, M.; D'Ursi, A. M. *Biopolymers* **2012**, *98* (6), 535–545.
[328] Sun, H.; Liu, L.; Lu, J.; Qiu, S.; Yang, C. Y.; Yi, H.; Wang, S. *Bioorganic Med. Chem. Lett.* **2010**, *20* (10), 3043–3046.
[329] Pehere, A. D.; Sumby, C. J.; Abell, A. D. *Org. Biomol. Chem.* **2013**, *11* (3), 425–429.
[330] Le Chevalier Isaad, A.; Papini, A. M.; Chorev, M.; Rovero, P. *J. Pept. Sci.* **2009**, *15* (7), 451–454.
[331] Pascal, R.; Sola, R. *Tetrahedron Lett.* **1998**, *39* (28), 5031–5034.
[332] Ueki, M.; Tsurusaki, T.; Katoh, T.; Aoki, H.; Nishigaki, N. *Chem. Lett.* **2006**, *22* (4), 721–724.
[333] Coin, I.; Beerbaum, M.; Schmieder, P.; Bienert, M.; Beyermann, M. *Org. Lett.* **2008**, *10* (17), 3857–3860.
[334] Presolski, S. I.; Hong, V. P.; Finn, M. G. *Curr. Protoc. Chem. Biol.* **2011**, *3* (4), 153–162.
[335] Luo, Y.-C.; Zhang, H.-H.; Wang, Y.; Xu, P.-F. *Acc. Chem. Res.* **2010**, *43* (10), 1317–1330.
[336] Saladino, R.; Crucianelli, G. B. M. *Mini-Reviews Med. Chem.* **2012**, *12* (4), 277–300.
[337] Dolenc, A. P. and M. S. *Curr. Org. Chem.* **2011**, *15* (22), 3750–3799.
[338] Sorochinsky, A. E.; Aceña, J. L.; Moriwaki, H.; Sato, T.; Soloshonok, V. A. *Amino Acids* **2013**, *45* (4), 691–718.
[339] Metz, A. E.; Kozlowski, M. C. *J. Org. Chem.* **2015**, *80* (1), 1–7.
[340] Lu, X.; Xiao, B.; Shang, R.; Liu, L. *Chinese Chem. Lett.* **2016**, *27* (3), 305–311.
[341] Brittain, W. D. G.; Cobb, S. L. *Org. Biomol. Chem.* **2018**, *16* (1), 10–20.
[342] O'Donnell, M. J.; Bennett, W. D.; Wu, S. *J. Am. Chem. Soc.* **1989**, *111* (6), 2353–2355.
[343] Lygo, B.; Andrews, B. I. *Acc. Chem. Res.* **2004**, *37* (8), 518–525.
[344] Corey, E. J.; Xu, F.; Noe, M. C. *J. Am. Chem. Soc.* **1997**, *119* (50), 12414–12415.
[345] Cook, T. C.; Andrus, M. B.; Ess, D. H. *Org. Lett.* **2012**, *14* (23), 5836–5839.
[346] Kmentova, I.; Sutherland, H. S.; Palmer, B. D.; Blaser, A.; Franzblau, S. G.; Wan, B.; Wang, Y.; Ma, Z.; Denny, W. A.; Thompson, A. M. *J. Med. Chem.* **2010**, *53* (23), 8421–8439.
[347] Corey, E. J.; Noe, M. C. *Org. Synth.* **2003**, *80*, 38–45.
[348] Belokon, Y. N.; Tararov, V. I.; Maleev, V. I.; Savel, F. *Tetrahedron: Asymmetry* **1998**, *9*, 4249–4252.
[349] Kawamoto, S. A.; Coleska, A.; Ran, X.; Yi, H.; Yang, C.-Y.; Wang, S. *J. Med. Chem.* **2012**, *55* (3), 1137–1146.
[350] Gouygou, M.; Kalck, P.; Urrutigoïty, M. In *Comprehensive inorganic chemistry*; Reedijk, J., Poeppelmeier, K. B. T.-C. I. C. I. I. (Second E., Eds.; Elsevier: Amsterdam, 2013; pp 223–247.

[351] Gude, M.; Ryf, J.; White, P. D. *Int. J. Pept. Res. Ther.* **2002**, *9* (4–5), 203–206.
[352] McLuckey, S. A.; Sallans, L.; Cody, R. B.; Burnier, R. C.; Verma, S.; Freiser, B. S.; Cooks, R. G. *Int. J. Mass Spectrom. Ion Phys.* **1982**, *44* (3), 215–229.

Appendix

Table appendix-1 Crystal and structure determination data

Compound	32	82a	9
Empirical fomula	$C_{22}H_{34}N_4O_2$	$C_{22}H_{27}N_5O_3$	$C_{22}H_{30}ClN_4O_3Re$
Formula weight	386.53	409.48	620.15
Temp, K	100 (2)	100 (1)	100 (2)
Wavelength, Å	0.71073	0.71073	0.71073
Crystal system	triclinic	triclinic	monoclinic
Space group	P-1	P -1	P 21/c
a, Å	4.6241 (2)	5.3006 (5)	25.962 (3)
b, Å	9.2658 (3)	9.8417 (11)	10.1786 (9)
c, Å	25.6348 (11)	20.075 (2)	9.6204 (9)
α, deg	97.699 (2)	88.410 (4)	90
β, deg	92.109 (2)	83.127 (4)	95.802 (3)
γ, deg	102.936 (2)	85.128 (4)	90
Volume, $Å^3$	1058.28 (7)	1035.81 (19)	2529.2 (4)
Z	2	2	4
Density (calcd), gcm^{-3}	1.213	1.313	1.629
Crystal size	0.230 × 0.180 × 0.040	0.130 × 0.040 × 0.010	0.090 × 0.080 × 0.020
Index ranges	$-6 \le h \le 5$, $-7 \le k \le 13$, $-36 \le l \le 36$	$-8 \le h \le 8$, $-14 \le k \le 14$, $-30 \le l \le 30$	$-39 \le h \le 39$, $-15 \le k \le 15$, $-14 \le l \le 14$
Reflections collected	16383	61142	121474
Independent reflection	6322 [R(int)= 0.0340]	7618 [R(int)= 0.1984]	9282 [R(int)= 0.1100]
GOF on F^2	1.037	0.994	0.927
Final R indices [$I > 2\sigma(I)$]	$R_1 = 0.0480$, $wR_2 = 0.1086$	$R_1 = 0.0599$, $wR_2 = 0.1135$	$R_1 = 0.0294$, $wR_2 = 0.0452$
Largest diff. Peak and hole, $eÅ^{-3}$	0.303 and -0.262	0.295 and -0.358	0.560 and -0.910

Table appendix-2. Cartesian coordinates of the optimized geometry of complex **3r'** at the B3LYP level of theory.

Atom	X	Y	Z
C	1.72175691	2.47390486	-0.07821989
C	-0.56871010	2.14488385	0.10811800
C	-0.80132711	3.51768485	0.07193497
C	0.27858189	4.38266385	-0.04392900
C	1.56271990	3.85138986	-0.11968692
H	2.70427291	2.02672086	-0.13512384
H	-1.81252811	3.89706384	0.13321491
H	0.11980989	5.45324085	-0.07425902
H	2.43348590	4.48656086	-0.21024889
N	0.68515291	1.62612685	0.03313807
N	-1.26315910	-0.16609115	0.26476700
N	-2.31398110	-0.92880716	0.38895396
C	-4.72571411	-0.66937217	0.53099484
H	-4.65637913	-1.53522716	1.18824086
H	-5.34121713	0.08381684	1.02165680
C	-5.28224504	-1.04812319	-0.83805718
H	-6.28295104	-1.46615320	-0.71217222
H	-5.35318901	-0.17561820	-1.49025720
H	-4.65269001	-1.79845020	-1.31928114
C	-1.62273410	1.14994084	0.23214696
C	-2.99633811	1.18761584	0.34661190
H	-3.70615911	1.99588484	0.36936285
N	-3.36640711	-0.10933416	0.44189690
Re	0.85657192	-0.61017314	0.05570111
C	1.15679682	-0.67613211	1.94015313
C	2.75149093	-0.73470414	-0.28178179
C	0.71047993	-2.52855915	-0.01864786
O	1.34132177	-0.71516309	3.08161714
O	0.59235894	-3.67397915	-0.07425285
O	3.88268694	-0.79045014	-0.50016174
Cl	0.38081904	-0.41344319	-2.47090891

Table appendix-3. Cartesian coordinates of the optimized geometry of complex **13'** at the B3LYP level of theory.

Atom	X	Y	Z
C	2.23130	0.45586	0.04407
C	0.35685	1.82026	0.17023

C	1.14839	2.96765	0.16504
C	3.08294	1.55731	0.03862
H	2.63119	-0.54577	-0.00403
H	0.68803	3.94511	0.21167
N	0.89812	0.57347	0.10827
N	-1.75428	0.64538	0.24455
N	-3.04078	0.83186	0.33183
C	-1.09297	1.83995	0.24666
C	-2.05372	2.82495	0.34517
N	-3.22484	2.15403	0.39604
Re	-0.53943	-1.15089	0.06108
C	-0.44605	-1.42855	1.94887
C	0.74417	-2.55928	-0.23949
C	-1.97774	-2.42200	-0.08367
O	-0.38717	-1.59831	3.09139
O	-2.85823	-3.15895	-0.18307
O	1.52477	-3.38527	-0.43446
Cl	-0.63858	-0.64917	-2.46300
C	-4.59202	2.69994	0.45453
H	-4.52243	3.65763	0.96907
H	-5.16552	2.01649	1.07927
C	-5.21139	2.84780	-0.93184
H	-5.26614	1.88265	-1.43820
H	-6.22442	3.24140	-0.82816
H	-4.63499	3.53912	-1.54944
C	2.52469	2.83516	0.09868
H	3.17239	3.70205	0.09305
H	-1.99772	3.89875	0.38538
C	4.56727	1.41252	-0.03046
O	5.32915	2.35292	-0.03966
O	4.94744	0.13170	-0.07944
C	6.37053	-0.11599	-0.14884
H	6.86493	0.29018	0.73344
H	6.47232	-1.19692	-0.18276
H	6.78655	0.33868	-1.04771

Table appendix-4. Cartesian coordinates of the optimized geometry of complex **16'** at the B3LYP level of theory.

Atom	X	Y	Z
C	1.02911	2.90749	0.15618

C	-0.90315	1.60883	0.14203
C	-1.69476	2.75239	0.20885
C	0.29637	4.08429	0.21605
H	2.10942	2.92974	0.13708
H	-2.76722	2.65776	0.22464
H	0.81228	5.03465	0.24078
N	0.45755	1.69331	0.12354
N	-0.46642	-0.75105	0.13677
N	-1.01761	-1.93364	0.15118
C	-1.41012	0.23198	0.11711
C	-2.64445	-0.41898	0.12273
N	-2.32500	-1.75108	0.15092
Re	1.62716	-0.20334	0.03627
C	1.87165	-0.26235	1.92948
C	3.39015	0.54603	-0.19885
C	2.35893	-1.97690	-0.14213
O	2.02229	-0.29618	3.07593
O	2.76368	-3.04948	-0.26140
O	4.43232	1.01432	-0.35526
Cl	1.19078	-0.06285	-2.50031
C	-3.23002	-2.93089	0.17402
H	-3.98569	-2.75969	-0.59044
H	-3.73252	-2.92306	1.14056
C	-2.49129	-4.23714	-0.06498
H	-1.75816	-4.44009	0.71527
H	-3.23204	-5.03912	-0.05888
H	-1.98534	-4.24282	-1.03131
C	-4.06778	0.00694	0.11856
O	-4.96731	-0.69576	0.51596
O	-4.22800	1.22583	-0.39230
C	-5.59051	1.72635	-0.44315
H	-6.19598	1.07893	-1.07569
H	-6.00975	1.76778	0.56117
H	-5.51002	2.72033	-0.87274
C	-1.08944	4.00280	0.24662
H	-1.69733	4.89722	0.29918

Table appendix-5. Cartesian coordinates of the optimized geometry of complex **9'** at the B3LYP level of theory.

Atom	X	Y	Z

C	1.63675900	2.51448200	-0.06851400
C	-0.62298900	2.09913900	0.09627700
C	-0.93582300	3.45081700	0.05647100
C	0.11110900	4.35597500	-0.05335300
C	1.41838700	3.88120000	-0.11609600
H	2.63484300	2.10350400	-0.11389600
H	-1.96095400	3.78694900	0.11009100
H	-0.09582900	5.41775300	-0.08780400
H	2.26031000	4.55426400	-0.20077900
N	0.63261100	1.62238800	0.03617100
N	-1.24808600	-0.19454300	0.26785600
N	-2.30512800	-0.93293800	0.38861900
C	-4.79031100	-0.66910300	0.53079600
H	-4.81213400	-1.38475000	1.35763500
H	-5.46659500	0.14611200	0.79766200
C	-5.27221900	-1.35453800	-0.75841000
H	-6.27819700	-1.75644500	-0.61898900
H	-5.29864100	-0.64821500	-1.59174500
H	-4.61047800	-2.17931600	-1.03211900
C	-2.97616200	1.18282700	0.30536400
H	-3.51589900	2.11258700	0.28814400
Re	0.87368600	-0.59525800	0.05829500
C	1.18913400	-0.66154100	1.94315800
C	2.76920800	-0.69411400	-0.28908400
C	0.75898500	-2.51692800	-0.01702400
O	1.38578600	-0.70218900	3.08134600
O	0.65551400	-3.66233700	-0.07394200
O	3.89839200	-0.72845600	-0.51548300
C	-3.40263200	-0.12193300	0.41734900
N	-1.62138200	1.10759000	0.21339200
Cl	0.38781300	-0.39879000	-2.46115000

Table appendix-6. Cartesian coordinates of the optimized geometry of complex **17'** at the B3LYP level of theory.

Atom	X	Y	Z
C	1.00745	2.78874	0.10279
C	0.38534	4.02463	0.08974
C	-1.00488	4.06914	0.06510
C	-1.72541	2.88308	0.05503
C	-1.02245	1.68340	0.06672

H	2.08423	2.70499	0.12409
H	0.98256	4.92575	0.09909
H	-1.53027	5.01541	0.05527
H	-2.80137	2.90220	0.03981
N	0.32406	1.62770	0.09122
C	-2.98411	0.02044	0.04265
C	-2.89799	-1.38784	0.07786
C	-4.22722	0.66313	-0.00511
C	-4.04093	-2.19866	0.07165
C	-5.34807	-0.15205	-0.01131
H	-4.34394	1.73436	-0.03946
C	-5.26419	-1.56104	0.02734
H	-3.94892	-3.27646	0.09950
H	-6.32533	0.31347	-0.04847
H	-6.17676	-2.14355	0.02036
N	-1.66374	0.42847	0.06306
N	-1.58003	-1.76136	0.11448
N	-0.86955	-0.69498	0.10559
Re	1.26513	-0.38189	0.05717
Cl	0.92108	-0.20401	-2.48542
C	1.77581	-2.23569	-0.09297
C	3.11564	0.14084	-0.13675
C	1.45842	-0.45417	1.95977
O	1.58149	-0.49624	3.10770
O	2.04392	-3.35035	-0.19699
O	4.20918	0.47553	-0.27086

Table appendix-7. Cartesian coordinates of the optimized geometry of complex **33a'** at the B3LYP level of theory.

Atom	X	Y	Z
C	-1.46312	-1.33431	2.68180
C	-1.38952	0.90059	2.06424
C	-1.30668	1.29941	3.39728
C	-1.30293	0.33211	4.39268
C	-1.38305	-1.00910	4.02806
H	-1.52633	-2.36540	2.36250
H	-1.24640	2.35110	3.64404
H	-1.23911	0.61990	5.43457
H	-1.38366	-1.79741	4.76884
N	-1.46764	-0.40766	1.70922

N	-1.49804	1.32304	-0.31735
N	-1.51536	2.28294	-1.19917
C	-1.38889	4.71084	-1.22864
H	-2.06320	4.61269	-2.07854
H	-1.79791	5.46143	-0.55308
C	0.02612	5.06647	-1.67513
H	0.00262	6.01744	-2.21104
H	0.69541	5.17046	-0.81891
H	0.42551	4.30282	-2.34468
C	-1.40647	1.83071	0.94603
C	-1.36728	3.20404	0.81980
H	-1.30031	4.00241	1.53810
N	-1.43962	3.42675	-0.51097
Re	-1.55259	-0.86408	-0.50460
C	-3.52298	-0.88361	-0.47767
C	-1.47554	-2.78005	-0.38292
C	-1.52031	-0.97216	-2.41972
O	-4.67726	-0.90902	-0.46845
O	-1.47965	-1.00856	-3.57465
O	-1.40640	-3.93077	-0.28655
C	0.58142	-0.74650	-0.42738
C	1.80271	-0.66731	-0.36407
C	3.22624	-0.57726	-0.28828
C	4.05615	-1.48244	-0.98562
C	3.85978	0.41224	0.48267
C	5.43642	-1.39844	-0.91198
H	3.60017	-2.25798	-1.58999
C	5.24801	0.50515	0.56334
H	3.25157	1.12292	1.03019
C	6.04798	-0.40367	-0.13614
H	6.06650	-2.09711	-1.45014
H	5.68932	1.28421	1.17019
O	7.41182	-0.40616	-0.12856
C	8.08896	0.58499	0.64376
H	9.15131	0.39466	0.50430
H	7.85179	1.59419	0.29290
H	7.84144	0.50017	1.70649

Table appendix-8. Cartesian coordinates of the optimized geometry of complex **33b'** at the B3LYP level of theory.

Atom	X	Y	Z
C	-1.39126	-1.45545	2.60723
C	-1.37899	0.80266	2.07316
C	-1.35010	1.15370	3.42163
C	-1.34177	0.15064	4.38097
C	-1.36306	-1.17789	3.96616
H	-1.40780	-2.47586	2.25016
H	-1.33428	2.19648	3.70930
H	-1.31936	0.40171	5.43400
H	-1.35759	-1.99272	4.67759
N	-1.40002	-0.49384	1.66882
N	-1.42552	1.30830	-0.29406
N	-1.44516	2.29837	-1.14202
C	-1.39309	4.72898	-1.08069
H	-1.96202	4.61441	-2.00229
H	-1.92510	5.42695	-0.43478
C	0.03395	5.19302	-1.35648
H	0.00281	6.15940	-1.86364
H	0.59733	5.31013	-0.42866
H	0.55623	4.48241	-1.99947
C	-1.39354	1.77241	0.98898
C	-1.39682	3.14974	0.91209
H	-1.38060	3.92366	1.65962
N	-1.43156	3.41803	-0.41184
Re	-1.40446	-0.86938	-0.55843
C	-3.37590	-0.94644	-0.59528
C	-1.27917	-2.78804	-0.50476
C	-1.31133	-0.90336	-2.47570
O	-4.52723	-1.00560	-0.62341
O	-1.23562	-0.89360	-3.62874
O	-1.18455	-3.93890	-0.44986
C	0.71673	-0.69823	-0.41127
C	1.93336	-0.58481	-0.30844
C	3.34237	-0.44904	-0.18894
C	4.19808	-0.77505	-1.26426
C	3.92935	0.01657	1.00837
C	5.57150	-0.64260	-1.15166
H	3.76706	-1.13390	-2.19056
C	5.30194	0.15087	1.12773
H	3.28992	0.27143	1.84429

C	6.13788	-0.17765	0.04720
H	6.21277	-0.89690	-1.98658
H	5.73512	0.50928	2.05340
C	7.55253	-0.03945	0.16690
N	8.69988	0.07323	0.26454

Table appendix-9. Cartesian coordinates of the optimized geometry of complex **33c'** at the B3LYP level of theory.

Atom	X	Y	Z
C	-1.47642	-1.38521	2.63809
C	-1.40212	0.86155	2.06234
C	-1.36504	1.23667	3.40407
C	-1.38535	0.25177	4.38183
C	-1.44222	-1.08321	3.99164
H	-1.52002	-2.41121	2.29977
H	-1.32086	2.28392	3.67191
H	-1.35728	0.52158	5.43008
H	-1.45946	-1.88451	4.71808
N	-1.45833	-0.44115	1.68215
N	-1.43660	1.32458	-0.31385
N	-1.42526	2.29907	-1.17970
C	-1.29289	4.72756	-1.16255
H	-1.84520	4.60734	-2.09342
H	-1.82176	5.45024	-0.54164
C	0.15008	5.15305	-1.41725
H	0.15228	6.10959	-1.94364
H	0.69693	5.27557	-0.48024
H	0.66863	4.41773	-2.03505
C	-1.38843	1.81097	0.96040
C	-1.34780	3.18608	0.85841
H	-1.30635	3.97213	1.59228
N	-1.37528	3.43109	-0.47016
Re	-1.48006	-0.85627	-0.53890
C	-3.45322	-0.88430	-0.55943
C	-1.40155	-2.77542	-0.45193
C	-1.40442	-0.92676	-2.45675
O	-4.60587	-0.91566	-0.57771
O	-1.34046	-0.93977	-3.61035
O	-1.33294	-3.92715	-0.37718
C	0.64584	-0.73808	-0.41366

C	1.86680	-0.66095	-0.32627
C	3.28054	-0.57081	-0.22326
C	4.10515	-1.66567	-0.56290
C	3.90175	0.62095	0.22371
C	5.48400	-1.57100	-0.45955
H	3.64509	-2.58407	-0.90653
C	5.27712	0.70914	0.32426
H	3.27973	1.46791	0.48709
C	6.08809	-0.38613	-0.01602
H	6.10504	-2.42119	-0.72393
H	5.74957	1.62262	0.66630
C	7.55130	-0.30593	0.08676
H	8.08430	-1.23178	-0.21082
O	8.17611	0.67050	0.46104

Table appendix-10. Cartesian coordinates of the optimized geometry of complex **33d'** at the B3LYP level of theory.

Atom	X	Y	Z
C	-1.61584	-1.34192	2.68058
C	-1.62406	0.88958	2.04429
C	-1.57866	1.30224	3.37470
C	-1.55109	0.34403	4.37857
C	-1.57058	-1.00225	4.02485
H	-1.63182	-2.37741	2.36994
H	-1.56539	2.35750	3.61302
H	-1.51551	0.64281	5.41868
H	-1.55086	-1.78377	4.77248
N	-1.64284	-0.42409	1.69981
N	-1.71149	1.28686	-0.34219
N	-1.75519	2.23720	-1.23364
C	-1.73032	4.66750	-1.28501
H	-2.39022	4.53451	-2.14143
H	-2.17687	5.40725	-0.62139
C	-0.32543	5.07514	-1.71860
H	-0.38046	6.02034	-2.26232
H	0.32929	5.21204	-0.85583
H	0.11138	4.32291	-2.37761
C	-1.66136	1.80888	0.91765
C	-1.67741	3.18133	0.77862
H	-1.65493	3.98799	1.49036

N	-1.73809	3.38875	-0.55532
Re	-1.67139	-0.89946	-0.50862
C	-3.64348	-0.99763	-0.51626
C	-1.52458	-2.81323	-0.37269
C	-1.60248	-1.01968	-2.42412
O	-4.79394	-1.06934	-0.52708
O	-1.54192	-1.06223	-3.57706
O	-1.41640	-3.95935	-0.26959
C	0.44624	-0.70280	-0.39646
C	1.66352	-0.57667	-0.30899
C	3.06951	-0.43065	-0.20295
C	3.93999	-1.10923	-1.08715
C	3.64111	0.39665	0.79156
C	5.31278	-0.97067	-0.98499
H	3.51984	-1.74659	-1.85472
C	5.01278	0.54028	0.90031
H	2.98943	0.92338	1.47698
C	5.83994	-0.14575	0.00975
H	5.97931	-1.48862	-1.65989
H	5.45108	1.17157	1.66019
N	7.28734	0.00272	0.12128
O	7.73229	0.73672	1.00269
O	7.99974	-0.61277	-0.67061

Table appendix-11. Cartesian coordinates of the optimized geometry of complex **37a'** at the B3LYP level of theory.

Atom	X	Y	Z
C	0.77280200	-3.01098200	-0.81260500
C	2.28220800	-1.25878800	-1.00652300
C	3.10796700	-2.01870100	-1.83276900
C	2.73657100	-3.31883700	-2.14618900
C	1.54782400	-3.82384800	-1.62633400
H	-0.15688700	-3.36974900	-0.39349100
H	4.02357000	-1.59353300	-2.22185300
H	3.36360200	-3.92711800	-2.78582900
H	1.21822400	-4.83085200	-1.84402500
N	1.12195500	-1.75152900	-0.49920400
N	1.67796800	0.74802100	0.19950300
N	2.08049700	1.96009100	0.46579200
C	3.94215700	3.41214800	-0.11156800

H	3.75895600	3.81012000	0.88557300
H	5.00670500	3.19976800	-0.20499500
C	3.46255600	4.37318600	-1.19534800
H	3.99886700	5.31891800	-1.09540600
H	3.65581700	3.97243500	-2.19234400
H	2.39386400	4.57010700	-1.09477700
C	2.57163800	0.11121900	-0.61287800
C	3.59449500	1.00455000	-0.85430200
H	4.50140400	0.93842800	-1.42944200
N	3.24526000	2.11633700	-0.16984600
Re	-0.10372700	-0.36999400	0.79221700
C	0.71620100	-1.01872500	2.40767400
C	-1.62156700	-1.52470600	1.05046600
C	-0.98833400	1.03683200	1.75571500
O	1.19207000	-1.41031300	3.38723300
O	-1.49948000	1.90581600	2.31874000
O	-2.52594800	-2.23161300	1.18043000
S	-1.03684600	0.46853400	-1.46456000
C	-2.80178300	0.74861100	-1.28392200
C	-3.72404400	-0.25633600	-1.61103700
C	-3.29455000	1.99430500	-0.86748400
C	-5.09568100	-0.02388200	-1.51971800
H	-3.36040800	-1.22328100	-1.93842200
C	-4.66636200	2.22444300	-0.77549100
H	-2.59646000	2.78393200	-0.61594500
C	-5.57447700	1.21705400	-1.10071900
H	-5.79066800	-0.81587700	-1.77783000
H	-5.02500300	3.19538700	-0.45060800
H	-6.64115900	1.39753400	-1.03066700

Table appendix-12. Cartesian coordinates of the optimized geometry of complex **37b'** at the B3LYP level of theory.

Atom	X	Y	Z
C	1.68717100	-2.87019400	-0.92194900
C	2.85367700	-0.87354200	-1.11807600
C	3.76412600	-1.45441600	-1.99876100
C	3.61479100	-2.79167700	-2.33905600
C	2.55710600	-3.51217900	-1.79061400
H	0.85445000	-3.39833100	-0.47895200
H	4.57319900	-0.86389600	-2.40739000

H	4.31128300	-3.26306800	-3.02096900
H	2.40101600	-4.55598000	-2.02764300
N	1.82208600	-1.57687000	-0.58179300
N	1.96128400	0.96270600	0.17698700
N	2.15506500	2.22010800	0.46577600
C	3.70051200	3.99482700	-0.14112900
H	3.56374600	4.30845400	0.89310800
H	4.76839300	3.98353000	-0.35651800
C	2.94142300	4.90043500	-1.10621100
H	3.31325600	5.92181700	-1.00347000
H	3.08669400	4.58334800	-2.14067600
H	1.87329300	4.89779600	-0.88270200
C	2.91397300	0.51596300	-0.69293900
C	3.74941500	1.58340700	-0.94872700
H	4.62469700	1.69542100	-1.56438400
N	3.24173600	2.59754500	-0.21387500
Re	0.43317000	-0.46878000	0.80353400
C	1.42685500	-1.00294800	2.36318400
C	-0.84602700	-1.87877000	1.08317200
C	-0.64189400	0.73472100	1.84492000
O	2.00690200	-1.32954800	3.31008500
O	-1.27390800	1.48550500	2.45376500
O	-1.60705200	-2.73635800	1.22569500
S	-0.73804000	0.24401800	-1.38360000
C	-2.51502200	0.24813100	-1.11876600
C	-3.29459500	-0.88048900	-1.42260200
C	-3.17902600	1.38890400	-0.65783200
C	-4.67394500	-0.86691000	-1.26691800
H	-2.81049100	-1.77950100	-1.78550300
C	-4.56628400	1.41634600	-0.49504500
H	-2.60680300	2.27747000	-0.41865800
C	-5.32394500	0.28266100	-0.80020200
H	-5.26955000	-1.74127100	-1.50358600
H	-5.03570300	2.32204100	-0.13474600
O	-6.68240600	0.19741200	-0.68237900
C	-7.39357100	1.33956400	-0.20845100
H	-8.44290300	1.05099100	-0.19292300
H	-7.07827500	1.61488500	0.80300300
H	-7.26337100	2.19699700	-0.87641700

Table appendix-13. Cartesian coordinates of the optimized geometry of complex **37c'** at the B3LYP level of theory.

Atom	X	Y	Z
C	-1.95916100	-2.60120200	1.55118700
C	-3.08778400	-0.57419900	1.47049700
C	-3.87955000	-0.93482200	2.55875000
C	-3.69045200	-2.17698000	3.14866500
C	-2.71318000	-3.02509400	2.63538700
H	-1.19093300	-3.23351600	1.12863500
H	-4.62873900	-0.25056200	2.93388400
H	-4.29525100	-2.47735400	3.99498200
H	-2.53062500	-4.00153200	3.06336800
N	-2.13366900	-1.40223500	0.96935200
N	-2.36111800	0.93105600	-0.27668200
N	-2.59030400	2.10479700	-0.79839500
C	-4.05662900	4.00175600	-0.39896300
H	-4.01010400	4.10050800	-1.48265900
H	-5.10209400	4.04624800	-0.09559000
C	-3.22164600	5.07160500	0.29814300
H	-3.60484900	6.05657800	0.02421800
H	-3.27748500	4.97036900	1.38365500
H	-2.17631000	5.01018200	-0.00913200
C	-3.19996400	0.69842500	0.77499600
C	-3.99988300	1.81532500	0.89759800
H	-4.79539400	2.07377400	1.57426400
N	-3.58676600	2.64091600	-0.08923800
Re	-0.93481300	-0.64368500	-0.78131200
C	-2.14460300	-1.44981500	-2.04609600
C	0.25846600	-2.14795600	-0.93786900
C	-0.03802800	0.28898900	-2.20342600
O	-2.85518800	-1.94040000	-2.81378400
O	0.47181900	0.88136500	-3.05302900
O	0.95419500	-3.06722000	-1.00592400
S	0.44748400	0.46959700	1.08039200
C	2.20591700	0.45876100	0.87015500
C	2.98862800	0.95783300	1.93452700
C	2.87986700	0.00165800	-0.27659400
C	4.36908600	0.99373100	1.85228600
H	2.49535300	1.31646600	2.83073500
C	4.26554600	0.03785400	-0.35660300

H	2.31620300	-0.38362100	-1.11375900
C	5.03335600	0.53324600	0.70509700
H	4.95502700	1.37828900	2.67834900
H	4.75791000	-0.32043600	-1.25151800
C	6.51102000	0.59099100	0.66901000
O	7.21032800	1.01260700	1.57053600
O	7.02340000	0.11979700	-0.48746500
C	8.45888000	0.14093700	-0.60223800
H	8.67784000	-0.27080100	-1.58437700
H	8.83395200	1.16227900	-0.52531600
H	8.91395500	-0.47128400	0.17738100

Table appendix-14. Cartesian coordinates of the optimized geometry of complex **37d'** at the B3LYP level of theory.

Atom	X	Y	Z
C	-1.73688500	-2.57100700	1.59834700
C	-2.81637400	-0.51676300	1.51822300
C	-3.59642400	-0.84736900	2.62417300
C	-3.42726400	-2.08831400	3.22274800
C	-2.48097400	-2.96541600	2.70031500
H	-0.99277800	-3.22645300	1.16804300
H	-4.32156800	-0.14118600	3.00582500
H	-4.02367900	-2.36558900	4.08277900
H	-2.31472700	-3.94202500	3.13446900
N	-1.89251200	-1.37349500	1.00786600
N	-2.08805400	0.95041900	-0.25976500
N	-2.29512800	2.12524100	-0.78830900
C	-3.69725200	4.06687800	-0.37731300
H	-3.73854900	4.13437200	-1.46380200
H	-4.71062100	4.16374400	0.01037500
C	-2.76404200	5.11850500	0.21479900
H	-3.13085400	6.11122900	-0.05338400
H	-2.72939100	5.04635100	1.30348700
H	-1.75253800	5.00637800	-0.17894600
C	-2.90961000	0.75165500	0.81221100
C	-3.67393100	1.89266500	0.94139400
H	-4.44552200	2.18081300	1.63363900
N	-3.25918800	2.69642600	-0.06259900
Re	-0.71258700	-0.66416500	-0.77420700
C	-1.96589000	-1.45484200	-2.00615900

C	0.44136600	-2.19898200	-0.94018100
C	0.17390500	0.23281800	-2.22682700
O	-2.70326700	-1.93603400	-2.75315000
O	0.67698200	0.80408100	-3.09415500
O	1.11468100	-3.13391400	-1.01379800
S	0.72862400	0.43226500	1.05451100
C	2.46793900	0.43442200	0.79389500
C	3.27685600	0.98144000	1.81916700
C	3.11411100	-0.06204500	-0.35728800
C	4.65185300	1.02950000	1.70363400
H	2.80478000	1.36925900	2.71374600
C	4.49212200	-0.01854400	-0.48157900
H	2.53072400	-0.48404700	-1.16177500
C	5.25996800	0.52659100	0.54861500
H	5.26255600	1.44774600	2.49140300
H	4.98039700	-0.40069700	-1.36716300
N	6.70339900	0.57242000	0.42011300
O	7.35987200	1.06477900	1.34072500
O	7.21815300	0.11758700	-0.60406300

Table appendix-15. Cartesian coordinates of the optimized geometry of complex **38a'** at the B3LYP level of theory.

Atom	X	Y	Z
C	0.96053200	-2.96055300	-0.87844000
C	2.34104000	-1.12104000	-0.99754500
C	3.24591600	-1.77768400	-1.82152200
C	2.96764100	-3.09106700	-2.17317500
C	1.80622700	-3.69253400	-1.69424600
H	0.04945700	-3.38851400	-0.48614200
H	4.13732500	-1.28137000	-2.17662500
H	3.65058500	-3.63443200	-2.81326400
H	1.55420800	-4.71345600	-1.94607200
N	1.21663100	-1.68574100	-0.52409000
N	1.61984700	0.79417800	0.22337900
N	1.99245600	2.00675700	0.48526100
C	3.86637200	3.57201200	-0.06680900
H	3.90037200	3.87637000	0.98312600
H	4.90054600	3.45023500	-0.39672900
C	3.17290300	4.66341000	-0.89889200
H	3.69829900	5.61453300	-0.78765100

H	3.16277200	4.40052800	-1.95950800
H	2.13982900	4.80442700	-0.57332500
C	3.53462400	1.10956400	-0.83867100
H	4.38433300	0.88430200	-1.45768900
Re	-0.10212600	-0.42229500	0.77280000
C	0.72608600	-1.05611300	2.39342600
C	-1.56979100	-1.64742800	1.00167000
C	-1.06176300	0.92717400	1.74883200
O	1.20147700	-1.44156300	3.37426800
O	-1.61380800	1.76414600	2.31894500
O	-2.44081500	-2.39650200	1.11054900
S	-1.06260300	0.37243200	-1.48526200
C	-2.81789500	0.69454000	-1.28051300
C	-3.76620200	-0.29686000	-1.57169200
C	-3.27550800	1.95982600	-0.88421800
C	-5.13073200	-0.03185800	-1.46375400
H	-3.42919600	-1.27824400	-1.88406900
C	-4.64026300	2.22222300	-0.77598900
H	-2.55615400	2.73906100	-0.66192800
C	-5.57509100	1.22821900	-1.06453400
H	-5.84706000	-0.81337000	-1.69374400
H	-4.97235600	3.20771800	-0.46728400
H	-6.63626800	1.43387800	-0.98175000
C	3.17660900	2.24719000	-0.15143500
N	2.54040000	0.21463200	-0.58714800

Table appendix-16. Cartesian coordinates of the optimized geometry of complex **38b'** at the B3LYP level of theory.

Atom	X	Y	Z
C	1.76569300	-2.82366900	-0.95214000
C	2.86329100	-0.80382300	-1.09277400
C	3.81521200	-1.31327900	-1.96652700
C	3.71137200	-2.64789900	-2.33231000
C	2.66949500	-3.41583000	-1.81764800
H	0.94306700	-3.38290100	-0.53053600
H	4.61051700	-0.69014200	-2.34860800
H	4.43580600	-3.07896800	-3.01108000
H	2.55409300	-4.45853500	-2.07958300
N	1.85334500	-1.53031900	-0.58320900
N	1.92950500	0.97186800	0.19302600

N	2.13435800	2.22246800	0.46097500
C	3.73665600	4.04931100	-0.14145400
H	3.78650800	4.33839900	0.91222300
H	4.75706300	4.08424100	-0.52973600
C	2.84685600	5.04196200	-0.90775800
H	3.23517100	6.05734600	-0.80162100
H	2.81432000	4.79800000	-1.97244500
H	1.82444300	5.02615100	-0.52362900
C	3.72937600	1.57455400	-0.94341900
H	4.57480400	1.48374300	-1.60141100
Re	0.42807200	-0.48744600	0.79390700
C	1.41111000	-1.01597200	2.36578400
C	-0.83591300	-1.91476000	1.06019800
C	-0.67376100	0.69662100	1.83185000
O	1.97944600	-1.34123200	3.31880500
O	-1.31814500	1.43829000	2.43630400
O	-1.58436300	-2.78354200	1.19076900
S	-0.74377600	0.19924200	-1.39799900
C	-2.51946700	0.22080900	-1.12542300
C	-3.30775400	-0.90752000	-1.40628200
C	-3.17223000	1.37497900	-0.68265900
C	-4.68614000	-0.88085400	-1.24472500
H	-2.83179400	-1.81618800	-1.75551100
C	-4.55839400	1.41540600	-0.51456000
H	-2.59228500	2.26345900	-0.46262200
C	-5.32549500	0.28174200	-0.79563000
H	-5.28923500	-1.75477700	-1.46316200
H	-5.01966900	2.33086100	-0.16884300
N	2.88727500	0.54144500	-0.66616800
C	3.24167900	2.63975200	-0.22106800
O	-6.68350800	0.20846300	-0.66980500
C	-7.38446600	1.36363600	-0.21194900
H	-8.43555000	1.08240500	-0.18586800
H	-7.06173400	1.65410400	0.79286700
H	-7.25208600	2.20833000	-0.89546800

Table appendix-17. Cartesian coordinates of the optimized geometry of complex **38c'** at the B3LYP level of theory.

Atom	X	Y	Z
C	2.15006000	-2.84174300	-0.86517700

C	3.24693100	-0.82859400	-1.08596000
C	4.18775400	-1.36714400	-1.95387900
C	4.07944200	-2.71345600	-2.27314000
C	3.04416300	-3.46324300	-1.72027500
H	1.33216600	-3.38605400	-0.41584600
H	4.97770800	-0.75706000	-2.36689600
H	4.79548700	-3.16743500	-2.94583900
H	2.92586600	-4.51421400	-1.94518800
N	2.24214100	-1.53676200	-0.54156100
N	2.32511500	0.99129400	0.14597100
N	2.53520200	2.24920100	0.37229600
C	4.13934700	4.05040400	-0.29697400
H	4.18410900	4.37697700	0.74585000
H	5.16195400	4.06807700	-0.68051600
C	3.25679200	5.01714100	-1.10378700
H	3.64759100	6.03457700	-1.03223300
H	3.22949200	4.73488300	-2.15910500
H	2.23222400	5.01806400	-0.72506400
C	4.12077100	1.55058300	-1.01825300
H	4.96308700	1.43538500	-1.67642700
Re	0.83091100	-0.44548300	0.81366900
C	1.83351800	-0.91855800	2.38872300
C	-0.42666200	-1.86505300	1.15092200
C	-0.25350400	0.77380500	1.83054000
O	2.41609100	-1.21008100	3.34328600
O	-0.88512000	1.53515800	2.42310900
O	-1.17027200	-2.72965100	1.32509100
S	-0.36534500	0.15942900	-1.39628100
C	-2.12882500	0.14030500	-1.09538300
C	-2.89147900	-1.00421900	-1.38107400
C	-2.79476600	1.28400100	-0.62522700
C	-4.26739900	-1.00565000	-1.19703400
H	-2.39575900	-1.89423900	-1.74892600
C	-4.17145200	1.28361200	-0.43955100
H	-2.22413800	2.17808000	-0.40651100
C	-4.92408400	0.13650700	-0.72338300
H	-4.84959000	-1.89177100	-1.41853100
H	-4.66746900	2.17406100	-0.07607700
C	-6.39739400	0.08192400	-0.54449700
O	-7.08375500	-0.89318300	-0.77664900

O	-6.90800300	1.24263600	-0.09084600
C	-8.33483900	1.27572700	0.11047400
H	-8.55267200	2.27534600	0.47784600
H	-8.85659400	1.09249300	-0.82954300
H	-8.63371500	0.52582800	0.84366100
N	3.27686600	0.53012000	-0.70383500
C	3.64006300	2.64054300	-0.32829400

Table appendix-18. Cartesian coordinates of the optimized geometry of complex **38d'** at the B3LYP level of theory.

Atom	X	Y	Z
C	-1.76232500	-2.53124600	1.62379300
C	-2.81258500	-0.48568300	1.48583400
C	-3.61915600	-0.75732500	2.58255300
C	-3.46825500	-1.98637300	3.20960200
C	-2.52535100	-2.88805900	2.72261200
H	-1.01894800	-3.20065200	1.21601000
H	-4.33938900	-0.03424300	2.93628200
H	-4.07995200	-2.23294200	4.06771800
H	-2.37756200	-3.85462100	3.18407400
N	-1.89744300	-1.34352900	1.00119900
N	-2.07692700	0.94010100	-0.27707700
N	-2.31801500	2.10935900	-0.77916600
C	-3.81236100	4.07429800	-0.36609600
H	-4.01702300	4.13004200	-1.43901400
H	-4.76412900	4.22591000	0.14799900
C	-2.81780700	5.17864500	0.02833800
H	-3.21643300	6.15931300	-0.24057300
H	-2.62867100	5.16990800	1.10453500
H	-1.86351900	5.04579800	-0.48622200
C	-3.68778600	1.83137600	0.94768900
H	-4.42756100	1.91116900	1.72394200
Re	-0.70004400	-0.67318600	-0.76883700
C	-1.93955200	-1.47666200	-2.01120200
C	0.46057900	-2.20454400	-0.92637700
C	0.19234700	0.22153500	-2.22069300
O	-2.66248800	-1.96724100	-2.76446100
O	0.69519100	0.79444100	-3.08530600
O	1.13442100	-3.13834700	-0.99017100
S	0.73512300	0.42341300	1.06056400

C	2.47521500	0.43534300	0.79729900
C	3.27914800	0.99297800	1.82011400
C	3.12420100	-0.06303400	-0.35072000
C	4.65409100	1.04889300	1.70504400
H	2.80412200	1.38298800	2.71212200
C	4.50223800	-0.01180900	-0.47446700
H	2.54483600	-0.49311000	-1.15371400
C	5.26549400	0.54342600	0.55324200
H	5.26167100	1.47540900	2.49075800
H	4.99332200	-0.39586600	-1.35763800
N	6.70959800	0.59722200	0.42528300
O	7.36191300	1.09873500	1.34342100
O	7.22715100	0.13955800	-0.59579000
N	-2.89672600	0.73668800	0.78443400
C	-3.31185400	2.69977200	-0.05269500

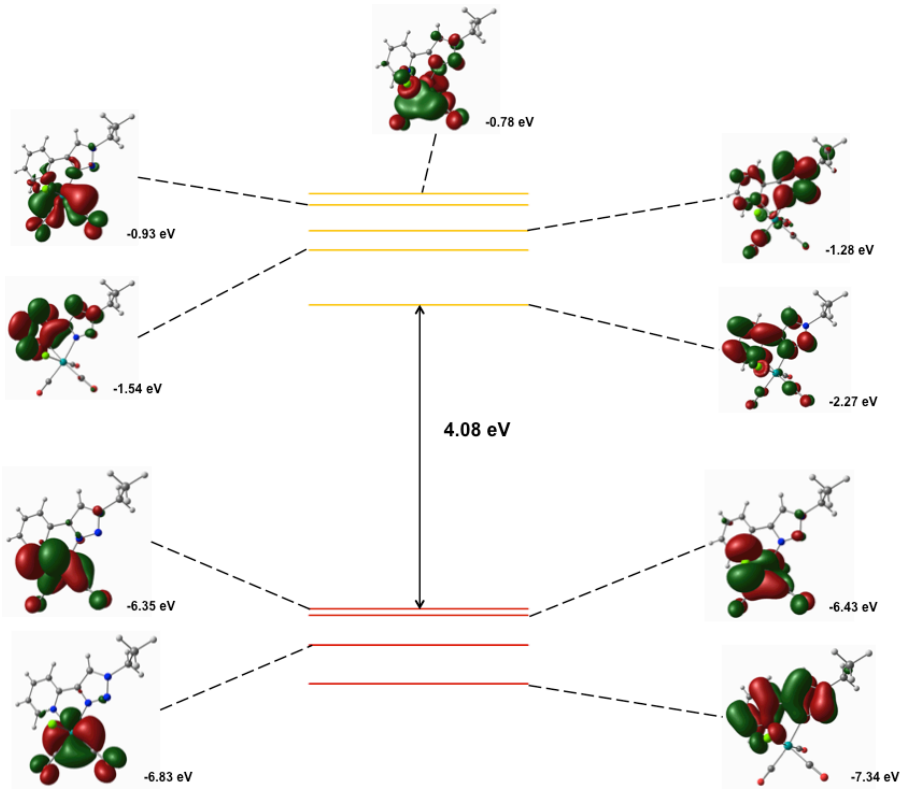


Figure appendix-1 Molecular orbitals diagram for complex 3r'.

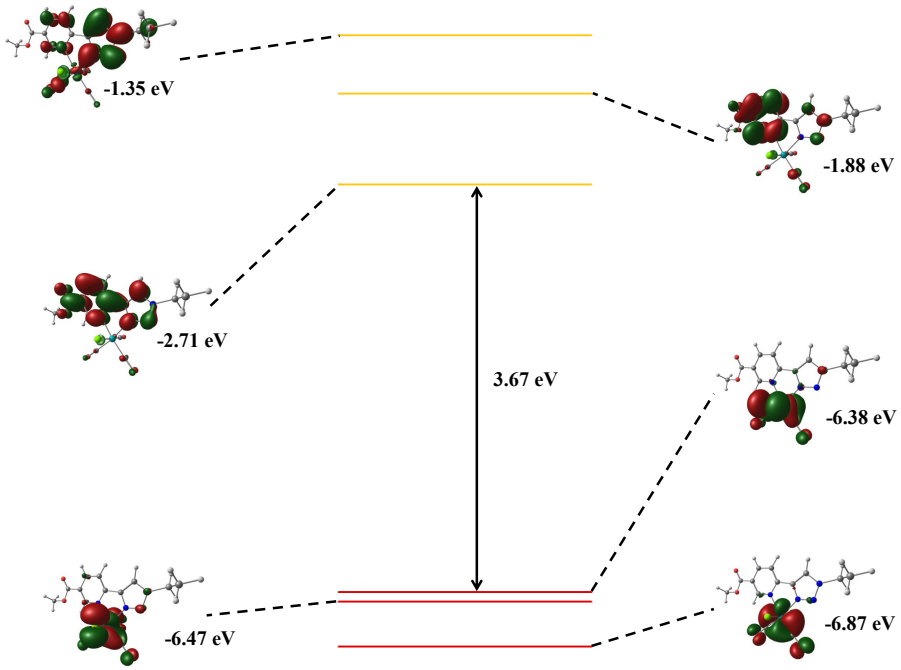


Figure appendix-2 Molecular orbitals diagram for complex 13'.

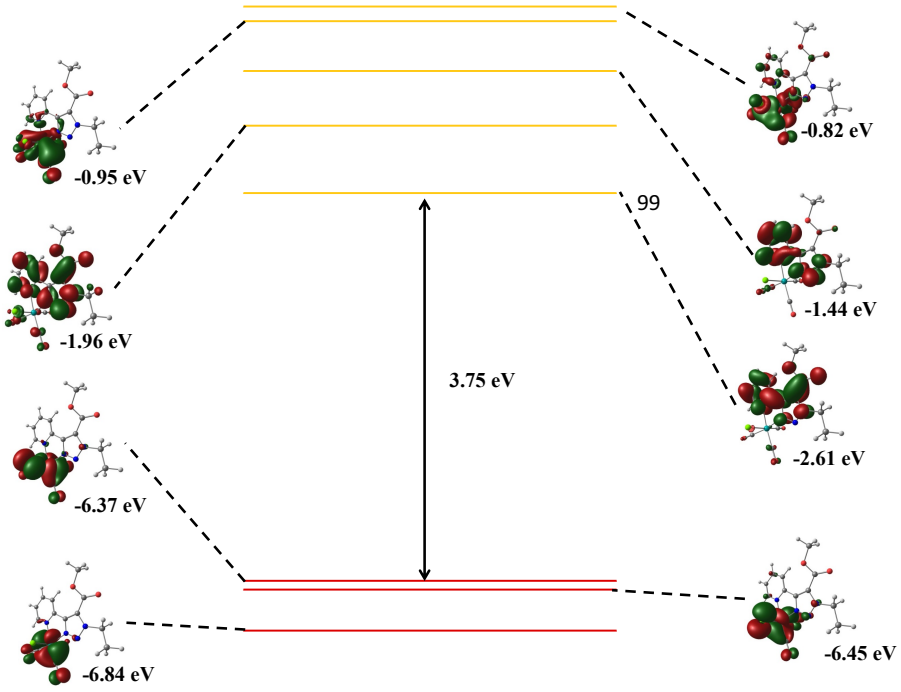


Figure appendix-3 Molecular orbitals diagram for complex 16'.

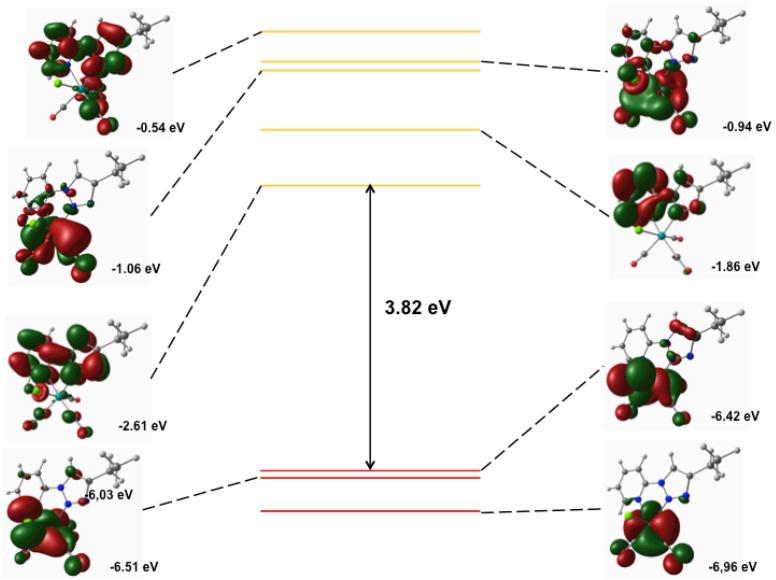


Figure appendix-4 Molecular orbitals diagram for complex 9'.

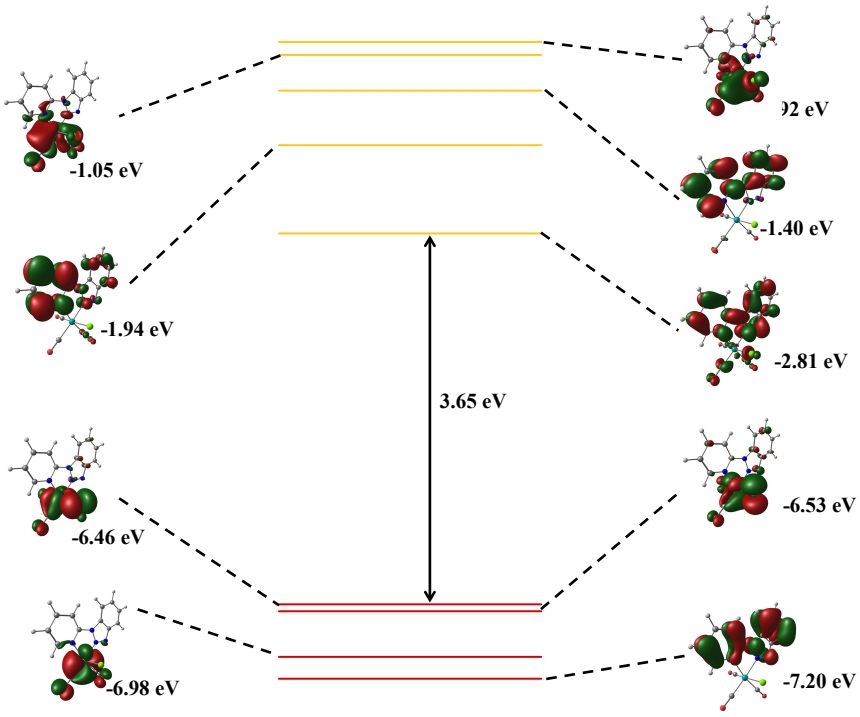


Figure appendix-5 Molecular orbitals diagram for complex 17'.

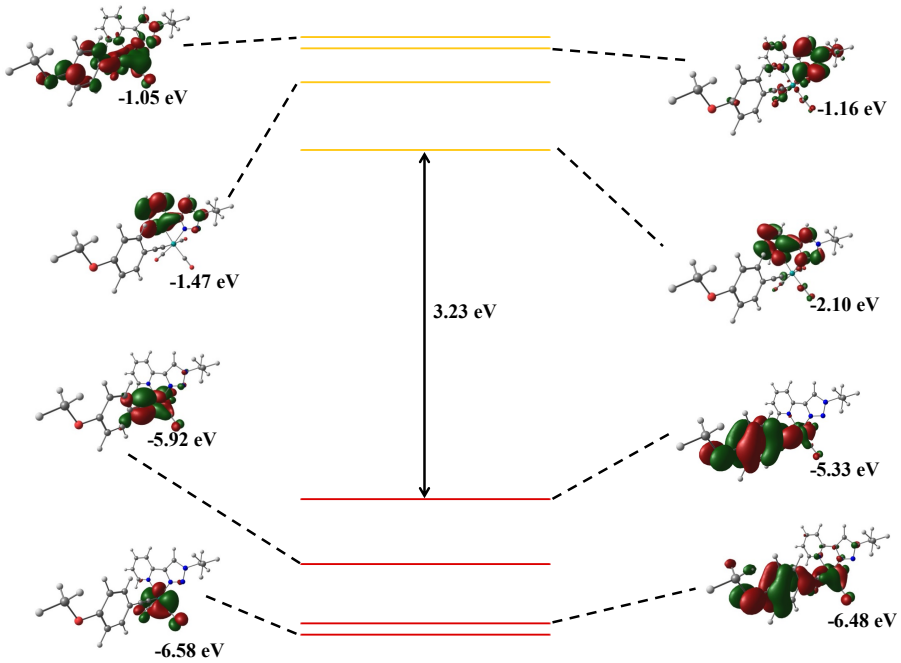


Figure appendix-6 Molecular orbitals diagram for complex 33a'.

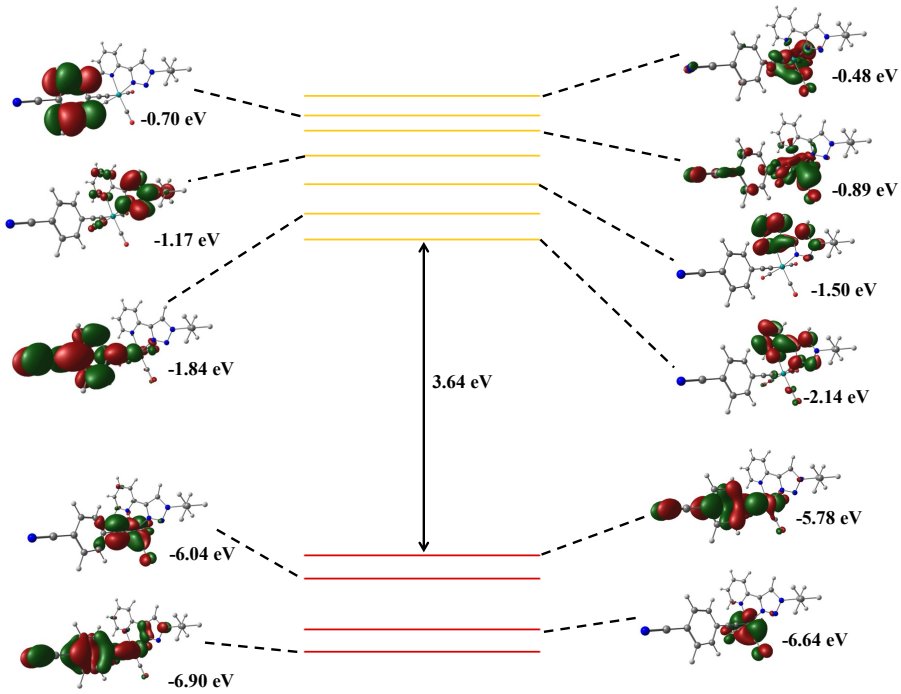


Figure appendix-7 Molecular orbitals diagram for complex 33b'.

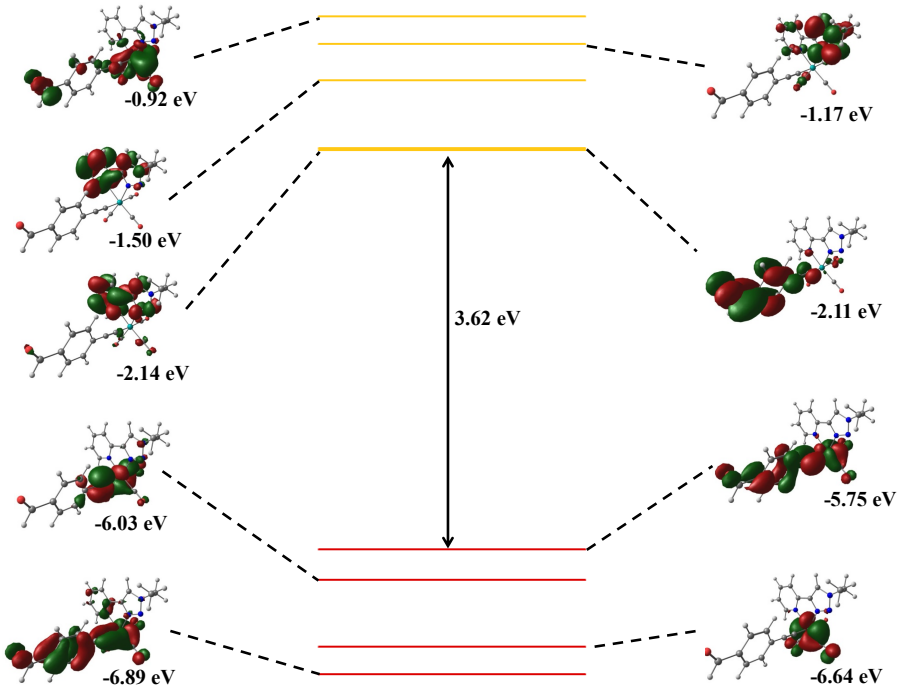


Figure appendix-8 Molecular orbitals diagram for complex 33c'.

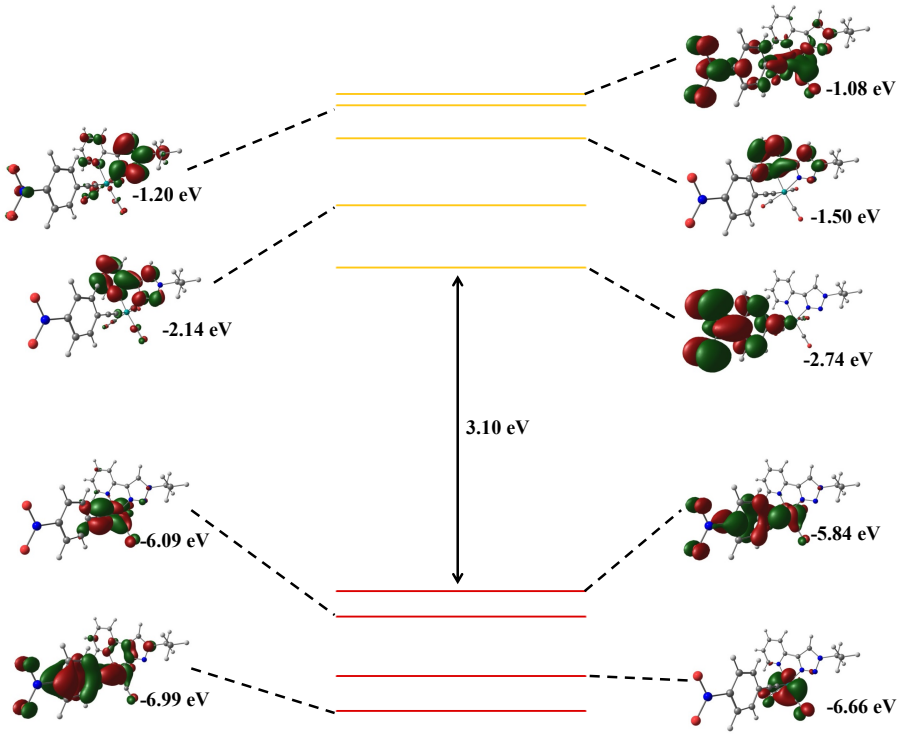


Figure appendix-9 Molecular orbitals diagram for complex 33d'.

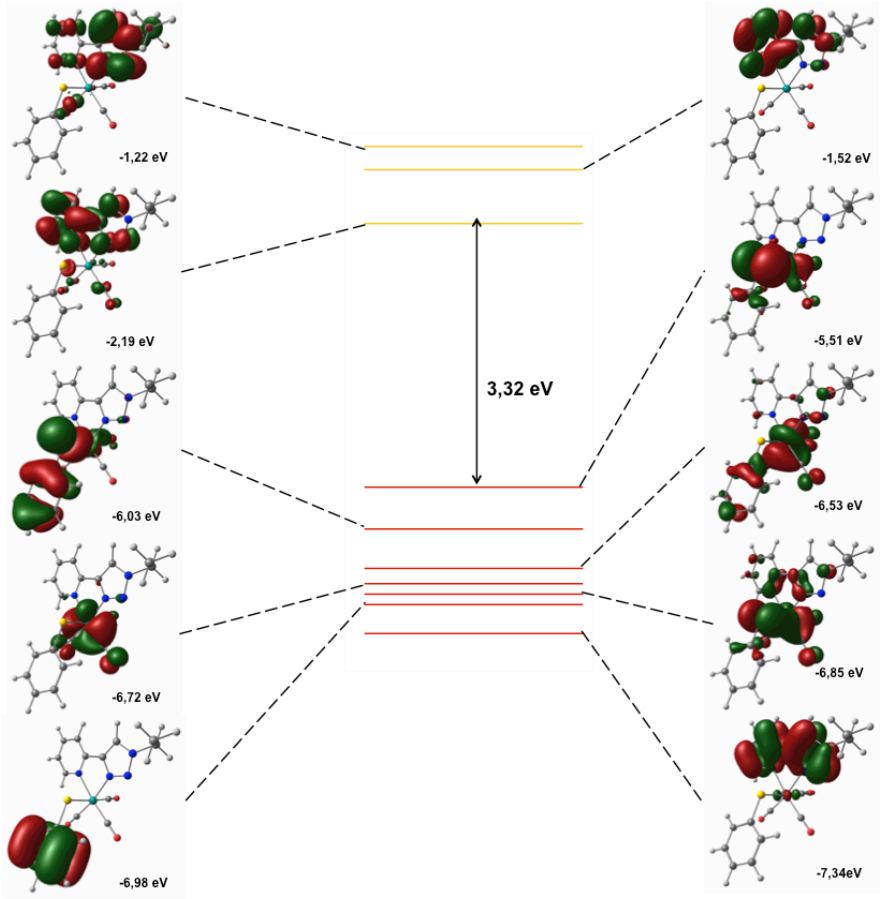


Figure appendix-10 Molecular orbitals diagram for complex 37a'.

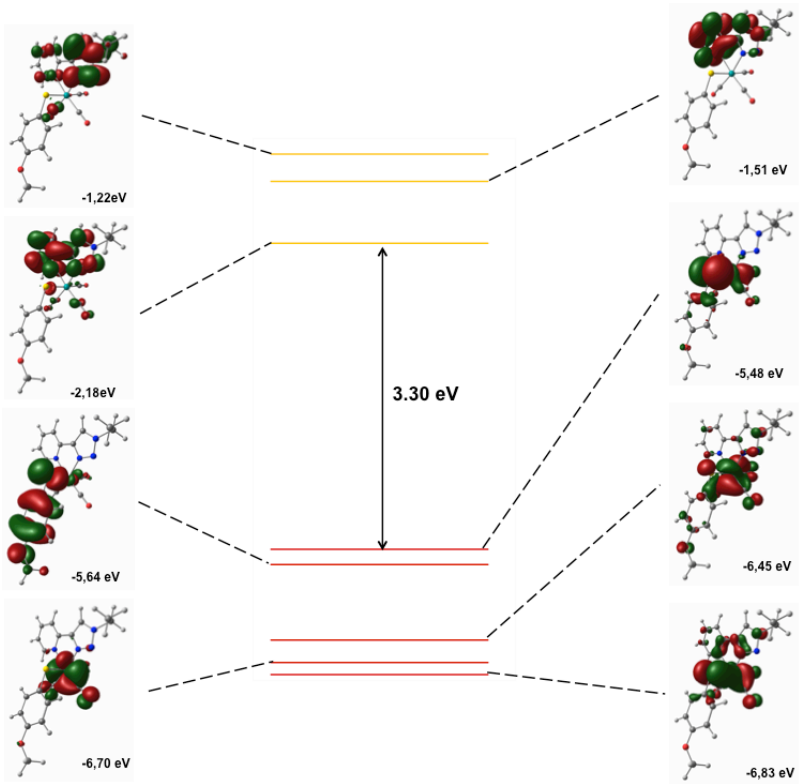


Figure appendix-11 Molecular orbitals diagram for complex 37b'.

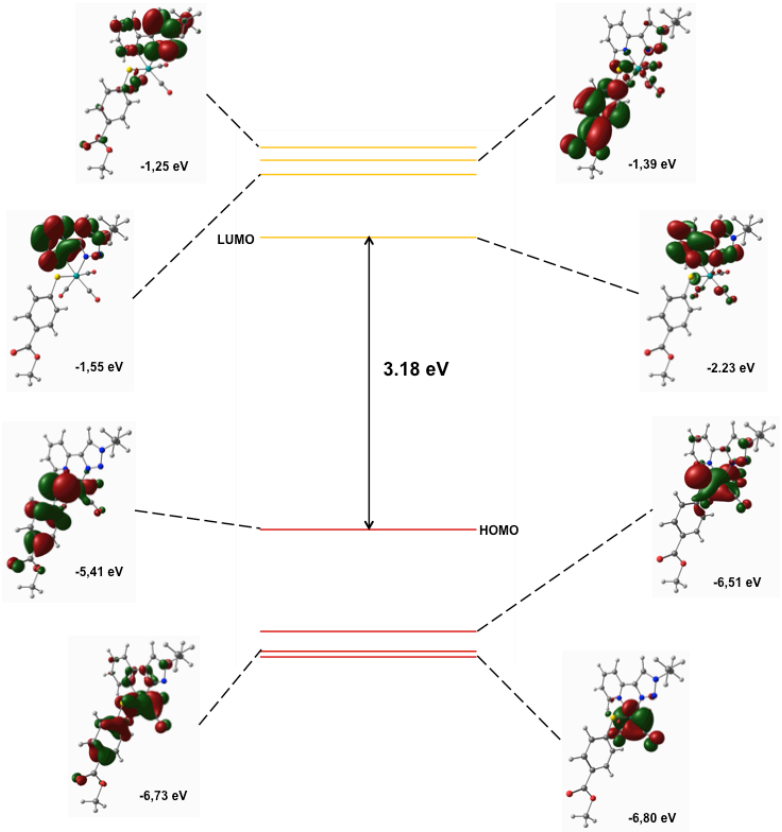


Figure appendix-12 Molecular orbitals diagram for complex 37c'.

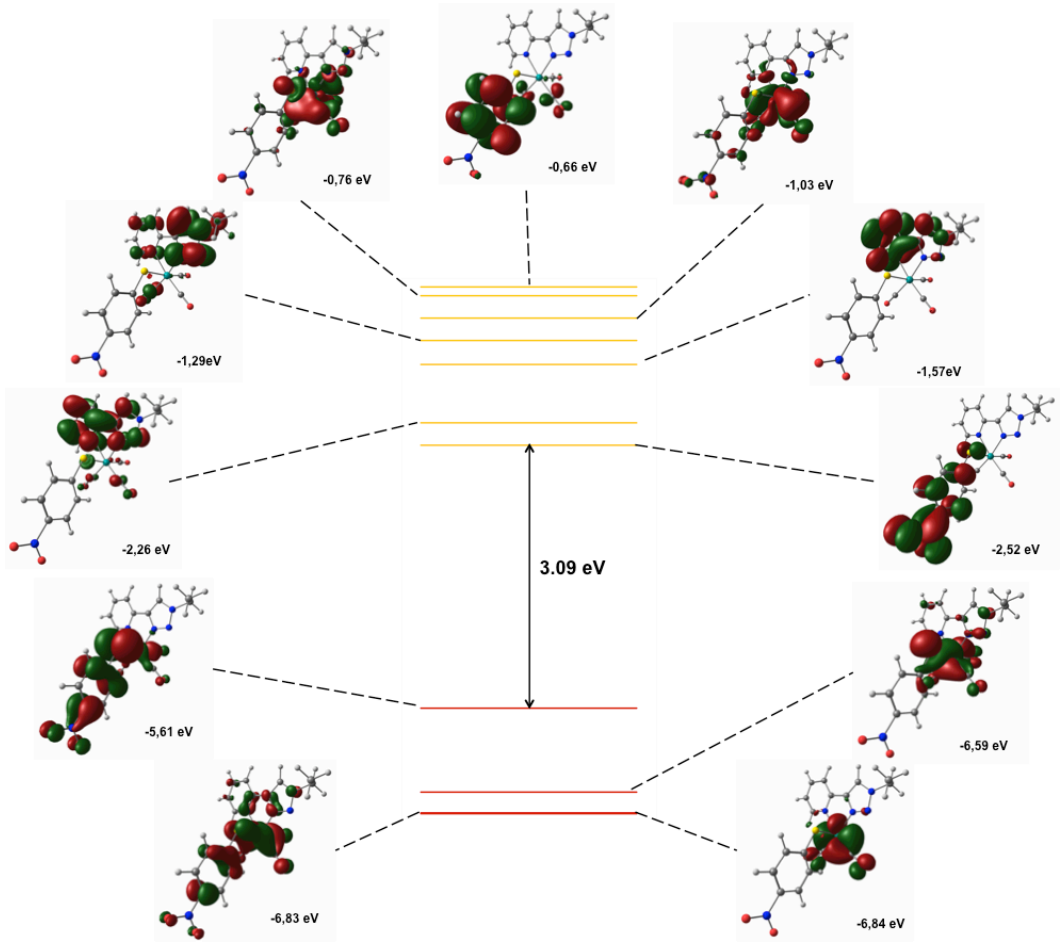


Figure appendix-13 Molecular orbitals diagram for complex 37d'.

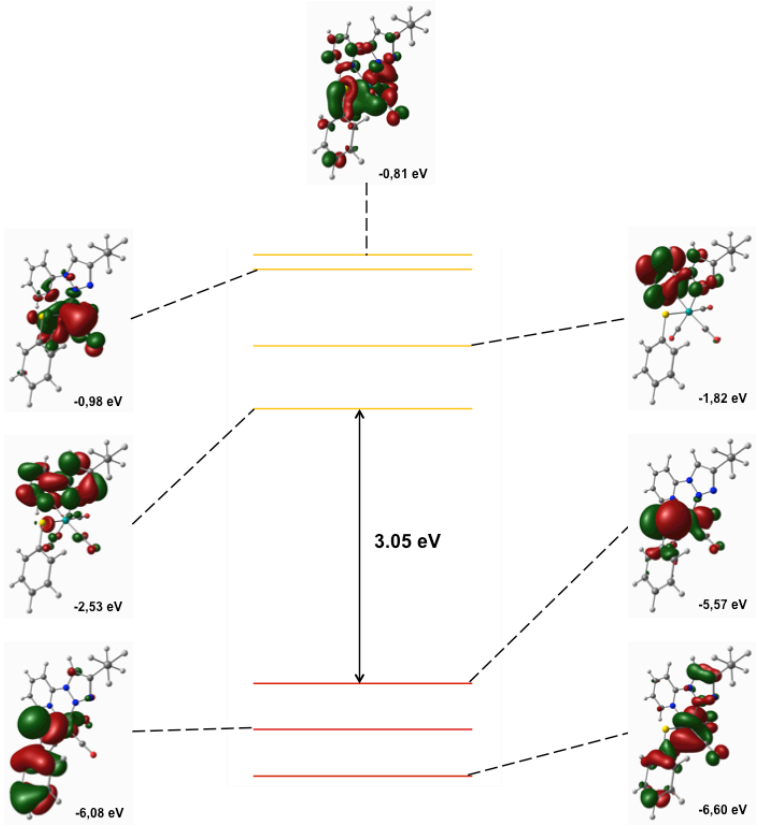


Figure appendix-14 Molecular orbitals diagram for complex 38a'.

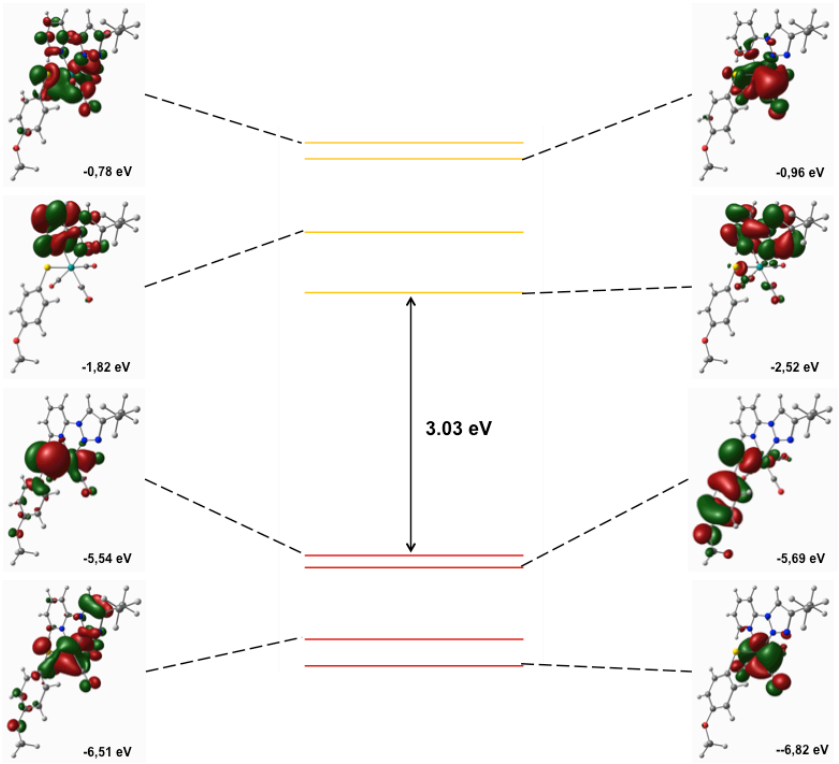


Figure appendix-15 Molecular orbitals diagram for complex 38b'.

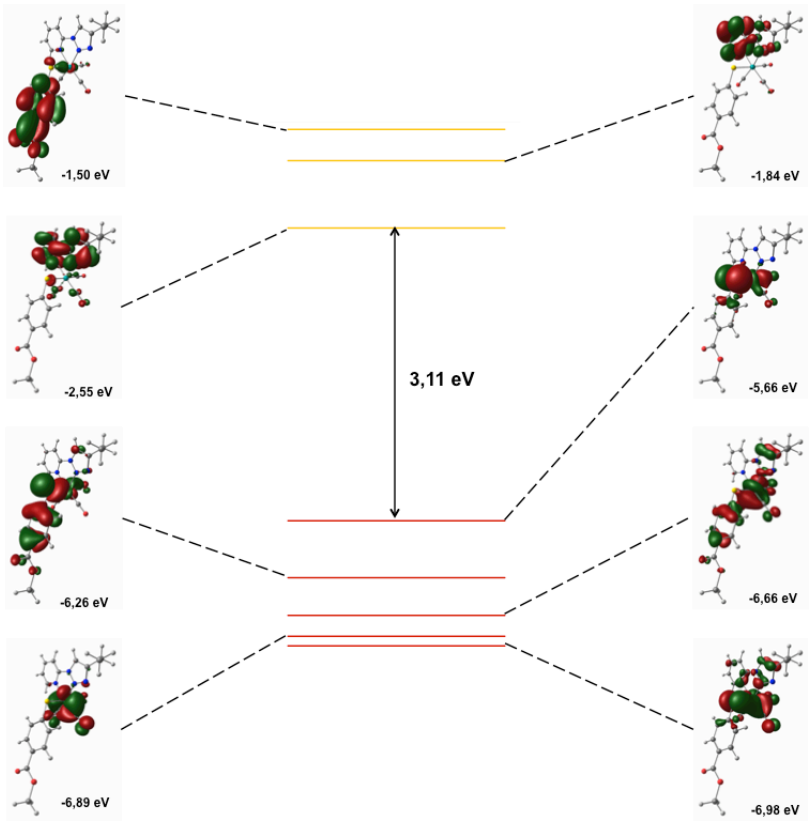


Figure appendix-16 Molecular orbitals diagram for complex 38c'.

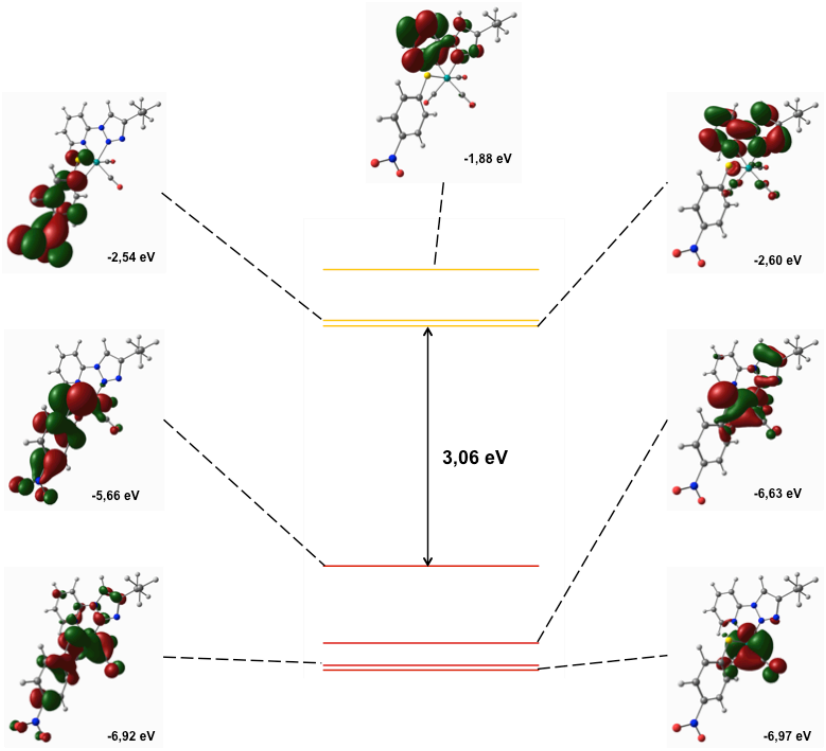


Figure appendix-17 Molecular orbitals diagram for complex 38d'.

Table appendix-19. Predicted transitions for complex **13'**.

State	Excitations	Ecal /eV	λcal /nm	f
S1	H → L	2.9566	419.34	0.0002
S2	H-1 → L	3.0855	401.83	0.0856
S3	H-2 →L	3.4198	362.55	0.0007
S4	H → L+1	3.7725	328.65	0.0096
S5	H-1 → L+1	3.8828	319.31	0.0311
S6	H-4, H-3 → L H-1, H → L+2	4.1601	298.03	0.4824
S7	H-3 → L H-2 → L+1 H-2, H-1 → L+3 H → L+2, L+3, L+4	4.1897	295.92	0.0490
S8	H-2 → L+1, L+4 H → L+2	4.2264	293.36	0.0036
S9	H-3 → L H-1 → L+2, L+3 H → L+3	4.2577	291.20	0.0534
S10	H-4 → L	4.3385	285.78	0.0080

	H-1 → L+3, L+4 H → L+2, L+3			

Table appendix-20. Predicted transitions for complex **16'**.

State	Excitations	Ecal /eV	λcal /nm	f
S1	H → L, L+1	3.0361	408.36	0.0022
S2	H-1 → L	3.1587	392.52	0.1044
S3	H-2 →L, L+1	3.4862	355.65	0.0007
S4	H → L, L+1	3/6812	336.81	0.0155
S5	H-1 → L+1	3.8010	326.19	0.0440
S6	H-2 → L, L+1, L+4	4.1175	301.12	0.0007
S7	H-3 → L H-1, H → L+2 H-1 → L+3, L+4	4.1809	296.55	0.0507
S8	H-3 → L H-1 → L+2, L+3 H → L+2, L+3	4.2303	293.08	0.0867
S9	H-3 → L H-1, H → L+2 H → L+3, L+4	4.2939	288.74	0.1402
S10	H-1 → L+2, L+3, L+4 H → L+2, L+3	4.3160	287.27	0.0206

Table appendix-21. Predicted transitions for complex **17'.**

State	Excitations	Ecal /eV	λcal /nm	f
S1	H → L	2.2450	552.28	0.0098
S2	H-1 → L	2.5877	479.12	0.2551
S3	H-2 →L	2.8843	429.85	0.0036
S4	H-3 → L H → L+1	3.4918	355.07	0.1693
S5	H-3 → L H-1, H → L+1	3.5160	352.63	0.2278
S6	H-3 → L H-1 → L+1	3.6939	335.65	0.2102
S7	H-7, H-4 → L	3.9822	311.34	0.2195
S8	H → L+2, L+4	4.0747	304.28	0.0819

S9	H-2 → L+1	4.1172	301.14	0.0008
S10	H-5 → L	4.2010	295.13	0.0434

Table appendix-22. Predicted transitions for complex **33a'**.

State	Excitations	Ecal /eV	λcal /nm	f
S1	H → L	1.9755	627.60	0.0011
S2	H-1 → L	2.5888	478.93	0.0846
S3	H → L+1	3.0579	405.46	0.0053
S4	H-3 → L H → L+2	3.2201	385.04	0.0242
S5	H-4, H-3 → L H-1 → L+2	3.2245	384.51	0.0108
S6	H-3 → L H-1 → L+2	3.3006	375.64	0.0109
S7	H-2 → L+4 H-1 → L+3	3.3284	372.51	0.5399
S8	H-2 → L+1, L+2, L+3	3.6367	340.93	0.0114
S9	H-2 → L+1, L+2, L+3	3.6437	340.27	0.0110
S10	H-2, H → L+4	3.7350	331.95	0.0416

Table appendix-23. Predicted transitions for complex **33b'**.

State	Excitations	Ecal /eV	λcal /nm	f
S1	H → L	2.3059	537.69	0.0019
S2	H-1 → L	2.6649	465.25	0.1050
S3	H →L+1	3.1186	397.56	0.0171
S4	H-1 → L+1	3.1812	389.74	0.0001
S5	H-2 → L	3.1922	388.40	0.0078
S6	H → L+2	3.4216	362.36	0.0107
S7	H → L+3	3.5740	346.90	0.0333
S8	H-3 → L H-1 →L+2, L+3	3.7263	332.73	0.0207
S9	H-3 → L H-1 → L+2	3.7468	330.90	0.0112
S10	H-1 → L+3 H → L+3, L+4	3.8620	321.03	0.0205

Table appendix-24. Predicted transitions for complex **33c'**.

State	Excitations	Ecal /eV	λcal /nm	f
S1	H → L	2.2925	540.84	0.0019
S2	H-1 → L H → L+1	2.6515	467.61	0.1136
S3	H-1 →L H → L+1	2.9289	423.31	1.0140
S4	H-1 → L+1, L+4	3.0212	410.38	0.0002
S5	H-2 → L	3.1967	387.85	0.0010
S6	H → L+2	3.4063	363.99	0.0101
S7	H-3 → L H → L+3	3.5586	348.41	0.0322
S8	H-3 → L H-1 → L+2, L+3	3.7123	333.98	0.0188
S9	H-3 → L H-1 → L+2	3.7242	332.91	0.0118
S10	H-4 → L+1, L+4, L+9	3.7785	328.13	0.0000

Table appendix-25. Predicted transitions for complex **33d'**.

State	Excitations	Ecal /eV	λcal /nm	f
S1	H-1, H → L	2.0782	596.60	0.0012
S2	H-1, H → L	2.3568	526.08	0.8793
S3	H → L+1	2.7848	445.22	0.0034
S4	H-1 → L+1	2.9712	417.29	0.0848
S5	H-2 → L	2.9864	415.16	0.0024
S6	H-7, H-5 → L	3.2862	377.29	0.0000
S7	H → L+2	3.5222	352.01	0.0098
S8	H-2 → L+1	3.5273	351.50	0.0016
S9	H-3 → L+1 H-1 → L+2 H → L+4	3.6431	340.33	0.2386
S10	H-3 → L H-1 → L+2	3.6454	340.11	0.0399

Table appendix-26. Predicted transitions for complex **37a'**.

State	Excitations	Ecal /eV	λcal /nm	f
S1	H → L	1.9106	648.93	0.0006
S2	H → L+1	3.0253	409.82	0.0026
S3	H-1 → L H →L+2	3.1414	394.68	0.0698
S4	H-2 → L H-1 → L H → L+2	3.1695	391.18	0.0967
S5	H-2 → L	3.3199	373.46	0.0238
S6	H-3 → L	3.3441	370.75	0.0034
S7	H → L+3	3.4382	360.61	0.1588
S8	H-2, H → L+4	3.6802	336.89	0.0098
S9	H-5 → L	3.9100	317.10	0.0454
S10	H-6 → L	4.0514	306.01	0.0002

Table appendix-27. Predicted transitions for complex **37b'**.

State	Excitations	Ecal /eV	λcal /nm	f
S1	H → L	1.6685	743.10	0.0004
S2	H → L+1	2.7766	446.53	0.0013
S3	H →L+2	2.9035	427.01	0.0046
S4	H-2 → L H-1 → L	3.1395	394.92	0.0345
S5	H-2, H-1 → L	3.1873	388.99	0.1318
S6	H → L+3	3.2042	386.94	0.1417
S7	H-3 → L	3.3764	367.21	0.0077
S8	H → L+4	3.4275	361.74	0.0047
S9	H-5, H-4 → L H-1 → L+5	3.8229	324.32	0.0178
S10	H-5, H-4 → L H-1 → L+5	3.8623	321.01	0.0793

Table appendix-28. Predicted transitions for complex **37c'**.

State	Excitations	Ecal /eV	λcal /nm	f
S1	H → L	2.0581	602.41	0.0008
S2	H-1 → L H → L+1	3.1717	390.91	0.1667

	H → L+2			
S3	H-1 → L H → L+1	3.1829	389.53	0.0994
S4	H-2 → L H-1 → L H → L+2 H → L+3	3.3032	375.34	0.0432
S5	H-3, H-2 → L H → L+3	3.3425	370.93	0.0484
S6	H-1 → L H → L+2, L+3, L+4	3.3627	368.70	0.5198
S7	H-3, H-2 → L H → L+2	3.3978	364.89	0.0111
S8	H → L+2, L+3, L+4, L+5	3.7231	333.01	0.0776
S9	H-2 → L+5 H → L+4, L+5	3.8308	323.65	0.0195
S10	H-5 → L H → L+6	4.0210	308.34	0.0260

Table appendix-29. Predicted transitions for complex **37d'**.

State	Excitations	Ecal /eV	λcal /nm	f
S1	H → L	2.1753	569.97	0.0015
S2	H → L+1	2.5934	478.07	0.5946
S3	H-2, H-1 →L	3.2120	386.00	0.1156
S4	H → L+2	3.3086	374.73	0.0085
S5	H-3, H-2, H-1 → L	3.3412	371.08	0.0211
S6	H-3 → L H → L+3	3.4326	361.19	0.0239
S7	H-3, H-2 → L H → L+3	3.4965	354.60	0.0160
S8	H-1 → L+1	3.5387	350.36	0.0027
S9	H → L+4, L+5	3.6881	336.17	0.0384
S10	H-3, H-2 → L+1	3.7975	326.49	0.0019

Table appendix-30. Predicted transitions for complex **38a'**.

State	Excitations	Ecal /eV	λcal /nm	f

S1	H → L	1.6302	760.54	0.0005
S2	H → L+1	2.7504	450.79	0.0031
S3	H-1 →L	2.9234	424.11	0.2004
S4	H-2 → L	3.0686	404.05	0.0061
S5	H-3 → L	3.1545	393.04	0.0043
S6	H → L+2	3.3849	366.29	0.1582
S7	H → L+3, L+4	3.6057	343.85	0.0015
S8	H-5 → L	3.6483	339.84	0.0536
S9	H-4 → L	3.7278	332.59	0.0000
S10	H → L+3, L+4	3.8557	321.56	0.0253

Table appendix-31. Predicted transitions for complex **38b'**.

State	Excitations	Ecal /eV	λcal /nm	f
S1	H → L	1.3671	906.90	0.0001
S2	H → L+1	2.4844	499.06	0.0024
S3	H-2, H-1 →L	2.8860	429.61	0.0565
S4	H-2, H-1 →L	2.9377	422.05	0.1502
S5	H-3 → L H → L+2	3.1286	396.29	0.1158
S6	H-3 → L H → L+2	3.1793	389.98	0.0160
S7	H → L+3, L+4	3.3249	372.90	0.0009
S8	H-5 → L H → L+4	3.5643	347.85	0.0399
S9	H-5 → L H → L+3, L+4	3.6161	342.87	0.0341
S10	H-6, H-4 → L	3.7404	331.48	0.0003

Table appendix-32. Predicted transitions for complex **38c'**.

State	Excitations	Ecal /eV	λcal /nm	f
S1	H → L	1.7829	695.42	0.0009
S2	H-1 → L H → L+1	2.9024	427.17	0.0334
S3	H-1 → L H → L+1	2.9564	419.38	0.2228
S4	H-2 → L H → L+1	3.1356	395.41	0.0018

S5	H-3, H-2 → L	3.1613	392.19	0.0158
S6	H → L+2, L+3	3.3564	369.40	0.5854
S7	H-5 → L H → L+2, L+3	3.7084	334.33	0.0879
S8	H → L+3, L+4, L+5	3.7416	331.37	0.0019
S9	H-5 → L H → L+2, L+3, L+5	3.7835	327.69	0.0933
S10	H-4 → L	3.9119	316.94	0.0000

Table appendix-33. Predicted transitions for complex **38d'**.

State	Excitations	Ecal /eV	λcal /nm	f
S1	H → L	1.9095	649.29	0.0015
S2	H-1 → L H → L+1	2.6446	468.82	0.6489
S3	H-1 → L H → L+2	2.9758	416.64	0.0965
S4	H-1 → L H → L+2	3.0565	405.64	0.0498
S5	H-3, H-2 → L	3.1527	393.26	0.0093
S6	H-3, H-2 → L	3.2461	381.95	0.0055
S7	H-1 → L+1	3.5967	344.72	0.0008
S8	H-4 → L H → L+3	3.6774	337.15	0.0376
S9	H-4 → L H-2 → L+1 H → L+4, L+5, L+6	3.8361	323.20	0.0074
S10	H-4 → L H-2 → L+1 H → L+4, L+6	3.8525	321.83	0.0348

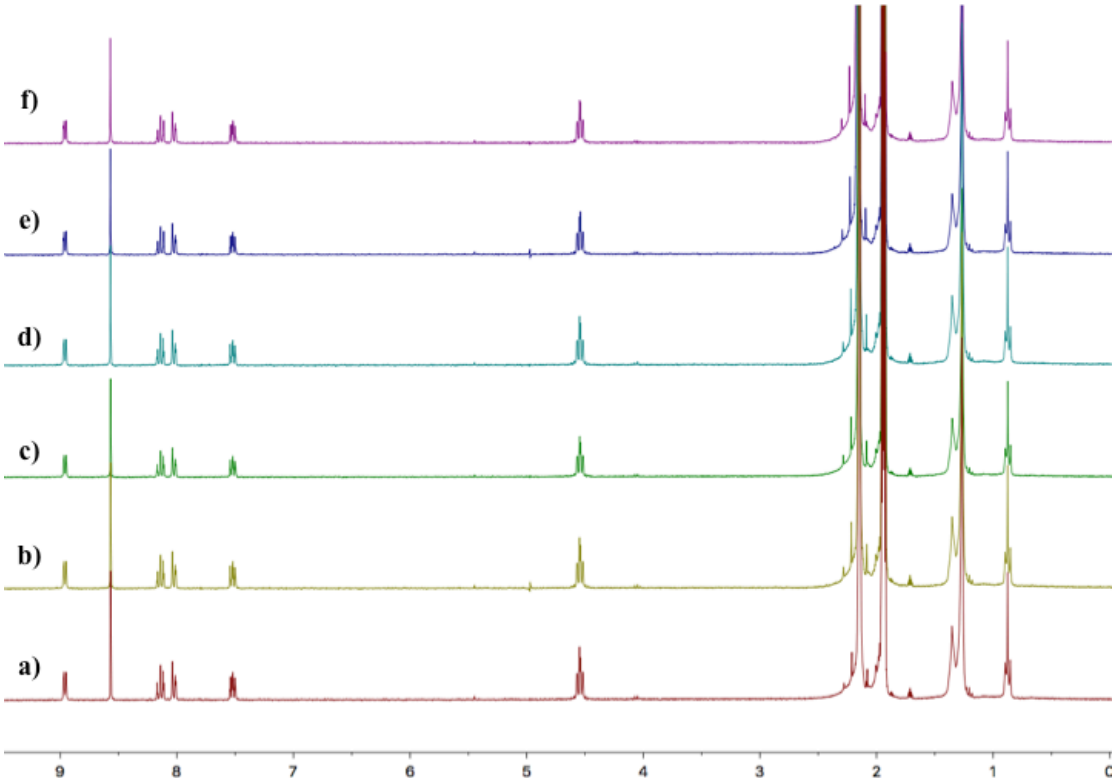


Figure appendix-18 ^{1}H NMR spectrum of complex **3r** in acetonitrile-d_3 at a concentration of 4 mM after 0 hour (a), 8 hours (b), 16 hours (c), 24 hours (d), 48 hours (e) and 72 hours (f).

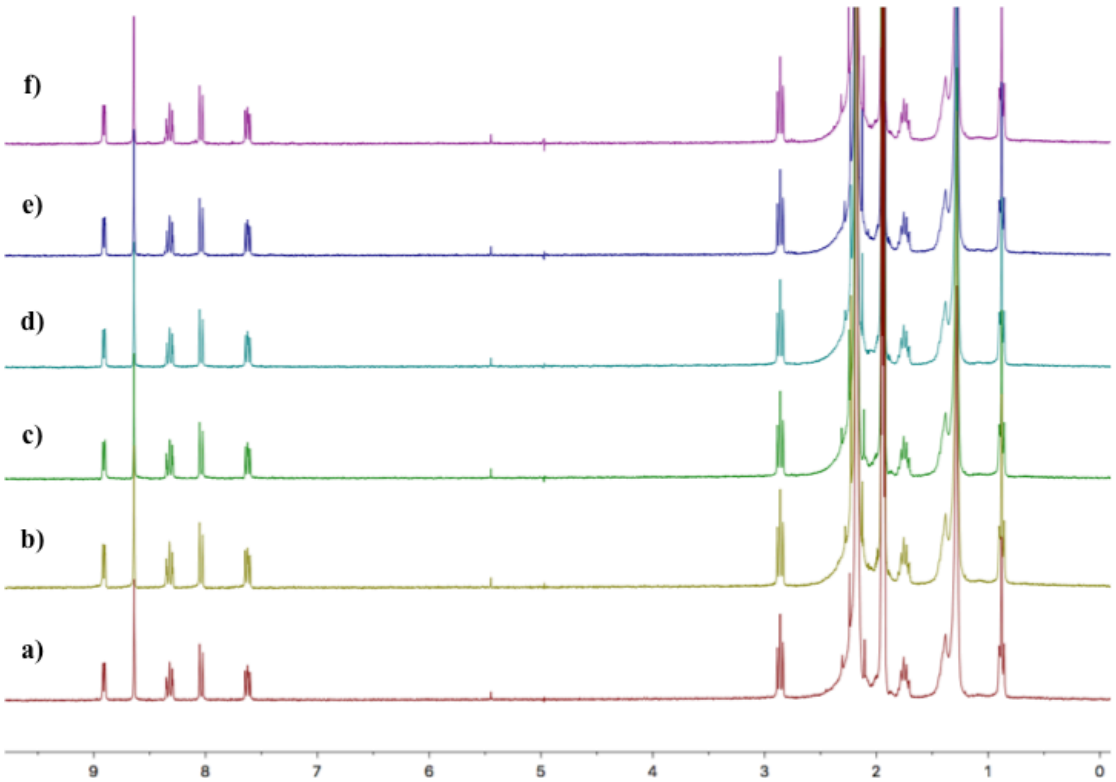


Figure appendix-19 ^{1}H NMR spectrum of complex **9** in acetonitrile-d_3 at a concentration of 4 mM after 0 hour (a), 8 hours (b), 16 hours (c), 24 hours (d), 48 hours (e) and 72 hours (f).

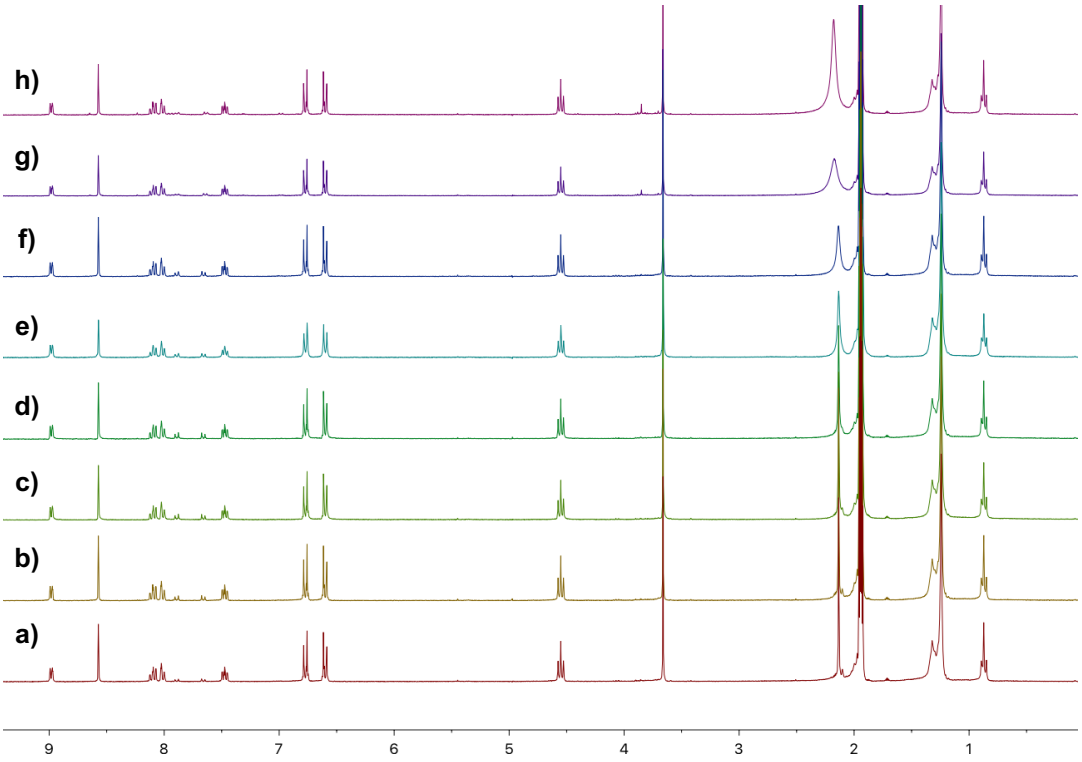


Figure appendix-20 ^{1}H NMR spectrum of complex **33a** in acetonitrile-d_3 at a concentration of 4 mM after 0 hour (a), 1 hours (b), 2 hours (c), 4 hours (d), 8 hours (e), 12 hours (f) 48 hours (g) and 72 hours (h).

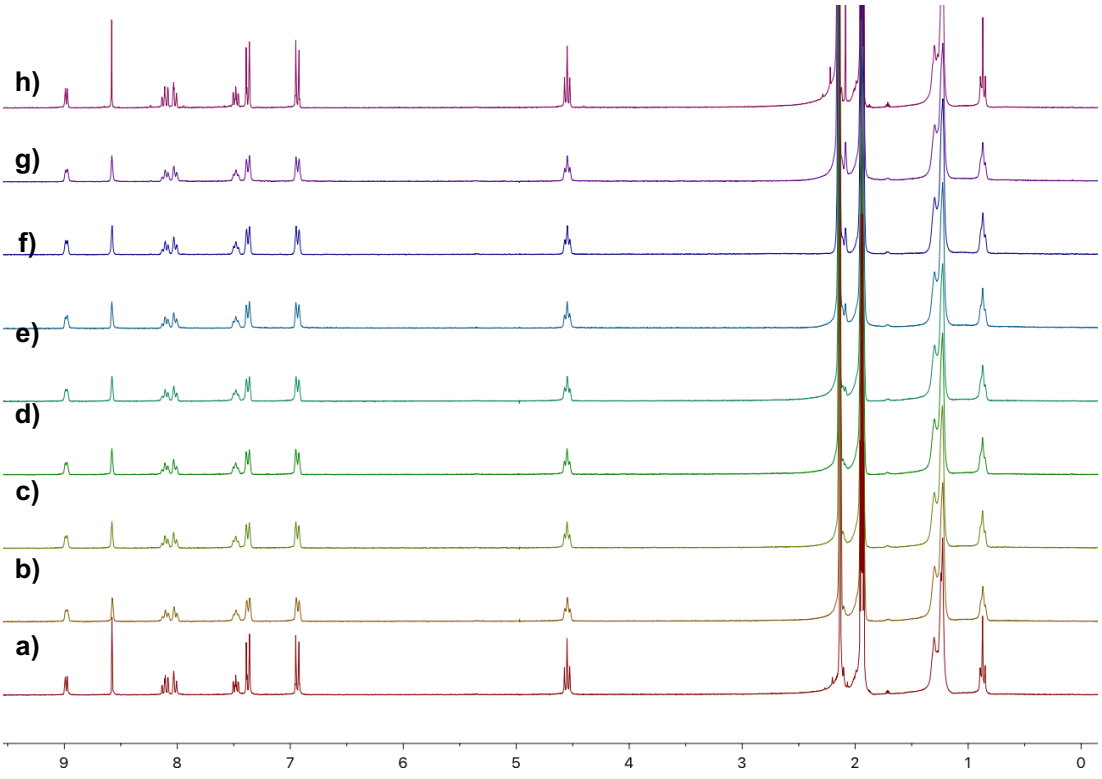


Figure appendix-21 ^{1}H NMR spectrum of complex **33b** in acetonitrile-d_3 at a concentration of 4 mM after 0 hour (a), 1 hours (b), 2 hours (c), 4 hours (d), 8 hours (e), 12 hours (f) 48 hours (g) and 72 hours (h).

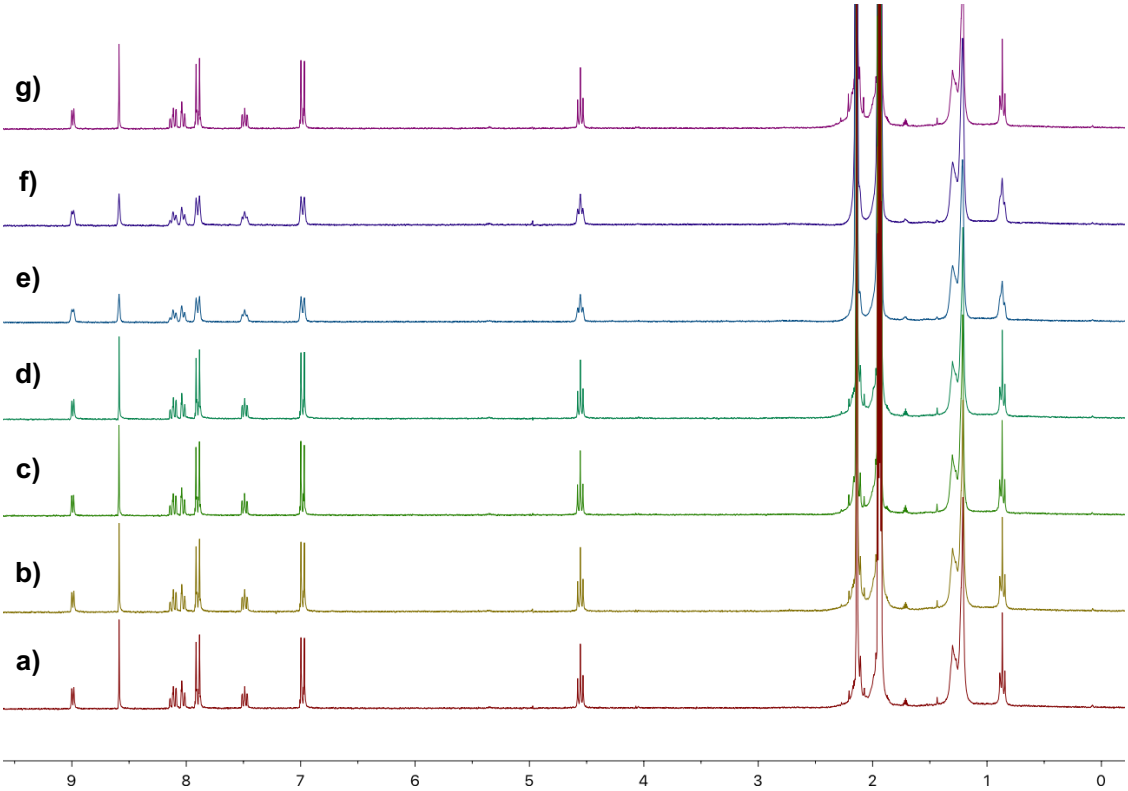


Figure appendix-22 ^{1}H NMR spectrum of complex **33d** in acetonitrile-d_3 at a concentration of 4 mM after 0 hour (a), 1 hours (b), 2 hours (c), 4 hours (d), 8 hours (e), 12 hours (f) and 24 hours (g).

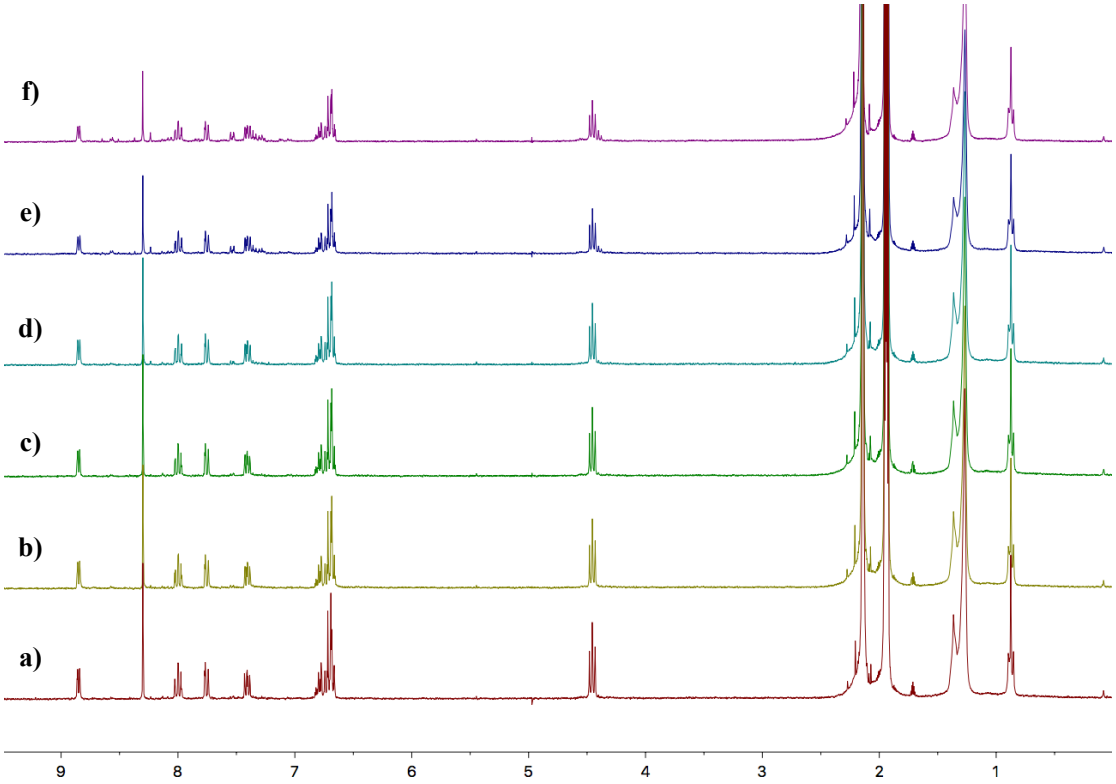


Figure appendix-23 ^{1}H NMR spectrum of complex **37a** in acetonitrile-d_3 at a concentration of 4 mM after 0 hour (a), 8 hours (b), 16 hours (c), 24 hours (d), 48 hours (e) and 72 hours (f).

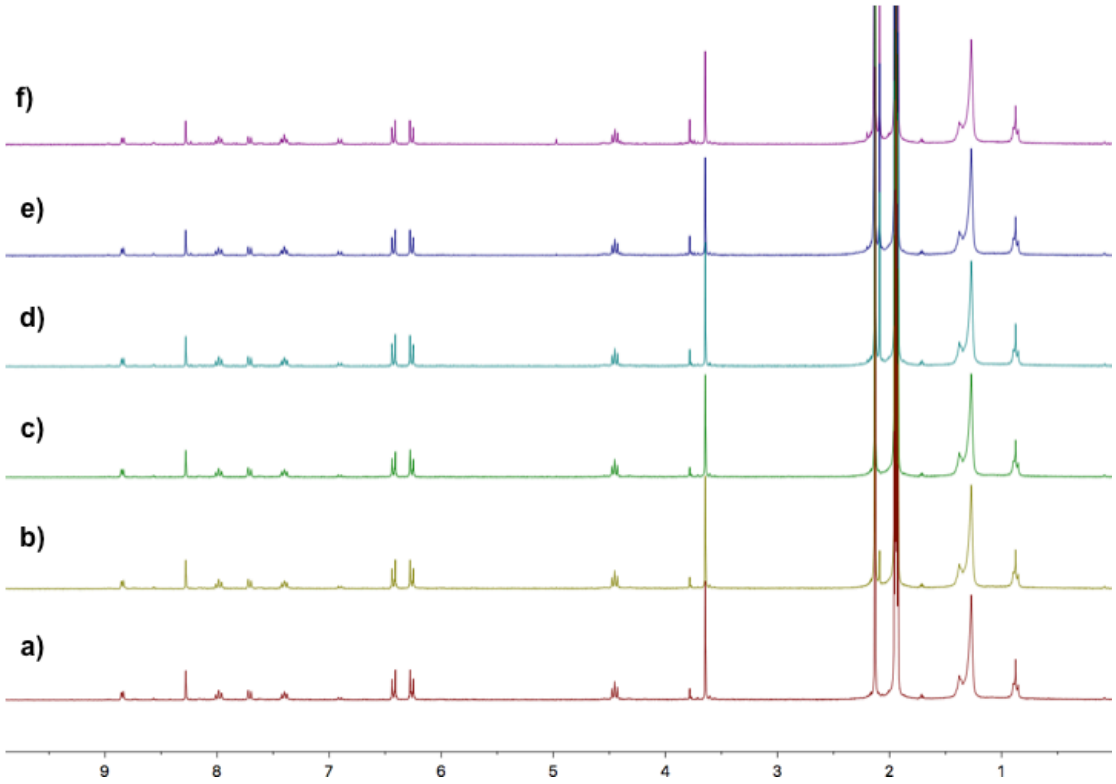


Figure appendix-24 ^{1}H NMR spectrum of complex **37b** in acetonitrile-d_3 at a concentration of 4 mM after 0 hour (a), 8 hours (b), 16 hours (c), 24 hours (d), 48 hours (e) and 72 hours (f).

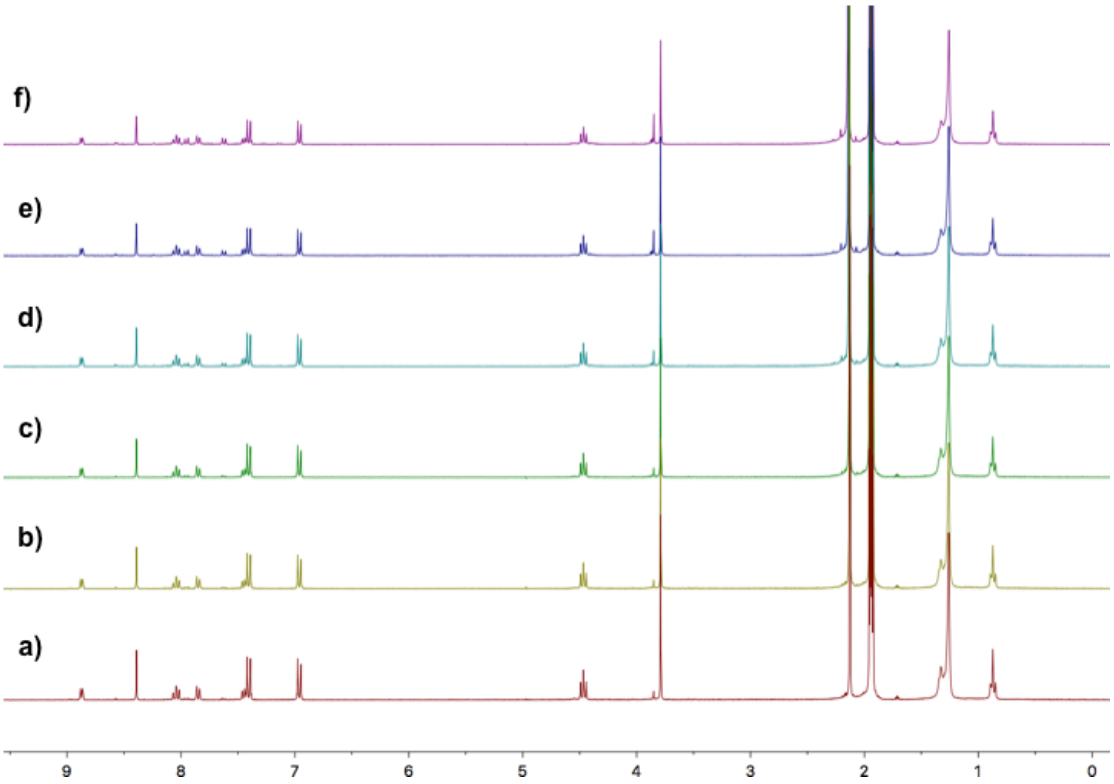


Figure appendix-25 ^{1}H NMR spectrum of complex **37c** in acetonitrile-d_3 at a concentration of 4 mM after 0 hour (a), 8 hours (b), 16 hours (c), 24 hours (d), 48 hours (e) and 72 hours (f).

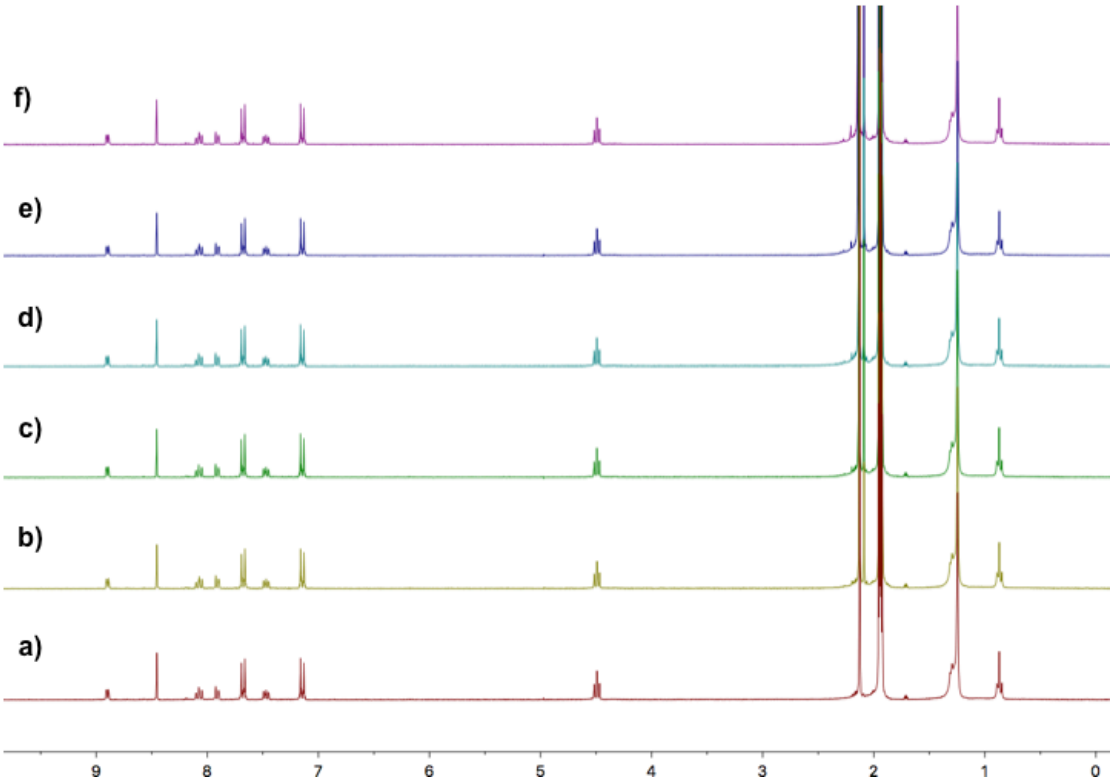


Figure appendix-26 ^{1}H NMR spectrum of complex **37d** in acetonitrile-d_3 at a concentration of 4 mM after 0 hour (a), 8 hours (b), 16 hours (c), 24 hours (d), 48 hours (e), and 72 hours (f).

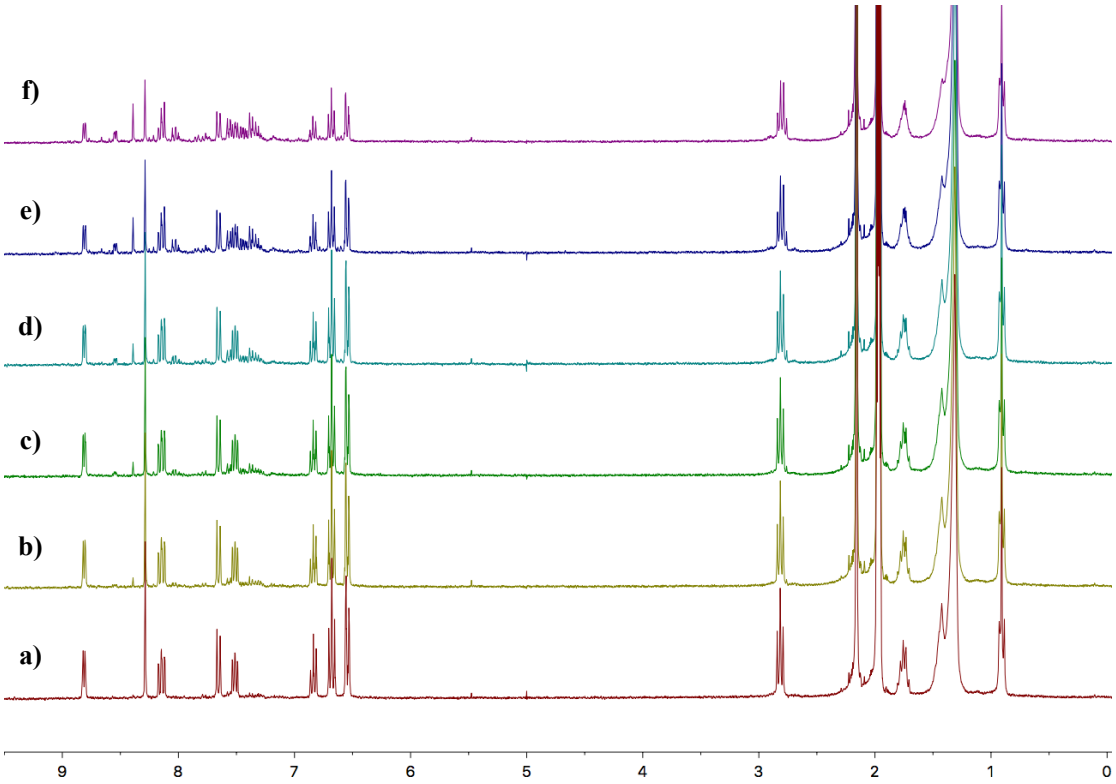


Figure appendix-27 ^{1}H NMR spectrum of complex **38a** in acetonitrile-d_3 at a concentration of 4 mM after 0 hour (a), 8 hours (b), 16 hours (c), 24 hours (d), 48 hours (e) and 72 hours (f).

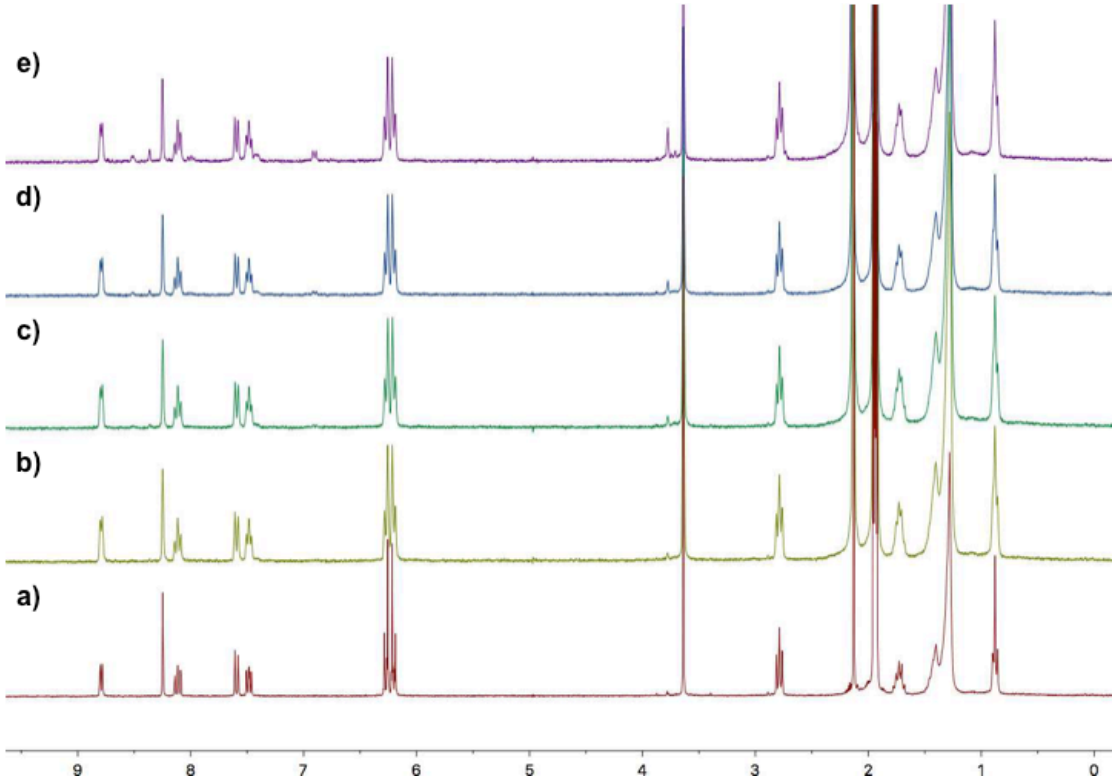


Figure appendix-28 ^{1}H NMR spectrum of complex **38b** in acetonitrile-d_3 at a concentration of 4 mM after 0 hour (a), 8 hours (b), 16 hours (c), 24 hours (d), 48 hours (e).

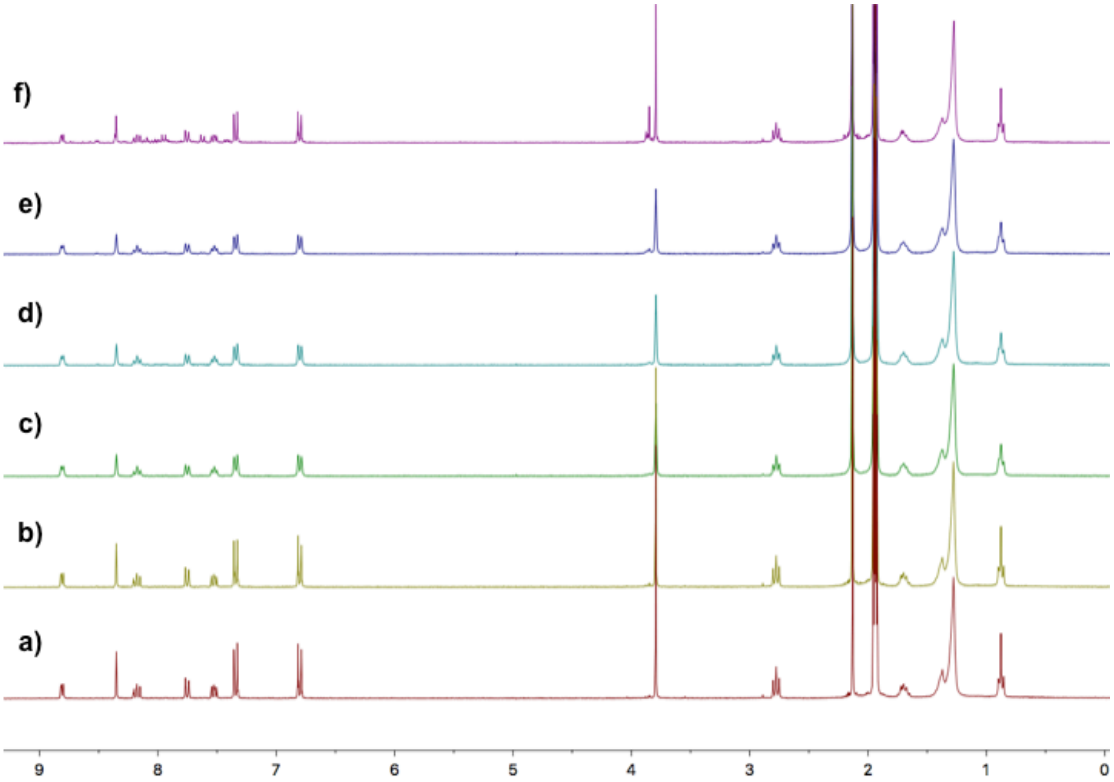


Figure appendix-29 ^{1}H NMR spectrum of complex **38c** in acetonitrile-d_3 at a concentration of 4 mM after 0 hour (a), 8 hours (b), 16 hours (c), 24 hours (d), 48 hours (e), and 72 hours (f).

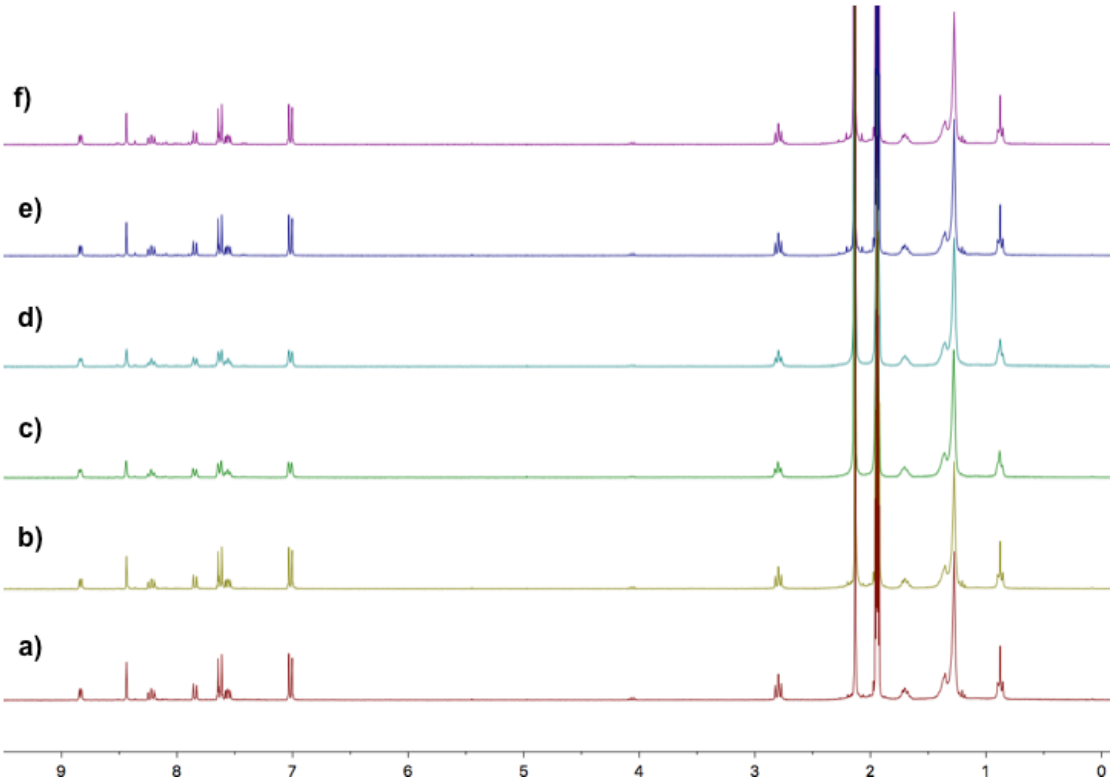


Figure appendix-30 ^{1}H NMR spectrum of complex **38d** in acetonitrile-d_3 at a concentration of 4 mM after 0 hour (a), 8 hours (b), 16 hours (c), 24 hours (d), 48 hours (e), and 72 hours (f).

RÉSUMÉ

Dans cette thèse, des complexes $[Re(N^N)(CO)_3X]^{n+}$ ont été conçus pour différentes applications. Dans le premier chapitre, l'impact de différentes modifications sur le ligand N^N ou le ligand X sur les propriétés photophysiques des complexes a été étudié. Dans le second chapitre, une série de nouveaux complexes a été conçue et étudiée comme catalyseurs homogènes/hétérogènes pour l'électroréduction du CO_2.
Dans le dernier chapitre, nous avons introduit un ligand diimine pour la coordination au Re en tant que lien dans la macrocyclisation de peptidomimétiques pour la modulation d'interaction protéine-protéine.

MOTS CLÉS

Rhenium tricarbonyles ; sondes luminescentes ; électroréduction du CO_2 ; ciblage d'interactions bioloqiques

ABSTRACT

In this thesis, $[Re(N^N)(CO)_3X]^{n+}$ complexes were designed towards different applications. In the first chapter, the impact of different modifications on either the N^N ligand or the X ligand on the photophysical properties were studied experimentally and computationally. In the second chapter, we designed and studied a series of new Re complexes as homogeneous/heterogeneous catalysts for CO_2 electroreduction and their catalytic abilities were evaluated. In the last chapter, the introduction of a Re complex as macrocyclic linker in macrocyclic peptidomimetics is used to both stabilize the active secondary structure and introduce imaging modalities towards modulation of protein-protein interactions.

KEYWORDS

rhenium carbonyle complexes; luminescent probes; CO_2 electroreduction ; targeting of biological interactions